Search for resonant Higgs boson pair production in the semi-leptonic $b\bar{b}WW^*$ decay channel with the ATLAS detector at the Large Hadron Collider

Nurfikri Bin Norjoharuddeen

St Cross College, University of Oxford

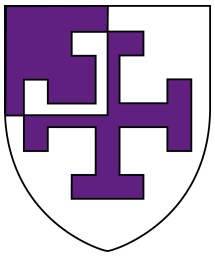

Thesis submitted in partial fulfilment of the requirements for the degree of Doctor of Philosophy at the University of Oxford

Trinity Term, 2018

Search for resonant Higgs boson pair production in the semi-leptonic $b\bar{b}WW^*$ decay channel with the ATLAS detector at the Large Hadron Collider

Nurfikri Bin Norjoharuddeen
St Cross College, University of Oxford

Thesis submitted in partial fulfilment of the requirements for the degree of
Doctor of Philosophy at the University of Oxford

Trinity Term, 2018

Abstract

This thesis presents the search for resonant Higgs boson pair production with the $b\bar{b}WW^*$ decay mode in the semi-leptonic final state containing one electron or muon with multiple jets and missing transverse momentum. The Standard Model of particle physics predicts only non-resonant pair production of Higgs bosons but a number of theoretical models predict massive new particles that decay to two Higgs bosons. The search is performed using $\sqrt{s} = 13$ TeV proton-proton collision data collected in 2015 and 2016, corresponding to an integrated luminosity of 36.1 fb^{-1}, recorded by the ATLAS detector at the Large Hadron Collider.

The search focuses on TeV-scale resonances which decay to two Higgs bosons with large transverse momenta. Jets with large radius parameter are used to reconstruct the kinematics of one of the Higgs bosons which decays hadronically into a pair of b-jets. The invariant mass of the reconstructed Higgs boson pair is used to test the compatibility of the observed data with the Standard Model background prediction. No statistically significant excess is observed in data over the expected Standard Model background and upper limits are placed with 95% confidence level on the resonant Higgs boson pair production cross section times branching ratio for narrow spin-0 and wide spin-2 resonant states.

Techniques which use advanced subjet reconstruction algorithms to improve identification of high momentum Higgs boson decays to b-jets are also presented. The three algorithms demonstrate significant performance improvements in simulation compared to the standard method currently used by the ATLAS collaboration.

Acknowledgements

I feel extremely lucky to have had Çiğdem İşsever as my DPhil supervisor. You have shared your wisdom and guided me not just in physics, but also on how to navigate through a huge scientific collaboration. Your critical advice have shaped me to be a better physicist and for that, I am truly grateful and forever will be indebted to you.

I want to express my deepest gratitude to the people of the Oxford ATLAS Exotics group: Todd Huffman, Tony Weidberg, James Frost, Jiahang Zhong, Katharina Behr, Kate Pachal, Lydia Beresford, Beojan Stanislaus, Santiago Paredes and Migle Stankaityte. Thank you for your mentorship and the friendly work environment.

To the dedicated people of the particle physics sub-department, it has been a pleasure to be part of this brilliant group of physicists. Special thanks to Ian Shipsey, in his capacity as the head of the sub-department, for awarding me the bursary to fund my last year so that I can complete my thesis. To the wonderful Sue Geddes, Kim Proudfoot, Francesca Oliver and Jennifer Matthews, I am forever grateful for all your help especially during the time when I had to move to Geneva from Oxford and back again. To Francesco Giuli, Mike Nelson, Jon Burr, Luigi Vigani, Luigi Marchese, Miha Zgubic, Luca Ambroz, Cecilia Tosciri, Kla Karava and Maria Giovanna Foti, our pleasant discussions about ATLAS projects have helped strengthen my understanding of various aspects of the experiment and for this, I sincerely thank you.

During my early days in ATLAS, my authorship qualification task was under the JetEtMiss performance group and the jet substructure sub-group. The JetEtMiss group is full of wonderful and passionate physicists and I am grateful to everyone for your guidance. I would like to especially mention Benjamin Nachman, whose insights on jet physics have hooked me on everything about jets. It was a pleasure to take part in the advanced subjet reconstruction project. To Shih-Chieh Hsu, Chunhui Chen, Dan Guest, Sam Meehan, Jie Yu, and Nikola Whallon, I thank you for all the fun times navigating through the ATLAS software.

To the hardworking people of the $hh \to b\bar{b}WW^*$ analysis group: Mark Neubauer, Haris Kagan, Biagio Di Micco, Eric Torrence, Suyog Shrestha, Monica Verducci, Bin Gui, Apara-

jita Dattagupta, Gabriel Palacino, Benjamin Tannenwald, John Myers, Muhammad Sohail; it has been a pleasure to work with all of you. I thank you for your key guidance on the boosted analysis. I would also like to thank the Editorial Board (Nikos Konstantinidis, Alison Lister, Chip Brock) for their patience following the progress of my search analysis. Special thanks to the Higgs physics group and HBSM sub-group convenors (Fabio Cerutti, Kerstin Tackmann, Liron Barak, Nikos Rompotis) for your careful ideas and insights which resulted in the approval of my analysis.

I am truly indebted to the Malaysian Ministry of Education (and by extension, the Malaysian taxpayers) for their financial support under University of Malaya's Academic Training Scheme (SLAI) and my professors in Malaysia's National Centre For Particle Physics (NCPP), Wan Ahmad Tajuddin and Zainol Abidin for their full recommendation of my application for the SLAI scholarship. Without them, this work would not have been achievable. I hope to offer my experience to the development of experimental particle physics in Malaysia as repayment of the support that was given to me.

To all my friends in the UK, in Geneva, and back home in Malaysia, I cherish your friendship and for making each place feel like a second home. I would like to especially thank Afiq Aizuddin, Siew Yan Hoh, Amjad Kotbi, Abu Ubaidah Amir, Noorkhallaf, Cristian Arcola, Jesus Lopez, Fatimah Mohamed, Izan Tahir and the Malaysian UCL/Camden/Oxford family. To Soefira, ma copine, your love is a constant reminder that there is always more to life than just smashing tiny particles and understanding how the universe works.

I have known Mariyan Petrov since the first day of my DPhil journey, as we were assigned to the same office (658a). Thank you for all the times that you have been here for me when I am in need of someone to share my joys and frustrations. I will certainly miss our friday night walks in Geneva and our cultured discussions on physics and on life in general. My dear friend, it has been my utmost privilege to share this journey with you.

Last but not least, I want to express my warmest thanks to my family, in particular my parents. You have have supported me in my endeavours to be a successful scientist and inspired me to pursue my dreams. You have shaped me into the person I am today. This thesis is dedicated to you.

Preface

This thesis summarises the work undertaken by the author throughout the duration of his DPhil studies. The work was performed for a period of over three and a half years from October 2014 to March 2018 within the ATLAS collaboration. The work presented in this thesis has been carried out in collaboration between the author and other members of the ATLAS experiment. Below are remarks by the author on his involvement and contribution in the ATLAS collaboration.

Figures with the label "ATLAS" or "ATLAS preliminary" have featured in ATLAS publications or conference/public notes, respectively. Figures without the "ATLAS" label have either been taken from non-ATLAS publications or have been included in the ATLAS-internal supporting documentation for an ATLAS publication and circulated internally.

Throughout this thesis, "natural units" are adopted where the reduced Planck constant and the speed of light are set to unity ($\hbar = c = 1$) and the unit of energy is electron-volts (eV).

Large-R jet mass reconstruction

Chapter 5 reports the author's work on studies of the large-R jet mass reconstruction. The work in this chapter was published in an ATLAS conference (CONF) note [1]. The following are the author's contributions to the note:

- The jet mass studies started off as an ATLAS collaboration authorship qualification task to derive the calorimeter-based jet mass calibration factors and provide an offical recommendation for ATLAS analyses in time for Run-2 of the LHC. The author designed the calibration procedure, set up the analysis framework and derived the calibration factors for the anti-k_t $R = 1.0$ trimmed calorimeter jet collection.

- The author participated in the commissioning of the track-assisted jet mass for general use by ATLAS analysis groups. He specifically worked on demonstrating the performance gain of the method, the track selections required for the calculation of the

track-assisted jet mass and developed its implementation within the ATLAS reconstruction software. The calibration factors for the track-assisted jet mass were also derived by the author. The author also demonstrated the potential improvement to the jet mass resolution with the combined jet mass definition.

- The author was one of the co-editors of the CONF note [1]. He was responsible for the text editing of the note and the coordination of the multiple performance analysis groups aiming to be included in the note.

Search for resonant Higgs boson pair production in the $hh \to b\bar{b}WW^*$ decay mode

In this thesis, the search for resonant Higgs boson pair production analysis focuses on what is called the "boosted" topology, and it is optimized for searches of TeV scale resonances. Another complimentary search analysis focuses on the "resolved" topology, which is optimized for resonances below the TeV scale. Both analysis presented regular updates of their results in the $hh \to b\bar{b}WW^*$ analysis group which is based in the ATLAS Higgs physics analysis group.

The author was fully involved in all aspects of the boosted analysis. The contents of Chapters 6 and 7 were solely produced by the author with supervision by Professor Cigdem Issever, Professor Todd Huffman and Dr James Frost.

The author was a key developer of the CxAOD_HHbbWW analysis framework used by the $hh \to b\bar{b}WW^*$ analysis group. The framework is used to produce ntuples for both the boosted and resolved analysis and it is also used to process the ntuples for the production of the histograms. The framework used for the statistical treatment of the boosted analysis results (Chapter 7) was adapted from the WSMaker statistical framework [2] maintained by the ATLAS $h \to b\bar{b}$ sub-group. The author adapted the WSMaker framework for it to be compatible with the strategy used in the boosted analysis. The data-driven multijet background estimation method (Section 6.2.2) was implemented first in the resolved analysis by other $hh \to b\bar{b}WW^*$ group members. The author adapted the principle of the method and modified its technical implementation and strategy to suit the needs of the boosted analysis.

At the time of writing, the combined publication of both resolved and boosted analysis results is currently in preparation within the ATLAS collaboration. The details of the resolved analysis is not included in this thesis as the author is not fully involved in the full chain of the resolved analysis. The interested reader is referred to a PhD thesis written by Benjamin Tannenwald, here in Reference [3], which details the resolved analysis strategy and results. A comparison of the upper limits on the scalar resonance cross-section between

the boosted and resolved analyses is presented in Section 7.2.3 to compare the sensitivity between the two analyses.

Advanced subjet reconstruction

Chapter 8 is a summary of a study on new subjet reconstruction techniques to improve the identification of $h \to b\bar{b}$ decay. The results were published as an ATLAS PUB note [4] with editorial involvements by the author. The results were presented by the author at the BOOST 2017 workshop [5]. The following are the author's contributions to the note:

- The author was one of the main developers of analysis framework to process signal and background samples for optimization and performance comparison.
- The optimisation of the variable radius jet algorithm parameter was the author's sole responsibility.
- The author assisted in the official implementation of variable radius track jets reconstruction in the ATLAS reconstruction software; such that it can be used by any ATLAS physics analysis groups.
- The author conducted the performance comparison of all subjet reconstruction techniques for the case when no reconstruction-level b-tagging is applied on the subjets.

Contents

List of Figures

List of Tables

Chapter 1

Introduction

The Standard Model (SM) represents one of the great achievements in the field of elementary particle physics with the ability to predict various physics phenomena and observables that have later been experimentally confirmed. The final component of the SM to be verified through experiment is the existence of the Higgs boson, the particle associated with the field that generates the mass of all elementary particles. In 2012, the ATLAS and CMS experiments at the Large Hadron Collider (LHC) presented the observation of a new boson with a mass of approximately 125 GeV. Numerous measurements of the properties of this new boson followed, and all have been found to be consistent with SM predictions indicating that the new particle is indeed a Higgs boson.

The discovery of the Higgs boson opens a new chapter of precision physics measurements at the LHC with the deluge of data that has been gathered so far, and also to be collected still. The measurements will provide stringent tests of the SM and in particular, will probe the electroweak symmetry breaking mechanism which forms a foundation of the SM by studying the properties related to the Higgs boson. One of the long term goals of the LHC is to measure the Higgs self-coupling which provides information on the shape of the Higgs potential, a key ingredient in the symmetry breaking mechanism. The self-coupling can be measured from the non-resonant production of Higgs boson pairs. With the mass of the Higgs boson known, the prediction of the self-coupling is made within the context of the SM.

Unfortunately, theoretical calculations predict the cross-section for non-resonant Higgs boson pair production at the LHC to be of the order of 30 fb, which is three order of magnitude smaller compared to the single Higgs boson production. This makes it extremely difficult for LHC experiments to observe Higgs boson pair events, let alone to actually measure the self-coupling. Phenomenological studies by theorists and projections by ATLAS and CMS experiments are in agreement with the prediction that the Higgs boson pairs can

be observed with the full LHC dataset, which is expected to have an integrated luminosity of 3000 fb^{-1} by 2035.

A rather pessimstic outlook on the observation of Higgs boson pairs in the short term can be made into an opportunity to search for signs of physics Beyond the Standard Model (BSM). BSM theories offer predictions of Higgs boson pair production through decays of massive new particles. Some theories predict a much higher rate of Higgs boson pair production when compared with the SM expectation. Therefore any observation of Higgs boson pairs in the present LHC dataset is a clear indication of BSM physics since such a signature is not expected to be observed with the limited LHC dataset. Furthermore, the pairs will manifest themselves as a resonant structure over SM backgrounds in the Higgs boson pair invariant mass spectrum, which makes it easier to establish the existence of new BSM particles.

This thesis presents a search for resonant Higgs boson pair production by analysing 36.1 fb^{-1} of proton-proton collision data at centre-of-mass energy of $\sqrt{s} = 13$ TeV. This data was collected by the ATLAS detector from the start of Run 2 of the LHC during 2015 and 2016. The probed Higgs boson pair decay mode in this search analysis is the $b\bar{b}WW^*$ decay mode where one of the Higgs bosons decays to a pair of b-quarks while the other Higgs boson decays to a pair of W bosons. The decay mode was explored in the semi-leptonic final state which consists of a single lepton from one of the W boson decays and multiple jets from the other W boson and the Higgs boson decay. The search is performed by looking for an excess of events in data over the expected SM background in the invariant mass distribution of the reconstructed Higgs boson pairs.

The search analysis is optimized for the so-called "boosted" topology, where resonant Higgs boson pair productions come from decays of massive BSM particles with masses at the TeV scale. Due to the very large masses of the BSM particles, they impart large transverse momentum ("boost") when decaying to the Higgs bosons. The resulting decay products of the Higgs boson then get collimated. In particular, the separation of the two b-quarks from the Higgs boson decay will be very small such that the default jet clustering algorithm with a small radius parameter is inefficient in resolving the b-quark pair. As an alternative, the strategy employed by this analysis is to reconstruct the Higgs boson decay with a single jet with a much larger radius parameter in the boosted topology. In contrast to the boosted topology, the "resolved" topology is when jet clustering with small radius parameter is efficient at resolving the two b-quarks from the Higgs boson decay. The resolved topology is more focused on searches for sub-TeV scale resonances and non-resonant production of Higgs boson pairs.

This thesis is structured as follows: Chapter 2 lays out the theoretical motivation behind

the search analysis. In Chapter 3, a description of the experimental apparatus is provided which is then followed by an overview of the reconstruction of particles by the ATLAS detector as physics objects used in the search analysis (Chapter 4). Chapter 5 discusses extensively the reconstruction of the mass of jets with large radius parameter in the ATLAS experiment. A detailed account of the analysis strategy for the search is given in Chapter 6, followed by the results in Chapter 7. Chapter 8 presents a study on new algorithms to improve the identification of high momentum Higgs boson decays to b-quarks which can improve analysis senstivity for future searches of Higgs boson pair production.

Chapter 2

Theoretical Background

This chapter contains a short overview of the relevant theoretical background. Section 2.1 covers a qualitative description of the SM, while focusing more on the electroweak interaction and the consequences of the symmetry breaking in the interaction. In Section 2.2, the physics of the Higgs boson at the LHC is summarized. Section 2.3 discusses extensively the phenomenology of Higgs boson pair production and provides the motivation of the search analysis presented in this thesis.

2.1 The Standard Model of Particle Physics

The Standard Model is a quantum field theory (QFT) [6, 7] which describes the electromagnetic, weak and strong interactions. The SM is a renormalizable, locally invariant gauge theory where the Lagrangian describing the theory is gauge invariant under transformations of the $SU(3)_C \times SU(2)_L \times U(1)_Y$ symmetry group. Within the SM, matter in the universe is described by spin-1/2 (fermionic) fields, while the interactions between fermions are mediated by the exchange of integer spin (bosonic) fields.

The fermions are split into three generations of particles. These generations are identical with respect to their quantum numbers but vary with respect to their masses. Each generation consists of one up-type and one down-type quark, which partake in the electroweak and strong interactions, and one charged lepton and its corresponding neutrino, which partake in the electroweak interaction. The particle content in the SM are the following:

- Quarks: the up, charm and top quarks (u, c, t); the down, strange and bottom quarks (d, s, b).
- Charged leptons: the electron, muon and tau leptons (e^-, μ^-, τ^-).

- Neutral leptons: the electron neutrino, muon neutrino and tau neutrino (ν_e, ν_μ, ν_τ).
- Gauge bosons: spin-1 (vector) bosons acting as mediators for the electromagnetic (the photon, denoted as γ), weak (W^+,W^-,Z^0) and strong (the gluon, denoted as g) interactions.
- Higgs boson: a spin-0 (scalar) boson arising from the electroweak symmetry breaking mechanism, giving mass to other particles in SM.

The theory of the strong interaction is described by Quantum Chromodynamics (QCD), which is briefly touched upon in Section 2.1.1. The electroweak interaction, which is a unification of the electromagnetic and weak forces, is discussed in Section 2.1.2 and it continues in Section 2.1.3 with the breaking of the local gauge symmetry in the interaction which gives masses to the W and Z bosons and the prediction of a scalar boson.

2.1.1 Strong interaction

The interaction between colour charged quarks is described by QCD, associated to the non-abelian $SU(3)_C$ symmetry group which has eight massless spin-one gauge bosons, the gluons. The gluons carry colour (and anti-colour) charge and, due to the non-abelian nature of QCD, they can interact with each other. Quarks and anti-quarks are the simplest representations of this group and different bound states follow from their interactions.

The QCD coupling α_S varies depending on the transferred momentum Q, the so called running α_S. Thus, the strength of the strong interaction between particles with colour charge increases with the distance, leading to a complex dynamic which cannot be described perturbatively. In a short range distance, i.e high-energy regime, QCD is instead well described in terms of weakly-interacting quarks and gluons allowing the use of perturbation theory for the description of the relative interactions. This phenomenon is the so-called asymptotic freedom [8, 9].

In the low energy regime of QCD, the quark confinement effect takes place. The characteristic energy scale at which this effect becomes important is $\Lambda_{\text{QCD}} \sim 1/\text{fm} \sim 200$ MeV. Thus, a coloured object produced in a collider cannot exist on its own but rather "confined" together with other coloured objects. Pairs of quarks and anti-quarks are produced from the vacuum and combined with gluons and the original quark until formation of colourless objects such as hadrons through a process called hadronization. Predictions for hadron formation are obtained using Monte Carlo models, tuned to experimental results. Phenomenological models [10, 11] are usually applied in order to describe completely the results of the hadronization process.

2.1.2 Electroweak interaction

The gauge theory of the electroweak interaction, a unification of the electromagnetic and weak interactions is described by the $SU(2)_L \times U(1)_Y$ gauge group. The electroweak interaction consists of the left-handed (L) weak isospin doublets ($T = 1/2$) and the right-handed (R) components which transform as singlets. Charged leptons and quarks interact under the electroweak symmetry with both left-handed and right-handed components while for neutrinos, only its left-handed component is present in the SM.

The interaction is mediated by four bosons, three ($W_\mu^1, W_\mu^2, W_\mu^3$) related to the $SU(2)_L$ group and the other one (B_0) related to the $U(1)_Y$ transformations. These four boson fields do not represent the observable states of the vector bosons responsible for the weak (charged and neutral) currents and the electromagnetic interaction. The physical fields A_μ, Z_μ, W_μ^+ and W_μ^- corresponding respectively to the photon, the Z^0 and $W^\pm$ bosons, are in fact described within the Glashow-Salam-Weinberg electroweak theory [12–15] as linear combinations of the W_μ and B_μ fields:

$$A_\mu = B_\mu \cos\theta_w + W_\mu^3 \sin\theta_w \tag{2.1}$$

$$Z_\mu = B_\mu \sin\theta_w + W_\mu^3 \cos\theta_w \tag{2.2}$$

$$W_\mu^\pm = \frac{1}{\sqrt{2}}(W_\mu^1 \pm W_\mu^2) \tag{2.3}$$

where θ_w is the Weinberg mixing angle. The gauge couplings of the $SU(2)_L$ and $U(1)_Y$ group, g and $g^{'}$ are related to θ_w and to the electromagnetic coupling constant (the electron charge e) by the following relation:

$$e = g \sin\theta_w = g^{'} \cos\theta_w. \tag{2.4}$$

2.1.3 Spontaneous breaking of electroweak symmetry

The renormalizability of the electroweak theory imposes that the mediators are massless bosons [16]. However, the limited range of the weak interaction implies that the mediators are massive, which was later confirmed experimentally by the discovery of the W boson [17, 18] and Z boson [19, 20], and attempts to add ad-hoc mass terms for the vector bosons in the Lagrangian of the electroweak interaction breaks the renormalizability of the theory. This contradiction is resolved by introducing a complex scalar field with non-zero vacuum expectation value, resulting in the spontaneous symmetry breaking of the $SU(2)_L \times U(1)_Y$ symmetry.

This mechanism, the Brout-Englert-Higgs mechanism [21–23] or more commonly known

as the Higgs mechanism, introduces a new component to the SM, ϕ, an $SU(2)_L$ complex scalar doublet with four real components, ϕ_i, the so-called the Higgs field:

$$\phi = \frac{1}{\sqrt{2}} \begin{pmatrix} \phi_1 + i\phi_2 \\ \phi_3 + i\phi_4 \end{pmatrix} \tag{2.5}$$

Its Lagrangian density and the Higgs potential $V(\phi)$ are defined:

$$\mathcal{L} = (D_\mu \phi)^\dagger (D^\mu \phi) - V(\phi) \tag{2.6}$$

$$V(\phi) = \mu^2 |\phi|^2 + \lambda |\phi|^4 \tag{2.7}$$

where μ and λ are the mass and self interaction coupling constant of the scalar field with their values chosen to be $\mu^2 < 0$ and $\lambda > 0$. The shape of the potential is visualized in Figure 2.1.

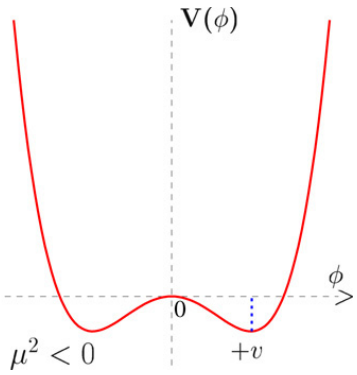

Figure 2.1: The shape of the Higgs potential for $\mu^2 < 0$. Retrieved from Reference [24].

The Higgs Lagrangian is, by construction, invariant under $SU(2)_L \times U(1)_Y$ transformation. However, the symmetry is spontaneously broken by a non-zero vacuum expectation value (VEV) of the Higgs field

$$\langle 0|\phi|0\rangle = \frac{1}{\sqrt{2}} \begin{pmatrix} 0 \\ \upsilon \end{pmatrix} \tag{2.8}$$

with the value of the VEV $\upsilon = \mu^2/\lambda$, while preserving the invariance under $U(1)_{EM}$ transformations. The masses of the W (m_{W}) and Z (m_{Z}) bosons, are acquired by absorbing three degrees of freedom of the ϕ doublet into the longitudinal components of the physical vector bosons. The masses of the W and Z bosons are proportional to υ and to g and g' coupling constants:

$$m_{\mathrm{W}} = \frac{vg}{2} \tag{2.9}$$

$$m_{\mathrm{Z}} = \frac{v\sqrt{g^2 + g'^2}}{2} \tag{2.10}$$

The remaining degree of freedom of the Higgs field manifests itself as a new elementary scalar particle, the Higgs boson (denoted as h). The value of the Higgs boson mass (m_{h}) is related to the parameters of the Higgs potential:

$$m_{\mathrm{h}} = v\sqrt{2\lambda} \tag{2.11}$$

Within the Higgs mechanism, the fermion masses are achieved without breaking the gauge symmetry of the Lagrangian by introducing a coupling term, known as Yukawa coupling, between the fermion fields and the Higgs field.

2.2 Higgs boson physics at the LHC

The observation of W and Z bosons consolidated the SM as the model for the electroweak interaction. The theory was renormalizable and very successful phenomenologically, but depended on the existence of a massive scalar field, the Higgs field. The Higgs field should interact with any other massive field, and the coupling should depend on the mass of the field. Unfortunately, in the SM the mass of the Higgs boson (Equation 2.11) is not predicted as λ is a free parameter, therefore the experimental search for the existence of the Higgs bosons had to be driven by its mass.

Prior to the LHC, the search for the SM Higgs boson was conducted at the Large Electron-Positron (LEP) collider [25], that had operated at CERN from 1989 to 2000 with centre of mass energies $\sqrt{s}$ between 90 and 209 GeV. The production mechanism of the Higgs boson in association with a Z boson was searched for at LEP but no discovery was ever claimed and a lower bound of $m_{\mathrm{h}} = 114.4$ GeV was established [26]. Searches were also performed at the Tevatron [27], the proton-antiproton collider at Fermilab, by the CDF and D0 experiments at $\sqrt{s} = 1.96$ TeV. The studied production process and decay mode was the associated production of a Higgs boson with a W or Z boson and the decay of the Higgs boson to a $b\bar{b}$ pair An excess of events was observed in the data compared with the background predictions in the mass range between 120 GeV and 135 GeV, with a significance of approximately 3 standard deviations, which can be interpreted as evidence of a particle compatible with the SM Higgs boson [28].

The discovery of a new particle with mass around 125 GeV was announced on the 4th July 2012 separately by the ATLAS and CMS collaborations [29, 30], after having analysed the data collected at $\sqrt{s} = 7$ TeV, around 5 fb^{-1}, and at $\sqrt{s} = 8$ TeV, around $5 - 6$ fb^{-1}. After the end of the Run 1 of the LHC, the total data sample collected at 8 TeV was increased up to an integrated luminosity of ~ 20 fb^{-1}, so it was possible to study some properties of this new particle which confirmed that it is compatible with the SM Higgs boson and that its spin and parity is consistent with 0^+ [31, 32]. The combined measured mass of the Higgs boson by ATLAS and CMS collaborations with Run 1 data is $m_{\mathrm{h}} = 125.09 \pm 0.24$ GeV [33].

The production of a Higgs boson at the LHC occurs mainly via four mechanisms: gluon-fusion (ggF), vector boson-fusion (VBF), associated production with a vector boson (Vh) and associated production with a pair of top quarks (tth). The primary production mechanism at the LHC is gluon-gluon fusion (Figure 2.2a), in which gluons annihilate via a quark loop. This occurs predominantly via loops of top quarks, due to their strong coupling to the Higgs boson. This is by far the dominant production mode, with a cross-section approximately an order of magnitude larger than any other. The second largest production mechanism is the VBF (Figure 2.2b), in which two W or Z bosons radiated from quarks annihilate to produce a Higgs boson. The VH production (Figure 2.2c) involves a Higgs boson being produced in association with a W or Z boson. The W or Z boson is produced by coupling to a quark-antiquark pair, and then the Higgs boson is radiated off the weak boson. The tth production (Figure 2.2d) accounts for only a very small fraction of the total production cross-section, approximately two orders of magnitude less than the dominant ggF production.

The Higgs boson couplings to the fundamental particles are directly related to their masses. More precisely, the SM Higgs boson couplings to fermions are linearly proportional to the fermion masses, whereas the couplings to vector bosons are proportional to the square of the boson masses. As a result, the dominant Higgs boson decay mechanisms involve the coupling of Higgs bosons to W, Z bosons and/or the third or second generation quarks and leptons. The Higgs boson may decay to many final states via a number of decay modes. The branching fraction of the decay modes for a SM Higgs boson with $m_{\mathrm{h}} = 125$ GeV is shown in Table 2.1. For the decay modes where the Higgs boson decays to a pair of W bosons ($h \to WW^*$) or Z bosons ($h \to ZZ^*$), one of the daughter vector boson is off-shell (denoted by the star symbol). The decay modes of interest in this thesis are the $h \to b\bar{b}$ and $h \to WW^*$ mode and they rank as the modes with the two highest branching fractions.

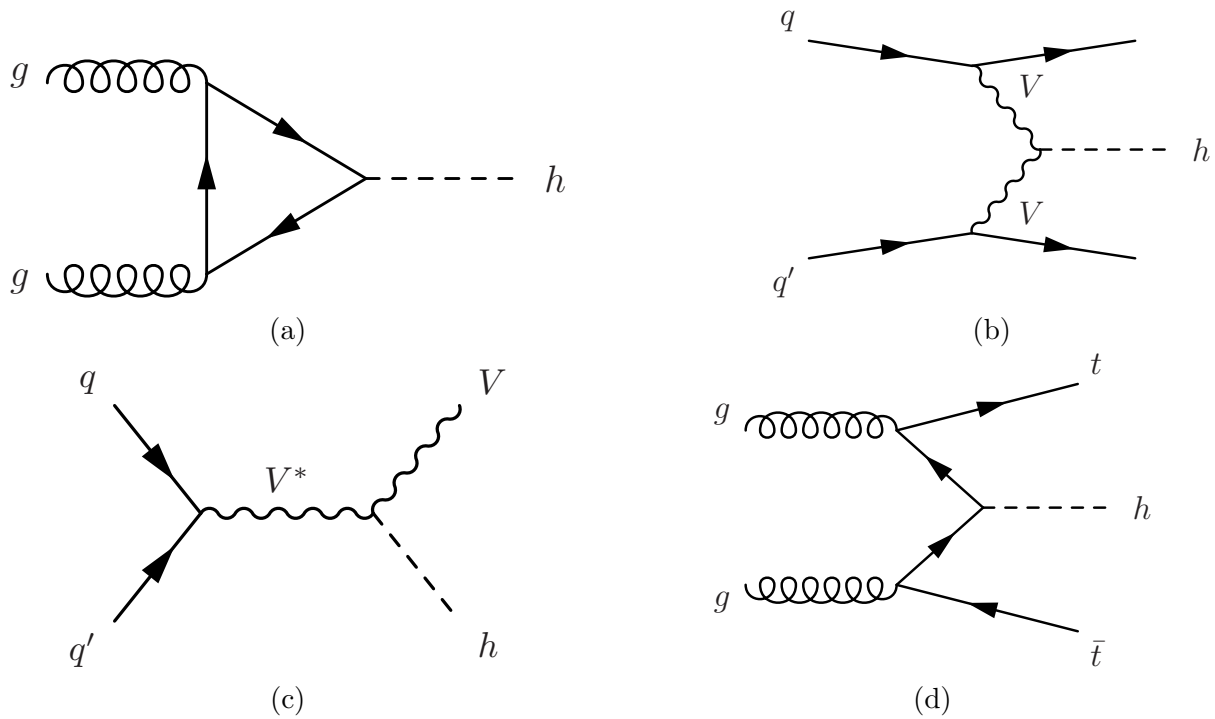

Figure 2.2: Feynman diagrams describing Higgs boson production mechanisms at the LHC: (a) ggh, (b) VBF, (c) Vh, (d) tth.

Decay mode	Branching ratio	Relative uncertainty
$h \to b\bar{b}$	5.8×10^{-1}	$\pm 0.7\%$
$h \to WW^*$	2.2×10^{-1}	$\pm 1.0\%$
$h \to gg$	8.2×10^{-2}	$\pm 3.4\%$
$h \to \tau\tau$	6.3×10^{-2}	$\pm 1.2\%$
$h \to c\bar{c}$	2.9×10^{-2}	$\pm 1.2\%$
$h \to ZZ^*$	2.6×10^{-2}	$\pm 1.0\%$
$h \to \gamma\gamma$	2.3×10^{-3}	$\pm 1.7\%$
$h \to \mu\mu$	2.2×10^{-4}	$\pm 1.2\%$

Table 2.1: Higgs boson decay modes and their corresponding branching ratio for a Higgs boson with a mass of $m_{\mathrm{h}} = 125.09$ GeV. The relative uncertainty is the theoretical uncertainty on the branching ratio. Branching ratio values retrieved from Reference [34].

2.3 Higgs bosons pair production at the LHC

The discovery of the Higgs boson and the detailed study of its properties have been an important confirmation of the validity of the SM. For Run 2 and beyond, the priorities of the LHC experiments are related to precise understanding of the SM and in particular, the electroweak symmetry breaking sector, and also continued searches for new physics phenomena predicted by BSM theories. Some of these searches can be performed using the

Higgs boson as a tool for discovery and a precise knowledge of the strength of the Higgs boson interactions with SM fields can shed light on its origin and push constraints on BSM scenarios.

The reconstruction of the Higgs potential involves the measurement of the Higgs self-coupling which is accessible in processes involving the production of Higgs boson pairs (di-Higgs) at the LHC. The main production mechanism for di-Higgs events predicted by the SM at the LHC is the gluon-fusion mechanism and the process is described at leading order by two Feynman diagrams shown in Figure 2.3. The triangle loop (Figure 2.3a) and the heavy quark box (Figure 2.3b) diagrams interfere destructively, and consequently result in a very small production cross section prediction. The predicted cross section of this process at the centre of mass energy of 13 TeV is of the order of 30 fb [34] which indicates that this is an extremely rare process compared to the expected irreducible SM backgrounds. To put into perspective how small the di-Higgs production cross-section is, the cross-section for single Higgs boson production via the gluon-fusion mechanism is calculated to be $48.85^{+4.56\%}_{-6.72\%}$ pb [34] at 13 TeV, which is about 1000 times larger than the predicted di-Higgs cross-section. The detection of the SM Higgs boson pair production at LHC is expected to be accessible realistically only with the High Luminosity (HL) LHC [35–42]. However, many phenomenological studies of BSM scenarios predict enhancements to the rate of di-Higgs production [43–62] and any observation of di-Higgs events at the LHC will be a clear indication of new physics beyond the SM. A selection of the relevant BSM theories is discussed in the next sections.

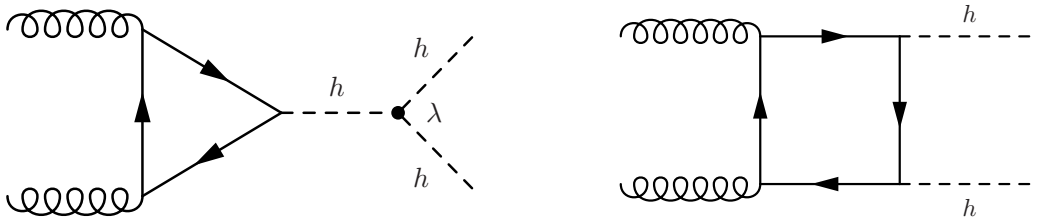

Figure 2.3: Feynman diagrams describing di-Higgs production from gluon fusion at leading order.

2.3.1 Non-resonant production

The term non-resonant Higgs bosons pair defines all the processes that lead to a pair of Higgs bosons without the presence of an intermediate state (resonance) in the production chain. The Higgs boson self-interaction is allowed in the SM and thus also the production of two Higgs bosons from the same vertex. The process is strongly suppressed due to the expected value of the Higgs boson self-coupling ($\lambda \simeq 0.13$ [63]). In the SM, Higgs boson

pair production occurs predominantly by gluon fusion via an internal fermion loop, where the top quark is dominant. The extension to BSM theories [45–48, 53–58, 62], brings four main variations in the Higgs boson pair production modes: the modification of the Higgs self-coupling; the presence of a BSM particle that acts in the internal fermion loop; the possibility of a direct contact interaction between Higgs bosons and top quarks (Figure 2.4a) and the possibility of a direct contact interaction between Higgs bosons and gluons (Figure 2.4b). The experimental implications of the BSM theories are the enhancement of the Higgs boson pair production cross section and a considerable modification of the kinematic properties of the Higgs boson pairs, which can be measured at the LHC.

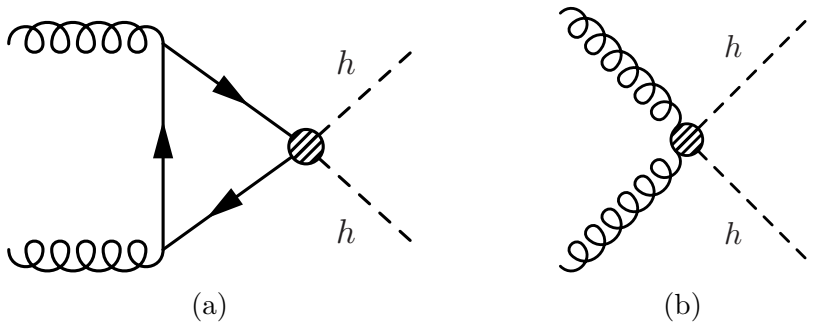

Figure 2.4: Feynman diagrams describing di-Higgs production with new vertices for di-Higgs production.

2.3.2 Resonant production

In the SM, there is no prediction of resonant di-Higgs production (Figure 2.5), hence any resonant-like signature in the di-Higgs system's invariant mass spectrum observed in data clearly indicates the existence of new particles from BSM. Several BSM scenarios predict new heavy particles decaying to a pair of Higgs bosons. BSM models which extend the Higgs sector by adding an additional scalar singlet [49] or doublet [64] predict heavy scalar particles that can decay to the lighter SM Higgs boson. Warped extra dimension theories also predict [43, 65] the existence of a massive scalar or a tensor (spin-two) particle which could decay to a pair of Higgs bosons.

Two-Higgs-doublet models

Two-Higgs-Doublet models (2HDM) postulate the existence of an additional Higgs doublet field. Such extension of the scalar sector is of particular interest since the presence of two Higgs doublets is required in low-energy supersymmetric (SUSY) scenarios to break the electroweak symmetry [66].

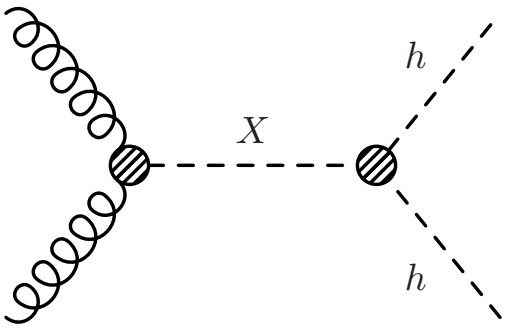

Figure 2.5: Feynman diagram for a generic BSM resonance (X) production and its decay to a pair of Higgs bosons.

The extension of the scalar potential with the addition of a Higgs doublet can be realized in two main ways by requiring that all quark fields couple with the same doublet (type I 2HDM) or that right-handed quarks of charge +2/3 and 1/3 couple to two distinct doublets (type II 2HDM). An extensive discussion of 2HDM models and the various phenomenological consequences arising from the models can be found in Reference [64].

The addition of another Higgs doublet implies the existence of five new particles: two CP-even neutral scalars h and H, one CP-odd pseudoscalar A^0, and two charged scalars H^+ and H^-. An assumption usually taken in this model is that the masses of the two neutral scalars obey $m_{\mathrm{H}} > m_{\mathrm{h}}$ with the lighter neutral scalar interpreted as the scalar boson observed at the LHC. The introduction of an additional doublet produces deviations of the couplings of the Higgs bosons and, more importantly for this context, implies the presence of a Hhh coupling that produces a resonant $H \to hh$ signature.

Warped extra dimensions

Proposals for a spacetime with more than three spatial dimensions have since long time been formulated as an attempt to unify the forces of Nature. Since the first idea by Kaluza and Klein back in the 1920s, extra dimensions have become an important part of quantum gravity theories and found a key role in string theories. In particular, as explained in Reference [67] the weakness of the gravitational force can be explained by its propagation through these additional dimensions.

A mechanism that differs from the one above is the Randall-Sundrum (RS) model [68] where the extra dimensions are compactified ("warped extra dimensions") between two points of the space referred to as "branes". One brane corresponds to the Planck scale (M_{Pl}) and the other brane to the electroweak scale (TeV brane) with the region separating the two branes (the "bulk") is controlled by an exponential metric. The gap between these

two fundamental scales of the Nature is parametrized by a warp factor k. This is illustrated in Figure 2.6.

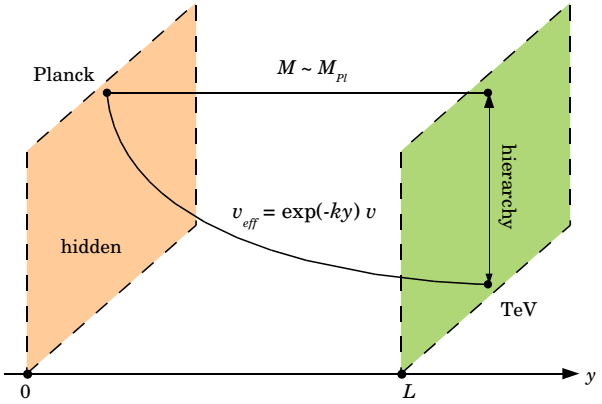

Figure 2.6: The generation of an exponential hierarchy. Taken from Reference [69].

In the original RS model, called "RS1", all SM particles are confined on the TeV-brane. An extension to the RS model which is of particular interest for LHC phenomenology [43,65] is the "bulk-RS" model whereby only the Higgs boson is confined to the TeV brane while gauge bosons and matter fields can propogate in the bulk. This is theoretically interesting because it allows for a Higgs sector at the TeV scale while, at the same time, allowing for high-energy unification of gauge couplings and providing a natural hierarchy of masses. The only free parameter of the bulk-RS model is defined as the ratio of the warp factor to the reduced[1] Planck mass ($c = k/\bar{M}_{Pl}$). The phenomenological consequence of these models is the existence of gravitons with spin-2, which can can be produced at the LHC and then decay to a pair of Higgs bosons.

2.3.3 Previous searches

Searches for di-Higgs production at the LHC in pp collisions at $\sqrt{s} = 8$ TeV (Run-1) and $\sqrt{s} = 13$ TeV (Run-2) have been performed by both the ATLAS and CMS collaborations.

Using Run-1 data, the ATLAS collaboration explored the $b\bar{b}b\bar{b}$ [70], $b\bar{b}\gamma\gamma$ [71], $b\bar{b}\tau\bar{\tau}$ and $WW^*\gamma\gamma$ [72] decay modes. No statistically significant deviation from the SM expectation was observed in the $b\bar{b}b\bar{b}$, $b\bar{b}\tau\bar{\tau}$ and $WW^*\gamma\gamma$ decay modes but a modest local excess of 2.4 standard deviation above the SM background expectation was observed in the $b\bar{b}\gamma\gamma$ decay mode. The combination of all the decay modes [72] does not show any significant deviations from the SM expectation and 95% confidence level upper limits are set on both resonant and non-resonant di-Higgs production cross-sections with the observed (expected) upper limits

[1]The reduced Planck mass is defined as $\bar{M}_{Pl} = M_{Pl}/\sqrt{8\pi}$.

on the non-resonant di-Higgs cross section corresponding to 70 (48) times the SM prediction. Figure 2.7a shows the observed and expected upper limits on cross-section of spin-0 heavy Higgs boson production decaying to Higgs boson pairs as a function of the heavy Higgs boson mass, for each of the decay modes and their combination.

The CMS collaboration explored the $b\bar{b}b\bar{b}$ [73, 74], $b\bar{b}\gamma\gamma$ [75], $b\bar{b}\tau\bar{\tau}$ [76–78] final states. Results were found to be in agreement with the SM predictions and used to set cross-section upper limits on both resonant and non-resonant production. Figure 2.7b shows the observed and expected upper limits on the cross-section of spin-0 resonance production decaying to Higgs boson pairs as a function of spin-0 resonance mass for all di-Higgs decay modes. A combination of all decay modes [76] was used to set upper limits on both resonant and non-resonant di-Higgs cross sections with the non-resonant upper limit observed to be 43 times the SM cross-section, for an expected upper limit of 47 times the SM prediction.

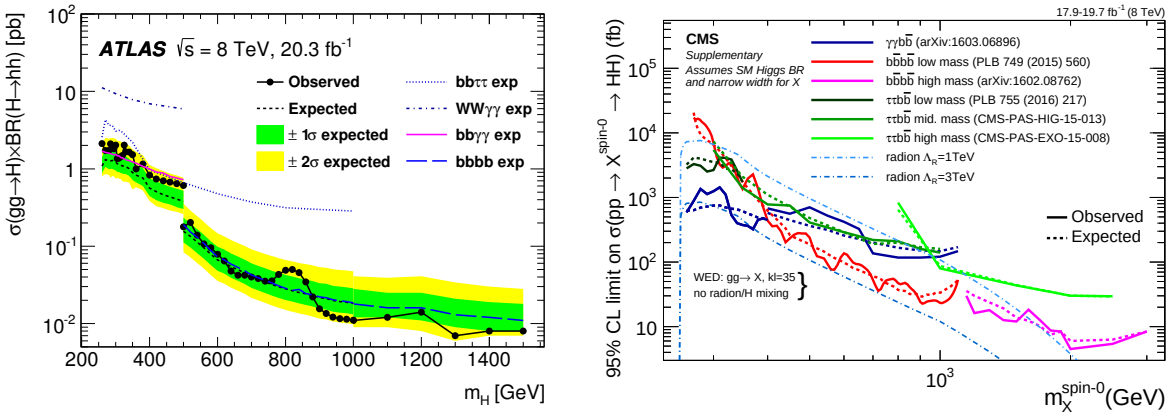

(a) (b)

Figure 2.7: Observed and expected upper limits on (a) cross-section of spin-0 heavy Higgs boson production decaying to Higgs boson pairs as a function of the heavy Higgs boson mass, for each of the di-Higgs decay modes and their combination in Run-1 by the ATLAS collaboration [79] and on (b) cross-section of spin-0 resonance production decaying to Higgs boson pairs as a function of spin-0 resonance mass for all di-Higgs decay modes in Run-1 by the CMS collaboration [80].

It is important to note the complementarity of the different decay modes as a function of the resonance mass, from the Run-1 results by both ATLAS and CMS collaborations. The exploration of several decay modes and final states is therefore necessary to probe in the most effective way BSM physics at the LHC in di-Higgs processes.

The ATLAS collaboration have updated the analysis results of each decay mode with $\sqrt{s} = 13$ TeV data collected in 2015 and 2016. For the $b\bar{b}\gamma\gamma$ decay mode [81], the local excess seen in Run-1 data was not confirmed with 3.2 fb^{-1} of 2015 dataset. In the updated $b\bar{b}b\bar{b}$ decay mode with 36.1 fb^{-1} [82], the sensitivity is now pushed to new resonance masses

as low as 300 GeV and as high as 3 TeV. As for the CMS collaboration, the $b\bar{b}b\bar{b}$ [83, 84], $b\bar{b}\gamma\gamma$ [85], $b\bar{b}\tau\bar{\tau}$ [86,87] decay modes have been updated with $\sqrt{s} = 13$ TeV data corresponding to 35.9 fb^{-1}. In addition to these channels, the collaboration has published the first result in the $b\bar{b}WW^*$ decay mode [88], focusing on the final state where each of the W bosons decays to a lepton and a neutrino. Of all the available results at the time of writing this thesis, the most stringent observed (expected) upper limit on the non-resonant SM di-Higgs production cross section, from each collaboration, is 13 (21) times the SM expectation which comes from the $b\bar{b}b\bar{b}$ decay mode by the ATLAS collaboration and 19 (17) times the SM prediction where $b\bar{b}\gamma\gamma$ is the most sensitive decay mode by the CMS collaboraton.

2.3.4 $hh \to b\bar{b}WW^*$ 1-lepton final state

The topic of this thesis focuses on the search for resonant di-Higgs production in the $b\bar{b}WW^*$ decay mode ($hh \to b\bar{b}WW^*$), where one of the Higgs bosons decays to a pair of b quarks, which then hadronizes to two b-jets, and the other Higgs bosons decays to a pair of W bosons. The branching fraction of the $b\bar{b}WW^*$ decay mode is the second largest (27.9%), after the $b\bar{b}b\bar{b}$ decay mode (33.6%). There are three possible classifications for this decay mode based on the number of leptons in the final state: 0-lepton (all-hadronic), 1-lepton (semi-leptonic) and 2-lepton (fully-leptonic).

The search analysis in this thesis explores the 1-lepton final state ($hh \to b\bar{b}WW^* \to b\bar{b} + \ell\nu q\bar{q}$), in which one W boson decays (leptonically) to a lepton (ℓ) and a neutrino and the other W boson decays (hadronically) to a pair of quarks; which then hadronizes to two jets. The lepton flavour considered is either an electron or a muon. The electron and muon can originate directly from the leptonic W boson decay or from the leptonically decaying τ lepton which originated from the W boson. The decay with hadronically decaying τ lepton is not considered in this search. Figure 2.8 shows a diagram of resonant di-Higgs production and the subsequent decay to the $b\bar{b}WW^*$ 1-lepton final state topology. This semi-leptonic final state constitutes about $\sim 35\%$ of the whole $b\bar{b}WW^*$ decay mode and 9.8% of the whole di-Higgs production final state decays.

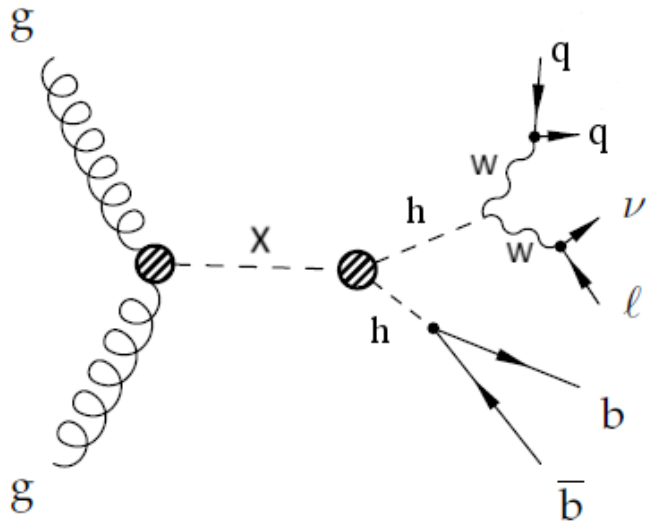

Figure 2.8: Diagram depicting a generic BSM resonance (X) decaying to pair of Higgs bosons (hh) with one of the pair decaying to a $b\bar{b}$ pair and while the other to WW^* pair. One of the W bosons decays to a pair of $q\bar{q}$ and the other decays to a lepton (ℓ) and a neutrino (ν).

Chapter 3

Experimental Setup

This chapter introduces the experimental setup for the search analysis presented in this thesis. It starts with a brief description of the Large Hadron Collider in Section 3.1. An overview of the ATLAS detector with its subcomponents is presented in Section 3.2, with the recorded dataset used for the search analysis in Section 3.3. Section 3.4 briefly discusses the procedure to simulate physics processes for comparison with data.

3.1 The Large Hadron Collider

The Large Hadron Collider at CERN [89] is a hadron collider, located in the same tunnel that was used to host the LEP collider. It is a circular proton accelerator of about 27 km in circumference and it is installed deep underground at about 100 m from the surface. It comprises 9600 magnets cooled down to a temperature of 1.9 K by superfluid helium. The main dipoles, used to steer the protons, produce a magnetic field of up to 8.33 T while the other magnets are used for focusing and tuning the proton beams.

The LHC is part of a bigger accelerator complex which reuses several of CERNs older accelerators as shown in Figure 3.1. The acceleration chain begins with a duoplasmatron that extracts protons from hydrogen molecules and accelerates the resultant protons into Linac2. Linac2 focusses this beam and accelerates it to 50 MeV, delivering it to the Proton Synchrotron (PS) Booster, which accelerates the protons in turn to 1.6 GeV. The PS Booster feeds into the PS which accelerates the beam to 26 GeV, and feeds into the Super Proton Synchrotron (SPS). The SPS accelerates the protons to an energy of 450 GeV and eventually injects them into the LHC in opposite directions and accelerates them further. The protons form spatial bunches separated by 50 or 25 ns of time.

The LHC supports four major experiments and they are located at different interaction points around the LHC ring, each of them designed for high sensitivity to a wide range of

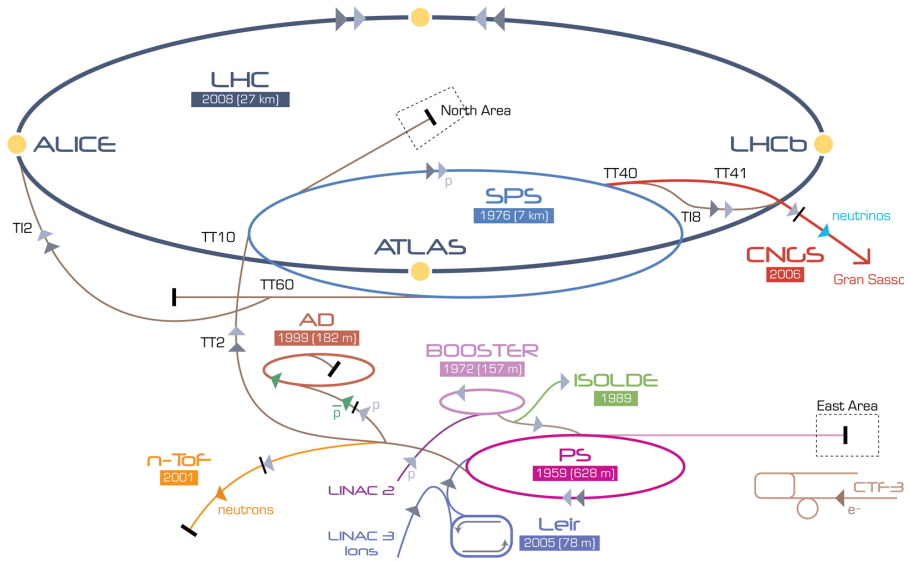

Figure 3.1: The CERN Accelerator Complex. Figure retrieved from Reference [90].

physics phenomena both within and beyond the SM:

- ATLAS, a general-purpose detector designed for high transverse momentum physics [91].
- CMS (**C**ompact **M**uon **S**olenoid), a general-purpose detector much like ATLAS in purpose but with different designs [92].
- LHCb, a single arm forward spectrometer dedicated to b-physics studies [93].
- ALICE(**A** **L**arge **I**on **C**ollider **E**xperiment), devoted to lead-ion collisions to study the properties of quark-gluon plasma [94].

3.2 The ATLAS detector

The ATLAS (**A** **T**oroidal **L**HC **A**pparatu**S**) detector [91] is one of the four main experiments at the LHC. It is 45m long, 25m tall and weighs about 7000 tonnes. Its structure has the shape of a cylinder centered at the interaction point with its axis along the beamline. The layout is typically broken down into 3 sub-detector systems: the Inner Detector, the calorimeters and the Muon Spectrometer. The detector is illustrated in Figure 3.2, showing the overall scale and also its main sub-detectors.

ATLAS and its sub-detectors were designed with the aim of probing for a wide range of phenomena at the TeV scale. These include not only the search and measurements of the SM Higgs boson and possible BSM processes, but also to test the SM to its limits in electroweak, QCD and flavour physics. The following specifications were required to maximise the physics potential of the detector:

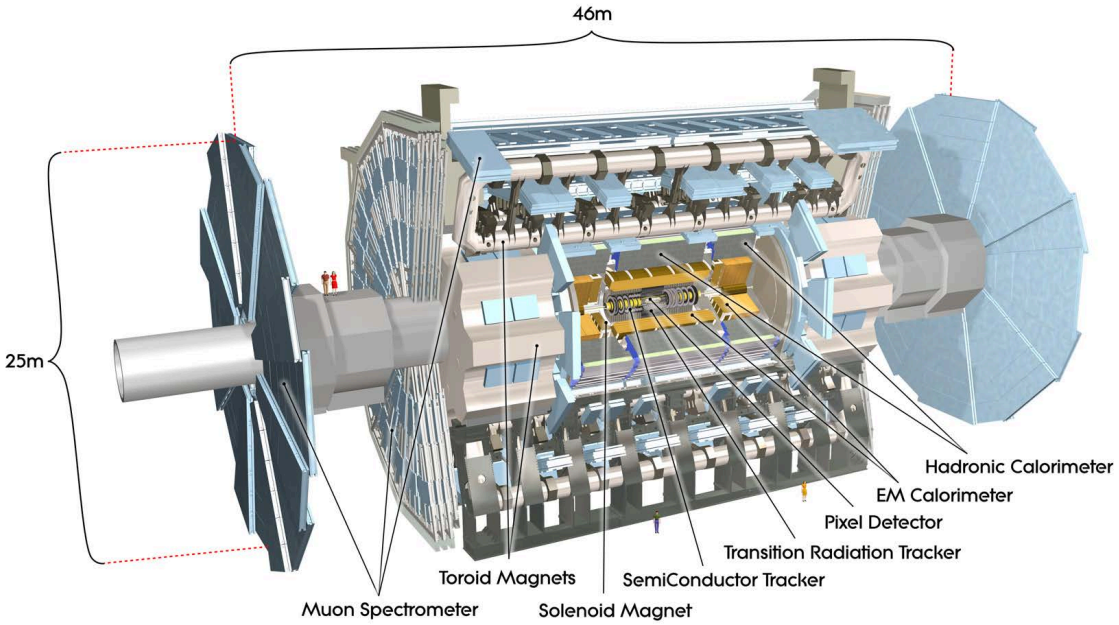

Figure 3.2: The ATLAS Detector. Figure retrieved from Reference [95].

- Radiation-hard and fast electronics due to the high bunch crossing rate and high luminosity.
- An excellent electromagnetic calorimeter for electron and photon identification.
- Good muon identification and momentum resolution.
- Good charged-particle momentum resolution and measurement in the inner detector. The ability to identify and reconstruct secondary vertices near the interaction point is also important.

3.2.1 Coordinate system

The coordinate system used in ATLAS is a right-handed Cartesian coordinate system and each axis is defined such that the x-axis points towards the center of the LHC ring, the y-axis points upwards and the z-axis is the beam line, with the origin of the system set at the nominal interaction point (IP) located in the center of the detector. Two angles, the polar angle, θ, and the azimuthal angle, ϕ, are defined respectively, as the angle from the z-axis in the y-z plane and the angle around the beam axis in the x-y plane. The radial

distance, R, measures the distance from the beam line.

The polar angle is not invariant under a Lorentz boost along the z-axis and it is more useful to use the rapidity, defined as

$$y = \frac{1}{2} \ln \frac{E + p_z}{E + p_z} \tag{3.1}$$

with E being the particle energy and p_z being its longitudinal momentum. In the limit of massless particles, the rapidity equals the pseudorapidity,

$$\eta = -\ln(\tan \frac{\theta}{2}). \tag{3.2}$$

An often used measure to quantify the distance between two objects in $\eta - \phi$ space is $\Delta R = \sqrt{(\Delta\eta)^2 + (\Delta\phi)^2}$. Apart from the pseudorapidity, another often used variable that is Lorentz invariant is the transverse momentum p_{T} which is defined as $p_{\mathrm{T}} = \sqrt{p_x^2 + p_y^2}$, where p_x and p_y are the transverse momentum components.

3.2.2 Magnet system

The ATLAS magnet system [96] is designed to induce magnetic fields inside the ATLAS detector, particularly in the inner detector and muon spectrometers, to bend the trajectories of charged particles to improve the resolution on their momentum measurement. A solenoid with an inner diameter of 2.46 m, a thickness of 0.1 m, and a length of 5.8 m generates a 2 T axial magnetic field within the tracking-focused inner detectors, from a 7730 A current running through the 1154 turns of wire. The solenoid was designed to minimize the impact of its material on particles energy loss before entering the calorimeters, and it contributes only 0.66 radiation lengths at $\eta = 0$. Three toroidal magnets generate a magnetic field for the muon spectrometers: a barrel toroid and two endcap toroids. The barrel toroid is a system of eight coils ringing the detector, 25.3 m long and with an inner diameter of 9.4 m.

3.2.3 Inner detector

The ATLAS Inner Detector (ID) system [97, 98] is built for precision tracking of charged particles. It covers the range $|\eta| < 2.5$. In this range, approximately 1000 particles are generated from every bunch crossing in the detector. This requires having fine granularity to achieve the resolutions required for good momentum measurement and vertex reconstruction.

The ID consists of three sub-components: the pixel detector, semiconductor tracker

(SCT), and transition radiation tracker (TRT). It is surrounded by a solenoid providing a 2 T axial magnetic field which bends particles in the transverse plane to allow for momentum measurements of charged particles. Figure 3.3 shows the layout of each of these components.

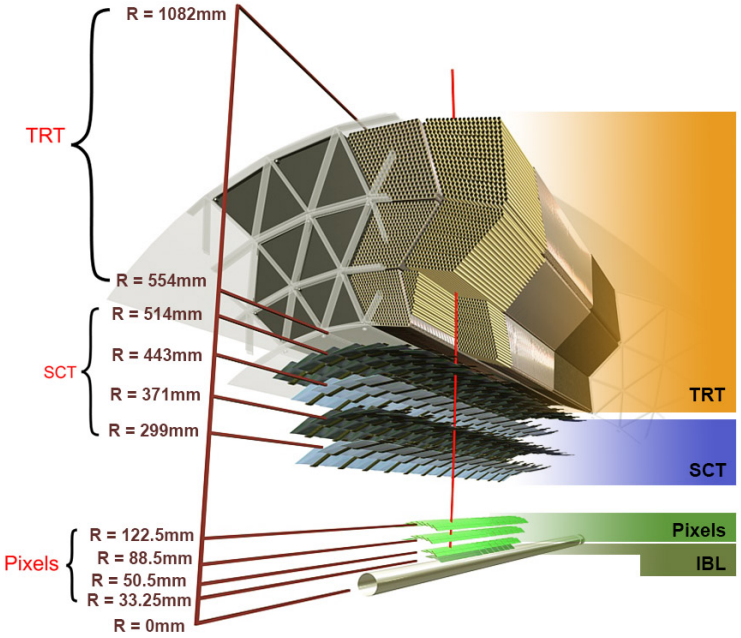

Figure 3.3: Section of the ATLAS inner detector (ID) in the barrel region showing the arrangement of its three subsystems: the pixel detector, the semiconductor tracker (SCT) and the transition-radiation tracker (TRT). The numbers mark the radial distance of the different layers from the beam line at $R = 0$ mm. The red vertical line in the centre marks the trajectory of a charged particle through the ID. The beam pipe is shown in grey. Figure retrieved from Reference [99].

Pixel detector

The pixel detector is the first detector particles traverse after being generated in proton collisions and is the most granular detector. Its operation is crucial for precision tracking and vertex reconstruction as well as higher level object reconstruction like tagging of jets from b-quarks. The basic sensing element in this subdetector is a silicon pixel detector. In the barrel region, the pixel detector has three concentric layers of sensors surrounding the beamline. In the endcap region, it consists of disks perpendicular to the beam axis. The detector is segmented in the $R - \phi$ plane and in z. Usually, three pixel layers are crossed by a charged particle track. The intrinsic accuracies of the sensors are 10 μm in $R - \phi$ and 115 μm in z (or R for the endcap). During the shutdown period between Run-1 and Run-2, a fourth layer called the Insertable B-Layer (IBL) [100] was installed in addition to the existing Pixel detector which improves the track reconstruction performance.

Semiconductor tracker

The semiconductor tracker (SCT) consists of silicon microstrips and comprises the next four layers of the ID. This sub-detector has 6.4 cm long sensors that are chained into strips with a strip pitch of 80 μm. Some of the strips have a small stereo angle to allow for measurement of both angular coordinates. The intrinsic accuracies are 17 μm in $R-\phi$ and 580 μm in z (or R in the endcap).

Transition radiation tracker

The transition radiation tracker (TRT) [101] serves two purposes: charged particle tracking and identification. It consists of 4 mm diameter straw tubes filled with a 70/27/3% gas mixture of xenon, carbon dioxide, and oxygen to provide tracking of charged particles. A track from a particle traversing the ID typically have more than 30 TRT straw hits. The material in between the straws is designed to induce transition radiation which can be useful for particle identification. As particles pass between media with different dielectric constants, they emit transition radiation that can cause additional showers in the TRT. This is particularly useful for discrimination between electrons and pions or other charged hadrons, as the amount of transition radiation is proportional to the Lorentz factor of the travelling particle.

3.2.4 Calorimeter system

The ATLAS calorimeter system consists of two main sub-components: a fine granularity electromagnetic calorimeter tailored for the measurement of photons and electrons and multiple coarser hadronic calorimeters dedicated to the measurement of hadronic showers. The calorimeter system has broader coverage than the inner detector, covering the region out to $|\eta| < 4.9$. It is also designed to deliver good containment of showers so as to limit leakage into the muon system. Figure 3.4 shows the layout of the calorimeter system.

Both the electromagnetic and hadronic calorimeters are sampling calorimeters. They alternate active material for energy measurement with passive material for energy absorption. The materials used for each purpose vary based on the type of calorimeter and its location in the detector. A comprehensive description of the calorimeter system can be found in Reference [103].

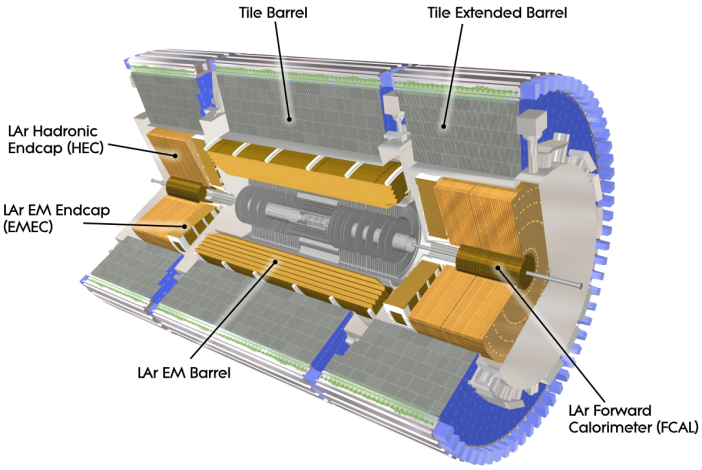

Figure 3.4: Schematic representation of the calorimeter system, comprising the EM and hadronic calorimeters. Figure retrieved from Reference [102].

Electromagnetic calorimeters

The electromagnetic (EM) calorimeters consist of two barrel segments and two endcaps. A liquid Argon (LAr) sampling medium fills the space around the lead absorbers, which are arranged in an accordion shape. This increases their stopping power for electromagnetic showers, with > 22 radiation lengths in the barrel and > 24 in the endcaps, and ensures complete azimuthal coverage.

The barrel, covering $|\eta| < 1.475$, is segmented into five layers with a minimum granularity in $\Delta\eta$ of 0.003125 and in $\Delta\phi$ of 0.025. The endcaps, divided into two wheels covering $1.375 < |\eta| < 2.5$ and $2.5 < |\eta| < 3.2$, are segmented into 2 to 3 layers with minimum granularity in $\Delta\eta$ of 0.003125 and in $\Delta\phi$ of 0.1. A LAr-filled presampler layer is located inside the EM calorimeter, in the region $|\eta| < 1.8$, and measures energy lost upstream from the calorimeter. The EM calorimeters are designed to have an overall energy resolution of $\sigma(E)/E = 10\%/\sqrt{E} \oplus 0.5\%$, where the first term represents stochastic variation and the second reflects local non-uniformities in calorimeter response, falling within the the desired accuracy for energy measurement resolution.

Hadronic calorimeters

The hadronic calorimeters consist of a tile calorimeter barrel composed of steel absorbers and plastic scintillators as the sampling medium, two liquid argon endcaps, and a LAr forward calorimeter which extends the reach in $|\eta|$ to improve hadronic shower energy measurements in the high-$|\eta|$ region. The tile calorimeter covers $|\eta| < 1.0$ in a central barrel and $0.8 < |\eta| < 1.7$ in two extensions, organized in 3 layers with a granularity in $\Delta\eta \times \Delta\phi$ of 0.1×0.1

in the inner two layers and 0.2×0.1 in the third layer. The endcaps are again separated into two wheels, covering $1.5 < |\eta| < 2.5$ and $2.5 < |\eta| < 3.2$ with granularities in $\Delta\eta \times \Delta\phi$ of 0.1×0.1 and 0.2×0.2 respectively. The energy resolution for the hadronic calorimeter systems varies with each component and particle species, but all are within the desired resolution of $\sigma(E)/E = 50\%/\sqrt{E} \oplus 3\%$.

Forward calorimeters

The forward calorimeters (FCal) extend the range of both electromagnetic and hadronic calorimetry with coverage in the region $3.1 < \Delta\eta < 4.9$, overlapping slightly with the endcaps to minimize gaps in coverage. They are divided into three modules; the first is electromagnetic, and contains copper absorbers, while the remaining hadronic modules contain tungsten absorbers. The FCal granularities are described in $\Delta x \times \Delta y$; they measure 3.0 cm $\times$ 2.6 cm in the electromagnetic layer, 3.3 cm $\times$ 4.2 cm in the first hadronic layer, and 5.4 cm $\times$ 4.7 cm in the second hadronic layer. The energy resolution of the FCals also fall within desired values of $\sigma(E)/E = 100\%/\sqrt{E} \oplus 10\%$

3.2.5 Muon spectrometer

Muons are unique among the detectable particles produced by high-energy interactions; their large mass makes them unlikely to shower in the calorimeters, and their long lifetime means that, at higher energies, they will decay outside the detector. The muon spectrometer [104] adds additional tracking capabilities in the region outside the hadronic calorimeter, so muons can be identified primarily from tracks in this and the inner detector. The system consists of chambers with complementary purposes: trigger chambers which measure the perpendicular coordinate and provide timing resolution, allowing a muon to be matched to a particular bunch crossing and tracking chambers which measure the projection of the muon track in the bending plane induced by the magnetic field to high precision. Figure 3.5 shows the layout of the ATLAS muon spectrometer system.

The precision tracking is provided by Monitored Drift Tube (MDT) chambers covering the $|\eta| < 2.7$ range and Cathode-Strip Chambers (CSC) in the $2 < |\eta| < 2.7$ range. The MDT subsystem consists of three layers of chambers arranged in concentric cylindrical shells around the beam axis in the barrel region and installed in planes perpendicular to the beam in the end-caps. The chambers are composed of three to eight layers of drift tubes with an average resolution of about 35 μm per chamber in the bending plane. The CSCs are used in the innermost tracking layer due to their higher rate capability and time resolution. They are multiwire proportional chambers with cathode planes segmented into strips in

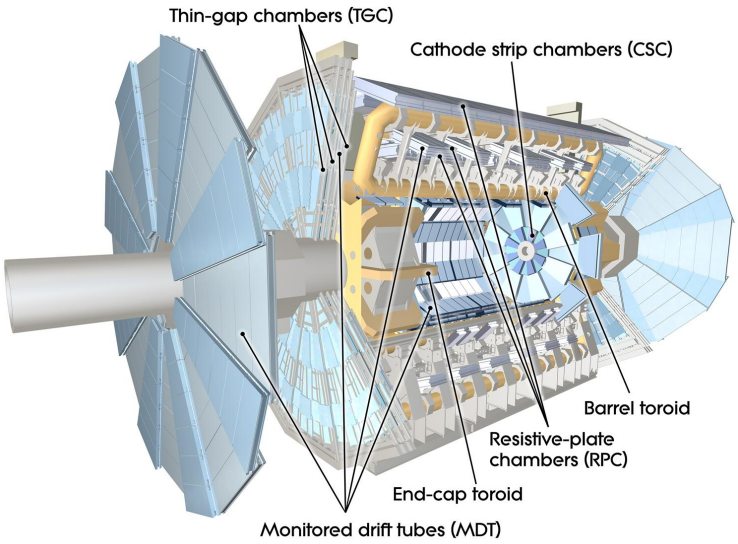

Figure 3.5: Cut-away view of ATLAS muon system. Figure retrieved from Reference [105].

orthogonal directions, allowing for both coordinates to be measured from the induced charge distribution. The resolution of a chamber is 40 μm in the bending plane (η) and about 5 mm in the transverse plane ϕ). The performance goal of the muon system is p_{T} resolution of about 10 % for high-p_{T} tracks, corresponding to a sagitta along the z direction of about 500 μm which has to be know to better than 50 μm.

The trigger system is composed of Resistive Plate Chambers (RPC) in the barrel ($|\eta| < 1.05$) and Thin Gap Chambers (TGC) in the end-cap ($1.05 < |\eta| < 2.4$). Both types of chambers deliver track information with a response time of less than 25 ns and are thus capable also of tagging the beam-crossing for the purpose of an event time calibration. The RPC consists of parallel electrode plates with gas-filled gaps and provides a resolution of about 10 mm in both bending and non-bending planes. The TGCs operate on the same principle as multi-wire proportional chambers. Their characteristic is that the wire-to-cathode distance is smaller than the wire-to-wire distance to achieve a fast collecting time.

3.2.6 Trigger system

At the LHC, an enormous number of pp collision events is produced, which can not be directly stored. These events need to be selected (triggered) during data taking in order to select events that are of interests for physics analyses. The ATLAS trigger system reduces an event rate of 40 MHz to an average recording rate of 1 kHz. The trigger system for Run 2 [106] consists of two levels of event selection: a hardware-based Level-1 (L1) trigger and a software-based high-level trigger (HLT). The ATLAS Trigger and Data Acquisition (TDAQ) system is shown in Figure 3.6.

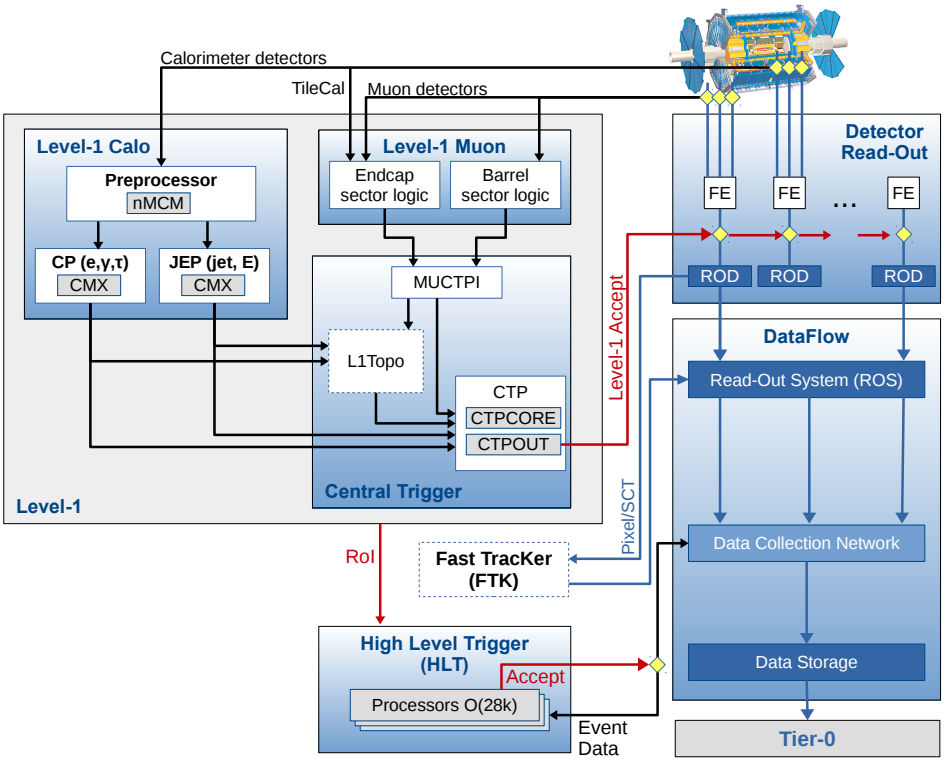

Figure 3.6: Overview of the ATLAS data acquisition and trigger system for Run 2. Figure retrieved from Reference [106].

The L1 trigger utilizes information from the muon trigger chambers and the calorimeters. Therefore, the L1 system consists of the L1 calorimeter trigger system (L1Calo), the L1 muon trigger system (L1Muon) and the Central Trigger Processors (CTP). Initially, front-end (FE) electronics read out and process signals received from the sub-detectors and keep it in pipeline memories. Then, the L1 trigger receives this output from the detectors and makes a decision whether to accept the event or discard it in less than 2.5 μs. It reduces the event rate from 40 MHz to 100 kHz and determines Regions-of-Interest (ROIs) with detailed trigger information (a geometrical region in $\eta \times \phi$ with information about a type of object and passed threshold). If the event is accepted, then the sub-detector will transfer data from its front-end pipelines to a Read-Out Driver (ROD). The ROD collects and formats the data and transfers it to the Read-Out System (ROS).

The L1Calo triggers on high-E_{T} objects (like electrons and jets) and events with large total transverse and missing energy. The L1Muon triggers on muons for each of the prede-

fined p_{T} thresholds. The CTP receives the inputs from the L1Calo and L1Muon and makes the final decision to accept events. It supports up to 512 items in trigger menus, where each item defines the objects to be triggered on with specific combination of requirements on the input data.

The output from the L1 trigger in the form of ROIs is passed to the HLT. The HLT was created by merging the Level-2 and Event Filter farms deployed in Run 1 [107, 108]. It runs on a computing cluster accessing data from the ROIs, applying offline-like algorithms using the full-event information. Objects, like muons and electrons, reconstructed by the HLT are said to be HLT-level objects. The final output from the HLT is around 1 kHz. After the events are accepted by the HLT, they are transferred to local storage at the experimental site and exported to the Tier-0 facility at CERN's computing centre for offline reconstruction.

3.3 ATLAS data

The expected event rate of a certain physics process is determined by the product of its cross section and the instantaneous luminosity: $Rate = \sigma \cdot L$. The instantenous luminosity is measured in units of $\mathrm{cm}^2\mathrm{s}^{-1}$ and it is defined as:

$$L = \frac{N_p^2 n_b f \gamma}{4\pi\epsilon\beta^*} F \tag{3.3}$$

N_p denotes the number of protons per bunch, n_b the number of bunches per beam, f the revolution frequency and γ the relativistic factor. The numerator gives the number of interactions per time interval while the denominator describes the area of overlap between the two colliding beams with the beam cross sectional size at injection (β^*) and the beam emittance (ϵ). The factor F can account for a possible beam crossing angle. The amount of collision data recorded over a certain time period is quantified by the integrated luminosity and is measured in units of inverse cross section.

The ATLAS experiment started collecting data from 2009 and the run period, where the LHC ran with $\sqrt{s} = 7$ TeV and 8 TeV from 2011 to the end of 2012, was called Run-1. The maximum instantaneous luminosity was about $0.35 \times 10^{34}\mathrm{cm}^2 s^{-1}$ and the total integrated luminosity was about 24 fb^{-1} in 2012. The LHC restarted in 2015 after a long shutdown period. For the run period from 2015 to 2018, designated as Run-2, the LHC operates with $\sqrt{s} = 13$ TeV and has already surpassed design instantaneous luminosity with a maximum instantaneous luminosity of $1.4 \times 10^{34}\mathrm{cm}^2 s^{-1}$ in 2016.

For each proton bunch, there are 10^{11} protons and because of this it is likely that more than one pp interaction occurs per bunch crossing. The presence of additional interactions for

each bunch crossing is called "in-time pile-up". Due to the low time distance of 25 ns between each bunch crossing, interactions which happen directly before or after the interaction of interest can also be recorded since the read out time of the calorimeters is much slower. This is called "out-of-time pile-up". Pile-up is either measured as the number of primary vertices (N_{PV}) or as the mean number of interactions per bunch crossing (μ). N_{PV} does not consider out-of-time pile-up and is built from reconstructed vertices, while the calculation of μ is based on the measured luminosity.

The data used for the search analysis in this thesis was recorded by the ATLAS detector between 2015 and 2016 data run periods at the LHC at a center of mass energy $\sqrt{s}$ of 13 TeV. Figures 3.7a and 3.7b show the total integrated luminosities as a function of time in 2015 and 2016 respectively. The total delivered luminosity by the LHC was 42.7 fb^{-1} and the total recorded luminosity in the ATLAS detector was 39.5 fb^{-1}. The loss of integrated luminosity is due to the detector operation efficiency, but the high efficiency more than 90% was kept from 2015 to the end of 2016. The average μ for data recorded in 2015 and 2016 is $\langle\mu\rangle = 23.7$ and the distribution of μ for the whole data taking period is shown in Figure 3.8.

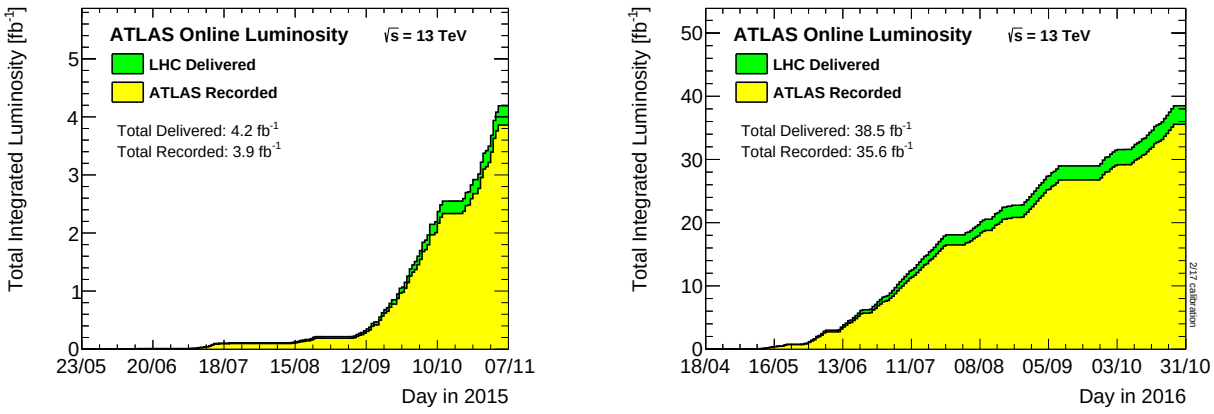

(a) (b)

Figure 3.7: Cumulative luminosity versus time delivered to (green) and recorded by (yellow) ATLAS during stable beams for pp collisions at $\sqrt{s} = 13$ TeV in (a) 2015 and (b) 2016. Figures retrieved from [109].

3.4 Event generation and detector simulation

The interpretation of collision data often relies heavily on the theoretical modelling of the physical processes arising from the collision and on a detailed simulation of the interactions of the outgoing particles resulting from the pp collision with the detector. The simulation of collision events uses Monte Carlo (MC) event generators [63] and undergoes several stages

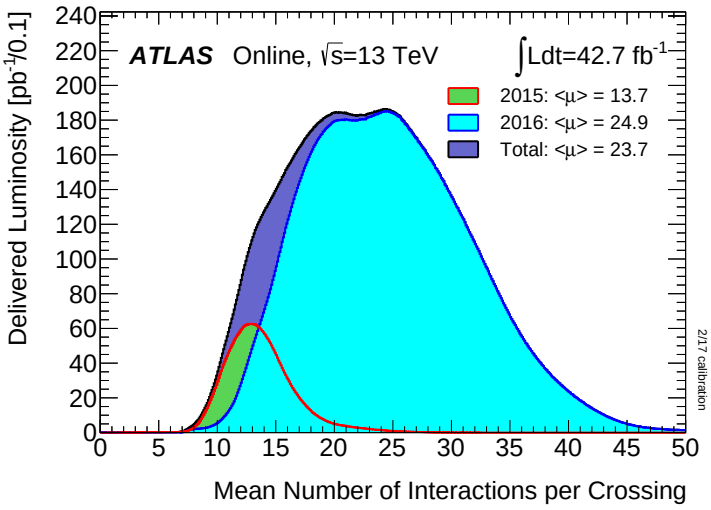

Figure 3.8: The mean number of interactions per bunch crossing for the 2015 and 2016 data taking periods. Figure retrieved from Reference [109].

of computation. MC generators calculate the matrix element of the physics processes of interest with the kinematics of the initial partons in the colliding protons selected from parton distribution functions (PDFs). Intermediate particles are then decayed according to their branching fractions. The showering of initial and final state partons involved in the process is also simulated, as is their hadronisation into observable final state particles. Finally, the underlying event (UE), the remnants of the incoming particles and their interactions, is simulated.

The final state particles from generated events are passed through a simulation of the ATLAS detector to model their interactions with the material of the sub-detectors using the ATLAS simulation infrastructure [110]. GEANT4 [111] is the standard detector simulator program used by the ATLAS collaboration. The GEANT4 program contains a description of the complete ATLAS detector geometry, with each sub-detector system represented by material volumes. The output particles from the event generation are propagated through these detector volumes to simulate the many different material interactions which provide the simulated detector response in each of these volumes. The output of the detector simulation stage is a file containing the location and magnitude of all measured interactions, which is in the same format as the actual detector output. These output files are passed through the same full reconstruction algorithm that is applied to actual recorded collision data.

Chapter 4

Physics Object Reconstruction

This chapter discusses the reconstruction of final state particles detected by the detector as physics objects to be used in any ATLAS analyses. Section 4.1 briefly describes the reconstruction of charged particles' trajectories and the vertices indicating the location of pp collisions. Section 4.2 and 4.3 present the reconstruction and identification method used to reconstruct and identify charged leptons. The reconstruction and definitions of the different types of jet used in this thesis are discussed in Section 4.4. The discussion on jets is further extended to Section 4.5 with the algorithms used to identify the jets' origin based on their properties. Section 4.6 presents the method employed to infer the presence of undetectable particles, like neutrinos, by calculating the momentum imbalance of all reconstructed final state objects in the transvese plane of the detector.

4.1 Tracks and primary vertices

Charged particles are reconstructed from signals detected in the ID. As a charged particle traverses the ID, it leaves hits in each subdetector along its trajectory. It is a reconstructed charged particle trajectory that is refered to as a track. The ATLAS track reconstruction algorithm [112] builds tracks for charged particles with momentum as low as 400 MeV/c. They are built with a three-dimensional fit using Kalman filtering tools which can account for multiple scattering as the charged particle traverses the material of the ID.

For every bunch crossing, multiple pp interactions are most likely to occur and a vertex reconstruction algorithm [113] is used to determine the precise points in space where the interactions take place. These interaction points are called primary vertices and the vertex algorithm determines if multiple tracks originate from a single pp collision in a bunch crossing. The output of the algorithm is a complete set of vertices per event and the association of each track to a vertex.

This aglorithm starts by selecting a set of tracks passing simple quality criteria. Then, it derives a vertex seed from the global maximum of z coordinates of the tracks, followed by the association of the tracks to that seed using a χ^2 fitting algorithm. Tracks incompatible with the vertex are then used as seeds for the next iteration of the vertexing algorithm until all tracks are exhausted.

Vertexing is required to identify the collision of interest amongst all the primary vertices for every bunch crossing. The vertex considered as the collision of interest is called the hard scatter (HS) vertex and it is conventionally the vertex with the highest sum of track p_{T}^2 associated to it. Tracks that are not consistent with having been originated from the HS vertex are ignored and are classified as originating from a pile-up interaction within the same bunch crossing.

4.2 Electrons

Inputs from both the ECAL, HCAL, and ID are used to reconstruct and identify electrons [114, 115] within the detector region $|\eta| < 2.47$ of the ATLAS detector. Multiple steps are considered for electron reconstruction, beginning with ECAL seed-cluster reconstruction. In the $\eta - \phi$ space, a sliding window compatible with the ECAL granularity, a size of 3×5 in units of 0.025×0.025, searches for deposits of energy within the window that contain $E_T > 2.5$ GeV. If duplicate seeds are identified, the seed with the smaller transverse energy is discarded. ID tracks, extrapolated to the middle layer of the ECAL, are matched in the $\eta - \phi$ space to the ECAL seed, with effects from bremsstrahlung and precision hits in the SCT considered in the matching requirements. If no tracks are matched to a seed, the cluster is discarded from electron reconstruction. If more than one track is matched to a seed, a primary track is identified considering the distance to the seed barycentre, number of pixel and SCT detector hits. After matching at least one track to a ECAL seed cluster, the cluster is re-formed using a larger window of in the barrel region. Once the reconstruction is complete, the electron position information, η and ϕ, is calculated using the primary track while the electron energy is determined by its ECAL cluster.

Electron candidates are identified using a MC-based likelihood ratio to discriminate between prompt (signal) and non-prompt (background) electrons. The input variables to the likelihood include hadronic leakage, primary track quality, cluster information from different parts of the ECAL, and track-cluster matching. The likelihood is parameterized as a function of η and E_{T} to maintain signal efficiency in different regions of the detector and for higher energy electrons, which deposit more of their energy in the deeper layers of the calorimeter. Additionally, the likelihood depends on the number of reconstructed primary vertices in the

event, removing sensitivity to pile-up conditions. From simulated $Z \to ee$ and dijet events, three identification working points are provided with increasing background rejections: *LH Loose*, *LH medium* and *LH Tight* which are defined for ATLAS analysers to select electrons. Figure 4.1 shows comparisons between MC simulation and data of the electron identification working point efficiencies as a function of the electron E_T and the number of primary vertices.

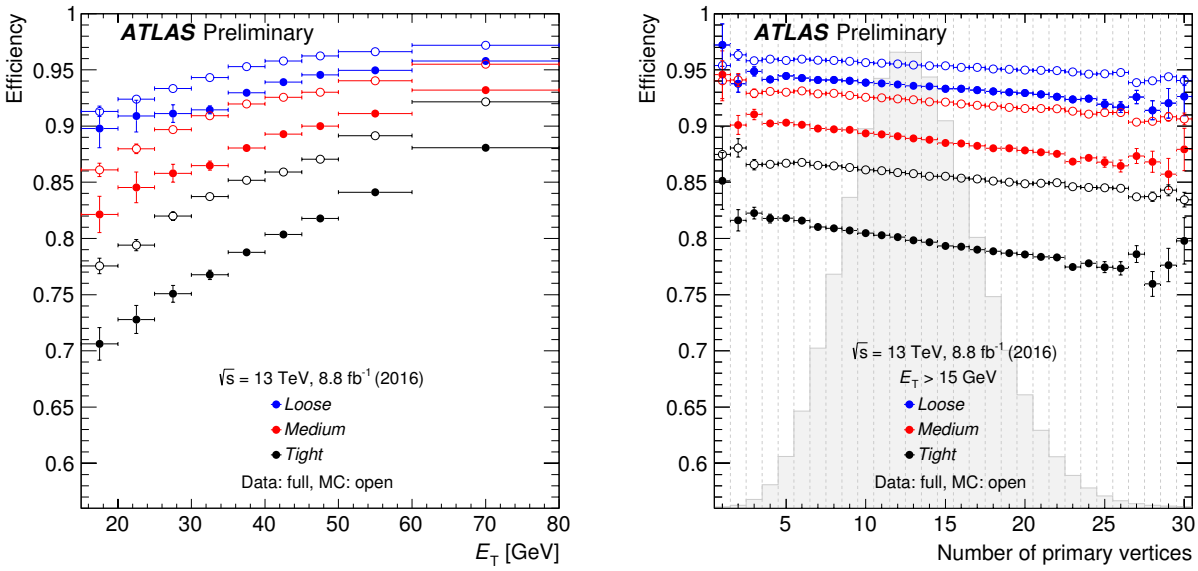

(a) (b)

Figure 4.1: MC simulation and data comparisons of the likelihood identification efficiency for electrons passing the three identification criteria as a function of (a) the electron p_{T} and (b) the number of primary vertices. Figures retrieved from Reference [116].

In addition to the identification criteria described above, electrons have an isolation requirement applied to reduce contamination from background electrons that may be non-prompt or mis-identified jets. Electron isolation is determined by using a track-based isolation variable, $p_{\mathrm{T}}^{varcone0.2}$, defined as the sum of p_{T} of all tracks[1] within a ΔR cone of $< \min(0.2, 10\mathrm{GeV}/E_{\mathrm{T}})$ around the electron track. Electrons are said to pass the *FixedCutTightTrackOnly* isolation working point selection if they fulfill the isolation criteria of $p_{\mathrm{T}}^{varcone0.2}/E_T < 0.06$.

Electrons are matched to the HS vertex by requiring their associated primary ID track to satisfy requirement on the transverse impact parameter (d_0), calculated with respect to the measured beam-line position, and longitudinal impact parameter (z_0) of the track.

[1]Tracks are required to originate from the HS vertex and satisfy quality requirements such as the number of hits in the pixel detector and SCT.

Specifically, the following requirements are imposed on the electron track

$$|d_0/\sigma_{d_0}| < 2 \tag{4.1}$$

$$|z_0 \sin\theta| < 0.5\text{mm} \tag{4.2}$$

where σ_{d_0} is the d_0 measured uncertainty and θ is the polar angle of the track. The d_0/σ_{d_0} variable is called the transverse impact parameter significance (d_0^{sig}).

The electron energy scale and resolution is calibrated using procedures that compare the electron energy measurement in data and MC simulation enriched with $Z \to ee$ and $J/\psi \to ee$ events [117, 118].

4.3 Muons

Muons are reconstructed [119] from information obtained from hits in the MS and tracks from the ID. Initially, muons candidates are reconstructed independently in the MS and ID. They are then combined with various algorithms to form the final muon candidates that are used in physics analyses. ATLAS has four different types of muons used for analyses and they are based on the detector subsystems used to identify the muon candidates:

- Combined (CB) muons: a combined muon track is formed with a global fit using the hits from both the ID and MS subdetectors. An outside-in pattern recognition, where the muons are first reconstructed in the MS and then extrapolated inward and matched to an ID track, are used to reconstruct muons.

- Segment-Tagged (ST) muons: A track in the ID is identified as an ST muon if the trajectory extrapolated to the MS is associated with at least one local track segment in the precision muon chambers. ST muons are used when muons cross only one layer of MS chambers, failing to form a proper MS track.

- Calorimeter tagged (CT) muons: A track in the ID is identified as a CT muon if it matches to an energy deposit in the calorimeters compatible with a minimum-ionizing particle. It is used to recover the efficiency in the region of $|\eta| < 0.1$ where the MS is only partially instrumented to allow for cabling and services to reach the calorimeters and ID.

- Extrapolated (ME) muons: the muon track is reconstructed based only on the MS track and a loose requirement on its compatibility with originating from the interaction

point. The parameters of the muon track are defined with respect to the interaction, taking into account the estimated energy loss of the muon in the calorimeters.

Muon identification is performed by applying a set of quality requirements based on the muon types described above. A set of track quality requirements are applied to the ID tracks to reject poorly reconstructed charged-particle trajectories. Different MS hit requirements are applied to different muon types to define identification selection criteria for muons. The *Loose* and *Medium* muon identification selection, as defined in Reference [119], are used in the search analysis.

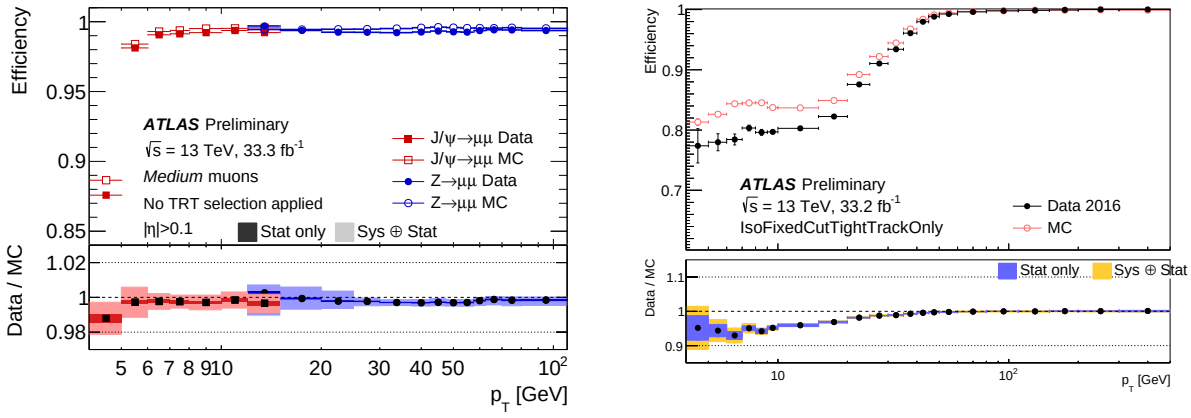

(a) (b)

Figure 4.2: MC simulation and data comparisons of the (a) reconstruction efficiency for muons passing the Medium identification and (b) isolation efficiency for muon passing the FixedCutTightTrackOnly working point as a function of muon p_{T}. Figures retrieved from Reference [120, 121].

The isolation requirement for reconstructed muons uses the same track-based method and track quality requirements as the electron but with a different ΔR cone definition, which is defined for muons as $\Delta R = \min(0.3, 10\ \mathrm{GeV}/p_{\mathrm{T}})$. Muons are considered to be isolated if they pass the FixedCutTightTrackOnly isolation working point, defined as $p_{\mathrm{T}}^{varcone0.3}/p_{\mathrm{T}} < 0.06$ which is similar to the electron FixedCutTightTrackOnly isolation working point. Figure 4.2 shows comparisons between MC simulation and data of the muon Medium identification efficiency and FixedCutTightTrackOnly isolation efficiency as a function of the muon p_{T}. Muons are also required to match to the HS vertex by imposing the same requirement as Equations 4.1 and 4.2.

The muon momentum is inferred from the curvature and coordinates of the reconstructed track. Both the momentum scale and resolution are determined independently in the ID and MS and their calibration factors are measured in events enriched $J/\psi \to \mu\mu$ and $Z \to \mu\mu$ by comparing data and MC simulation.

4.4 Jets

Although the existence of quarks has been experimentally proven for the last 30 years, free quarks have never been observed in any experiment. Due to the extremely short range of the strong force and quark confinement, the production of highly energetic partons in a collision results in a spray of collimated hadrons. These hadrons are what is finally observed in a detector and classified as jets. The energy of the initial parton (quark or gluon) is carried by the hadrons and the energy and angular direction of jets represent a proxy for the energy and direction of the intial parton. To reconstruct jets, the hadrons are clustered together using jet clustering algorithms.

At the LHC experiments, sequential clustering algorithms are used to build jets rather than cone-type algorithms. Cone-type algorithms are strongly disfavoured as the jet observables built from this type of algorithm are found to be sensitive to soft and collinear splitting, thus infrared and collinear (IRC) un-safe [122]. On the other hand, sequential clustering algorithms are IRC-safe by construction, and thus adopted by the experiments.

A typical sequential jet algorithm can be summarized as the following:

$$d_{ij} = min(p_{T,i}^{2p}, p_{T,j}^{2p}) \frac{\Delta R_{ij}^2}{R^2} \tag{4.3}$$

$$d_{i,B} = p_{T,i}^{2p} \tag{4.4}$$

where $\Delta R_{ij}^2 = (y_i - y_j)^2 + (\phi_i - \phi_j)^2$. The parameter R acts as a resolution parameter which sets the relative distance between jets such that they are resolved from each other. The algorithm creates a list for each pair of inputs. For each pair, the value of d_{ij} and $d_{i,B}$ are computed. From the list of pairs, the smallest d_{ij} and $d_{i,B}$ values are identified and compared between them. If d_{ij} is smaller than $d_{i,B}$, then objects i and j are merged and the list is recompiled. If $d_{i,B}$ is smaller than d_{ij}, then object i is deemed as a complete jet, it is removed from the list and the list is recompiled. The procedure is repeated until no objects remain in the list.

Three different values of p are used, corresponding to different type of algorithms: $p = 1$ for the k_t algorithm [123, 124], $p = 0$ for the Cambridge/Aachen (C/A) algorithm [125, 126] and $p = -1$ for the anti-k_t algorithm [127]. For the purpose of calculating the energy and momenta of a jet, the four-vector recombination scheme is utilised, in which the four-vector for the jet is calculated as the sum of the four-vector of its constituents.

Within ATLAS, the primary jet clustering algorithm is the anti-k_t algorithm and the FastJet implementation [128] of the jet algorithms is used to build all jet collections.

The anti-k_t algorithm typically starts with the hardest objects in the list of inputs at each clustering iteration and then merges them with nearby softer objects. This feature leads to much more regular jet areas [129] for anti-k_t jets as illustrated in Figure 4.3.

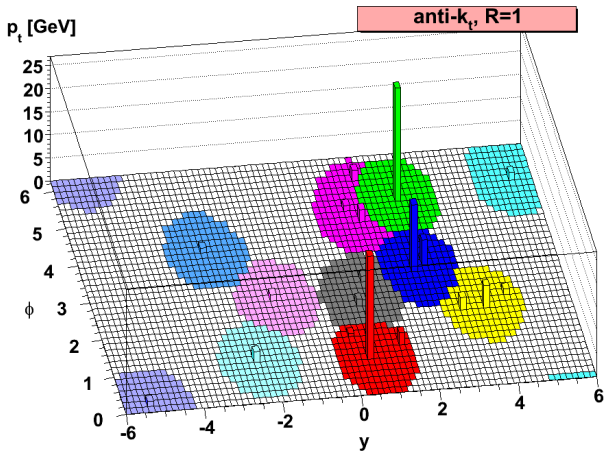

Figure 4.3: A sample parton-level event clustered with the anti-k_t algorithm. Figure retrieved from Reference [127].

Four different jet collections formed using different inputs are used in this thesis. Jets built from stable particles in MC simulation (truth jets) are used for performance studies. Detector level jets with different radius parameter built from calorimeter clusters (small-R and large-R jets) and tracks (track jets) are used to reconstruct and identify hadronically decaying particles.

Truth jet

For the purpose of studying the reconstruction performance in MC simulation, truth jets are built in MC simulated events from stable particles with lifetimes greater than 10 picoseconds, except for muons and neutrinos, which are not included. The exclusion of muons and neutrinos ensures that particle jets are built from particles that leave significant energy deposits in the calorimeters.

The same jet clustering algorithm used for detector level jets is also used to build truth jets. The kinematics of a truth jet is said to be at truth-level, and it is often used as one of the reference object to calibrate the kinematics of a jet at the detector level.

Small-R jet

Small-R jets are built from topological calorimeter-cell clusters (topoclusters) calibrated at the EM scale [130], using the anti-k_t algorithm with radius parameter of $R = 0.4$. After

they are reconstructed, a series of calibrations [131], as shown in Figure 4.4 are applied to the jets to restore the reconstructed jet energy scale (JES) to the true jet energy.

First, the direction of the jets is corrected by shifting its origin from the ATLAS coordinate system origin to the location of the HS vertex. Next, a correction is applied to remove excess contributions to calorimeter cell energies from particles arising from pile-up interactions. A correction, derived purely from MC simulation, on the jet energy and pseudorapidity is then applied to correct the jets to the truth-level energy and pseudorapidity. To improve the jet energy resolution (JER), a series of independent corrections, which are parameterized based on the calorimeter, track and muon segment variables of the jets, are applied. The final calibration step applies a residual in situ calibration to correct jets in data only and it aims at correcting any differences between data and MC.

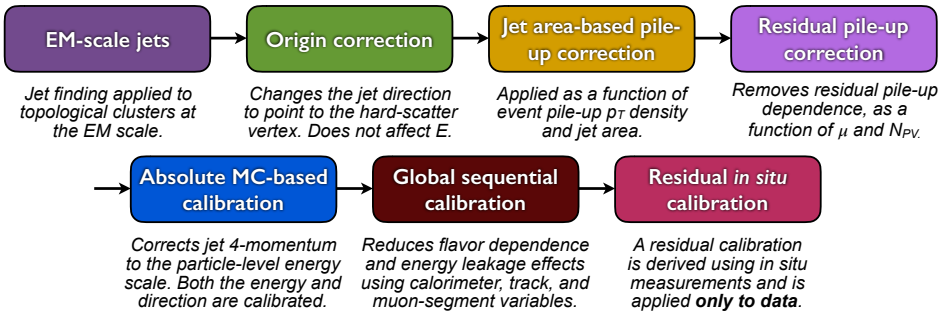

Figure 4.4: The calibration chain for small-R jets. Figure retrieved from Reference [131].

The discrimination of small-R jets originating from the HS vertex and from pile-up vertices is important given the high luminosities at the LHC. To identify pile-up originated jets, a pile-up mitigation technique called jet vertex tagger (JVT) [132] is applied to small-R jets. This is a likelihood-based method that uses two variables: the ratio of the scalar sum of p_{T} of the tracks in the jet originating from the HS vertex to the calibrated jet p_{T} and the corrected jet vertex fraction (corrJVF) variable, which is defined as the fraction of the scalar sum of the p_{T} of the tracks of a jet which are associated to the HS vertex with respect to the scalar sum of all jet tracks. In this thesis, small-R jets are considered to originate from the HS vertex if it passes a JVT > 0.59 requirement (*Default* working point), which provides a 92% efficiency to select jets from the HS vertex. Since the contamination of pile-up is significant for low-p_{T} jets, the requirement is applied only to jets with $p_{\mathrm{T}} < 60$ GeV and $|\eta| < 2.4$. The comparison between MC simulation and data for the JVT variable distribution and the Default working point JVT selection efficiency is shown in Figure 4.5.

Small-R jets can be faked from non-collision backgrounds, such as beam induced backgrounds, cosmic showers and calorimeter noise. A jet cleaning strategy is set, as described in Reference [134], in order to suppress jets coming from all these backgrounds (fake jets)

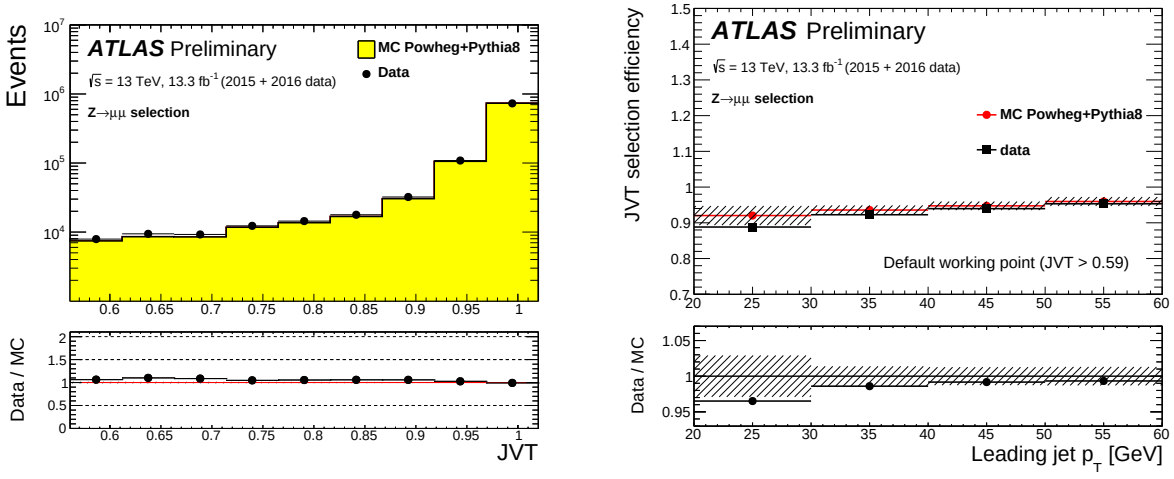

(a) (b)

Figure 4.5: MC simulation and data comparison of (a) the distribution of the Jet Vertex Tagger and (b) the selection efficiency of the Default working point for jets from the HS vertex are shown for jets balanced against Z bosons decaying to muons. Figures retrieved from Reference [133].

and retain jets originating from a pp collision event (good jets). It consists in selecting only jets which satisfy several quality criteria. These criteria involve variables that quantify the quality of the signal pulse shape of the LAr calorimeters or measure the fraction of energy deposited in the electromagnetic calorimeters or in the hadronic calorimeters to the total energy of the jet, or the ratio between the scalar sum of the jet tracks coming from the HS vertex to the total jet p_{T}. A set of selections on the quality criteria, corresponding to the *Loose* working point (as defined in Reference [134]), is used to identify good jets in this thesis, which has a selection efficiency for good jets close to 100%.

Large-R jet

For massive particles, such as the Higgs boson, produced with high p_{T}, the angular separation of the decay products is approximately $\Delta R \sim 2m/p_{\mathrm{T}}$, where m and p_{T} are the mass and transverse momentum of boosted massive parent particle. As a result, the decay products get more collimated and they cannot be reconstructed as individual jets and get merged into a single jet.

Jets with large radius parameter (large-R jets) are typically used for jet clustering so that all decay products can be contained within a single jet and the kinematics of that jet are considered as a proxy for the original massive particle kinematics. For example, $h \to b\bar{b}$ jets, a jet radius parameter of 1.0 is needed for Higgs bosons with $p_{\mathrm{T}} > 250$ GeV. In the search analysis presented in this thesis, the large-R jet is used primarily to reconstruct boosted

$h \to b\bar{b}$ decays.

However, a jet reconstruction with simply a larger radius is not enough. When the chosen jet radius parameter gets much larger, the reconstructed jet is increasingly sensitive to various soft components accompanying the jet production in LHC. This includes contributions from pile-up acitivity, underlying events and soft components of the radiation. Therefore, an additional step after jet clustering, called jet grooming, is applied to remove the unwanted contributions so that a real hard substructure within jets from massive particle decays can be revealed.

One such grooming method available is the trimming algorithm [135]. The algorithm takes advantage of the fact that contamination from pile-up, multiple parton interactions and initial state radiation in reconstructed jet is usually much softer than the partons from the HS or final state radiation process. An illustration of the trimming algorithm is shown in Figure 4.6. For a given large-R jet, subjets are built by reconstructing constituents of the un-groomed jet with the k_t jet clustering algorithm with a smaller radius parameter denoted as R_{sub}. The subjets are then removed if they carry less than a fraction f_{cut} of the original un-groomed large-R jet p_{T}. The k_t clustering algorithm is used to build the subjets because the algorithm prefers to cluster soft components first.

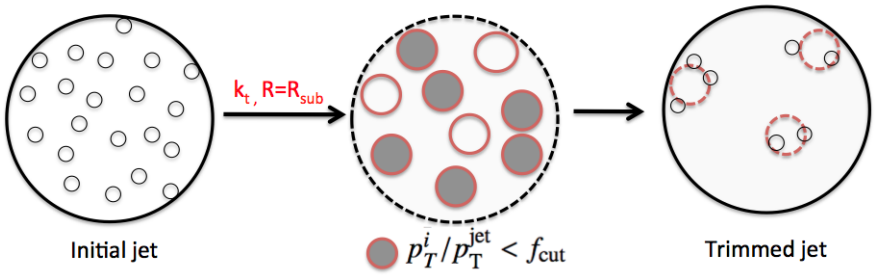

Figure 4.6: Diagram illustrating the jet trimming algorithm. Figure retrieved from Reference [136].

In ATLAS, large-R jets are built with topoclusters calibrated to the hadronic scale[2] with the anti-k_t jet algorithm with $R = 1.0$. The jets are then groomed with the trimming algorithm configured with $R_{sub} = 0.2$ and $f_{cut} = 5\%$. After grooming, the large-R jet energy and pseudorapidity are calibrated to truth-level using correction factors derived from MC simulation [136]. In addition to the energy, the mass of the large-R jet is also calibrated to its true-level mass [1]. The reconstructed jet mass used in this thesis is the combined jet mass defintion which uses calorimeter and ID track information. An extensive discussion on the reconstruction of large-R jet mass and its calibration is presented in Chapter 5.

[2]Topoclusters are calibrated to the hadronic scale by using the local hadronic cell weighting (LCW) method [130].

Track jet

To identify a large-R jet that is consistent with decay of $h \to b\bar{b}$, a method developed by ATLAS is to reconstruct subjets within the large-R jet and identify if the subjets have originated from b-quarks. The subjets, called track jets, are reconstructed with ID tracks using the anti-k_t algorithm with a radius parameter of $R = 0.2$. The small radius parameter enables the anti-k_t algorithm to reconstruct two distinguishable b-jets with small ΔR separation between them. The track jets are then b-tagged (see Section 4.5) to identify those originating from b-quarks.

Track-jets are associated to the large-R jets by using the ghost-association method [137]. The method consists of "Ghost"-ing the track jets by altering their p_{T} to an infinitesimally small value. The ghost track jets are then included in the list of objects used to reconstruct large-R jets. The small value of the ghost track jets' p_{T} ensures that the large-R jet reconstruction is not altered by their presence of during the large-R jet clustering sequence. After large-R jets have been reconstructed, the track jet ghosts are unique constituents of the large-R jets and they can be identified as to which large-R jet they are associated[3].

4.5 Flavour-tagging

The identification of b-quark initiated jets, typically referred to as b-tagging or flavor tagging, plays an important role in ATLAS physics. After the fragmentation of b-quarks, most of the original b-quark energy goes into the weakly decaying b-hadrons whose intrinsic lifetime is about 1.5×10^{12} s. Consequently, for b-hadrons of 30 GeV, the average decay length could be about 3 mm, a distance large enough to be measured by the ID in the form of secondary vertices. The b-hadrons can also subsequently decay to c-hadrons and which have similar average lifetime thus leading to an additional decay forward as tertiary vertices.

In order to exploit the unique characteristics of b-jets above, b-tagging algorithms are developed by taking advantage of different aspects of the decay patterns. The b-tagging algorithms use tracks reconstructed from the ID, representing the charged particles from b-hadron and c-hadron decays, as inputs to discriminate jets from different parton origins. Tracks are associated to each jet if they are within a certain p_{T}-dependent ΔR cone around the jet axis[4]. The collection of selected tracks is then given as input to three different b-tagging algorithms [139] and they provide complementary information to each other:

[3] This is just one of the cases of where ghost-association method is used in ATLAS. Other reconstructed objects such as tracks are also used for association to jets.

[4] Tracks are associated to a jet with p_{T} (in MeV) if they satisfy the following requirement [138, 139]:

$$\Delta R(\mathrm{track}, \mathrm{jet}) < 0.239 + e^{-1.220 - 1.64 \times 10^{-5} \cdot p_{\mathrm{T}}} \tag{4.5}$$

- Impact parameter based algorithms (IP2D and IP3D).
- Inclusive secondary vertex reconstruction algorithm (SV).
- Decay chain multi-vertex reconstruction algorithm (JetFitter) [140].

After each b-tagging algorithm has been run on the input track collections, the discriminating output variables of each algorithm are then combined using a boosted decision tree (BDT) based algorithm called MV2c10 [141, 142]. The kinematic properties of jets are also included in the training in order to capture the kinematic dependency of the disciminating output variables. The training of the BDT is performed on MC samples of top quark pair ($t\bar{t}$) production. The signal jets are always the b-jets, while background jets are a mixture of light-jets and c-jets. The "c10" string in the algorithm name denotes the approximate fraction of c-jets (in this case 10%) in the background jets sample. The MV2c10 discriminant (output of the BDT) is used to b-tag a reconstructed jet by requiring the discriminant to pass a specific threshold. The distribution of the MV2c10 discriminant for small-R b-jets, c-jets and light-jets is shown in Figure 4.7a and its performance for discrimination against light-jet and c-jet is shown in Figure 4.7b.

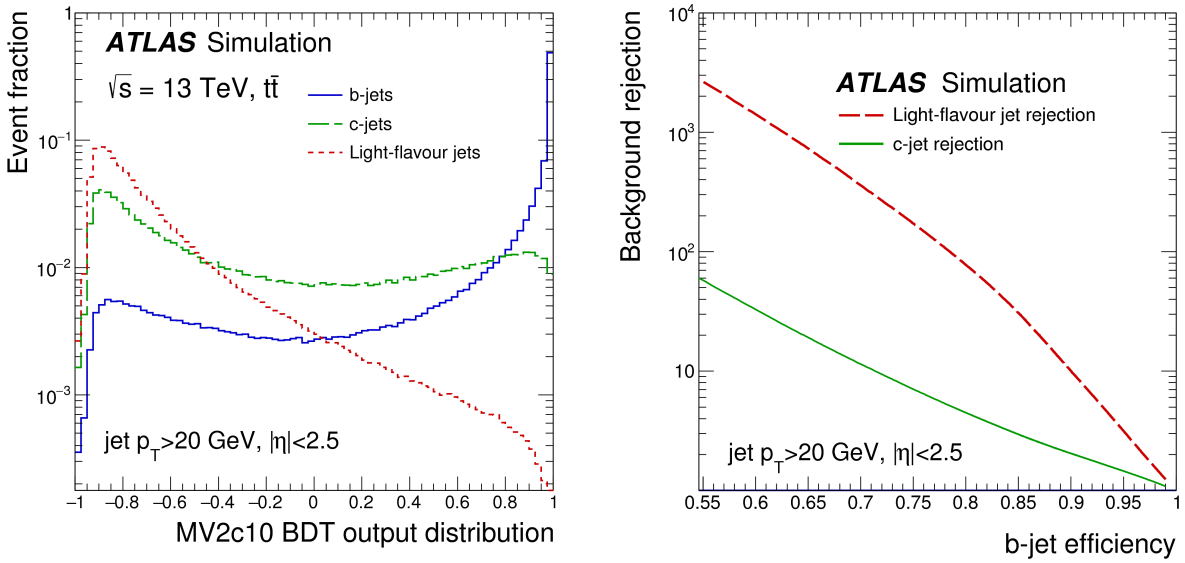

(a) (b)

Figure 4.7: (a) The MV2c10 algorithm output for b-jets (solid blue line), c-jets (dashed green line) and light-jets (dotted red line). (b) Light-jet (dashed red line) and c-jet (solid green line) rejection versus b-jet efficiency of the MV2c10 algorithm. The performance was evaluated using MC simulated $t\bar{t}$ events. Figures retrieved from Reference [143].

The MV2c10 b-tagging efficiency for b-jets [143] and the mistagging rate of c-jets [144] are measured in samples enriched with $t\bar{t}$ events while the mistagging rate of light-flavour

In cases when a track passes the above requirement for more than one jet, the track is assigned to the closest jet.

jets [145] is measured with multijet events. The modelling of b-tagging efficiency and mistagging rates in MC simulations are validated by comparing to data and calibration scale factors are derived to correct the modelling in MC simulations.

4.6 Missing transverse momentum

Neutrinos cannot be detected in the ATLAS detector, since they interact only weakly and their cross sections are extremely small. However, their presence can be inferred and reconstructed indirectly through the imbalance of the transverse momentum of the event. In an ideal event the total transverse momentum of all particles coming out of the HS vertex should sum up to zero but if neutrinos are involved this is generally not the case. The absolute value of this momentum is called $E_{\mathrm{T}}^{\mathrm{miss}}$, the missing transverse momentum. The z component cannot be reconstructed, since the longitudinal momentum of the colliding partons is unknown.

The missing transverse momentum vector [146] is calculated by the negative vectorial sum of transvese momenta, $\mathbf{p}_{\mathrm{T}}^{\mathrm{obj}} = (p_x^{\mathrm{obj}}, p_y^{obj})$, of all measured reconstructed objects:

$$\mathbf{E}_{\mathrm{T}}^{\mathrm{miss}} = -\sum_{\mathrm{obj}} \mathbf{p}_{\mathrm{T}}^{\mathrm{obj}} - \sum \mathbf{p}_{\mathrm{T}}^{\mathrm{soft}} \tag{4.6}$$

$$= -\sum \mathbf{p}_{\mathrm{T}}^{e} - \sum \mathbf{p}_{\mathrm{T}}^{\gamma} - \sum \mathbf{p}_{\mathrm{T}}^{\tau_{\mathrm{had}}} - \sum \mathbf{p}_{\mathrm{T}}^{\mu} - \sum \mathbf{p}_{\mathrm{T}}^{\mathrm{jet}} - \sum \mathbf{p}_{\mathrm{T}}^{\mathrm{soft}} \tag{4.7}$$

where $\sum_{\mathrm{obj}} \mathbf{p}_{\mathrm{T}}^{\mathrm{obj}}$ is called the "hard" term and $\sum \mathbf{p}_{\mathrm{T}}^{\mathrm{soft}}$ is called the "soft" term. The hard term consists of the vector sum of the transverse momenta of reconstructed objects (obj) in the event such as electrons (e), photons (γ), hadronically-decaying tau leptons (τ_{had}), muons (μ) and jets[5]. The soft term is calculated from the vectorial sum of transverse momenta of ID tracks emerging from the HS vertex but not associated with any reconstructed electron, muon, or jet used in the $\mathbf{E}_{\mathrm{T}}^{\mathrm{miss}}$ reconstruction. Since only ID tracks associated to the HS vertex are considered, the soft term is highly insensitive to effects from pile-up.

The modulus of the $\mathbf{E}_{\mathrm{T}}^{\mathrm{miss}}$ vector gives the magnitude of the missing transvese momentum:

$$E_{\mathrm{T}}^{\mathrm{miss}} = |\mathbf{E}_{\mathrm{T}}^{\mathrm{miss}}| = \sqrt{(E_x^{\mathrm{miss}})^2 + (E_y^{\mathrm{miss}})^2}. \tag{4.8}$$

[5]In the search analysis, photons and hadronically-decaying tau leptons are not used for the event selection so for the calculation of the $E_{\mathrm{T}}^{\mathrm{miss}}$, they are assumed to be reconstructed as jets.

The $E_{\mathrm{T}}^{\mathrm{miss}}$ performance depends on the event topology affected by the presence of true $E_{\mathrm{T}}^{\mathrm{miss}}$ (from neutrinos as an example), leptons, jets, and others. The $E_{\mathrm{T}}^{\mathrm{miss}}$ performance is generally studied with processes with and without genuine $E_{\mathrm{T}}^{\mathrm{miss}}$, such as $t\bar{t}$, $W \to \ell\nu$ and $Z \to \ell\ell$ events. The scale and resolution for the reconstructed $E_{\mathrm{T}}^{\mathrm{miss}}$ in these processes are indicative of the quality of the reconstruction. For illustration, results obtained with $Z \to \mu\mu$ events are shown in Figure 4.8.

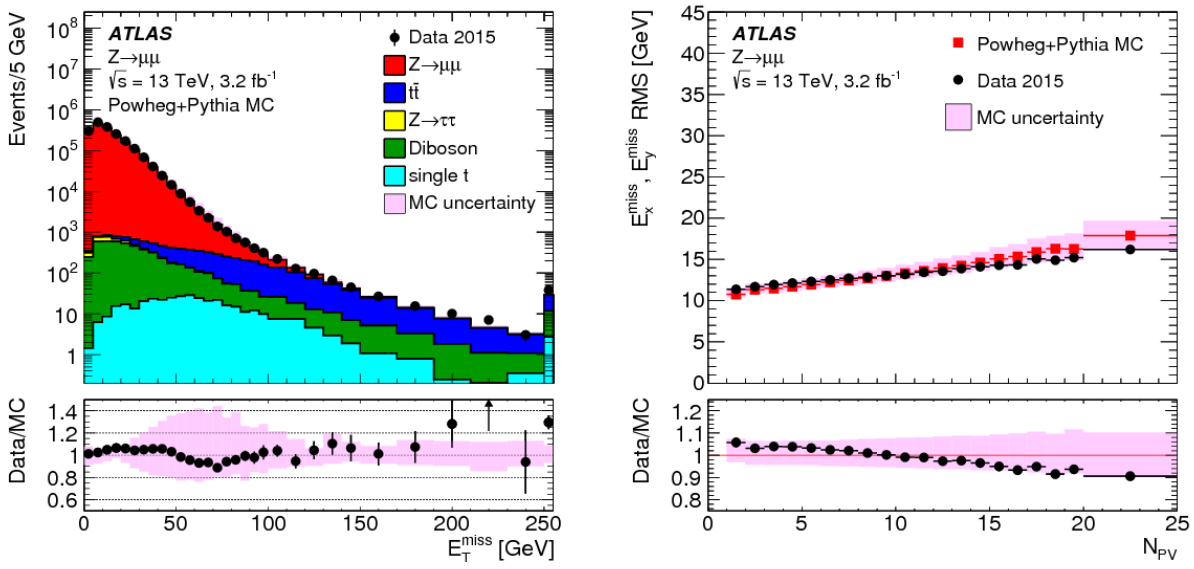

(a) (b)

Figure 4.8: MC simulation and data comparisons of the (a) $E_{\mathrm{T}}^{\mathrm{miss}}$ distribution and (b) the RMS width of the $E_{x(y)}^{miss}$ distribution as a function of the number of primary vertices. Figures retrieved from Reference [146].

Chapter 5

Jet Mass Reconstruction

The invariant mass of jets is one of the most powerful observables for distinguishing jets from massive particle decays and jets originating from QCD-induced processes; therefore, it is critical to improve the reconstructed jet mass by improving its resolution and any associated systematic uncertainties. In Run-1, the jet mass was constructed solely from calorimeter information via the constituents of a jet. At the beginning of Run-2, a new definition of the jet mass was introduced which augments the calorimeter information using finer granularity inputs from ID tracks.

This chapter documents the reconstruction of the jet mass and its performance with the ATLAS detector. Two jet mass definitions, each with strength in specific kinematic regimes, and their calibration procedure are presented in Section 5.1 and 5.2. Section 5.3 compares the performance of the two definitions and then in Section 5.4, the methods to derive their systematic uncertainties are described. Section 5.5 briefly explores the improvement in the jet mass resolution when the two jet mass definitions are combined. The results in this chapter were published in Reference [1] and the author's main contributions are listed in the Preface at the beginning of this thesis.

5.1 Jet mass definitions

The jet mass is mainly used as a discriminant to identify jets originating from boosted massive particles. For these topologies, large-R calorimeter jets are used and the following results are presented for such jets. The classical jet mass definition within ATLAS is the "calorimeter-based" jet mass (m^{calo}). For a calorimeter jet J consisting of topoclusters i

with energy E_i and three-vector momentum $\vec{p}_i$, m^{calo} is defined as:

$$m^{\text{calo}} = \sqrt{\left(\sum_{i \in J} E_i\right)^2 - \left(\sum_{i \in J} \vec{p}_i\right)^2}. \tag{5.1}$$

Since this jet mass definition depends on both energy and angular information of the topoclusters, the resolution of both individual measurements will determine the resolution of the mass. However, the spatial granularity, which determines the angular resolution, can become a limiting factor for very collimated streams of particles. For a sufficiently high Lorentz boost of the parent particle, the spatial separation of its decay products is so small such that it reaches the limit of the calorimeter granularity. In the limit of a jet reconstructed from a single topocluster, the jet mass following the definition above becomes zero.

To mitigate this effect, high resolution angular information from the ID can be used to complement the calorimeter measurements. Similar approaches have previously shown to provide superior performance, for example in the particle-flow paradigm [147, 148]. There have been previous attempts to improve the reconstructed jet mass, the first of which extended the electromagnetic calorimeter measurement by using the hadronic information [149, 150]. In the context of identifying jets originating from a top quark, information from the ID was used for the first time to complement the calorimeter measurement of the mass [151]. Phenomenological studies for future colliders discussed a track-assisted jet mass in connection with highly boosted (p_{T} of $\mathcal{O}(10)$ TeV) jets from W/Z bosons and top quarks [152,153].

Information from the ID and the calorimeter can be combined into the "track-assisted" jet mass (m^{TA}):

$$m^{\text{TA}} = \frac{p_{\text{T}}^{\text{calo}}}{p_{\text{T}}^{\text{track}}} \times m^{\text{track}}, \tag{5.2}$$

where $p_{\text{T}}^{\text{calo}}$ is the transverse momentum of a calorimeter jet, $p_{\text{T}}^{\text{track}}$ is the transverse momentum of the sum of four-vectors of all tracks ghost-associated to the jet, and m^{track} is the invariant mass of the tracks. For a single reconstructed track, the mass is set to the pion mass (m_π), a good approximation since $p_{\text{T}}^{\text{track}} \gg m_\pi$. The ratio of the transverse momenta $p_{\text{T}}^{\text{calo}}/p_{\text{T}}^{\text{track}}$ corrects for the missing component from neutral particles, which the ID cannot detect and reconstruct, in the $p_{\text{T}}^{\text{track}}$ term. This minimizes the effect of charged-to-neutral fluctuations, and improves the resolution with respect to a track-only jet mass definition (m^{track}). Figure 5.1 compares the uncalibrated calorimeter-based jet mass to the uncalibrated track-assisted jet mass, and shows that the track-assisted mass is superior in resolution with respect to the uncalibrated track-only jet mass for jets with very high p_{T}.

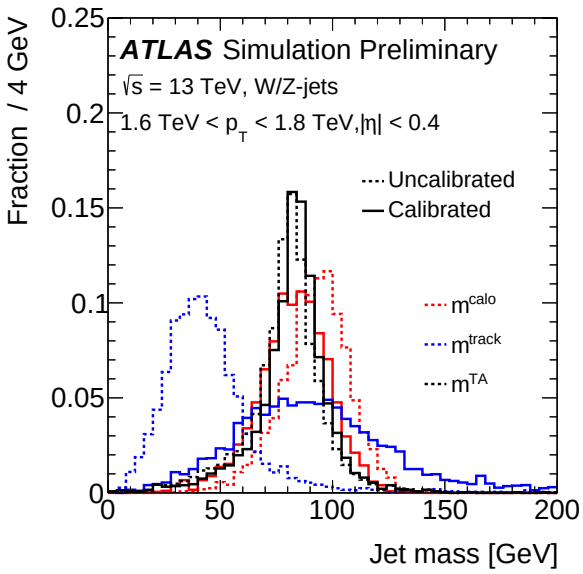

Figure 5.1: Uncalibrated and calibrated calorimeter-based, track-only and track-assisted jet mass distribution. Figure produced by the author and published in Reference [1].

5.2 Jet mass calibration

Just like the jet energy scale (JES), the jet mass scale (JMS) needs to be calibrated. The goal of this calibration is to correct the reconstructed jet mass on average to the truth-level jet mass. The calibration factor used to correct the jet mass is derived using isolated jets that are matched to isolated truth jets in an MC simulated sample of QCD dijet processes. The isolation criteria requires no other jet within $\Delta R < 1.5(2.5)$ for calorimeter jets (truth jets). A calorimeter jet is considered matched to a truth jet if the truth jet has a p_{T} of greater than 100 GeV and is within $\Delta R < 0.6$ of the calorimeter jet. The following calibration procedure is valid for any of the reconstructed jet mass definitions introduced in the previous section, hence for generality, the calorimeter jet reconstructed mass (m^{reco}) can be m^{calo} or m^{TA}.

For each matched pair of calorimeter and truth jets, the jet mass response ($\mathcal{R}_{\mathrm{m}}$) for a given jet mass definition is calculated as the ratio between the calorimeter jet reconstructed mass (m^{reco}) and the mass of the truth jet (m^{truth})

$$\mathcal{R}_{\mathrm{m}} = \frac{m^{\mathrm{reco}}}{m^{\mathrm{truth}}}. \tag{5.3}$$

The mass calibration is performed with the JES calibration already applied to the four-vector of the calorimeter jet. The average jet mass response ($\langle \mathcal{R}_{\mathrm{m}} \rangle$) is determined by the mean of a Gaussian fit to the jet mass response distribution in bins of $p_{\mathrm{T}}^{\mathrm{truth}}$, $|\eta_{\mathrm{det}}|$ and m^{truth}. Figure 5.2 is an example of a gaussian fit to the calorimeter-based mass response distribution

for a particular ($p_{\mathrm{T}}^{\mathrm{truth}}$, $|\eta_{\mathrm{det}}|$, m^{truth})-bin.

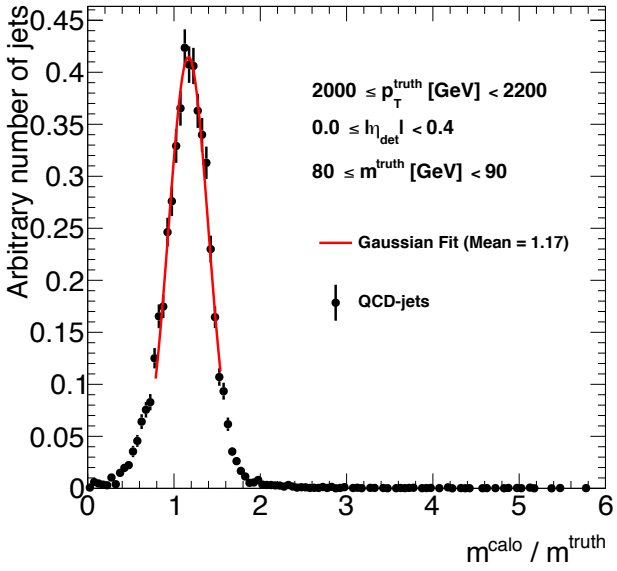

Figure 5.2: Calorimeter-based mass response distribution for jets with $2000 \leq p_{\mathrm{T}}^{\mathrm{truth}} < 2200$ GeV, $|\eta_{\mathrm{det}}| < 0.4$ and $80 \leq m^{\mathrm{truth}} < 90$ GeV. A gaussian function is used to fit (red line) the mass response distribution to extract the average mass response. Figure produced by the author.

At this point, the calibration depends on truth-level quantities ($p_{\mathrm{T}}^{\mathrm{truth}}$ and m^{truth}) which are only available in MC simulation. To transform the dependence of $\langle \mathcal{R}_{\mathrm{m}} \rangle$ from truth-level quantities to its corresponding reconstructed-level quantities, such that it can be used in both MC simulation and data, the average of the reconstructed-level quantities, $p_{\mathrm{T,est}}^{\mathrm{reco}}$ and $m_{\mathrm{est}}^{\mathrm{reco}}$, are estimated for a given ($p_{\mathrm{T}}^{\mathrm{truth}}$, $|\eta_{\mathrm{det}}|$, m^{truth})-bin by using the following relation:

$$p_{\mathrm{T,est}}^{\mathrm{reco}} = \langle \mathcal{R}_{\mathrm{p_T}} \rangle \cdot \langle p_{\mathrm{T}}^{\mathrm{truth}} \rangle \tag{5.4}$$

$$m_{\mathrm{est}}^{\mathrm{reco}} = \langle \mathcal{R}_{\mathrm{m}} \rangle \cdot \langle m^{\mathrm{truth}} \rangle \tag{5.5}$$

where $\langle p_{\mathrm{T}}^{\mathrm{truth}} \rangle$ ($\langle m^{\mathrm{truth}} \rangle$) is the mid-point of the $p_{\mathrm{T}}^{\mathrm{truth}}$ (m^{truth}) bin boundaries. The JMS calibration factor is used to correct m^{reco} and defined as the inverse of the average response ($c_{\mathrm{reco}}^{\mathrm{JMS}} = 1/\langle \mathcal{R}_m \rangle$). It is parameterized as a function of $p_{\mathrm{T}}^{\mathrm{reco}}$ and m^{reco}, $c_{\mathrm{reco}}^{\mathrm{JMS}}(p_{\mathrm{T}}^{\mathrm{reco}}, m^{\mathrm{reco}})$, for a given $|\eta_{\mathrm{det}}|$ bin, by using a kernel density estimation technique. The function is constructed by using a two dimensional Gaussian kernel:

$$c_{\text{reco}}^{\text{JMS}}(p_{\text{T}}^{\text{reco}}, m^{\text{reco}}) = \frac{\sum_{i=1}^{N_{\text{points}}} (1/\langle\mathcal{R}\rangle)_i w_i}{\sum_{i=1}^{N_{\text{bins}}} w_i}, \tag{5.6}$$

$$w_i = \frac{1}{((1/\Delta\langle\mathcal{R}\rangle)_i)^2} \times \text{Gauss}\left(\frac{p_{\text{T}}^{\text{reco}} - (p_{\text{T,est}}^{\text{reco}})_i}{\sigma_{p_{\text{T}}^{\text{reco}}}} \oplus \frac{m^{\text{reco}} - (m_{\text{est}}^{\text{reco}})_i}{\sigma_{m^{\text{reco}}}}\right) \tag{5.7}$$

where i denotes a given point in $(p_{\text{T,est}}^{\text{reco}}, m_{\text{est}}^{\text{reco}})$-space, $(\Delta\langle\mathcal{R}\rangle_i)$ is the statistical uncertainty of $\langle\mathcal{R}\rangle_i$, Gauss$(x)$ is the amplitude of a Gaussian function with $\mu = 0$ and $\sigma = 1$, $\sigma_{p_{\text{T}}^{\text{reco}}}$ and $\sigma_{m^{\text{reco}}}$ are width-parameters of the Gaussian kernel and $\oplus$ denotes addition in quadrature. Figure 5.3 is an example visualisation of the jet mass calibration factor, for m^{calo}, as a function of m^{calo} and calorimeter jet p_{T} for jets with $|\eta_{\text{det}}| < 0.4$.

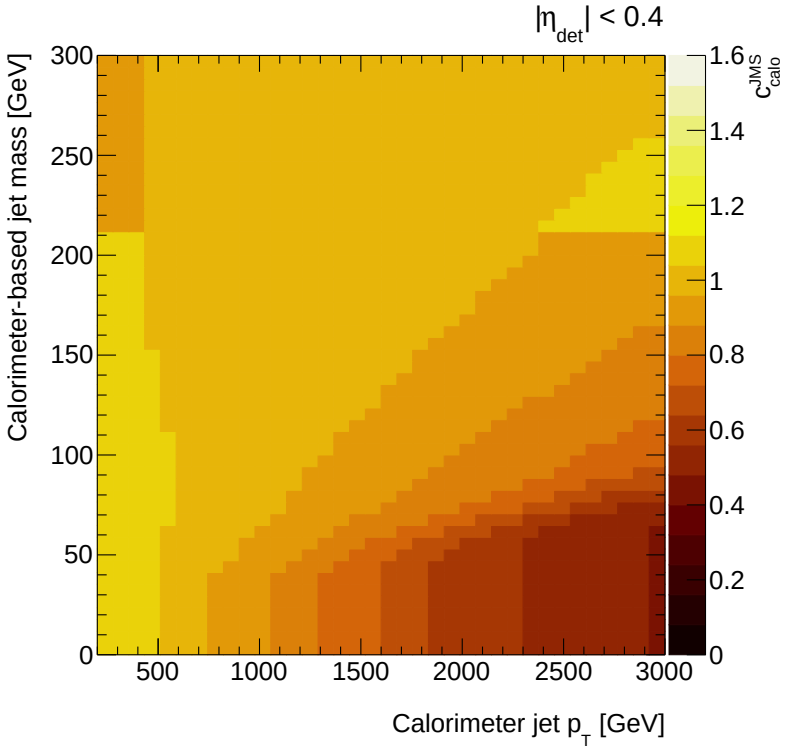

Figure 5.3: A 2D histogram visualisation of the the jet mass calibration factors for m^{calo} ($c_{\text{calo}}^{\text{JMS}}$) as a function of calorimeter-based jet mass and calorimeter jet p_{T} for jets with $|\eta_{\text{det}}| < 0.4$. Figure produced by the author.

The reconstructed jet mass is corrected, on a jet-by-jet basis, by employing a numerical inversion technique [154]. For a calorimeter jet with energy E^{reco}, transverse momentum $p_{\text{T}}^{\text{reco}}$, detector pseudorapidity $|\eta_{\text{det}}|$, reconstructed jet mass m^{reco}, the JMS calibration for the reconstructed jet mass is

$$m_{\text{calibrated}}^{\text{reco}} = c_{\text{reco}}^{\text{JMS}}(p_{\text{T}}^{\text{reco}}, |\eta_{\text{det}}|, m^{\text{reco}}) \cdot m^{\text{reco}}, \tag{5.8}$$

where $c_{\text{reco}}^{\text{JMS}}$ is the JMS calibration factor for reconstructed jet mass with a dependence on the JES-calibrated $p_{\text{T}}^{\text{reco}}$, $|\eta_{\text{det}}|$ and the JES-calibrated m^{reco}. The reconstructed jet mass is said to be calibrated if the average response $\langle \mathcal{R} \rangle = 1$. The calibration procedure is deemed to fulfil *closure* when the same calibration factors are applied to the same sample from which it is derived.

The calorimeter-based jet mass response is shown to have dependences to $p_{\text{T}}^{\text{truth}}$ (Figure 5.4a), m^{truth} (Figure 5.4c) and $|\eta_{\text{det}}|$ (Figure 5.4e). The response increases as $p_{\text{T}}^{\text{truth}}$ and $|\eta_{\text{det}}|$ gets larger but decreases for larger values of m^{truth}. In contrast, a much more uniform response for the uncalibrated m^{TA} is observed compared to m^{calo}, as shown in Figures 5.5a, 5.5c and 5.5e, since $p_{\text{T}}^{\text{calo}}$ in Equation 5.2 is already corrected with the JES calibration. After applying the mass calibration, the jet mass response is uniform within 3% across all bins of $p_{\text{T}}^{\text{truth}}$, m^{truth} and $|\eta_{\text{det}}|$ as shown in Figures 5.4b, 5.4d and 5.4f for m^{calo} and in Figures 5.5b, 5.5d and 5.5f for m^{TA}.

The calibration of the calorimeter-based mass and the track-assisted mass reasonably retain the shape of the response distributions as shown in Figures 5.6a, 5.6b and 5.6d. For low m^{truth} and high $p_{\text{T}}^{\text{truth}}$ the calibration of the calorimeter-based mass results in a double peak structure for the mass response distribution, as can be seen for the red solid histogram in Figure 5.6c. Due to rapidly falling response of m^{calo} in this region, two jets on the high and low edges of the same m^{truth} bin can receive very different corrections. In combination with the poor jet mass resolution (JMR) in this region, two populations of jets will exist: those with a higher reconstructed mass where a calibration factor close to one is applied, and those with lower m^{calo} where a large correction is applied (calibration factor $\ll 1$). The m^{TA} calibration is not affected by this because its average mass response is closer to one compared to m^{calo} hence no double peak structure can be seen for the blue solid histogram in Figure 5.6c.

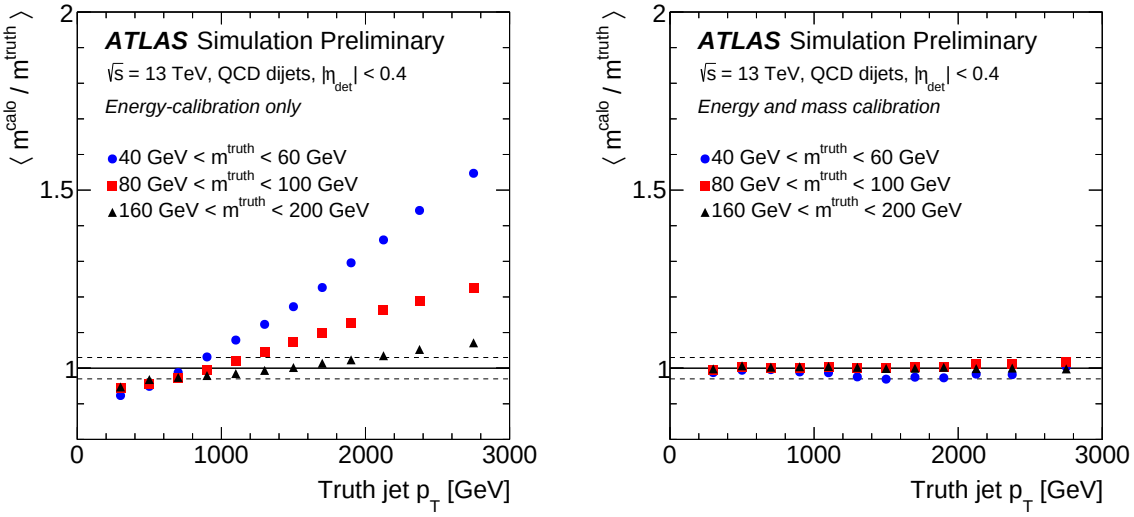

(a)

(b)

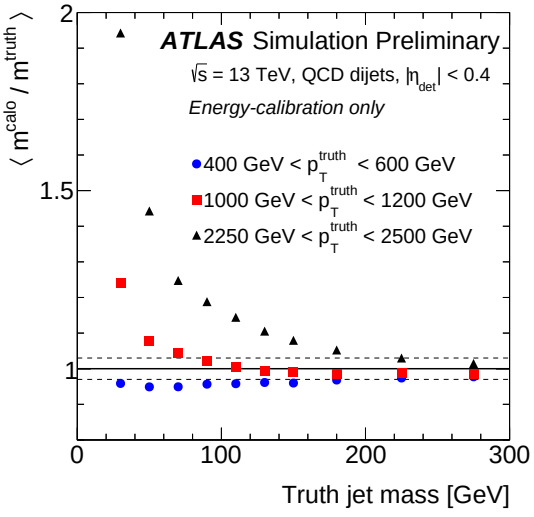

(c)

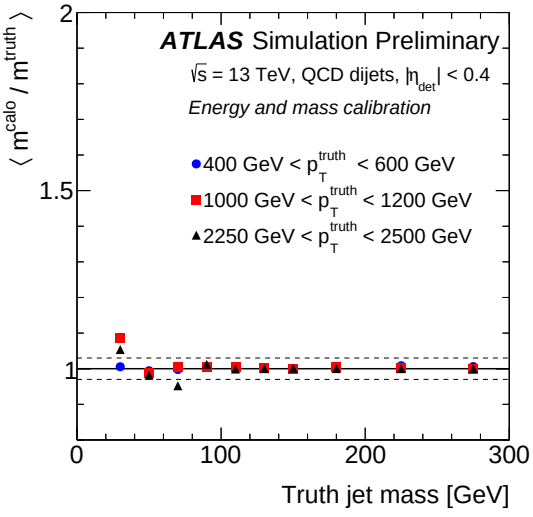

(d)

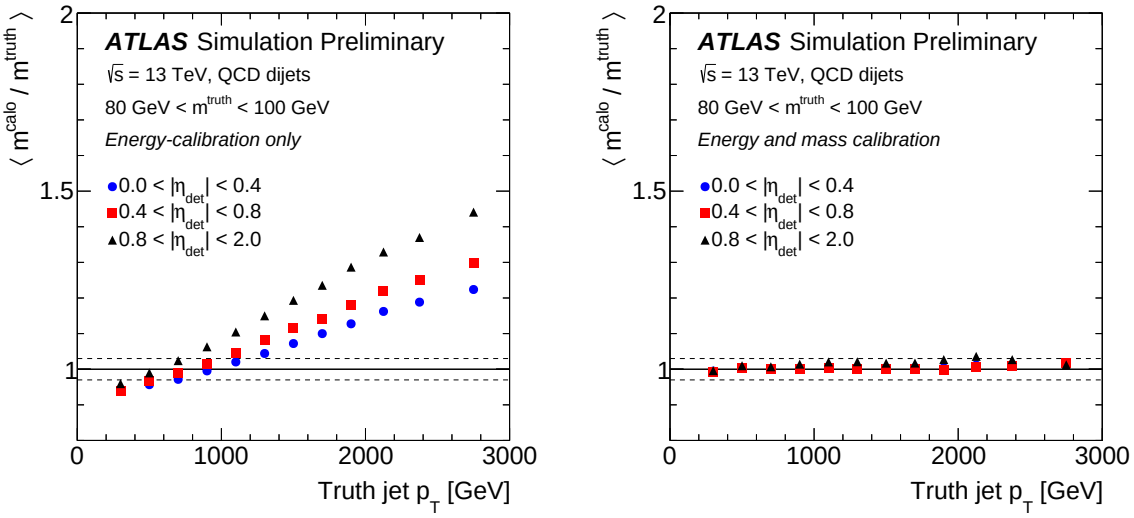

(e)

(f)

Figure 5.4: The average calorimeter-based jet mass response as functions of $p_{\mathrm{T}}^{\mathrm{truth}}$ before (left) and after (right) the mass calibration is applied. The dashed lines are at 1 ± 0.03. Figure produced by the author and published in Reference [1].

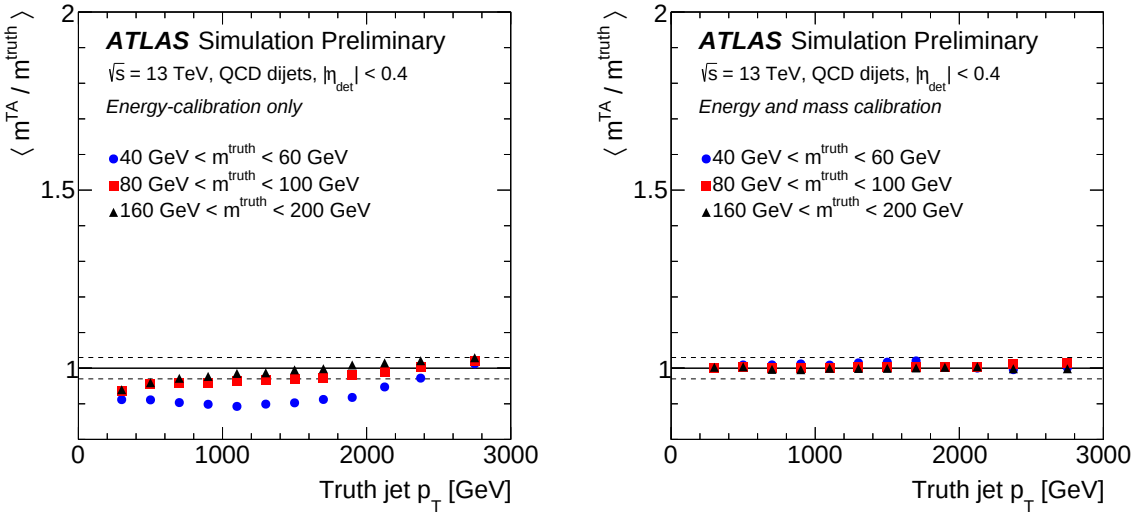

(a)

(b)

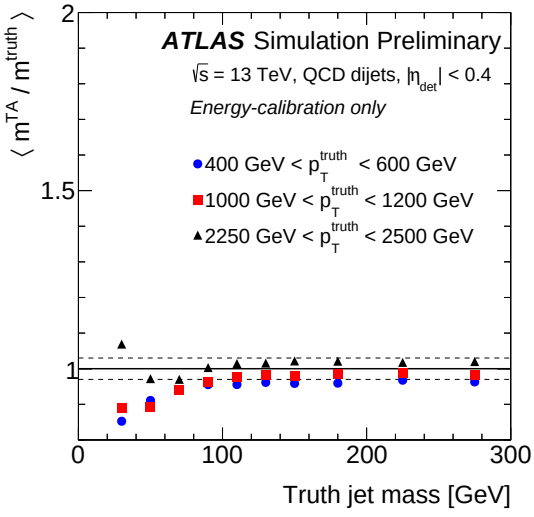

(c)

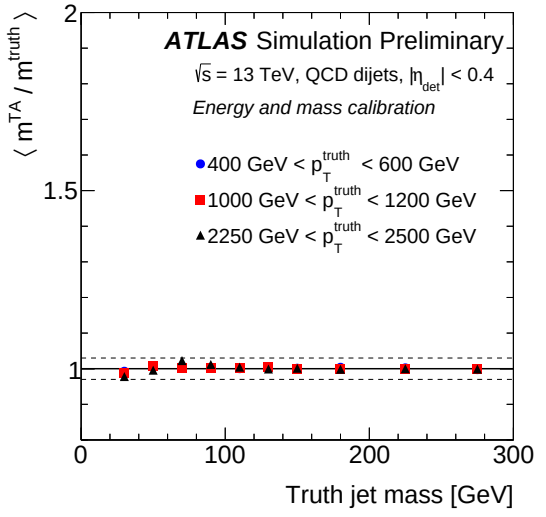

(d)

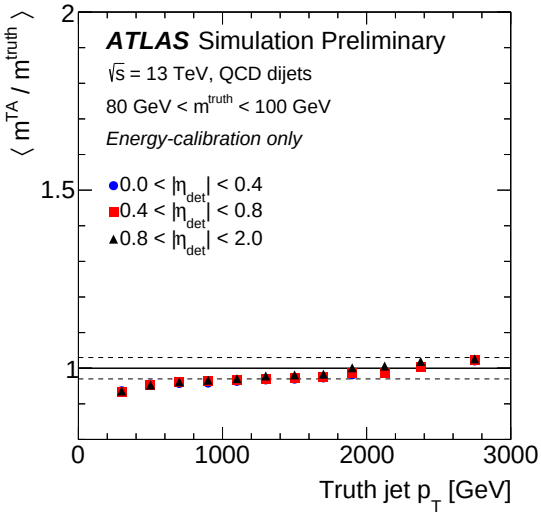

(e)

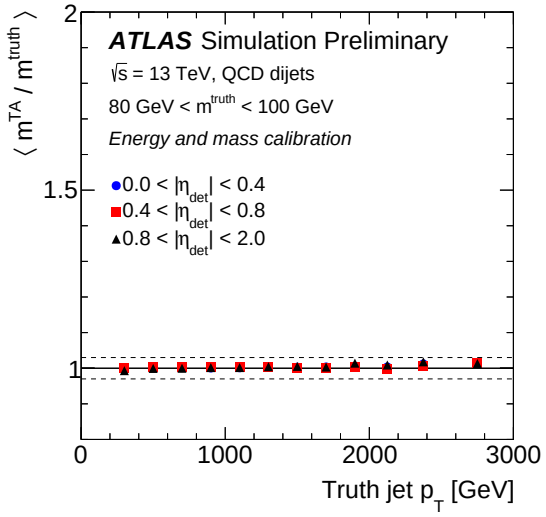

(f)

Figure 5.5: The average track-assisted jet mass response as functions of $p_{\mathrm{T}}^{\mathrm{truth}}$ before (left) and after (right) the mass calibration is applied. The dashed lines are at 1 ± 0.03. Figure produced by the author and published in Reference [1].

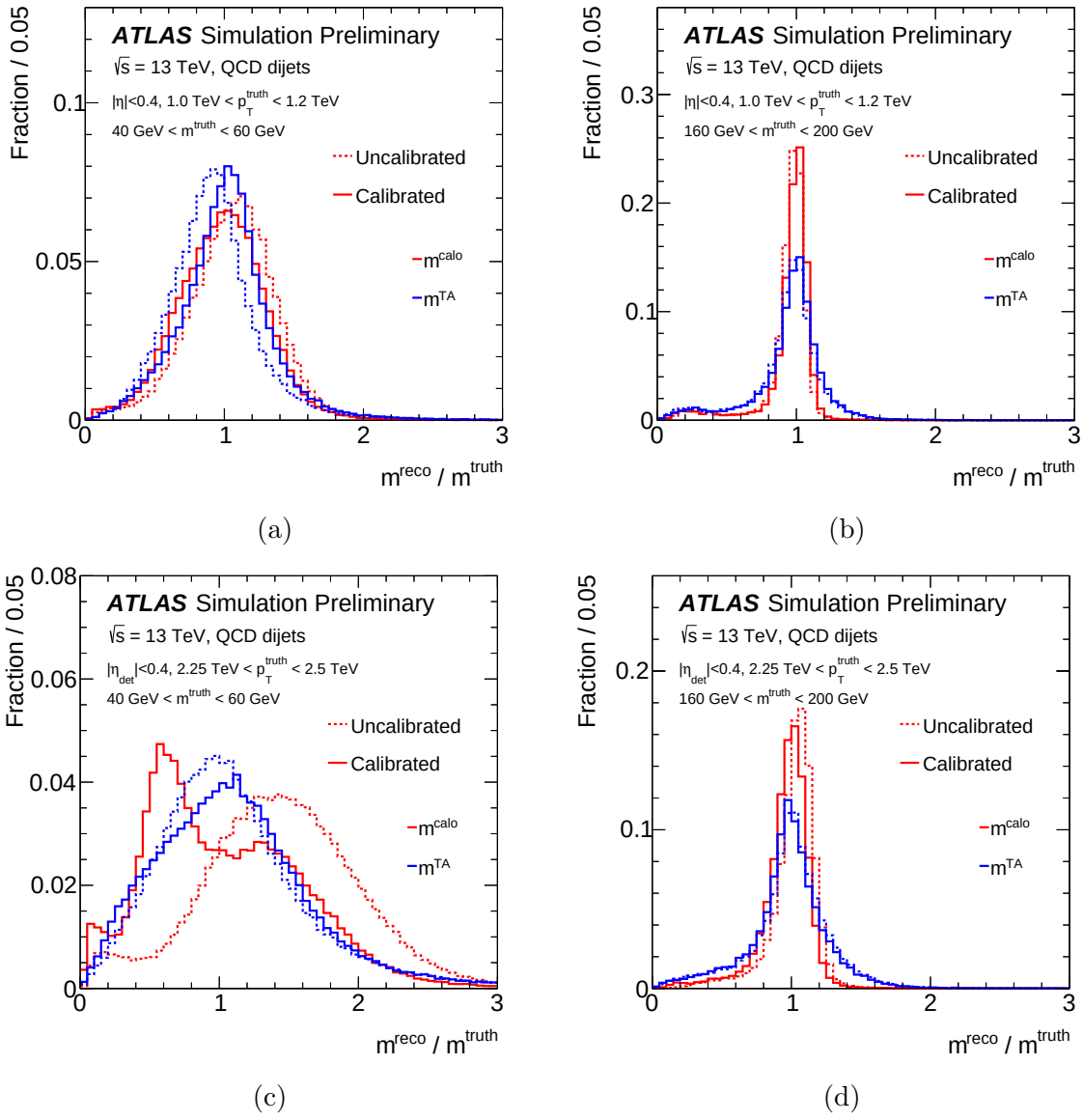

Figure 5.6: Uncalibrated (dashed line) and calibrated (solid line) jet mass response distributions for calorimeter-based jet mass (red) and track-assisted jet mass (blue) for central jets with 1.0 TeV $< p_{\mathrm{T}}^{\mathrm{truth}} <$ 1.2 TeV (a,b) and 2.25 TeV $< p_{\mathrm{T}}^{\mathrm{truth}} <$ 2.5 TeV (c,d). Figure produced by the author and published in Reference [1].

5.3 Performance in simulation

Figure 5.7 shows the resolution of the jet mass response as a function of truth jet p_{T} for jets originating from boosted W and Z bosons as well as top quarks. The resolution of the mass response distribution is quantified by using half of the 68% interquantile range (IQnR)[1] divided by the median has proved to be a robust measure for this quantity, which is insensitive to outliers. This quantity equals the standard deviation of a gaussian distribution if the mass response is normally distributed. Both the calorimeter-based and track-assisted jet mass resolution degrade at high p_{T}, as shown in Figure 5.7. For the calorimeter-based mass this is due to finite granularity of the calorimeter and for the track-assisted mass it is mainly due to a degradation of resolution of the track momentum.

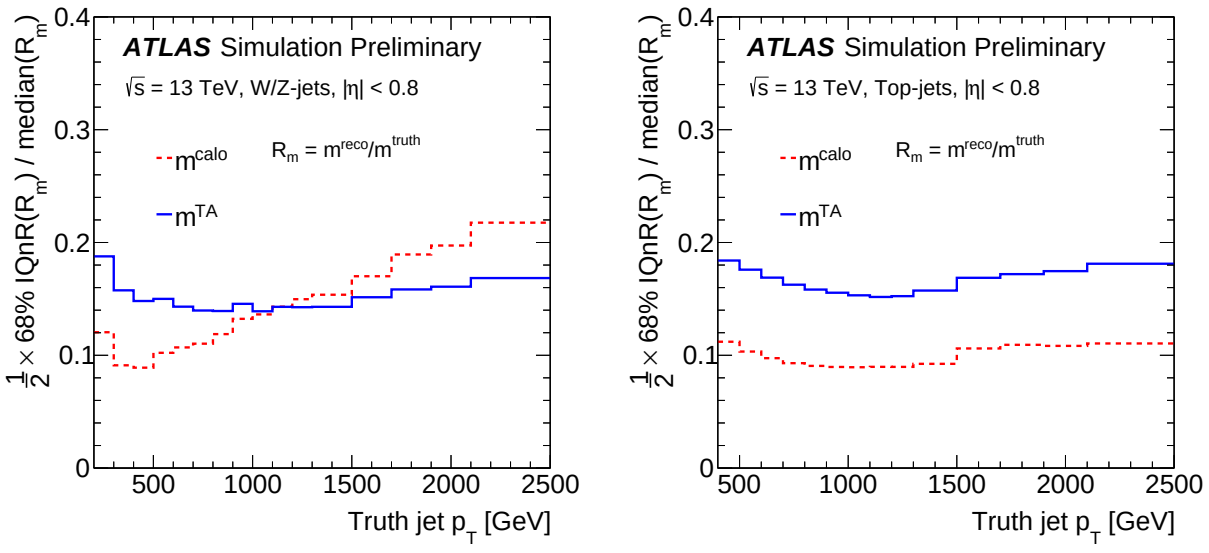

(a) (b)

Figure 5.7: The resolution of the jet mass response as a function of truth jet p_{T} for W and Z boson jets (a) and top-quark jets (b) for calorimeter-based jet mass (red dashed line) and track-assisted jet mass (blue solid line). Figures produced by the author and published in Reference [1].

For jets initiated by W or Z bosons, the m^{TA} resolution surpasses m^{calo} large-R jets with p_{T} greater than 1 TeV. At lower p_{T} the charged-to-neutral fluctuations significantly limit the resolution of m^{TA} so m^{calo} provides a better performance. For different reasons the m^{TA} is unable to match the performance of the m^{calo} for top jets in the studied phase space. Since the mass of the top is higher than the W and Z boson, a greater p_{T} is needed to achieve the same collimation of its decay products. At sufficiently high p_{T}, a cross-over point where the m^{TA} resolution is better than m^{calo} resolution is still expected.

[1]This is defined as $q_{84\%} - q_{16\%}$, whereby $q_{16\%}$ and $q_{84\%}$ are the $16^{\mathrm{th}}$and 84^{th} percentiles of a given distribution.

5.4 Jet mass scale systematic uncertainty

The systematic uncertainty on the calorimeter-based mass scale is determined by using a method called the r^{track} double ratio method [136, 155]. In this method, large-R track jets are built from ID tracks and use the same jet clustering and grooming algorithms as large-R calorimeter jets. The track jets are then matched to the calorimeter jets. For each matched pair of calorimeter and track jets, the r^{track} mass ratio ($r_{\text{m}}^{\text{track}}$) of the calorimeter-based mass to the track jet mass ($m^{\text{track jet}}$) is calculated as

$$r_{\text{m}}^{\text{track}} = \frac{m^{\text{calo}}}{m^{\text{track jet}}}. \tag{5.9}$$

This $r_{\text{m}}^{\text{track}}$ variable is calculated in both MC simulation and data enriched with QCD dijet events, and the following double ratio can be computed

$$R_m^{\text{track}} = \frac{\langle r_m^{\text{track}} \rangle_{\text{data}}}{\langle r_m^{\text{track}} \rangle_{\text{MC}}} \tag{5.10}$$

where $\langle r_m^{\text{track}} \rangle_{\text{data}}$ and $\langle r_m^{\text{track}} \rangle_{\text{MC}}$ are the average of the $r_{\text{m}}^{\text{track}}$ distribution in data and MC respectively. The R_m^{track}ratio should be equal to unity if detector effects are well modelled, and any deviation from this expectation can be taken as an uncertainty on the calorimeter-based mass scale. This method is designed around the fact that the ATLAS detector provides two independent measurements of the properties of the same jet from the ID and calorimeter. Figure 5.8 shows the average r^{track} mass ratio of the calorimeter-based mass to the track jet mass as a function of the calorimeter jet p_{T}. The PYTHIA8 sample is used as the baseline MC sample to compare with data. To asses the systematic uncertainty of this measurement, the PYTHIA8 sample is varied by the uncertainties on track reconstruction. An alternative MC sample in the form HERWIG++ is used to assess the uncertainty due to the physics process modelling differences.

In the case of the track-assisted mass, both the uncertainties on the track reconstruction and the calorimeter jet p_{T} are known[2], so the systematic uncertainties the track-assisted mass scale can be evaluated directly by propagating the uncertainty on the individual components of Equation 5.2. This is one of the key advantages of the track-assisted mass compared to the calorimeter-based mass, and the uncertainties on the track related components are derived as explained below.

The material in the ID is not precisely known. Since hadronic interactions with its material are the main source of track reconstruction inefficiencies for isolated particles, the

[2]The uncertainty on $p_{\text{T}}^{\text{calo}}$ is estimated by using the same r^{track} double ratio with the mass variable replaced with p_{T}.

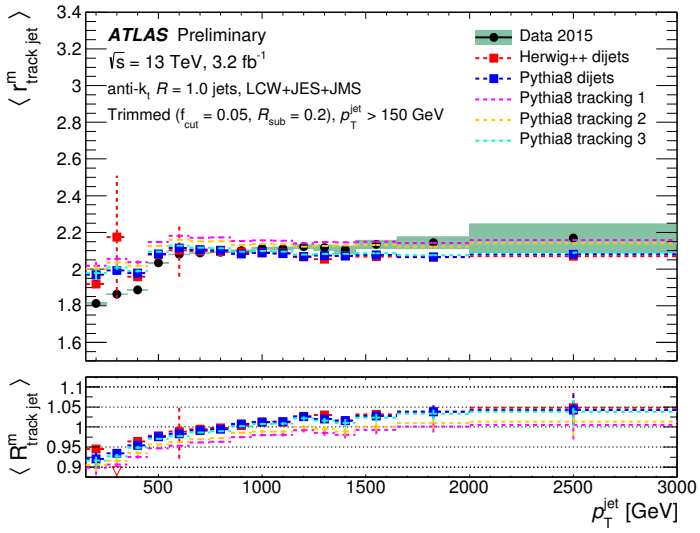

Figure 5.8: The average r^{track} mass ratio of the calorimeter-based mass to the track jet mass as a function of the calorimeter jet p_{T} in 2015 data and two dijet MC samples:PYTHIA8 and HERWIG++. Shown also are three variations of the PYTHIA8 sample taking uncertainties related to the track reconstruction. The $R_m^{\text{track}}$is shown in the lower part of the plot. Figure retrieved from Reference [156].

introduced uncertainty is evaluated by varying the amount of material within its measured uncertainty [157]. A residual track reconstruction inefficiency in the core of highly energetic jets exists and the uncertainties on it are derived as described in Reference [158]. Fake tracks provide the second biggest source of uncertainty on track reconstruction. Using the assumption that the number of reconstructed tracks is expected to increase linearly as a function of pileup interactions, given there are no fake tracks, the fraction of fake tracks can be measured from the deviation from this linearity. By comparing this non-linearity in data and MC, an uncertainty on the fake rate is obtained [159]. A possible uncertainty due to a bias in the reconstructed momentum of the tracks can be assessed using $Z \to \mu\mu$ events, where the momentum is reconstructed iteratively to obtain the mass of the Z boson [99]. The fragmentation modeling differs between different MC event generators, which leads to differences in the track reconstruction performance. Such differences can lead to changes in m^{TA} and their magnitude is estimated by comparing PYTHIA8 and HERWIG++.

The individual components of the JMS uncertainties for both m^{TA} and m^{calo} are shown in Figure 5.9. Full correlation is assumed between the track reconstruction uncertainties on m^{TA} and m^{calo}, since for both quantities a variant of the r^{track} method is used to estimate parts of the uncertainty. The track-assisted mass is built through $m^{\text{track}}/p_{\text{T}}^{\text{track}}$ (Equation 5.2) so the overall uncertainty on the JMS due to track reconstruction uncertainties is much smaller as they cancel out in the ratio. In the region of $p_{\text{T}} = 300 \sim 1000$ GeV, the uncertainty is about 4% for m^{calo} and about 2% for m^{TA}. At higher p_{T}, the uncertainty is limited for both

mass definitions by the statistics available in the data set, which limits the precision of the $r_{\mathrm{m}}^{\mathrm{track}}$ measurement.

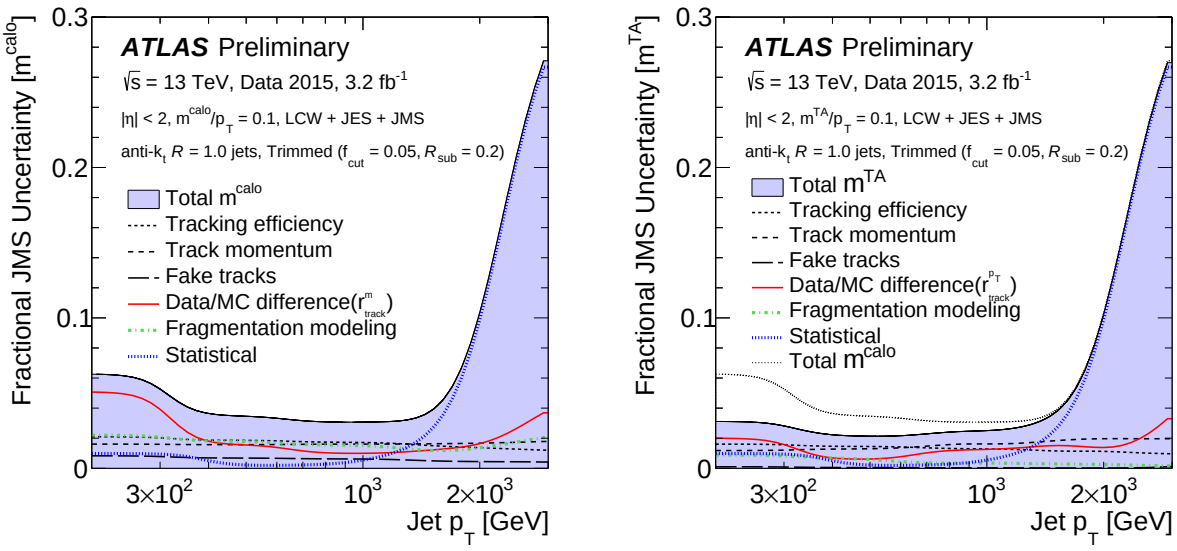

(a) (b)

Figure 5.9: A breakdown of the systematic uncertainties on the jet mass scale for (a) m^{calo} and (b) m^{TA} as a function of jet p_{T} for $m^{\mathrm{reco}}/p_{\mathrm{T}} = 0.1$ and $|\eta| < 2$. The total JMS uncertainty for m^{calo} is included for comparison with the total JMS uncertainty for m^{TA}. The uncertainty is parameterised as a function of m/p_{T} and these two plots show a slice at $m/p_{\mathrm{T}} = 0.1$. Figures produced by another collaborator and published in Reference [1].

5.5 Combination of m^{TA} and m^{calo}

The calorimeter-based jet mass is not explicitly used in calculating the track-assisted mass (Equation 5.2) and as Figure 5.10 shows, the correlation between the two masses is indeed very small. For jets with $p_{\mathrm{T}} > 1$ TeV the correlation coefficient is just 0.1. Both m^{calo} and m^{TA} are influenced by local fluctuations in the energy response of the calorimeter, but the impact on m^{TA} is smaller, due to $p_{\mathrm{T}}^{\mathrm{calo}}$ (used to calculate m^{TA}) being less sensitive to local fluctuations compared to m^{calo}.

From this observation of small correlation, a combination of the two masses, the so called combined jet mass, can potentially provide a more powerful mass definition. Under the assumption that both individual jet mass responses are Gaussian, the combined jet mass is given by a linear combination of m^{calo} and m^{TA},

$$m^{\mathrm{comb}} = w_{\mathrm{calo}} \times m^{\mathrm{calo}} + w_{\mathrm{TA}} \times m^{\mathrm{TA}}. \tag{5.11}$$

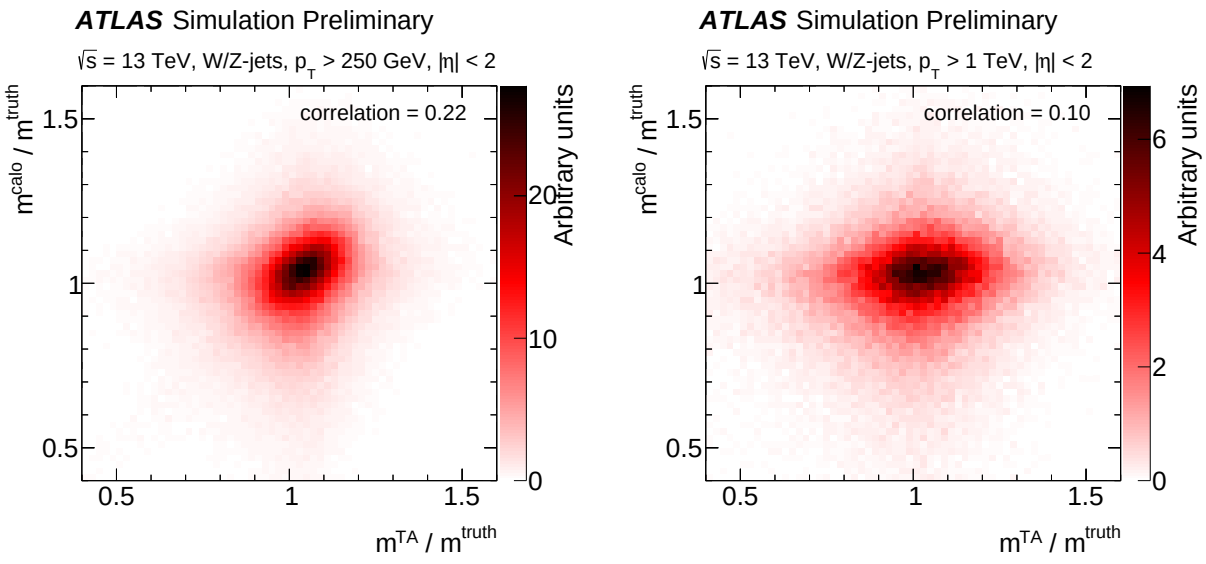

(a) (b)

Figure 5.10: Correlation between the mass responses of m^{calo} and m^{TA} for W/Z-jets in MC with $|\eta_{\text{det}}| < 2$ and (a) $p_{\text{T}} > 250$ GeV and (b) $p_{\text{T}} > 1$ TeV. Figures produced by the author and published in Reference [1].

Furthermore, since both m^{calo} and m^{TA} are already calibrated, m^{comb} is also calibrated by requiring the sum of the weights to be $w_{\text{calo}} + w_{\text{TA}} = 1$. Considering these two points, choosing weights which are proportional to the individual mass resolutions is an appropriate choice for the combination:

$$w_{\text{calo}} = \frac{\sigma_{\text{calo}}^{-2}}{\sigma_{\text{calo}}^{-2} + \sigma_{\text{TA}}^{-2}} \qquad w_{\text{TA}} = \frac{\sigma_{\text{TA}}^{-2}}{\sigma_{\text{calo}}^{-2} + \sigma_{\text{TA}}^{-2}}, \tag{5.12}$$

In Equation 5.12, σ_{calo} and σ_{TA} are the calorimeter-based and track-assisted mass resolutions respectively. The resolution of all three mass definitions is compared in Figure 5.11 for W-jets and Z-jets in MC as a function of the truth jet p_{T}. At low jet p_{T}, the resolution of m^{comb} is very close to m^{calo} and at higher p_{T}, m^{TA} contribution dominates m^{comb} with a smooth interpolation in the intermediate p_{T} region. There is a non-trivial increase in resolution of the intermediate jet p_{T} range, and the combined JMR is always superior to the individual jet masses.

Systematic uncertainties on m^{comb} are obtained by propagating the individual uncertainties on m^{TA} and m^{calo} through Equation 5.12, while the contributions of the track reconstruction uncertainties need to be treated as fully correlated.

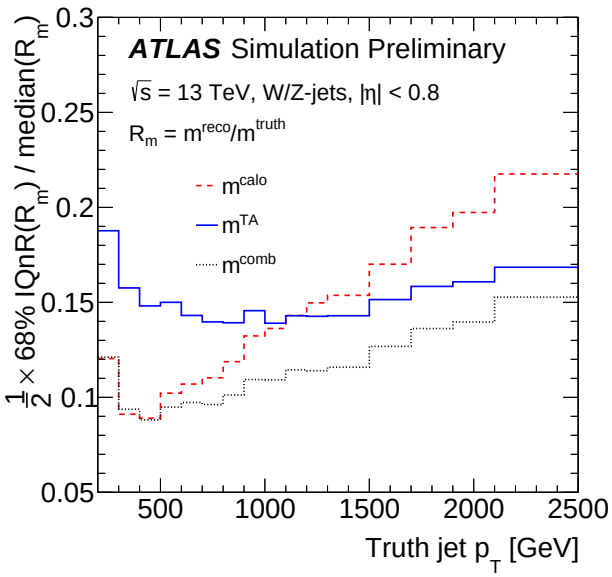

Figure 5.11: Resolution of m^{calo}, m^{TA} and m^{comb} for W/Z-jets in MC as a function of $p_{\text{T}}^{\text{truth}}$. The resolution is defined as half of the 68% interquantile range (IQnR) divided by the median of the distribution. Figure produced by the author and published in Reference [1].

Chapter 6

Analysis Strategy

This chapter describes the analysis strategy for the search of resonant di-Higgs production in $\sqrt{s} = 13$ TeV pp collision data recorded by the ATLAS detector. The search is conducted in the $b\bar{b}WW^*$ decay mode with the semi-leptonic final state consisting of a single lepton, multiple jets and missing transverse energy. This analysis is designed to search for high mass TeV-scale resonances and due to the high boost of the decaying Higgs bosons, the $h \to b\bar{b}$ decay is reconstructed using a large-R jet instead of two small-R jets.

As this analysis is the first TeV-scale resonant Higgs boson production search in the $b\bar{b}WW^*$ decay mode by the ATLAS collaboration, a simple analysis strategy is utilised and the reconstructed objects and event selections are not optimised in detail. It is designed to assess the level of sensitivity of the decay mode with the semi-leptonic final state and establish a baseline strategy for future iterations of this analysis to improve upon.

Section 6.1 details the selections imposed on reconstructed objects and events to extract resonant di-Higgs signals among the SM backgrounds. Section 6.2 and 6.3 discusses the procedure of modelling the expected signal and background processes with the validation of the background modelling in dedicated control regions. Section 6.4 describes the method to evaluate the systematic uncertainties related to the modelling of signal and background processes.

6.1 Event selection

The dataset used in this search corresponds to data recorded at a center-of-mass energy of $\sqrt{s} = 13$ TeV with integrated luminosity of 3.2 fb^{-1} in 2015 and 32.9 fb^{-1} in 2016 making the total integrated luminosity 36.1 fb^{-1}. This total integrated luminosity is smaller than the recorded luminosity as mentioned in Section 3.3 because the collision data used for physics analysis in ATLAS are required to be recorded during stable beam conditions with

all relevant sub-detectors providing high-quality data. The ATLAS Data Quality Group provides a list containing the runs with high-quality data, the Good Runs List (GRL), and the list[1] corresponds to 36.1 fb^{-1} of data suitable for physics analysis.

6.1.1 Trigger selection

Events are required to have fired a logical OR of single lepton triggers. For the 2015 dataset, the muon trigger with the lowest p_{T} threshold trigger requires a HLT level reconstructed muon to have $p_{\mathrm{T}} > 20$ GeV and to pass the loose isolation requirement (mu20_iloose). A muon trigger with no isolation requirement and a tighter p_{T} (> 50 GeV) requirement is also used (mu50). For the 2016 dataset, the mu50 trigger is still used but the lowest p_{T} threshold trigger has a higher $p_{\mathrm{T}} > 26$ GeV requirement and a tighter isolation criteria (mu26_ivarmedium).

Electron triggers for the 2015 dataset have different E_{T} threshold and likelihood identification criteria. The lowest E_{T} threshold electron trigger is the e24_lhmedium_L1EM20VH trigger and it is fired if there is a HLT level reconstructed electron with $E_{\mathrm{T}} > 24$ GeV which passes the medium likelihood identification. It is seeded by an L1 trigger with E_{T} threshold of 20 GeV and E_{T} dependent veto against energy deposited in the hadronic calorimeter behind the electron candidates electromagnetic cluster. Two more electron triggers are used with higher E_{T} threshold, > 60 GeV (e60_lhmedium) and > 120 GeV (e120_lhloose) with the highest E_{T} threshold trigger having a looser likelihood identification requirement. Since the triggering rates scale with the instantaneous luminosity, the lowest E_{T} threshold for electron triggers was increased to 26 GeV (e26_lhtight_nod0_ivarloose) with tighter likelihood identification requirement and an additional isolation criteria to ensure managable event recording rates for data taking in 2016. The higher E_{T} triggers, e60_lhmedium_nod0 and e140_lhloose_nod0, have looser likelihood identification requirement and no requirement on the electron track d_0.

6.1.2 Object selection

Leptons

For electrons and muons, three type of selections are defined: *Loose*, *Tight* and *AntiTight*. The definitions of the selections are summarised in Table 6.1. Loose leptons are first identified

[1]The GRL XML files used for selection good data in this analysis are:

- data15_13TeV.periodAllYear_DetStatus-v79-repro20-02_DQDefects-00-02-02_PHYS_StandardGRL_All_Good_25ns.xml
- data16_13TeV.periodAllYear_DetStatus-v84-pro20-16_DQDefects-00-02-04_PHYS_StandardGRL_All_Good.xml

and then used as inputs to $E_{\mathrm{T}}^{\mathrm{miss}}$ reonstruction and the overlap removal procedure. Leptons which pass the Loose requirement and survive the overlap removal procedure are then used to define the Tight and AntiTight leptons which have more stringent requirements than the Loose definition and they are subsets of Loose leptons.

Tight leptons are used as the lepton candidate in the event selection while AntiTight leptons are used to identify control regions for the purpose of data-driven estimation of background. Both definitions are almost exactly the same apart from the lepton d_0^{sig} requirement. In this analysis, the $|d_0^{\mathrm{sig}}|$ selection value (< 2) used for electrons and muons is not the recommended value by the ATLAS e/γ and muon performance groups. The recommended value for electrons is 5 while for muons it is 3. The motivation for the tighter selection than the recommended value is to define regions in data with enhanced contribution of fake leptons for the purpose of multijet background estimation in the search region. The data-driven method to estimate the multijet background is discussed extensively in Section 6.2.2.

Selection	p_{T}	$\lvert\eta\rvert$	ID	$\lvert d_0^{\mathrm{sig}}\rvert$	$\lvert\Delta z_0^{\mathrm{BL}} \sin\theta\rvert$	Isolation
			Electrons			
Loose	>7 GeV	< 2.47	LH Loose	< 10	< 0.5 mm	-
Tight	>27 GeV	< 2.47 and $\notin [1.37, 1.52]$	LH Tight	< 2	< 0.5 mm	FixedCutTightTrackOnly
AntiTight	>27 GeV	< 2.47 and $\notin [1.37, 1.52]$	LH Tight	< 10 and > 2	< 0.5 mm	FixedCutTightTrackOnly
			Muons			
Loose	>7 GeV	< 2.7	Loose quality	< 6	< 0.5 mm	-
Tight	>27 GeV	< 2.4	Medium quality	< 2	< 0.5 mm	FixedCutTightTrackOnly
AntiTight	>27 GeV	< 2.4	Medium quality	< 6 and > 2	< 0.5 mm	FixedCutTightTrackOnly

Table 6.1: Reconstructed electron and muon selections defined in this analysis. The definitions of the identification and isolation criteria were presented in Sections 4.2 and 4.3.

Small-R jets

In order to reconstruct the hadronic W boson candidates in this analysis, small-R jets are used. They are first required to pass Loose jet cleaning selection and then pass kinematic requirements of $p_{\mathrm{T}} > 20$ GeV for jets with $\eta < 2.5$. Furthermore, small-R jets are required to pass the Default working point JVT requirement to ensure that they originate from the hard scatter vertex. The jet cleaning and JVT selections were defined in Section 4.4. Jets that pass all the requirements are used as inputs to the overlap removal procedure.

A small-R jet is said to be b-tagged if its MV2c10 discriminant is larger than 0.6459. This corresponds to a fixed-cut b-tagging efficiency working point of 77% [142] with light-jets (c-jets) rejection rate of 134 (6). For the purpose of $E_{\mathrm{T}}^{\mathrm{miss}}$ reconstruction, all fully calibrated small-R jets are used as inputs which is the recommendation by the ATLAS JetEtMiss performance group.

Large-R jets and track jets

Large-R jets are used to reconstruct $h \to b\bar{b}$ candidates. They are required to have $p_{\mathrm{T}} > 250$ GeV and $|\eta| < 2.0$. To identify large-R jets that are consistent with the decay of $h \to b\bar{b}$, track jets are used as subjets to identify the b-jets within the large-R jets.

The track jets are required to have $p_{\mathrm{T}} > 10$ GeV, $|\eta| < 2.5$ and have at least 2 track constituents. A track jet is considered to be b-tagged if its MV2c10 discriminant is larger than 0.5140. This b-tagging selection corresponds to a fixed-cut efficiency working point of 77% with light-jets (c-jets) rejection rate of 58 (4).

Overlap removal

In order to uniquely identify reconstructed objects, a procedure for removing objects that geometrically overlap must be applied as the algorithms used to reconstruct electrons, muons, and jets use the same sub-detector signals as inputs. To avoid double counting objects created from the same tracks and calorimeter deposits within an event, rules for object priority are applied for removing objects in close proximity to one another. This is known as overlap removal and the procedure used in this analysis is defined in the following order:

- remove any calorimeter-tagged muons sharing an ID track with an electron.
- remove any electrons sharing an ID track with remaining muons.
- reject small-R jets within $\Delta R < 0.2$ of any remaining electrons.
- reject electrons that satisfy $\Delta R < \min(0.4, 0.04 + 10\mathrm{GeV}/E_{\mathrm{T}}^{\mathrm{electron}})$ of any suriving small-R jets.
- reject remaining small-R jets satisfying both:
  - within $\Delta R < 0.2$ of a muon
  - less than three associated tracks or ($p_{\mathrm{T}}^{\mathrm{muon}}/p_{\mathrm{T}}^{\mathrm{jet}} < 0.5$ and $p_{\mathrm{T}}^{\mathrm{muon}}/p_{\mathrm{T}}^{\mathrm{tracksjet}} < 0.7$.)
- reject remaining muons if within $\Delta R < \min(0.4, 0.04 + 10\ \mathrm{GeV}/p_{\mathrm{T}}^{\mathrm{muon}})$

Only the surviving muons, electrons and small-R jets from the overlap removal procedure are used in the event selection.

6.1.3 Event cleaning

Before the event selection begins, a preselection is imposed for every event to reject events with detector and reconstruction problems. The first stage is called event cleaning which is a standard requirement for ATLAS physics analyses:

- Good Runs List: A GRL selection is applied to ensure the data corresponds to periods of time (lumi-blocks) where the detector was fully operational and the data collected was of adequate quality.
- HS Vertex: The event is required to have at least one primary vertex, where the vertex should have at least two tracks. The tracks are required to have $p_{\mathrm{T}} > 400$ MeV. If there is more than one primary vertex, the one with the largest $\sum p^2_{\mathrm{T,track}}$ is selected as the hard scatter vertex.
- Subdetector Error Veto: Corrupted events from LAr and Tile calorimeters, and the SCT are vetoed. Events are also rejected if there is a noise burst in the LAr calorimeter.
- Incomplete Events: If a recorded event is missing detector information, it is rejected.

After the cleaning selections, events are preselected based on the reconstructed physics objects. Events are required to have at least one Tight lepton, 1 large-R jet and 2 small-R jets, to be considered for event selection.

6.1.4 Selections

The event selection begins by identifying the lepton from the leptonic W boson decay. Events are required to have at least one Tight muon or one Tight electron for the selection of the lepton candidate. If both type of leptons are present in an event, the muon is chosen as the lepton candidate. The lepton candidate will be referred to as the *selected* lepton for the rest of thesis in the context of this analysis. The selected lepton is required to be matched to the HLT lepton object which fired the trigger item of the recorded event.

The identifcation of the $h \to b\bar{b}$ candidate starts by requiring events to have at least one large-R jet with an angular separation of $\Delta R > 1.0$ from the selected lepton. The highest p_{T} large-R jet that passes this requirement is chosen as the $h \to b\bar{b}$ candidate. The angular separation requirement ensures that the selected lepton and $h \to b\bar{b}$ candidate are well separated in the detector. The large-R jet is then required to have at least two track jets associated to it. Events with the large-R jet mass (m_J) in the range of 30 GeV $< m_J <$ 300 GeV are retained for further analysis.

In order to select the hadronic W boson candidates, at least two small-R jets with an angular separation requirement of $\Delta R > 1.4$ from the $h \to b\bar{b}$ candidate are required. This ensures that the small-R jets do not overlap with the $h \to b\bar{b}$ candidate. If there are exactly two small-R jets, they are used to reconstruct the candidate. If there are at least three small-R jets, the hadronic W boson is reconstructed from the combination of pairs of the three highest p_{T} small-R jets with the smallest ΔR between the small-R jets.

After the selection of the hadronic W boson candidate, the kinematics of the $h \to WW^* \to \ell\nu q\bar{q}$ system can now be fully reconstructed. Among all four-momenta of the final state particles, only the component of the neutrino longitudinal momentum p_z^ν, is unknown while its transverse momentum components, p_x^ν and p_y^ν are measured as the transverse components of the missing transverse momentum vector ($\mathbf{E}_{\mathrm{T}}^{\mathrm{miss}}$). The neutrino p_z^ν is deduced by imposing the conservation of four momenta of the final state particles $h \to WW^* \to \ell\nu q\bar{q}$ with the mass of the Higgs boson:

$$m^2_{h\to WW} = (\mathbf{p}^\ell + \mathbf{p}^\nu + \mathbf{p}^{W_{had}})^2 \tag{6.1}$$

where $\mathbf{p}^\ell$, $\mathbf{p}^\nu$ and $\mathbf{p}^{W_{had}}$ are the four-momenta of the selected lepton, neutrino and hadronic W candidate respectively. The mass of the $h \to WW^*$ system ($m_{h\to WW}$) is set to 125.09 GeV. The neutrino p_z^ν can then be calculated using the following relations:

$$E^\nu = \sqrt{(p_x^\nu)^2 + (p_y^\nu)^2 + (p_z^\nu)^2}; \quad p_x^\nu = E_{\mathrm{T}}^{\mathrm{miss}} \cos(\phi); \quad p_y^\nu = E_{\mathrm{T}}^{\mathrm{miss}} \sin(\phi) \tag{6.2}$$

where ϕ is the azimuthal angle of $\mathbf{E}_{\mathrm{T}}^{\mathrm{miss}}$ and E^ν is the neutrino energy. Equation 6.1 leads to a quadratic expression when solving for p_z^ν. It can have two real, one real or two complex solutions although it is highly unlikely to calculate exactly one solution. In the first case the solution which gives the neutrino direction closest to the selected lepton is chosen. In the complex case, only the real part of the complex solution is taken into account, therefore a single value of p_z^ν is obtained. The frequency of the complex case varies from 3% to 8% depending on the heavy scalar resonance signal mass considered.

With the $h \to b\bar{b}$ candidate identified and $h \to WW^* \to \ell\nu q\bar{q}$ system fully reconstructed, the di-Higgs (hh) system is reconstructed by the sum of four-momenta of the $h \to b\bar{b}$ candidate and the reconstructed $h \to WW^* \to \ell\nu q\bar{q}$ system.

After the di-Higgs system has been reconstructed, two b-tagging requirements are imposed on the event. Firstly, all small-R jets (with $\Delta R > 1.4$ from $h \to b\bar{b}$ candidate) are required to fail b-tagging. This anti b-tagging requirement is called the "top veto" as it rejects $t\bar{t}$ events. The second b-tagging requirement is on the two highest p_{T} track jets associated with the $h \to b\bar{b}$ candidate large-R jet. If both track jets are b-tagged, the event falls into the

"2-tag" category. If one of the two track jet is b-tagged while the other is not b-tagged, the event is categorised as "1-tag".

Finally, the $E_{\mathrm{T}}^{\mathrm{miss}}$ is required to be more than 50 GeV to reject events from multijet background. Throughout the rest of this thesis, the distinction between lepton flavours are not made explicitly and events are considered to be in the lepton+jets (ℓ+jets) channel. In cases where the lepton flavour is explicitly required for discussion such as in Section 6.2.2, events can be categorized according to the flavour of selected lepton. If an event has an electron as the selected lepton, it is considered to be in the electron+jets (e+jets) channel event and if it is a muon, it is considered in the muon+jets (μ+jets) channel.

Region definition

In order to enhance the sensitivity of this analysis to a resonant di-Higgs signal, it is required that the $h \to b\bar{b}$ candidate large-R jet has a mass consistent with the Higgs boson mass. Events which have the large-R jet mass in a window of 90 GeV $< m_J <$ 140 GeV are considered to be in the "signal region" (SR). It is expected to be enriched with signal events hence the naming convention of the region. Any event which has a large-R jet mass $m_J <$ 90 GeV or $m_J >$ 140 GeV falls into the "mBB control region" (mBBcr). By construction, this region is orthogonal to the signal region. The mBB control region is used to validate the modelling of the predicted background in a region that is close to the signal region but has negligible expected signal event contamination.

Search strategy

In this analysis, the search for di-Higgs resonances is performed in the 2-tag signal region. The discriminating variable used to perform the search in the observed data is the invariant mass of the reconstructed di-Higgs system (m_{hh}). The search is performed using a binned maximum likelihood fit of the m_{hh} distribution. The details of the statistical treatment of the search and its result are presented in Chapter 7.

Initially, the analysis is "blinded". This means that before making any observation of the m_{hh} distribution in the 2-tag signal region in data, the expected total background is first estimated with its corresponding uncertainty. Section 6.2 discusses the strategy to predict the expected background processes and continues, in Section 6.3, with the validation of the background predictions in dedicated control regions. Section 6.4 presents the systematic uncertainties on the predicted background and signal processes.

6.1.5 Signal efficiency

The signal efficiency is calculated as the fraction of signal events passing a certain event selection and reconstruction level. Figure 6.1 shows the signal efficiency as a function of heavy scalar resonance mass at various levels of the event selection for the ℓ+jets channel and in each e+jets and μ+jets channel. If only considering the semi-leptonic final state for the $b\bar{b}WW^*$ decay mode, the maximum efficiency achievable is $\sim 35\%$. The efficiency at the end of the selection is at about 1.7% for a 800 GeV resonance mass and then increases slightly up until 2.6% for a resonance mass of 1500 GeV. From 1500 GeV and above, the signal efficiency drops as the resonance mass increases.

From Figure 6.1a, it is interesting to note that the "1 lepton" selection (black circle) is very inefficient for high mass resonance signals. When the signal efficiency is split between the lepton channels as in Figures 6.1b and 6.1c, the inefficiency is driven more by the e+jets channel rather the μ+jets channel. This is due to the the degradation of the likelihood identification of the reconstructed electron when it overlaps with a jet, and in this signal topology the jet comes from the decay of the hadronic W boson. The higher the mass of the resonance signal, the more collimated the flight direction of the lepton and the jets.

The efficiency of the identification of $h \to b\bar{b}$ candidates also shows a decreasing trend as a function of resonance mass. This can be seen for the "2 track jets" (blue upward triangle) and the "2 b-tag track jet" (light blue cross) requirements. The selection efficiency for 2 track jets in the large-R $h \to b\bar{b}$ candidate decreases for increasing resonance mass. This is due to the increasing collimation of the two b-quarks from the Higgs boson resulting from the boost that it obtains from the resonance decay. The $R = 0.2$ anti-k_t jet algorithm is unable to properly distinguish the two b-jets in the large-R jet as the b-jets are getting closer together in their flight direction. The performance of the MV2c10 b-tagging algorithm degrades as a function of jet p_{T} and this effect can be seen in the 2 b-tag track jets selection. As the mass of the resonance increases, the track jets' p_{T} gets larger and the MV2c10 algorithm's ability to identify b-hadrons is more inefficient. This is due to highly energetic b-hadrons that decay beyond the first ID layer and the charged particles within high p_{T} jets are more collimated compared to low p_{T} jets which results in degradation of track reconstruction efficiency.

6.2 Signal and background modelling

While the di-Higgs resonance search is by its nature generic (as it is a simple search for an excess over the predicted total background in m_{hh} spectrum), there are two benchmark signal models that are tested by this analysis. The first is a heavy spin-0 narrow resonance.

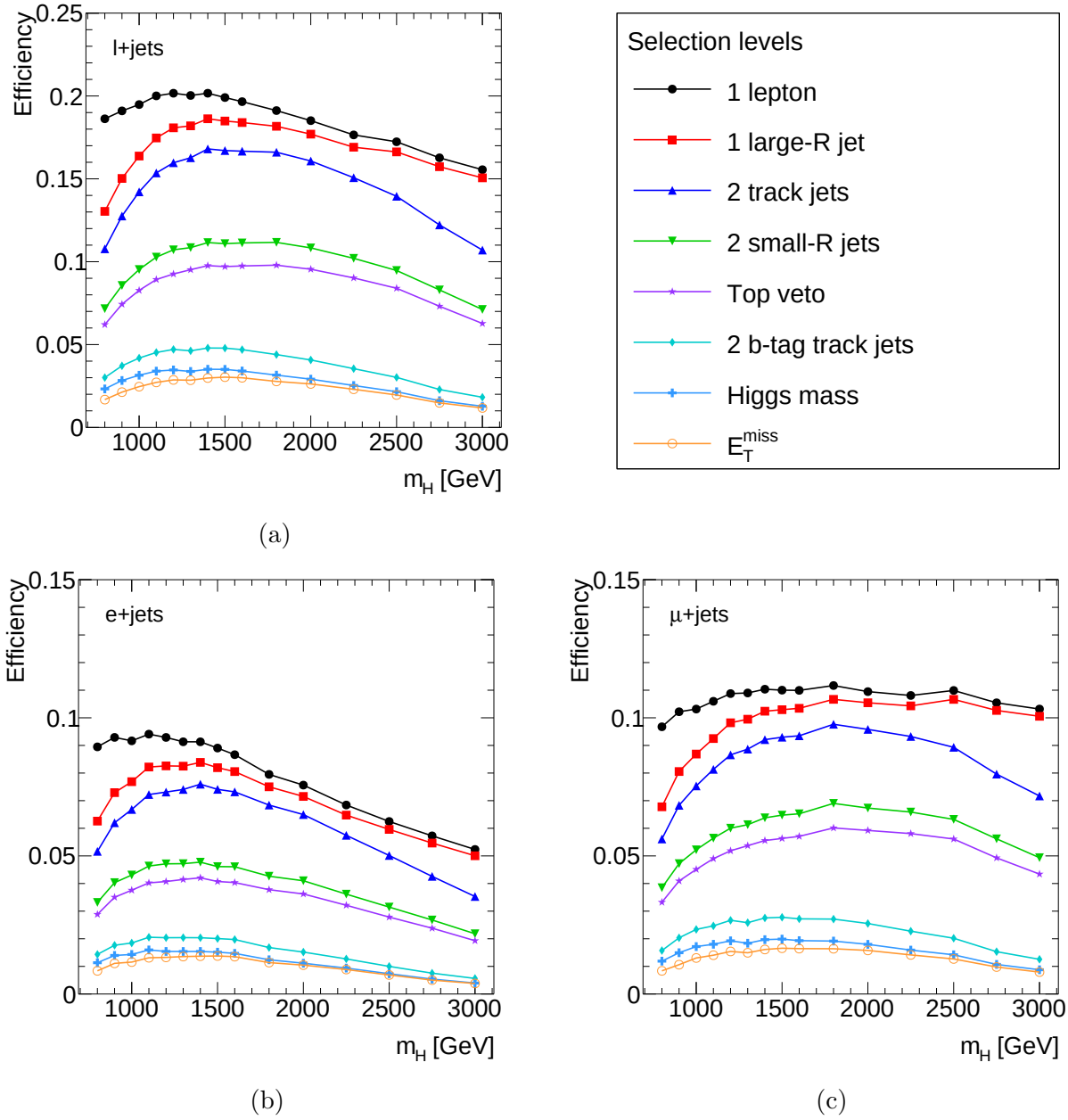

Figure 6.1: Signal efficiency at various stages of the event selection as function of the heavy scalar resonance mass in the (a) ℓ+jets, (b) e+jets and (c) μ+jets channel.

This type of resonance arises, for example, in the two Higgs doublet model. The second benchmark is the spin-2 graviton in the bulk-RS model. More details about the physics of these models and their motivation is given in Section 2.3.2.

Various SM processes can pass the event selection in Section 6.1 because they have a similar final state as the signal topology. In order to make an accurate description of the observed data, these backgrounds must be estimated and understood as well as possible.

The most significant SM background in this analysis comes from top-antiop quark pair

($t\bar{t}$) production. The top quark predominantly decays to a b-quark and a W boson. The $t\bar{t}$ background is dominated by the semi-leptonic final state decays where one of the W boson decays hadronically (hadronic top) while the other W boson decays leptonically (leptonic top). As this search focuses on topologies which involve boosted massive particles, the high p_{T} hadronic top then fakes a $h \to b\bar{b}$ candidate when 2 or 3 quarks (depending on the top p_{T}) from the hadronic top are reconstructed with as a large-R jet with two b-tagged track jets. The track jet which originated from the b-quark is b-tagged while the other track jet, which may originate from a c-quark or a light quark get mis-tagged by the MV2c10 b-tagging algorithm. Even after requiring events to pass the top veto, the $t\bar{t}$ background is still the largest background in this analysis.

Another SM background which contributes substantially is the production of a leptonically decaying W boson in association with multiple quarks and gluons which hadronise and are reconstructed as jets. This background is denoted by W+jets. A similar process for the Z boson (denoted as Z+jets) is also a SM background for this search but unlike the W+jets background, Z+jets mimics the single lepton final state if one of the leptons is incorrectly reconstructed or missing due to the limited detector acceptance. The Z+jets background is expected to be much smaller compared to the W+jets background.

In addition to the $t\bar{t}$ process, the single production of a top quark (single-top) can produce the semi-leptonic final state of the signal topology. Finally, the SM production of two vector bosons (called dibosons) is also considered.

All the backgrounds explained above are modelled using MC simulation and the samples are presented Section 6.2.1. One particular background which requires a data-driven method to estimate its contribution in the signal region is the multijet background. This background arises from QCD production and it has an extremely large cross section. Contamination of this background occurs when one of the jets is incorrectly reconstruced as a lepton or the reconstructed lepton comes from a (non-prompt) weakly decaying hadron inside the jets. Since the modelling of the multijet background is difficult with MC simulation, due to the large rejection rate of fake leptons, the multijet background is estimated with a data driven approach which is presented extensively in Section 6.2.2.

6.2.1 MC signal and background samples

The primary benchmark signal model used in this analysis is a heavy scalar resonance (H) with a narrow fixed width of $\Gamma_H = 1$ GeV. The signal event is generated at NLO [160] with MadGraph5_aMC@NLO [161] and uses the CT10 PDF set [162]. The parton shower, hadronization, and simulation of the underlying event are handled by Herwig++ [163]

with the CTEQ6L1 PDF set and the UE-EE-5 underlying event event tune [164]. Sample mass points were generated between 800 GeV and 3000 GeV in steps of 100 GeV from 800 GeV to 1600 GeV, in 200 GeV steps up to 2000 GeV and in 250 GeV steps up to 3000 GeV. The scalar signal samples are arbitrarily normalized to a cross-section value of 0.041 pb.

The second benchmark signal model is the bulk RS graviton (G). It is generated at LO with MadGraph5_aMC@NLO interfaced to PYTHIA 8.186 [165] for the modeling parton shower and hadronization, and is used with the A14 tune [166] for the underlying event tune. The PDF set used is the NNPDF 2.3 LO set [167]. The graviton samples were generated with two model parameter value $c = 1$ and 2 for 4 mass points: 1000 GeV, 1500 GeV, 2000 GeV and 3000 GeV and they are normalized to the cross section prediction calculated by MadGraph5_aMC@NLO. Both the production cross section and width of the graviton resonance are proportional to c^2. The widths of the graviton signals depend on the resonance mass and the value of c. Relative to the resonance mass, they range from 13% (25%) at the highest mass for $c = 1$ ($c = 2$).

The generation of $t\bar{t}$ events uses the POWHEGv2 generator [168–170] with the CT10 PDF set is used in the matrix-element calculations. The parton shower, fragmentation, and the underlying event are simulated using PYTHIA6.428 [171] with the CTEQ6L1 PDF set [172] and the corresponding Perugia 2012 tune [173]. The samples are normalized to their next-to-next leading order (NNLO) cross-section including the resummation of soft gluon emission at next-to-leading-logarithmic (NLL) accuracy using Top++ 2.0 [174].

The single top-quark production has three mechanism: Wt-associated, s-channel and t-channel. All of them are simulated with the POWHEG v1 generator with the CT10 PDF set for in the matrix-element calculations. The parton shower, fragmentation, and the underlying event are simulated using the same generator, PDFs, and tune as the $t\bar{t}$ sample. The samples are normalized to cross-sections using NLO calculations in QCD using Hathor v2.1 [175–177]. The top-quark mass is fixed to 172.5 GeV for the $t\bar{t}$ and single-top samples.

Events containing W or Z bosons in association with jets (V+jets) are simulated using the SHERPA v2.2.1 generator [178]. Matrix elements are calculated for up to two partons at NLO and four partons at leading order (LO) using the Comix [179] and OpenLoops [180] and merged with the SHERPA parton shower using the ME+PS@NLO prescription [181]. The NNPDF 3.0 NNLO set [182] is used in conjunction with a dedicated parton shower tuning developed by the Sherpa authors. The cross-sections for W/Z+jets were calculated at NNLO accuracy [183].

Diboson processes (WW, WZ, and ZZ) are generated using SHERPA v2.1.1 which

calculates up to one (ZZ) or zero (WW, WZ) additional partons at NLO and up to three additional partons at LO using the CT10 PDF set. These samples are normalized to cross sections calculated at NLO.

All simulated event samples include the effect of multiple pp interactions in the same and neighbouring bunch crossings by overlaying simulated minimum-bias events on each generated event. The minimum-bias events were simulated with the single-, double- and non-diffractive pp processes of PYTHIA v8.186 using the A2 tune [184] and the MSTW2008 LO PDF [185]. For all MadGraph5_aMC@NLO and POWHEG samples, the EvtGen v1.2.0 program [186] was used for the b-hadron and c-hadron decays.

The samples for the background processes are the recommended baseline samples to be used by ATLAS analyses. Studies on the samples by the ATLAS Physics Modelling Group can be found in Reference [187–189]. A summary of event generators used for the simulation of background processes is shown in Table 6.2.

Process	ME generator	ME PDF	PS and Hadronisation	MC tune
Background				
$t\bar{t}$	POWHEG v2	CT10	PYTHIA 6	Perugia 2012
Single-t	POWHEG	CT10	PYTHIA 6	Perugia 2012
V + jets	SHERPA v2.2.1	NNPDF 3.0 NNLO	SHERPA 2.2.1	Default
Diboson	SHERPA v2.1.1	CT10	SHERPA 2.2.1	Default
Signal				
Heavy scalar	MadGraph5_aMC@NLO	CTEQ6L1	Herwig++	UE-EE-5
Graviton	MadGraph5_aMC@NLO	NNPDF 2.3 LO	PYTHIA 8	A14

Table 6.2: MC event generators used for the simulation of background and signal processes.

6.2.2 Data driven estimation for multijet background

Multijet events from QCD processes can pass the event selections when a jet is mis-reconstructed and mis-identified as an electron or a muon. Since there are no reliable MC simulation samples, a data-driven approach, so-called the ABCD method, is used to estimate the multijet contribution in the 2-tag signal region.

The ABCD method defines three control regions (the B, C, and D regions) to estimate the contribution of a given background in the region of interest (region A). Selection on two ideally orthogonal variables are used to create the signal and various control regions, e.g. region A passes both selection, the regions B and C each passes one selection and fails the other, while the region D fails both selection. In this analysis, the control regions B, C, and

D follow the same event selections in Section 6.1 with the exceptions of the requirement on the type of selected lepton, which differs by the selection on the lepton's d_0^{sig}, and $E_{\text{T}}^{\text{miss}}$. The regions are defined by the following combination of selections:

- Region A: $E_{\text{T}}^{\text{miss}} > 50$ GeV; $|d_0^{\text{sig}}| < 2.0$ (Tight lepton)
- Region B: $E_{\text{T}}^{\text{miss}} < 50$ GeV; $|d_0^{\text{sig}}| < 2.0$ (Tight lepton)
- Region C: $E_{\text{T}}^{\text{miss}} > 50$ GeV; $|d_0^{\text{sig}}| > 2.0$ (AntiTight lepton)
- Region D: $E_{\text{T}}^{\text{miss}} < 50$ GeV; $|d_0^{\text{sig}}| > 2.0$ (AntiTight lepton)

Figure 6.2 shows the four regions represented on the lepton $|d_0^{\text{sig}}|$ vs $E_{\text{T}}^{\text{miss}}$ plane. Assuming that the two variables chosen to define the control regions are completely uncorrelated, the multijet background yield in region A can be predicted using the following relation

$$N_A^{\text{multijet}} = N_C^{\text{multijet}} \cdot \frac{N_B^{\text{multijet}}}{N_D^{\text{multijet}}} \tag{6.3}$$

where $N_{B/C/D}^{\text{multijet}}$ is calculated by subtracting all prompt lepton backgrounds ($t\bar{t}$, W/Z+jets, single-top, diboson processes) from data ($N_i^{\text{data}} - N_i^{\text{Prompt}}$) in control regions B, C and D.

The ABCD method is employed separately between the μ+jets and e+jets channel as it is expected that the $N_B^{\text{multijet}}/N_D^{\text{multijet}}$ ratio and multijet contribution to the total background will be different between the channels. This method is used to predict the multijet contribution to the total background in the 2-tag signal region which is the region where the search is performend. It is also used to predict the multijet contribution in the 2-tag mBB control region, the region used to validate the total background prediction in a signal depleted region.

Normalization prediction

The ABCD method starts by calculating $N_B^{\text{multijet}}/N_D^{\text{multijet}}$ ratio using the multijet yield in region B and region D. Table 6.3 lists the MC predicted prompt lepton backgrounds, observed data and estimated multijet yields in Region B and D before the large-R jet mass is applied.

The $N_B^{\text{multijet}}/N_D^{\text{multijet}}$ ratio is calculated inclusively in the large-R jet mass distribution. In other words, the ratio is calculated without the jet mass window selection, which defines the signal region and mBB control region, applied. The ratio is then used to scale the multijet yield in the signal region and mBB control region of region C to predict the multijet

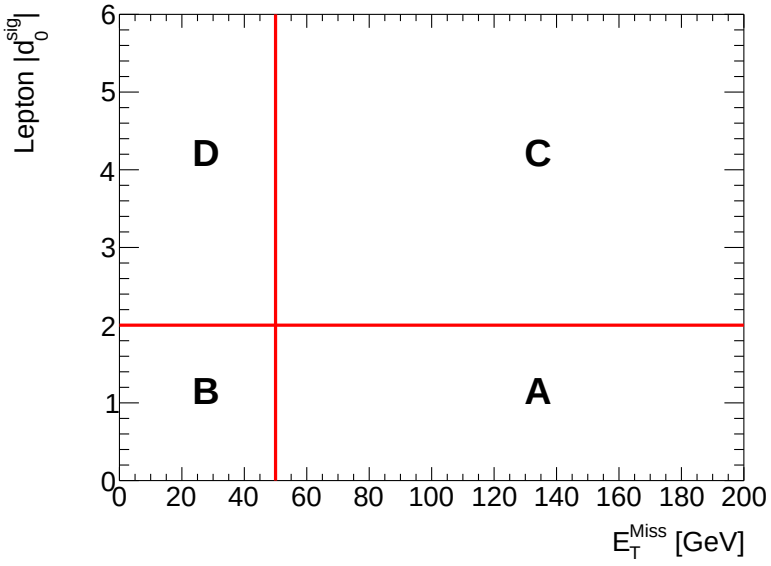

Figure 6.2: Regions defined in the ABCD method based on the lepton d_0 significance vs $E_{\mathrm{T}}^{\mathrm{miss}}$ plane. Region A is the signal enriched region for which we want to estimate the multijet background. Region C is where the shape template is derived from and used as shape prediction of the multijet background in region A. The ratio of the multijet yields in region B to region D is used to scale the multijet yield in region C to predict the multijet background yield in region A.

Samples	Region B		Region D	
	e+jets	μ+jets	e+jets	μ+jets
$t\bar{t}$	308 ± 12	280 ± 11	21 ± 3	18 ± 4
W+Jets	173 ± 5	179 ± 6	12 ± 1	11 ± 1
Single-top	43 ± 3	34 ± 4	3 ± 1	0.8 ± 0.5
Z+Jets	79 ± 2	73 ± 2	6 ± 1	5.5 ± 0.5
Diboson	19 ± 2	18 ± 2	1.6 ± 0.4	2.2 ± 0.8
Total prompt	621 ± 13	583 ± 13	44± 3	37 ± 3
Data	1003 ± 32	711 ± 27	144± 12	98 ± 10
Multijet	382 ± 34	128 ± 30	100± 12	61 ± 10

Table 6.3: MC predicted prompt lepton backgrounds, observed data and calculated multijet yields in Region B and D. The multijet yield is calculated by subtracting the estimated total prompt lepton backgrounds from the observed data. The statistical uncertainty on the yields is shown.

multijet yield in region A. Table 6.4 shows the ratio calculation in the e+jets channel and μ+jets channel. The e+jets channel ratio is observed to be larger than the μ+jets channel. The μ+jets channel ratio has a larger uncertainty due to the more limited statistics in region B and region D compared to the e+jets channel.

	e+jets	μ+jets
N_B^{multijet}	382 ± 34	128 ± 30
N_D^{multijet}	100 ± 12	61 ± 10
$N_B^{\text{multijet}}/N_D^{\text{multijet}}$	3.8 ± 0.6	2.1 ± 0.6

Table 6.4: Multijet yields in region B and region D and also the ratio of the yields for each lepton channel. The error on the $N_B^{\text{multijet}}/N_D^{\text{multijet}}$ ratio is propagated from the statistical uncertainties on the multijet yields in each region.

Table 6.5 shows the multijet yield in region C of the mBB control region and signal region. With the $N_B^{\text{multijet}}/N_D^{\text{multijet}}$ ratio in Table 6.4, the multijet background yield prediction in region A of mBB control region and signal region is calculated by using Equation 6.3. The final multijet predictions are shown in Table 6.6. The uncertainties include all the systematic uncertainties that are estimated related to the ABCD method. Section 6.4.3 discusses the different sources of uncertainties for the multijet prediction.

Samples	Region C mBBcr		Region C SR	
	e+jets	μ+jets	e+jets	μ+jets
$t\bar{t}$	40 ± 4	47 ± 8	29 ± 3	22 ± 3
W+Jets	22 ± 2	20 ± 2	10 ± 1	10 ± 2
Single-top	8 ± 2	7 ± 1	7 ± 3	2.7 ± 0.8
Z+Jets	4.6 ± 0.8	3.8 ± 0.5	1.6 ± 0.3	1.9 ± 0.6
Diboson	2.2 ± 0.6	1.2 ± 0.4	0.8 ± 0.3	1.7 ± 0.4
Total Prompt	75 ± 5	78 ± 8	48 ± 4	38 ± 3
Data	148 ± 12	126 ± 11	91 ± 10	71 ± 8
Multijet	73 ± 13	48 ± 14	44 ± 10	33 ± 9

Table 6.5: Predicted prompt lepton backgrounds, observed data and calculated multijet yields in Region C mBBcr and SR. The multijet yield is calculated by subtracting the estimated total prompt lepton backgrounds from the observed data. The statistical uncertainty on the yields is shown.

Multijet shape prediction

In order to predict the shape of the m_{hh} mass distribution (and also other kinematic distribution) of the multijet background, the shape template of all kinematic distributions are obtained by subtracting the total non-prompt backgrounds from data in region C.

It was found that distributions in region C suffer from lack of statistics due the low number

Region	e+jets	μ+jets	ℓ+jets
SR	166 ± 145 (88%)	69 ± 109 (158%)	235 ± 182 (77%)
mBBcr	277 ± 245 (88%)	101 ± 218 (216%)	378 ± 328 (87%)

Table 6.6: Predicted multijet yield in region A SR and mBBcr for the e+jets, μ+jets and combined lepton channel. The evaluation of the uncertainty on the predicted yield is presented in Section 6.4.3.

of data events, as shown in Figures 6.3a and 6.3b, as an example for the m_{hh} distribution region C signal region in each lepton channel. The lack of statistics renders it difficult to use the multijet shapes from region C for predictions in region A. To overcome this, the multijet shape templates are derived from a sample of 1-tag category events in region C. Figures 6.3c and 6.3d show the 1-tag region C m_{hh} distribution for each lepton channel. It can be seen that in the 1-tag category, the available statistics is higher.

6.3 Background validation

6.3.1 Top control region

The selection criteria for the top control region are almost exactly the same as outlined in Section 6.1 with the exception of a different b-tagging requirement impose on the events. The top control region is defined for events that fall into the 1-tag category and have at least one b-tagged small-R jet, which reverses the top veto requirement. The large-R jet mass selection is required to be the same as the signal region.

Table 6.7 shows the event yield of predicted background contributions and the observed data in the top control region. The $t\bar{t}$ background is the most dominant background ($\sim 93\%$) followed by the single-top ($\sim 4\%$) background making this region to be very pure with events containg top quarks. The total background prediction agrees well with observed number events in data. Figure 6.4 shows several kinematic distributions of predicted background and data events in the top control region and the agreement between background prediction and data is very good. The transverse mass of leptonic W boson ($m_{\mathrm{T}}^{\mathrm{W}}$) is defined as $\sqrt{2p_{\mathrm{T}}^{\mathrm{lepton}} E_{\mathrm{T}}^{\mathrm{miss}}(1-\cos\Delta\phi)}$ where $\Delta\phi$ is the difference in azimuthal angle between the selected lepton and $E_{\mathrm{T}}^{\mathrm{miss}}$ direction. A selection of kinematic distributions in the top control region can be found in Appendix A.

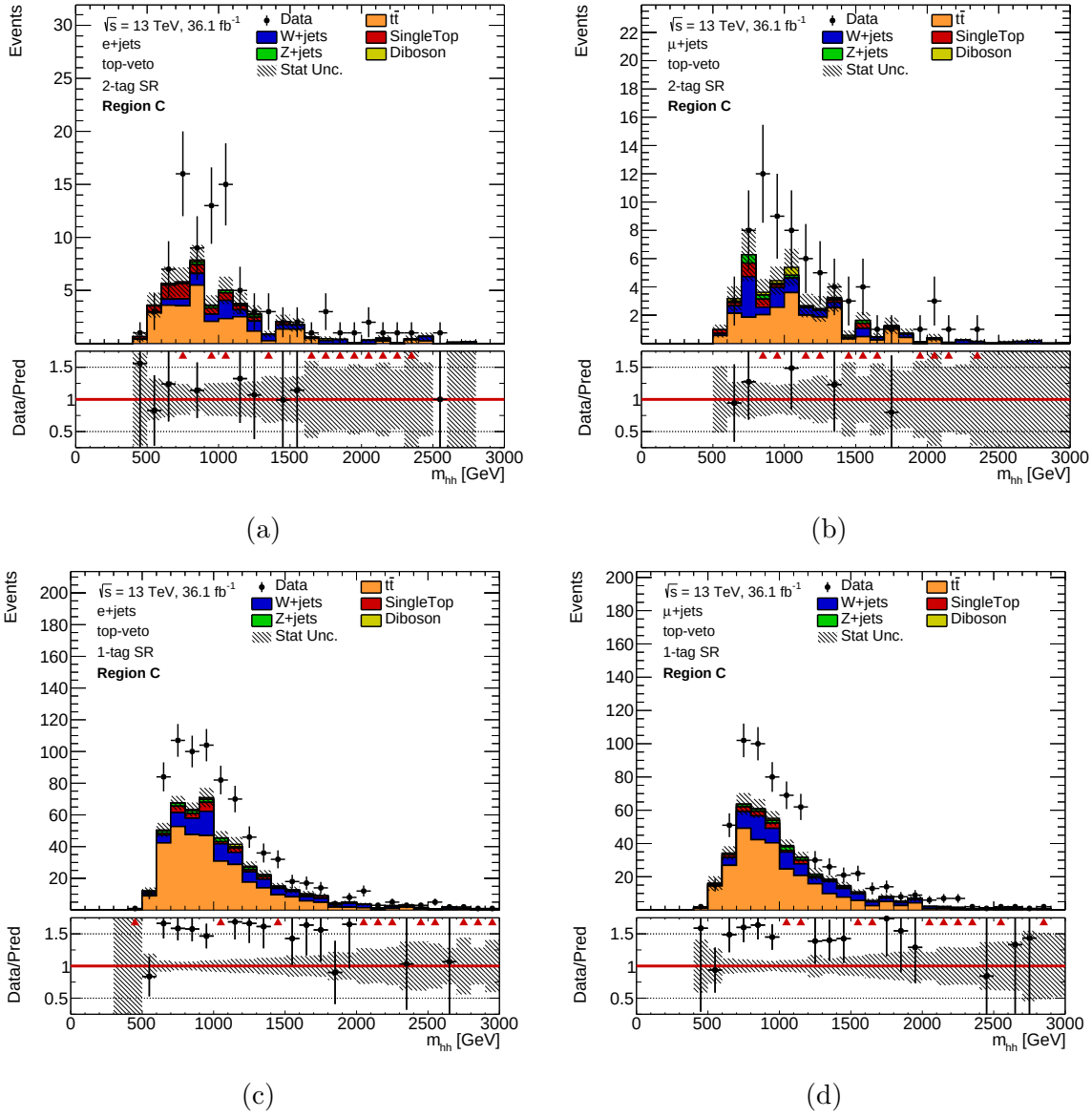

Figure 6.3: m_{hh} distribution in SR region C in the e+jets (left) and μ+jets (right) channels of 2-tag events (top) and 1-tag events (bottom). The hashed band represents the statistical uncertainty on the total background prediction.

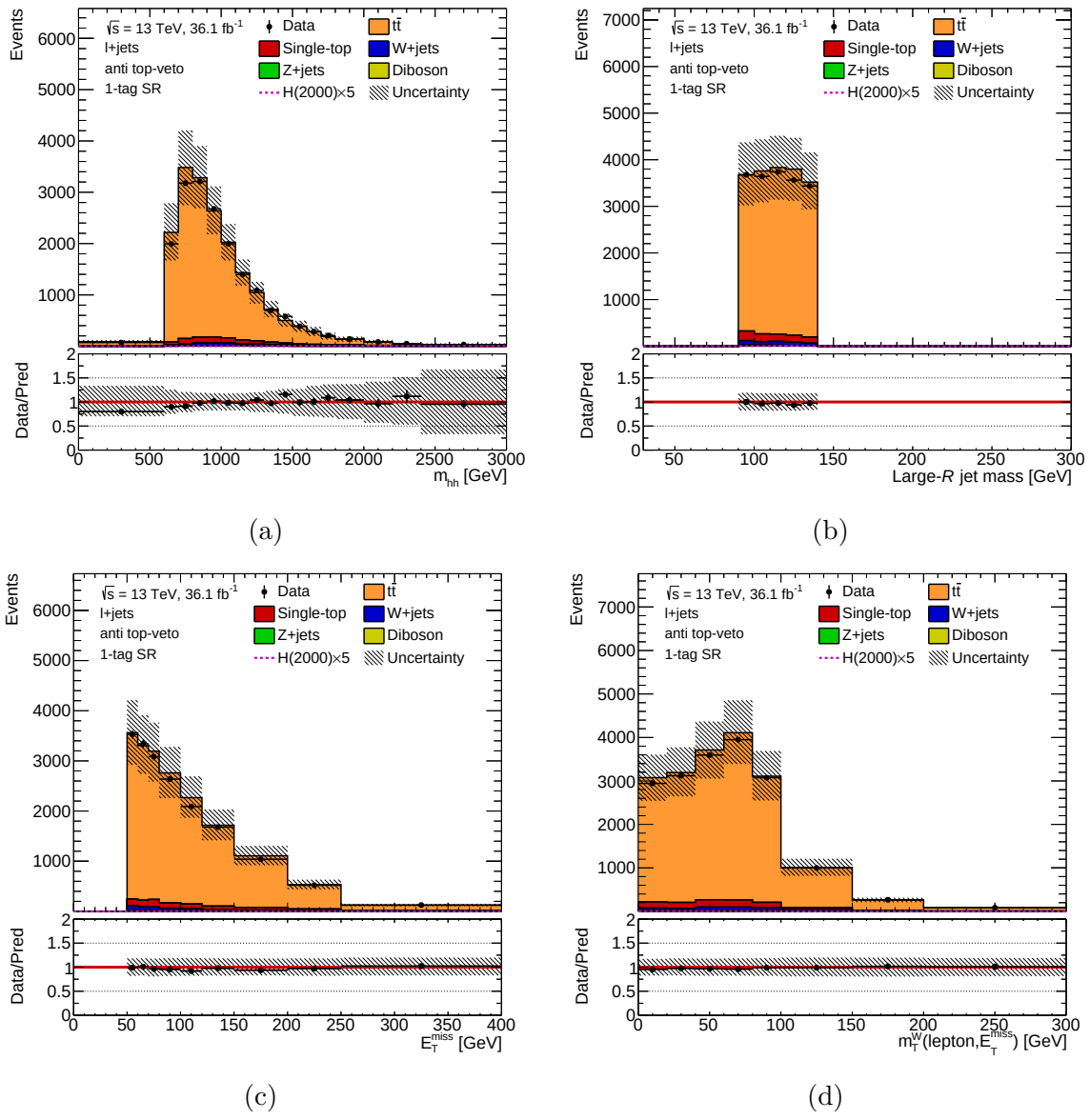

Figure 6.4: Distributions of (a) m_{hh}, (b) m_J, (c) $E_{\mathrm{T}}^{\mathrm{miss}}$ and (d) $m_{\mathrm{T}}^{\mathrm{W}}$ in the top control region. The hashed band represents the overall uncertainty on the total background prediction. The detector modelling and background modelling systematic uncertainties are taken into account in the overall uncertainty.

Sample	Event yield	Statistical uncertainty	Systematic uncertainty
$t\bar{t}$	17317	± 87	$^{+3142(+18\%)}_{-3075(-18\%)}$
Single-top	803	± 16	$^{+104(+13\%)}_{-85(-11\%)}$
W+jets	380	± 12	$^{+97(+25\%)}_{-98(-26\%)}$
Z+jets	55	± 2	$^{+12(+21\%)}_{-11(-20\%)}$
Diboson	33	± 3	$^{+8(+23\%)}_{-8(-23\%)}$
Prediction	18588	± 90	$^{+3234(+17\%)}_{-3153(-17\%)}$
Data	18061	-	-
Data/Pred	0.97	-	-

Table 6.7: Predicted and observed yields in the top control region. Detector modelling uncertainties and MC background modelling uncertainties are considered for the systematic uncertainties for all backgrounds.

6.3.2 mBB control region

The 2-tag mBB control region is the closest region to the 2-tag signal region as it is only different by the selection on the large-R jet mass. Table 6.8 shows the event yield of predicted background contributions and the observed data in the mBB control region. The $t\bar{t}$ background is the biggest background followed by W+jets, multijet and single-top backgrounds. The Z+jets and diboson contributions are very small. The 2-tag signal region background composition is expected to be similar as in the 2-tag mBB control region because this control region is the sideband of the large-R jet mass window selection, which defines the signal region. The total background prediction agrees well with observed number of events in data. Figure 6.5 shows several kinematic distributions of predicted background and data events in the mBB control region and the background prediction is shown to predict data very well. The excellent $E_{\mathrm{T}}^{\mathrm{miss}}$ and $m_{\mathrm{T}}^{\mathrm{W}}$ modelling in this region gives confidence to the multijet background prediction with the ABCD method. A selection of kinematic distributions in the 2-tag mBB control region can be found in Appendix A.

6.4 Systematic uncertainties

The prediction of the expected background and signal processes in the 2-tag signal region relies heavily on MC simulation. The prediction of each process is sensitive to both experi-

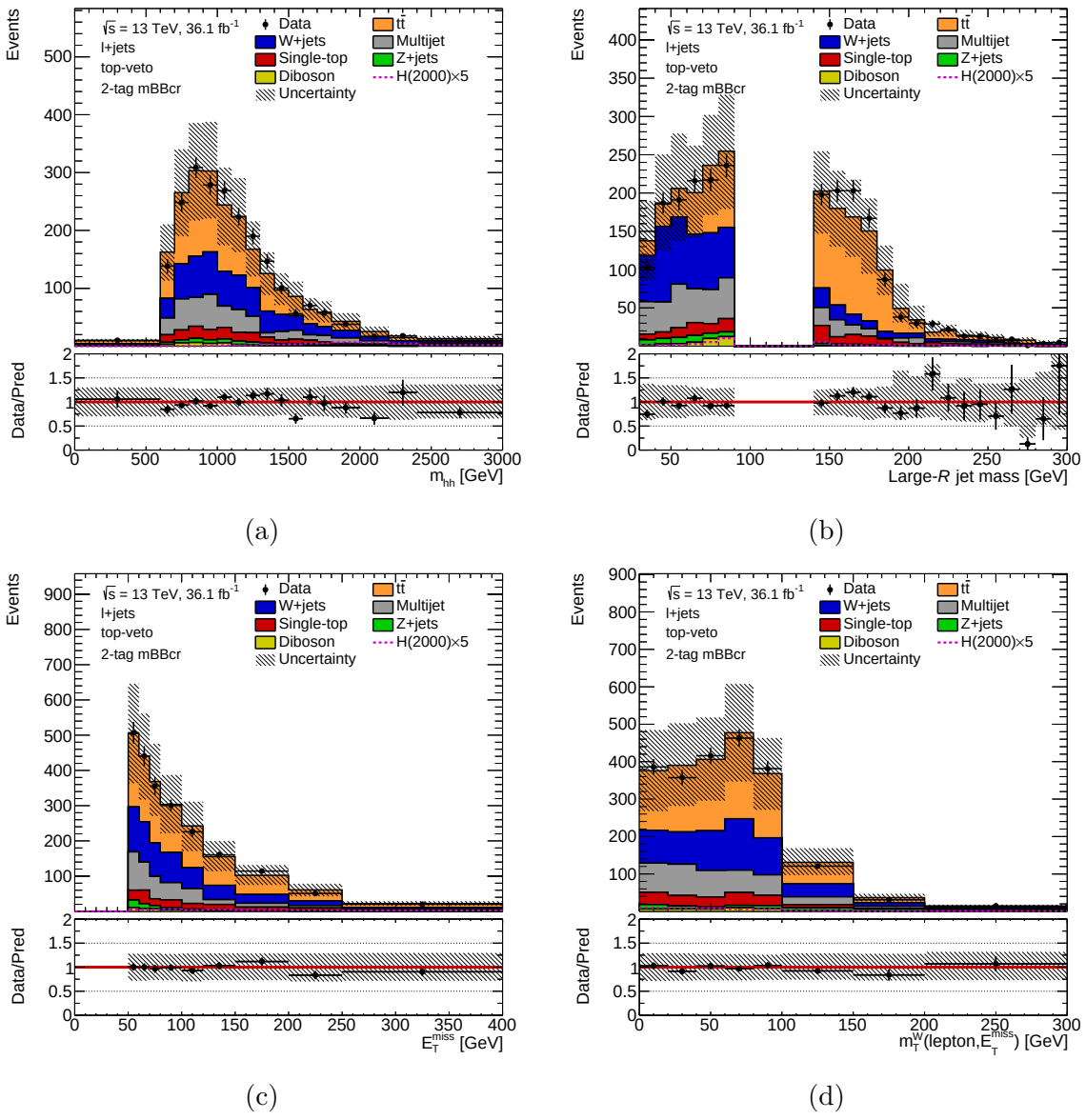

Figure 6.5: Distributions of (a) m_{hh}, (b) m_J, (c) $E_{\mathrm{T}}^{\mathrm{miss}}$ and (d) $m_{\mathrm{T}}^{\mathrm{W}}$ in the 2-tag mBB control region. The hashed band represents the overall uncertainty on the total background prediction. The detector modelling and background modelling systematic uncertainties are taken into account in the overall uncertainty.

Sample	Event yield	Statistical uncertainty	Systematic uncertainty
$t\bar{t}$	1006	± 21	$^{+284(+28\%)}_{-290(-29\%)}$
W+jets	566	± 10	$^{+278(+49\%)}_{-270(-48\%)}$
Multijet	378	± 20	$^{+328(+87\%)}_{-328(-88\%)}$
Single-top	161	± 7	$^{+114(+71\%)}_{-114(-71\%)}$
Z+jets	56	± 2	$^{+28(+50\%)}_{-27(-49\%)}$
Diboson	40	± 3	$^{+23(+59\%)}_{-23(-59\%)}$
Prediction	2206	± 31	$^{+594(+27\%)}_{-586(-27\%)}$
Data	2179	-	-
Data/Pred	0.99	-	-

Table 6.8: Predicted and observed yields in the mBB control region. Detector modelling uncertainties, MC background modelling uncertainties and QCD background modelling uncertainties from ABCD method are considered for the systematic uncertainties.

mental and theoretical systematic biases, which are addressed through the use of systematic uncertainties. These uncertainties accounts for theoretical unknowns and detector effects and when simulating the physics processes and their detector response; which can affect both the normalization and the shape of the m_{hh} distribution for the simulated signals and backgrounds. All sources of uncertainties will be addressed in this section.

The systematic uncertainties are included in the statistical analysis of the search as additional parameters to the binned likelihood. They are called nuisance parameters (NP) and for every source of systematic uncertainty, a nuisance parameter is assigned. The details of the statistical analysis is presented in Section 7.1.

6.4.1 Detector modelling

Lepton reconstruction modelling

The uncertainties on the reconstruction, identification, isolation and trigger efficiencies are taken into account in this analysis. The momentum scale and resolution uncertainties are evaluated by scaling and smearing the lepton energy. The efficiencies, scale and resolution uncertainties were determined from measurements in data and MC with events enriched with $Z \to \ell\ell$ and $J/\psi \to \ell\ell$. The uncertainty on the muon (electron) reconstruction and

identification efficiencies is $< 1.0\%$ ($< 0.5\%$) with the isolation efficiency to be less than 1%. The momentum scale and momentum resolution have uncertainties of approximately 0.05%(0.5%) and 2% (1%) for muons (electrons), respectively [115, 118, 119].

There are two NPs related to the uncertainty on momentum scale and resolution of electrons and four NPs related to their uncertainties on reconstruction, identification, isolation and trigger efficiencies. For muons, there are three NPs related to the momentum scale and resolution and three additional NPs for the identification, isolation and trigger efficiencies.

As mentioned in Section 6.1.2, the $|d_0^{\text{sig}}|$ selection value (< 2) used for electrons and muons are not the recommended value by the ATLAS e/γ and muon performance groups. The recommended value for electrons is 5 while for muons it is 3. The modelling of the $|d_0^{\text{sig}}|$ selection efficiency is measured in the top control region, defined in Section 6.3.1. For the purposes of studying the modelling of the $|d_0^{\text{sig}}|$ distribution, no $|d_0^{\text{sig}}|$ requirement is applied on the selected lepton at first.

Figure 6.6 shows the d_0^{sig}distribution for the selected electron and muon in the top control region without the large-R jet mass selection applied. In order to take into account the observed mismodelling of the d_0^{sig}on the d_0^{sig}selection used in this analysis, the efficiency of the $|d_0^{\text{sig}}|$ selection is evaluated and compared between data and MC simulation. Table 6.9 shows the efficiency of the $|d_0^{\text{sig}}|$ selection measured in data and MC simulation and the data/MC efficiency ratio in each lepton channel. The deviation from unity for the data/MC efficiency ratio is taken as the uncertainty on the $|d_0^{\text{sig}}|$ significance selection efficiency and it is assigned for all prompt lepton signal and background processes modelled by MC. A single NP is assigned for the $|d_0^{\text{sig}}|$ selection efficiency uncertainty.

	Electron	Muon
$\|d_0^{\text{sig}}\| < 2.0$		
Data	0.88	0.90
MC	0.92	0.94
Data/MC	0.96	0.96
$\|d_0^{\text{sig}}\| > 2.0$		
Data	0.12	0.10
MC	0.07	0.06
Data/MC	1.56	1.65

Table 6.9: Efficiency of the $|d_0^{\text{sig}}|$ cut for electrons and muons measured in data and MC. The data/MC ratio is also calculated and the difference from unity is taken as the systematic uncertainty on the $|d_0^{\text{sig}}|$ efficiency modelling for leptons that pass (< 2.0) or fail (> 2.0) the $|d_0^{\text{sig}}|$ selection in processes with prompt leptons.

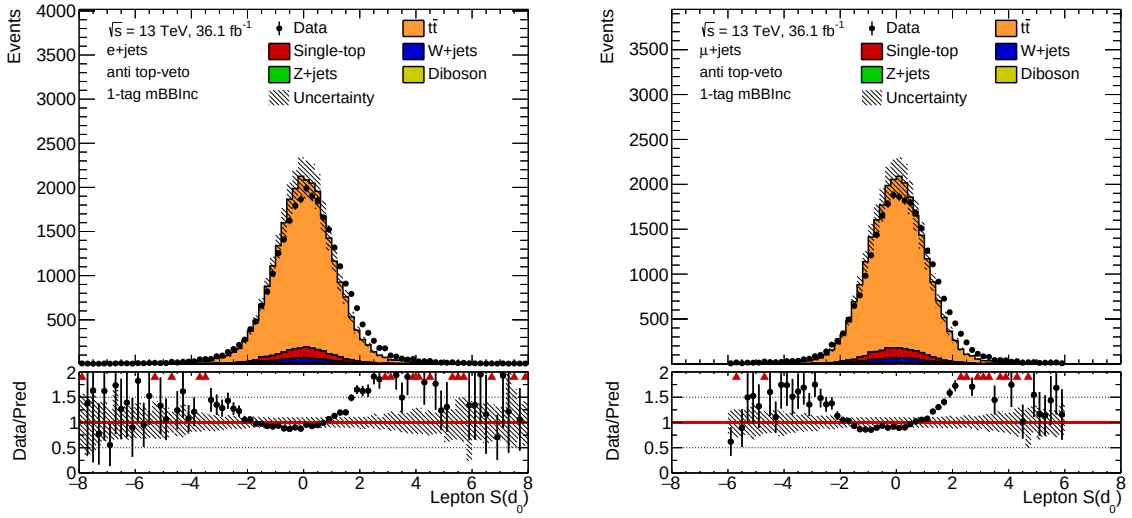

(a) (b)

Figure 6.6: The selected (a) electron and (b) muon d_0^{sig}distributions in the top control region without the large-R jet mass selection applied. The hashed band represents the overall uncertainty on the total background prediction. The detector modelling and background modelling systematic uncertainties are taken into account in the overall uncertainty. The red arrows in the lower panels indicate points beyond the y-axis range.

Small-R jets reconstruction modelling

The energy scale uncertainty for small-R jets is evaluated by scaling the jet energy by the uncertainties determined from in-situ measurements of the jet response balance in dijet, Z+jet and γ+jet events, as well as for high p_{T} multijet events in MC and data samples. For central jets, the jet energy scale relative uncertainty ranges from approximately 6% for jets with p_{T} of 30 GeV to 1% for jets with $p_{\text{T}} > 300$ GeV. There are over 80 separate sources of uncertainties of the JES but instead, a strongly reduced set of four NPs is used in this analysis. The strongly reduced set was determined [131] first by an eigenvalue decomposition of the 62 in-situ measurement uncertainties into 6 distinct NPs and then the remaining NPs with small correlation are quadratically combined resulting in four strongly reduced NPs.

A single NP is assigned for the jet energy resolution uncertainty and it is evaluated by smearing the jet energy according to the systematic uncertainties of the resolution measurement [190]. The uncertainty on the JVT selection efficiency is also taken into account [132] and they are at a level of 1-3% (Figure 4.5b) in the jet p_{T} range where the JVT is used.

Large-R jets reconstruction modelling

The large-R jet p_{T} and mass scale systematic uncertainties are evaluated by scaling the jet energy and mass by the uncertainties determined from r^{track} double ratio method measurement (Section 5.4). Four NPs are considered, which take into account the differences between data and MC simulation, modeling differences between MC generators, tracking uncertainties and statistical uncertainties. The jet energy scale has an associated uncertainty ranging from 2% to 3% for jets with p_{T} from 200 GeV to 1500 GeV and for the mass scale uncertainty, it ranges from approximately 2% to 6% in the same p_{T} range [155].

The large-R jet p_{T} and mass resolution uncertainties are also taken into account for large-R jets. The recommended procedure by the ATLAS JetEtMiss performance group is to apply a 5% absolute uncertainty for the p_{T} resolution, and a 20% relative uncertainty for the mass resolution. Each large-R jet resolution uncertainty is assigned as a single NP.

b-tagging modelling

Systematic uncertainties on the b-tagging and mistagging efficiencies are considered separately for small-R jets and track jets. For small-R jets, the uncertainty on the b-tagging efficiency ranges from 2% to 12% depending on the jet p_{T} [143]. The c-jet mistagging rate uncertainty is at a level of 6-7% [144] and for light-jets, the uncertainty ranges from 15% to 35% [145]. The b-tagging and mistagging uncertainties for track jets are at a similar level as the small-R jets.

The uncertainties are propagated to the scale factors applied to MC samples using a reduced set of 14 NPs. There are three NPs for the tagging efficiency of jets with b-hadrons, four NPs for mistagging rate of jets with c-hadrons and five NPs considered for the mistagging rate of light-jets. Additional NPs account for jets with p_{T} values above the kinematic reach of the calibration analysis, and for extrapolation c-jet scale factors to jets originating from hadronically decaying tau leptons.

Missing transverse momentum modelling

The systematic uncertainty on the hard-term of the $E_{\mathrm{T}}^{\mathrm{miss}}$ is calculated by propagating the effects of the energy/momentum scale and resolution uncertainties for leptons and small-R jets through the $E_{\mathrm{T}}^{\mathrm{miss}}$ reconstruction. The uncertainties related to the measurement of the soft-term of $E_{\mathrm{T}}^{\mathrm{miss}}$ have been evaluated using different MC generators [146]. There are three NPs related to the scale and resolution of the $E_{\mathrm{T}}^{\mathrm{miss}}$ soft-term.

Luminosity

The total integrated luminosity for the 2015+2016 dataset used in this analysis has a 3.2% uncertainty, measured following the prescription in Reference [191]. A calibration of the luminosity scale was performed in August 2015 and May 2016 with x-y beam separation scans. This uncertainty is applied to the scaled event yields of all MC samples. A single NP is assigned for the uncertainty on the luminosity.

6.4.2 Theoretical modelling

Signal production

The sources of systematic uncertainties on the theoretical modelling of the heavy scalar signals are evaluated by comparing the nominal MC samples with variation MC samples. The following variations and their sample configurations are used:

- **Scale:** Configured in the same manner as the nominal signal samples but the renormalization and resummation scales are varied up/down by a factor of 2.
- **Parton Shower (PS):** Configured in the same manner as the nominal signal samples but with PYTHIA8 chosen as the parton shower generator instead of HERWIG++.

Each source of systematic uncertainty can affect the the modelling of the acceptance of the signal. The uncertainty is evaluated by comparing the acceptance of the variation samples with respect to the nominal; the relative difference is taken as the uncertainty. The acceptance uncertainty affects the normalization of the signals. Table 6.10 shows the uncertainties from the two sources for heavy scalar signals with different masses. The PS variation is generally larger compared to the scale variation and increases for higher heavy scalar resonance mass. A single NP for the acceptance uncertainty is assigned for the heavy scalar signals.

Top background modelling

The sources of systematic uncertainties on the theoretical modelling of top backgrounds are evaluated by comparing the nominal MC samples with variation MC samples. The following variations and their sample configurations are used:

- **Matrix Element (ME):** The effect of a different hard scatter generator is determined by comparing top samples generated with POWHEG and MADGRAPH5_AMC@NLO;

Variation	Scalar mass (m_{H}) [GeV]				
(%)	1000	1500	2000	2500	3000
Scale	0.2	0.2	0.4	0.4	0.4
PS	0.4	0.8	1.2	1.5	2.0
Total	0.5	0.8	1.3	1.6	2.0

Table 6.10: The systematic uncertainties (in percentage), from different sources, on the acceptance of heavy scalar signal for various mass points. The total uncertainty is calculated as the sum in quadrature from all sources.

both interfaced to HERWIG++ for parton showering. This fixes the parton show generator, but alters the matrix element generator.

- **Parton Shower (PS):** The uncertainty due to the choice of PS generator is determined by comparing the nominal POWHEG+PYTHIA6 sample with a sample that uses the same setup as the nominal but swapped with HERWIG++ for PS generator.

- **Radiation:** Using the same setup as that used for the nominal POWHEG+PYTHIA6 sample, two samples correspond to either the enhancement or reduction of initial and final state radiation (ISR/FSR) are used to estimate the impact of the radiation uncertanty. This is done by increasing and decreasing the renormalization and factorisation scales by a factor of 2. The two samples are compared to the nominal sample.

- **DSvsDR:** Only relevant for the Wt-production of the single-top background. The Wt-production single-top process at NLO (in QCD) interferes with the LO $t\bar{t}$ production process. In the nominal Wt single-top sample, the resonant $t\bar{t}$ effects are subtracted from Wt at the amplitude level prior to the calculation (Diagram Removal). An alternative sample, called the DS (Diagram Substraction) sample, performs the subtraction at the cross-section level [192].

Each source of uncertainty may affect the modelling of the acceptance and also the m_{hh} distribution shape of the top backgrounds. The acceptance uncertainty is evaluated by comparing the acceptance of the variation samples with respect to the nominal; the relative difference is taken as the uncertainty. The acceptance uncertainty affects the normalization of the backgrounds. The total uncertainty on the acceptance is calculated as the sum in quadrature from all sources.

The uncertainty on the m_{hh} shape is evaluated by comparing the shape of the variation samples to the nominal sample. The variation samples are normalized such that the event yield is the same as the nominal sample. The ratio between the nominal and variation m_{hh}

shape is taken as the uncertainty and a linear fit to the ratio characterizes the uncertainty on the m_{hh} shape modelling.

For the $t\bar{t}$ background, the estimated acceptance uncertainties are shown Table 6.11. The largest source of uncertainty comes from the radiation variation with similar level of uncertainties as the ME and PS variation.

Variation	Uncertainty (%)
ME	7
PS	8
Radiation	8
Total	14

Table 6.11: The systematic uncertainties (in percentage), from different sources, on the acceptance of the $t\bar{t}$ background. The total acceptance uncertainty is calculated as the sum in quadrature from all sources.

For the m_{hh} shape uncertainty, the radiation and PS variations are found to have noticeable differences with respect to the nominal $t\bar{t}$ sample. The shape comparisons of the m_{hh} distribution between the nominal $t\bar{t}$ sample and the radiation (PS) variation sample is shown in Figure 6.7a(6.7c).

There are four NPs related to the theoretical modelling uncertainties of the $t\bar{t}$ background: the total acceptance uncertainty, the m_{hh} shape uncertainty due to radiation variation, the shape uncertainty due to PS variation and the uncertainty on the cross-section which is about 6%.

For the single-top background, only the uncertainty on the acceptance of the Wt production process are considered since it is the dominant single-top process in the 2-tag signal region. Table 6.12 shows the estimated uncertainties from different sources. The biggest uncertainty comes from the comparison of the nominal Wt sample with the DS sample variation.

There are two NPs related to the theoretical modelling uncertainties of the single-top background: the total acceptance uncertainty and the uncertainty on the cross-section which amounts to 5%.

V+jets modelling

The sources of systematic uncertainties on the theoretical modelling of V+jets backgrounds are evaluated by comparing the nominal MC samples with variation MC samples. The following variations and their sample configurations are used:

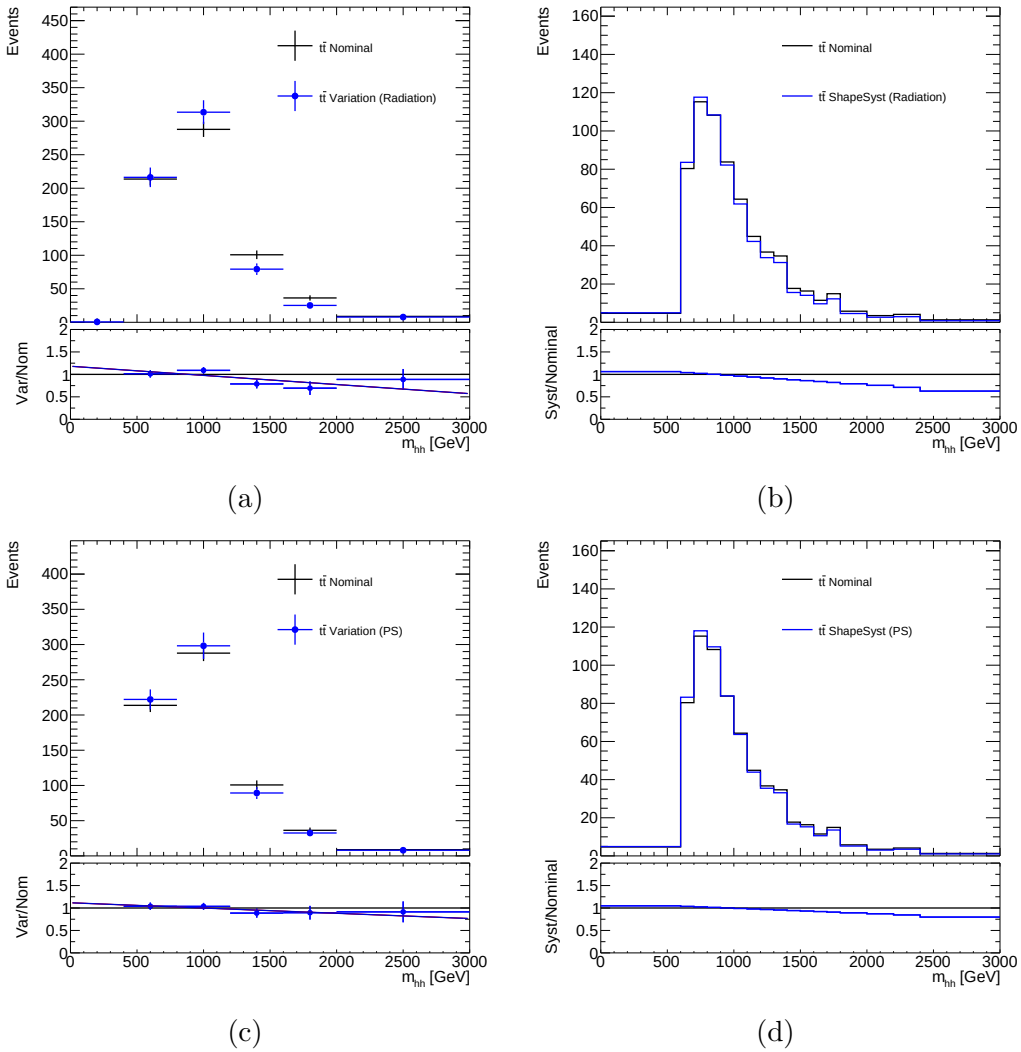

Figure 6.7: m_{hh} distribution shape comparison between nominal $t\bar{t}$ sample and variation samples. Plots on the left are direct comparison between the nominal and variation sample while on the right, the shape systematic uncertainty comes from the reweighted function applied to the nominal $t\bar{t}$ sample. The linear fit in the ratio of the left plot is used as the reweighted function to characterize the uncertainty on the shape modelling.

Variation	Uncertainty (%)
ME	25
PS	34
Radiation	19
DSvsDR	73
Total	86

Table 6.12: The systematic uncertainties (in percentage), from different sources, on the acceptance of the Wt production process for the single-top background. The total acceptance uncertainty is calculated as the sum in quadrature from all sources.

- **Scale:** Configured in the same manner as the nominal sample but with the renormalization and factorization scales varied up/down by a factor of 2.
- **PDF:** Configured in the same manner as the nominal SHERPA v2.2.1 sample. The 100 NNPDF3.0NNLO replicas variations are used. Additionally, 2 alternative PDF sets, CT14NNLO [193] and MMHT2014NNLO [194] are also used.
- $\alpha_{\mathbf{s}}$**(PDF):** Configured in the same manner as the nominal sample but the α_s value used by the nominal NNPDF 3.0 NNLO PDF is varied up and down according to a variation of the renormalization scale by a factor of 2.
- **Matrix Element and Parton Shower (ME+PS):** The uncertainty due to the ME and PS choice is estimated by comparing V+jets event generated using MadGraph5 interfaced to PYTHIA8 for parton showering with the nominal sample. Due to the limited statistics of this sample at reconstruction level, the comparison is made at truth level.

The same procedure employed for the top backgrounds are used to estimate the acceptance and m_{hh} distribution shape uncertainties for V+jets background. For the W+jets background, Table 6.13 shows the estimated acceptance uncertainty. The largest uncertainty comes from scale variation, which is about $\sim 42\%$ and the variation dominates the total acceptance uncertainty on W+jets background.

Variation	Uncertainty (%)
Scale	42
α_S(PDF)	8
PDF set	6
ME+PS	11
Total	45

Table 6.13: The systematic uncertainties (in percentage), from different sources, on the acceptance of the W+jets background. The total acceptance uncertainty is calculated as the sum in quadrature from all sources.

As for the m_{hh} shape uncertainty, almost all variations were found to be negligible. The variation with the most noticeable difference in shape compared to the nominal is the scale variation as shown in Figure 6.8.

There are three NPs related to the theoretical modelling uncertainties of the W+jets background: the total acceptance uncertainty, the m_{hh} shape uncertainty due to scale variation and the uncertainty on the cross-section which is about 5%.

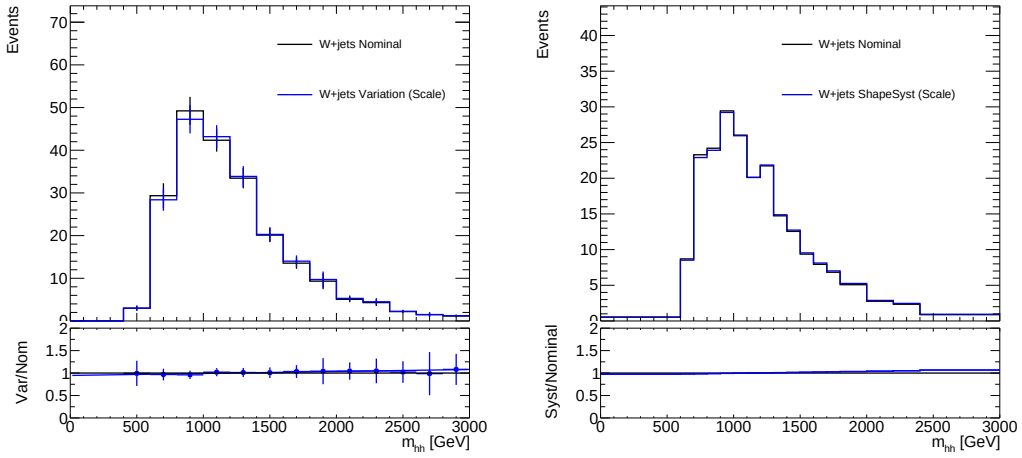

(a) (b)

Figure 6.8: m_{hh} distribution shape comparison between nominal W+jets sample and scale variation sample. Plot on the left is a direct comparison between the nominal and variation sample while on the right, the variation comes from the reweighted function applied to the nominal W+jets sample. The linear fit in the ratio of the left plot is used as the reweighted function.

Table 6.14 shows the estimated acceptance uncertainty on the Z+jets background. The largest uncertainty comes from the scale variation and it dominates the total uncertainty on Z+jets background. The m_{hh} shape uncertainty, for all variations, is found to be negligible and therefore are not taken into account. Two NPs, related to the theoretical modelling uncertainties, are assigned to the Z+jets background: the acceptance uncertainty and the cross-section uncertainty of 5%.

Variation	Uncertainty (%)
Scale	48
PDF α_S	2
PDF set	3
Total	48

Table 6.14: The systematic uncertainties (in percentage), from different sources, on the acceptance of the Z+jets background. The total acceptance uncertainty is calculated as the sum in quadrature from all sources.

Diboson modelling

For the diboson background, only one source of systematic uncertainty on the acceptance is taken into account which is the renormalization and factorization scale variation. It is

estimated by comparing the acceptance of nominal sample to SHERPA v2.1.1 diboson samples with the renormalization and factorization scale varied by a factor of two. The uncertainty is estimated to be be 40% and the impact on the shape of m_{hh} is negligible. There are two NPs related to the theoretical modelling uncertainties of the diboson background: the acceptance uncertainty and the uncertainty on the cross-section which is about 5%.

6.4.3 Multijet background

Normalization uncertainties

Statistical The prediction on the normalization of the multijet yield in Region A is affected by the data and MC statistics in the control regions. The statistical uncertainty on the multijet normalization is determined by propagating the statistical uncertainty of the $N_B^{\mathrm{multijet}}/N_D^{\mathrm{multijet}}$ ratio, as shown in Table 6.4, and the statisical uncertainty on the multijet yield in region C (N_C^{multijet}), as in Table 6.5.

1-tag/2-tag jet mass acceptance Another source of uncertainty on the multijet normalization is the the difference in multijet acceptance of the large-R jet mass selection between 1-tag and 2-tag category in region C. This uncertainty is included since the multijet shape prediction uses the shape from the 1-tag region C. Table 6.15 shows the acceptance difference between 1-tag and 2-tag region C for the two different mBB regions (defined by the selection on the large-R jet mass). The relative difference between the acceptance in 1-tag region C and in 2-tag region C is taken as an uncertainty on the multijet normalization.

$t\bar{t}$ and W+jets theoretical modelling In all of the control regions, the $t\bar{t}$ and W+jets backgrounds are the two biggest backgrounds with prompt lepton. The multijet normalization in all regions are calculated by subtracting the total prompt lepton background from data, and the $t\bar{t}$ and W+jets contributions to the total prompt lepton background are estimated by using MC samples.

The uncertainty on the multijet normalization prediction in region A due to the theoretical modelling of the acceptance of the $t\bar{t}$ and W+jets backgrounds is estimated by varying the normalization of the backgrounds in each region by their respective acceptance uncertainties. The acceptance uncertainty for each background in each control regions are evaluated using the same procedure as discussed in Section 6.4.2.

The uncertainty on the multijet normalization in region A is estimated, first, by varying the $t\bar{t}$ and W+jets normalization within their acceptance uncertainty and propagating

	e+jets	μ+jets
SR		
1-tag $N_{\text{C,SR}}^{\text{multijet}}/N_{\text{C,Inc}}^{\text{multijet}}$	32 ± 3	28 ± 3
2-tag $N_{\text{C,SR}}^{\text{multijet}}/N_{\text{C,Inc}}^{\text{multijet}}$	38 ± 10	41 ± 10
Rel. difference between 1-tag and 2-tag	17	32
mBBcr		
1-tag $N_{\text{C,mBBcr}}^{\text{multijet}}/N_{\text{C,Inc}}^{\text{multijet}}$	68 ± 3	72 ± 3
2-tag $N_{\text{C,mBBcr}}^{\text{multijet}}/N_{\text{C,Inc}}^{\text{multijet}}$	63 ± 7	59 ± 7
Rel. difference between 1-tag and 2-tag	9	22

Table 6.15: The acceptance (in percentage) of the large-R jet mass selection for the multijet prediction in the 1-tag and 2-tag region C and the relative difference (in percentage) between the tag categories. The relative difference is taken as the uncertainty on the multijet yield prediction due the large-R jet mass selection acceptance. $N_{\text{C,SR}}^{\text{multijet}}$ ($N_{\text{C,Inc}}^{\text{multijet}}$) is the multijet yield with (without) the signal region large-R jet mass selection and $N_{\text{C,mBBcr}}^{\text{multijet}}$ is when an event does not pass the selection.

through the ABCD method to obtain the resulting multijet normalization in region A. It is then compared to the nominal multijet prediction in region A and their difference is taken as the uncertainty on the multijet normalization due to the acceptance uncertainty of the $t\bar{t}$ and W+jets background. Table 6.16 shows the uncertainty on the multijet yield prediction in region A signal and mBB control region due to the uncertainty on the $t\bar{t}$ and W+jets acceptance modelling in each lepton channel.

	e+jets	μ+jets
SR		
$t\bar{t}$	27	60
W+jets	25	70
mBBcr		
$t\bar{t}$	37	101
W+jets	30	78

Table 6.16: The uncertainty (in %) on the multijet yield prediction in region A mBBcr and SR due to the acceptance modelling uncertainty for the $t\bar{t}$ and W+jets backgrounds in region B, C and D.

Detector modelling of prompt backgrounds The detector modelling systematic uncertainties on the MC predicted total prompt background are sources of uncertainties on the multijet normalization in region A. They are taken into account by propagating the detector

modelling uncertainties in the control region through the ABCD method. This is done for each detector modelling uncertainty (Section 6.4.1) and the resulting multijet normalization in region A is compared to the nominal; with their difference taken as the uncertainty on the multijet normalization for a given detector modelling uncertainty. Table 6.17 shows the total uncertainty due to detector modelling uncertainties on the predicted multijet normalization for each lepton channel.

	e+jets	μ+jets
SR		
Uncertainty	46	106
mBBcr		
Uncertainty	46	127

Table 6.17: The uncertainty (in percentage) on the predicted multijet yield in region A due to the detector modelling uncertainties of the prompt backgrounds in region B, C and D.

$|d_0^{\text{sig}}|$ cut efficiency modelling The $|d_0^{\text{sig}}|$ cut efficiency modelling uncertainty for the prompt MC backgrounds are also taken into account in for the multijet normalization due to the tigther cut on the leptons' $|d_0^{\text{sig}}|$. The determination of the $|d_0^{\text{sig}}|$ cut efficiency modelling uncertainty was discussed previously in Section 6.4.1. This uncertainty is propagated through the ABCD method by varying the normalization of the prompt backgrounds in regions B, D and C simultaneously to estimate the uncertainty on the multijet yield prediction region A and is treated as anti-correlated between regions B and regions D, C. Table 6.18 shows the uncertainty on the multijet normalization due to the $|d_0^{\text{sig}}|$ selection efficiency modelling uncertainty on prompt backgrounds for both lepton channels.

	e+jets	μ+jets
SR		
Uncertainty	46	51
mBBcr		
Uncertainty	42	111

Table 6.18: The uncertainty (in %) on the predicted multijet yield in region A due to the $|d_0^{\text{sig}}|$ cut efficiency modelling uncertainties of the prompt backgrounds in region B, D and C.

mBB control region closure A maximum likelihood fit of the large-R jet mass distribution in the mBB control region is performed with the normalization of the multijet background allowed to float from the nominal prediction. In the μ+jets channel, the post-fit

normalization factor is consistent with unity but in the e+jets channel, the normalization factor is calculated to 0.68 ± 0.13. Due to this significant deviation from unity in the e+jets channel, a non-closure uncertainty of 32% on the multijet normalization in both the mBB control region and signal region.

Total uncertainty on the yield The total uncertainty on the multijet normalization is calculated as the sum in quadrature of the uncertainties from the sources explained above. Table 6.19 summarizes the systematic uncertainties on the predicted multijet yield for the e+jets and μ+jets channel. The uncertainty in the μ+jets channel is much larger than in the e+jets channel. This is due to relatively lower data statistics for the μ+jets channel in all control regions. When the two channels are combined, the uncertainty on the multijet normalization in the ℓ+jets channel is 77%. A single NP is assigned for the normalization uncertainty on the multijet background.

Source	e+jets	μ+jets
SR		
Statistical	28	40
2-tag/1-tag m_J acceptance	16	32
$t\bar{t}$ MC modelling	27	60
W+jets MC modelling	25	70
Prompt backgrounds detector modelling	46	106
$\lvert d_0^{\text{sig}} \rvert$ cut efficiency modelling	46	51
mBB control region closure	32	-
Total	88	158
mBBcr		
Statistical	24	41
2-tag/1-tag m_J acceptance	9	22
$t\bar{t}$ MC modelling	37	101
W+jets MC modelling	30	78
Prompt backgrounds detector modelling	46	127
$\lvert d_0^{\text{sig}} \rvert$ cut efficiency modelling	42	111
mBB control region closure	32	-
Total	88	216

Table 6.19: A summary of systematic uncertainties (in percentage) from different sources on the multijet yield in the SR and mBBcr for each lepton channel. The total uncertainty on the multijet background normalization is calculated by adding in quadrature the uncertainties from all sources.

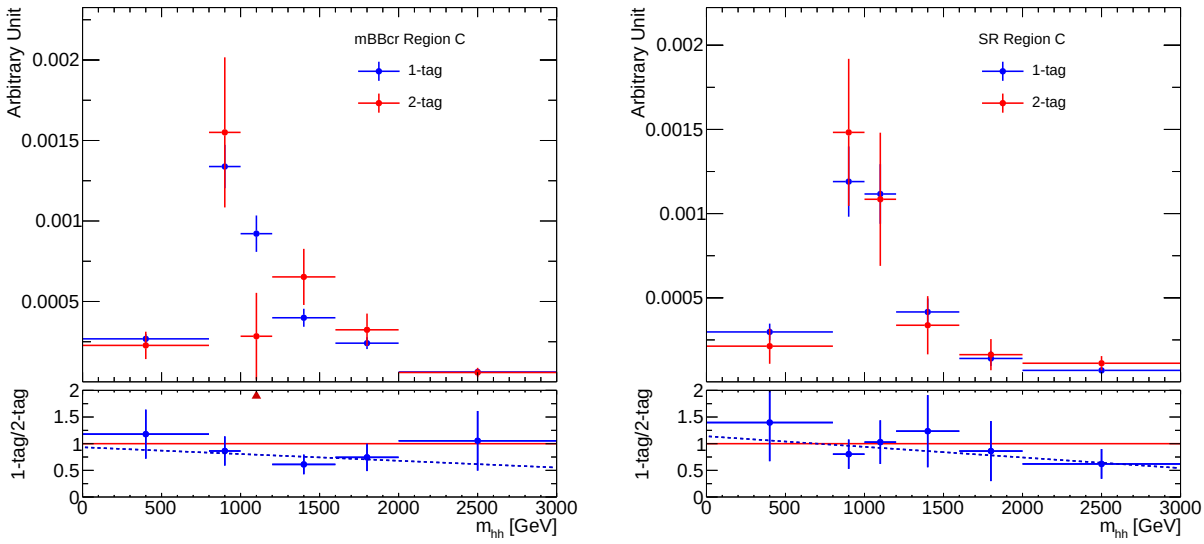

(a) (b)

Figure 6.9: Multijet background shape comparison of the m_{hh} distribution in region C between 1-tag and 2-tag category in (a) mBBcr and (b) SR. The linear fit (blue dashed line) to the ratio is used to smoothen and parameterize the shape variation of the of multijet m_{hh} distribution prediction.

Shape uncertainties

The uncertainty on the m_{hh} distribution prediction for the multijet background is estimated by comparing the m_{hh} distribution shape in region C between the 1-tag category and 2-tag category. The difference between the shape is taken as the systematic uncertainty on the multijet background m_{hh} distribution shape prediction. A linear fit to the m_{hh} distribution ratio of the two categories is used to parameterize the m_{hh} distribution shape variation. The m_{hh} distribution shape comparison between 1-tag and 2-tag category and the linear fit to the ratio between the two categories is shown in Figure 6.9a. Figure 6.9b shows the final shape prediction of the m_{hh} distribution with its corresponding systematic uncertainty. A single NP is assigned for the m_{hh} shape uncertainty on the multijet background.

6.4.4 Impact of systematic uncertainties

The impact of the systematic uncertainties can be assessed by comparing the relative change of the predicted event yields to the nominal prediction. Tables 6.20 and 6.21 gives the average impact of the detector modelling systematic uncertainties on the predicted event yields for the total background and heavy scalar signals of different masses. The systematic uncertainty with the largest impact on the predicted total background yield is the light-jets mistagging rate uncertainty followed by the uncertainty on the c-jets mistagging rate. The large-R jet energy and mass scale uncertainty also have noticeable impact on the total background yield. As for the heavy scalar signals, the b-jet tagging efficiency uncertainties are the most impactful of all the uncertainties and their impact grows larger for higher resonance masses. The large-R jet mass resolution has a sizable impact also, followed by the small-R jet energy scale.

For the theoretical modelling uncertainties of each background process, the impact on the total background event yield is shown in Table 6.22. The normalization uncertainty on the multijet background has, by far, the biggest impact on the total background yield, followed by the acceptance uncertainty on the W+jets, $t\bar{t}$ and single-top backgrounds which have similar impact.

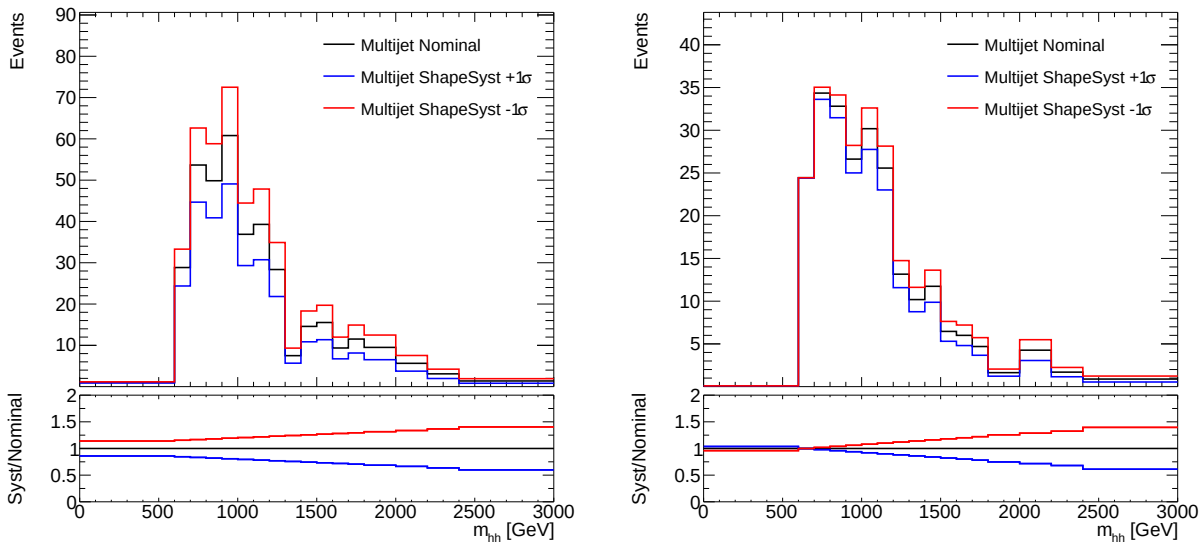

(a) (b)

Figure 6.10: The multijet nominal shape prediction (black) and its systematic uncertainties (red and blue) for the predicted m_{hh} distribution in the (a) mBB control region and (b) SR.

Systematic uncertainty	Total background	H(1000)	H(2000)	H(3000)
Muon momentum scale	< 0.1	0.1	< 0.1	< 0.1
Muon ID track momentum resolution	< 0.1	< 0.1	< 0.1	< 0.1
Muon MS track momentum resolution	< 0.1	< 0.1	< 0.1	< 0.1
Electron momentum scale	0.2	< 0.1	< 0.1	< 0.1
Electron momentum resolution	< 0.1	< 0.1	< 0.1	< 0.1
Muon identification efficiency (statistics)	0.1	0.1	0.1	0.1
Muon identification efficiency (systematic)	0.4	0.5	0.9	1.1
Muon isolation efficiency (statistics)	< 0.1	< 0.1	< 0.1	< 0.1
Muon isolation efficiency (systematic)	< 0.1	0.1	0.1	0.2
Electron reconstruction efficiency	0.2	0.2	0.2	0.2
Electron identification efficiency	0.1	0.1	0.1	0.1
Electron isolation efficiency	0.4	0.5	0.5	0.4
Electron trigger efficiency	0.2	0.3	0.6	0.6
Large-R jet energy and mass scale (baseline)	6.5	1.0	0.3	0.6
Large-R jet energy and mass scale (statistics)	< 0.1	0.1	< 0.1	0.1
Large-R jet energy and mass scale (modelling)	1.9	0.1	0.2	0.4
Large-R jet energy and mass scale (tracking)	1.9	0.1	0.2	0.5
Large-R jet energy resolution	0.5	0.2	< 0.1	< 0.1
Large-R jet mass resolution	0.5	5.0	5.5	6.1
Small-R jet energy resolution	< 0.1	0.8	0.1	0.3
Small-R jet energy scale NP1	3.1	3.7	2.9	2.5
Small-R jet energy scale NP2	0.5	0.7	0.7	0.8
Small-R jet energy scale NP3	0.5	0.6	0.5	0.3
Small-R jet energy scale η Intercalibration	0.3	0.1	0.1	< 0.1
$E_{\mathrm{T}}^{\mathrm{miss}}$ soft-term resolution (Parallel)	0.4	0.2	0.1	0.1
$E_{\mathrm{T}}^{\mathrm{miss}}$ soft-term resolution (Perpendicular)	0.2	0.2	< 0.1	< 0.1
$E_{\mathrm{T}}^{\mathrm{miss}}$ soft-term scale	0.4	0.5	0.1	0.1
Small-R jet JVT efficiency	0.3	0.3	0.2	0.2
Lepton $\lvert d_0^{\mathrm{sig}} \rvert$ selection efficiency	3.3	4.0	4.0	4.0
Luminosity	2.2	3.2	3.2	3.2

Table 6.20: The impact (in percentage) on the total predicted background and heavy scalar signals yields for systematic uncertainties related to the detector modelling of leptons, jets, $E_{\mathrm{T}}^{\mathrm{miss}}$, pile-up reweighting and luminosity. The heavy scalar resonance signals with masses of 1000 GeV, 2000 GeV and 3000 GeV are shown.

Systematic uncertainty	Total background	H(1000)	H(2000)	H(3000)
(Small-R jet) b-jets tag NP0	2.9	0.1	0.1	0.1
(Small-R jet) b-jets tag NP1	1.0	< 0.1	< 0.1	< 0.1
(Small-R jet) b-jets tag NP2	0.1	< 0.1	< 0.1	< 0.1
(Small-R jet) c-jets mistag NP0	0.3	0.8	0.8	0.8
(Small-R jet) c-jets mistag NP1	< 0.1	0.1	0.3	0.3
(Small-R jet) c-jets mistag NP2	< 0.1	< 0.1	0.1	0.1
(Small-R jet) c-jets mistag NP3	< 0.1	< 0.1	< 0.1	< 0.1
(Small-R jet) light-jets mistag NP0	1.0	1.2	1.4	1.5
(Small-R jet) light-jets mistag NP1	< 0.1	< 0.1	< 0.1	< 0.1
(Small-R jet) light-jets mistag NP2	0.1	0.1	0.1	0.1
(Small-R jet) light-jets mistag NP3	< 0.1	< 0.1	< 0.1	< 0.1
(Small-R jet) light-jets mistag NP4	< 0.1	< 0.1	< 0.1	< 0.1
(Small-R jet) b-jets high p_{T} extrapolation	0.1	0.1	0.4	0.7
(Small-R jet) c-jets to τ-jets extrapolation	< 0.1	0.1	0.1	< 0.1
(Track jet) b-jets tag NP0	2.8	5.4	6.8	6.9
(Track jet) b-jets tag NP1	2.1	5.5	8.2	8.1
(Track jet) b-jets tag NP2	0.4	0.3	0.7	0.7
(Track jet) c-jets mistag NP0	8.6	0.1	< 0.1	0.1
(Track jet) c-jets mistag NP1	1.4	< 0.1	< 0.1	< 0.1
(Track jet) c-jets mistag NP2	0.2	< 0.1	< 0.1	< 0.1
(Track jet) c-jets mistag NP3	0.3	< 0.1	< 0.1	< 0.1
(Track jet) light-jets mistag NP0	10	0.5	0.4	0.5
(Track jet) light-jets mistag NP1	0.8	0.1	< 0.1	< 0.1
(Track jet) light-jets mistag NP2	0.2	< 0.1	< 0.1	< 0.1
(Track jet) light-jets mistag NP3	0.3	< 0.1	< 0.1	< 0.1
(Track jet) light-jets mistag NP4	< 0.1	< 0.1	< 0.1	< 0.1
(Track jet) b-jets tag high p_{T} extrapolation	0.5	0.5	4.0	5.6
(Track jet) c-jets to τ-jets extrapolation	0.4	< 0.1	< 0.1	< 0.1

Table 6.21: The impact (in percentage) on the total predicted background and heavy scalar signals yields for systematic uncertainties related to the detector modelling of the flavour tagging efficiencies. The heavy scalar resonance signals with masses of 1000 GeV, 2000 GeV and 3000 GeV are shown.

Systematic uncertainty	Total background
$t\bar{t}$ acceptance	6.7
$t\bar{t}$ cross-section	2.8
W+jets acceptance	7.3
W+jets cross-section	0.9
Z+jets acceptance	0.8
Z+jets cross-section	0.1
Single-top acceptance	6.7
Single-top cross-section	0.4
Diboson acceptance	0.8
Diboson cross-section	0.8
Multijet normalization	15

Table 6.22: The impact (in percentage) on the total predicted background yield in the 2-tag signal region for theoretical systematic uncertainties that affect the normalization of the MC predicted backgrounds flavour tagging efficiencies.

Chapter 7

Analysis Results

The invariant mass of the reconstructed di-Higgs system distribution is used as the discriminant to perform the search in the 2-tag region. A maximum-likelihood fit is used to fit the predicted m_{hh} distribution to the observed data. In the absence of a statistically significant excess in data, upper limits on the resonant di-Higgs production cross-section for different BSM signal models are placed at 95% confidence level.

Section 7.1 describes the statistical treament used in this analysis. In Section 7.2, the unblinded data and comparison to the total predicted background in the search region is presented. Section 7.2.1 presents the observed and expected upper limits on the resonant di-Higgs production cross-section and Section 7.2.2 discusses the impact of the systematic uncertainties on the expected upper limit. In Section 7.2.3, the sensitivity of this analysis is compared with a complementary "resolved" analysis and $b\bar{b}b\bar{b}$ ATLAS analysis.

7.1 Statistical treatment

A binned maximum likelihood fit of the m_{hh} distribution in the 2-tag signal region is performed on the total background prediction to the observed data. The m_{hh} distribution is binned with varying bin sizes such that the relative statistical uncertainty of the total background in each bin is less than 20%. Figure 7.1 compares the total background m_{hh} distribution with fixed-size bins and variable-size bins.

A statistical analysis quantifies the compatibility between the observed data, expected SM background, and expected signal. Hypothesis testing is performed using a modified frequentist method and based on a profile likelihood that includes a treatment of the systematic uncertainties as nuisance parameters. The binned likelihood function is a product of Poisson

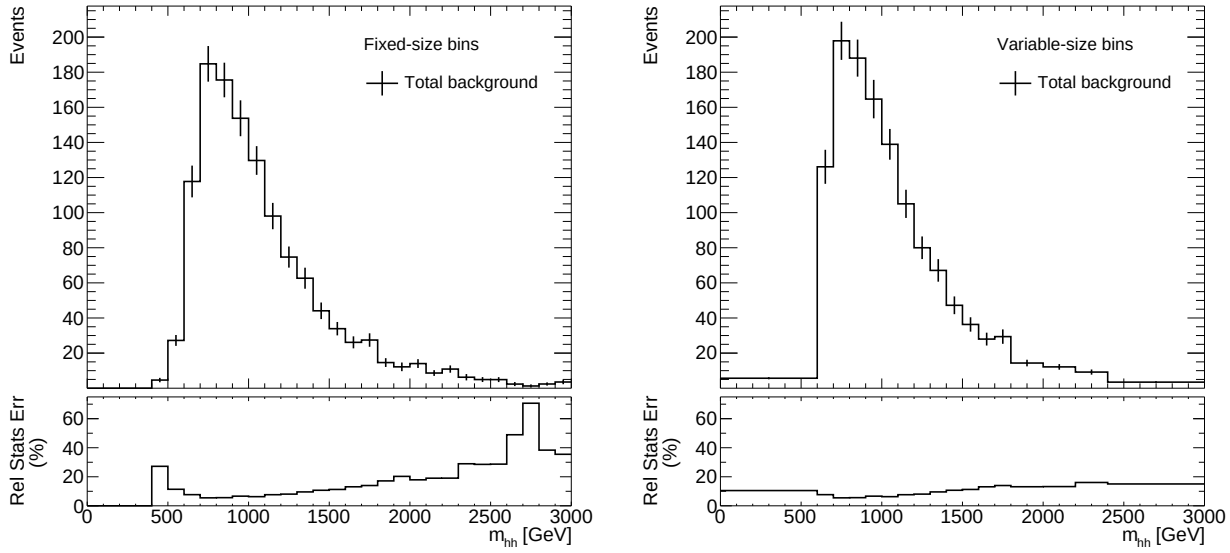

(a) (b)

Figure 7.1: The total background m_{hh} distribution with (a) fixed-size bins and (b) variable-size bins. The error bars are the statistical uncertainty on the total background and the lower pad shows the relative statistical uncertainty (in %) for each bin.

probability terms,

$$L(\mu) = \prod_{i=1}^{N_{bins}} \mathrm{Pois}(N_i|\mu s_i + b_i) \tag{7.1}$$

where μ is the signal strength parameter, s_i (b_i) is the expected signal (background) yield, N_i is the observed number of events from the data in bin i of the m_{hh} distribution histogram with N_{bins} number of bins. The signal strength parameterizes the production of signal events and is considered as the Parameter of Interest (POI). When $\mu = 1$, it corresponds to the nominal signal hypothesis and $\mu = 0$ corresponds to the background-only hypothesis.

Systematic uncertainties are parameterised by a vector of nuisance parameters ($\boldsymbol{\alpha}$) which affect the expected signal, $s_i(\boldsymbol{\alpha})$, and background yields, $b_i(\boldsymbol{\alpha})$. The nominal values of the nuisance parameters have been determined from auxiliary measurements (Section 6.4). The nuisance parameters are constrained by additional terms added to the likelihood function. In this analysis for each nuisance parameter α_j, from a total of N_{NP} nuisance parameter, is constrained by a standard normal distribution:

$$\prod_{j=1}^{N_{\mathrm{NP}}} \mathrm{Gauss}(0|\alpha_j, 1) \tag{7.2}$$

where the nominal value of each α is zero and the parameter is assumed to follow a Gaussian distribution with a standard deviation of $\sigma = 1$ is multiplied to the likelihood. The statistical uncertainty of the total background prediction is also taken into account in the maximum likelihood fit by introducing nuisance parameters γ_i, for each bin i. They are constrained by Poisson terms added to the likelihood:

$$\prod_{i=1}^{N_{bins}} \text{Pois}(n_i|\gamma_i n_i) \tag{7.3}$$

where $n_i = 1/\sigma^2_{i,\text{stat}}$ and $\sigma_{i,\text{stat}}$ is the relative statistical uncertainty of the total background in bin i following the "Beeston-Barlow light" prescription [195]. The final form of the likelihood function which is used in this statistical analysis for the maximum likelihood fit is given as:

$$L(\mu, \boldsymbol{\theta} = (\boldsymbol{\alpha}, \boldsymbol{\gamma})) = \Big\{ \prod_{i=1}^{N_{bins}} \text{Pois}(N_i|\mu s_i(\boldsymbol{\alpha}) + b_i(\boldsymbol{\alpha}, \boldsymbol{\gamma})) \times \text{Pois}(n_i|\gamma_i n_i) \Big\} \times \prod_{j=1}^{N_{\text{NP}}} \text{Gaus}(0|\alpha_j, 1) \tag{7.4}$$

The result from the likelihood fit in terms of μ is obtained by maximizing the likelihood function with respect to all parameters. The test statistic is constructed as a ratio of profile likelihoods [196]:

$$\widetilde{q_\mu} = \begin{cases} -2\ln \frac{L(\mu, \hat{\hat{\boldsymbol{\theta}}}(\mu))}{L(0, \hat{\hat{\boldsymbol{\theta}}}(0))} & \hat{\mu} < 0 \\ -2\ln \frac{L(\mu, \hat{\hat{\boldsymbol{\theta}}}(\mu))}{L(\hat{\mu}, \hat{\boldsymbol{\theta}})} & 0 \leq \hat{\mu} < \mu \end{cases} \tag{7.5}$$

where $\hat{\mu}$ and $\hat{\boldsymbol{\theta}}$ are the parameters that maximize the likelihood and $\hat{\hat{\boldsymbol{\theta}}}$ are the nuisance paramater values that maximize the likelihood for a given μ value. The $\hat{\hat{\boldsymbol{\theta}}}$ values are obtained after a *conditional* (i.e fixed μ value) maximum likelihood fit to the observed data and for $\hat{\mu}$ and $\hat{\boldsymbol{\theta}}$, they are obtained after an unconditional (i.e μ value is left unconstrained) fit to the observed data.

In order to quantify the level of agreement between prediction and observed data, a p-value can be calculated from the test statistic with the probability distribution function (PDFs) of the test statistic, $f(\tilde{q}_\mu|\mu)$ using the following equation:

$$p_\mu = \int_{\tilde{q}_\mu^{obs}}^{\infty} f(\tilde{q}_\mu|\mu) d\tilde{q}_\mu, \tag{7.6}$$

where p_μ is the p-value of the *signal + background* hypothesis for a given signal strength μ. The $f(\tilde{q}_\mu|\mu)$ distribution can be numerically determined by generating a large number of

pseudo-experiment, but this approach is computationally intensive as a new set of pseudo-data has to be generated for each value of μ and for each tested signal mass hypothesis. For this reason, an asymptotic approximation to the distribution is used and it is described in Reference [196].

Upper limits on the signal strength of a particular signal model are set using a modified frequentist approach called the CL_s method [197]. The CL_s method uses the ratio of two frequentist confidence levels:

$$\mathrm{CL}_s(\mu) = \frac{\mathrm{CL}_{s+b}(\mu)}{\mathrm{CL}_b} \tag{7.7}$$

$$= \frac{p_\mu}{1 - p_b} \tag{7.8}$$

where p_μ is calculated with Equation 7.6 and p_b can be calculated from

$$1 - p_b \; = \; \int_{\tilde{q}_0^{obs}}^{\infty} f(\tilde{q}_\mu|0) d\tilde{q}_\mu. \tag{7.9}$$

Values of $\mathrm{CL}_{s+b}(\mu)$ close to zero indicate the signal model with signal strength μ is highly disfavoured. Upper limits at 95% confidence level (C.L.) on the value of the signal strength μ for given signal model are computed by scanning values of the μ hypothesis, computing the CL_s exclusions and identifying the μ^{upper} for which $\mathrm{CL}_s \leq 0.05$.

The CL_s method is said to be conservative. The denominator of Equation 7.8 is always less than or equal to one thus the $\mathrm{CL}_s \leq 0.05$ requirement is more stringent than $p_\mu < 0.05$. The advantage of the CL_s method is that the p-value is penalized for regions where the search has no sensitivity. If a search has little sensitivity to μ (i.e expected signal yield is small or zero with respec to the background yield), the model will still be rejected with a probability close to 5%. In the CL_s method, the PDFs of the test statistic for the signal model and for the background only model have a large overlap if the search has a low senstivity

The software packages that are used to construct and perform the fit on the likelihood model are the HistFactory [198], RooStats [199] and RooFit [200] packages, which are all based on ROOT [201].

7.2 Results

The search for resonant di-Higgs signature is performed in the 2-tag signal region by unblinding the data in the region and compare the distribution in the observed data with the total background prediction. Table 7.1 presents the comparison of the total predicted background yield and the observed number of events in data in the search region. The total

predicted background yield is found to be overestimated by 12% compared to the observed data yield although the difference is well within the normalization systematic uncertainty on the predicted background yield which is estimated to be around $\sim 25\%$. Figure 7.2 compares the m_{hh} distribution between the predicted background and observed data. In general, the observed data distribution is reasonably well described by the predicted background distribution reasonably describes and no statistically significant excess is observed in data over the expected background.

Sample	Event yield	Statistical uncertainty	Systematic uncertainty
$t\bar{t}$	649	$\pm$ 16	$^{+177(+27\%)}_{-169(-26\%)}$
W+Jets	217	$\pm$ 7	$^{+104(+48\%)}_{-101(-47\%)}$
Multijet	235	$\pm$ 19	$^{+182(+77\%)}_{-182(-77\%)}$
Single-top	109	$\pm$ 6	$^{+86(+79\%)}_{-86(-79\%)}$
Z+Jets	21	$\pm$ 1	$^{+11(+55\%)}_{-11(-53\%)}$
Dibosons	24	$\pm$ 2	$^{+15(+63\%)}_{-15(-60\%)}$
Prediction	1255	$\pm$ 27	$^{+324(+26\%)}_{-311(-25\%)}$
Data	1107	-	-
Data/Pred	0.88	-	-

Table 7.1: Predicted and observed yields in the signal region. Detector modelling uncertainties and background modelling uncertainties are included for the total systematic uncertainties for each background.

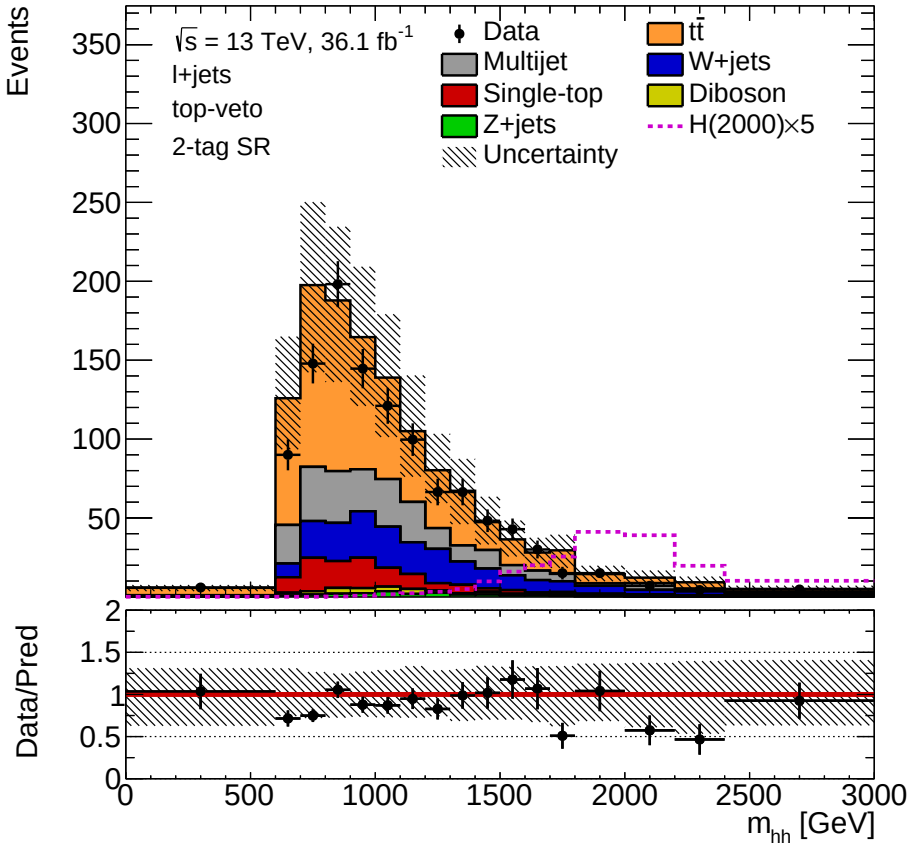

Figure 7.2: The invariant mass of the reconstructed di-Higgs system distribution (m_{hh}) of events in the 2-tag signal region. The hashed grey band is the uncertainty on the total predicted background, which consists of the statistical and systematic uncertainties. The detector modelling and background modelling systematic uncertainties are taken into account in the overall systematic uncertainty.

7.2.1 95% confidence level upper limits

Given that there are no significant deviations from the expected background prediction, the results can be interpreted as a constraint on the presence of BSM physics. Figure 7.3a shows the expected and observed 95% confidence level upper limits on the the production cross-section of heavy scalar resonance which decays into a pair of Higgs boson as a function of the resonance mass.

In Figures 7.3b and 7.3c, the expected and observed 95% confidence level upper limits on the the production cross-section of graviton resonance in the bulk RS graviton models with parameter $c = 2$ and 1 are shown. The theoretical cross sections for both bulk RS graviton models are overlaid and as can be seen, no exclusion can be made for any resonance masses as the observed upper limit is higher than the theoretical cross-sections. As mentioned in Section 6.2.1, 4 mass points were generated for the graviton with large spacing between them. In order to place limits on signal graviton resonance masses which do not have MC samples generated, a signal interpolation procedure is derived to predict the expected graviton signal yield and m_{hh} shape in the 2-tag signal region for each missing mass points. The procedure is briefly described in Appendix B.

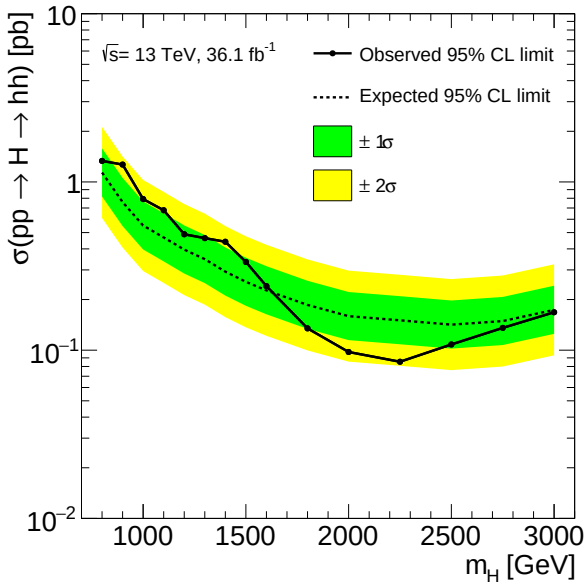

(a)

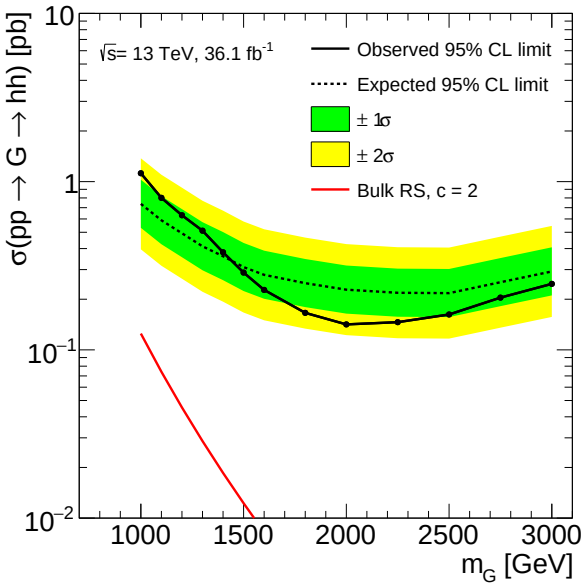

(b)

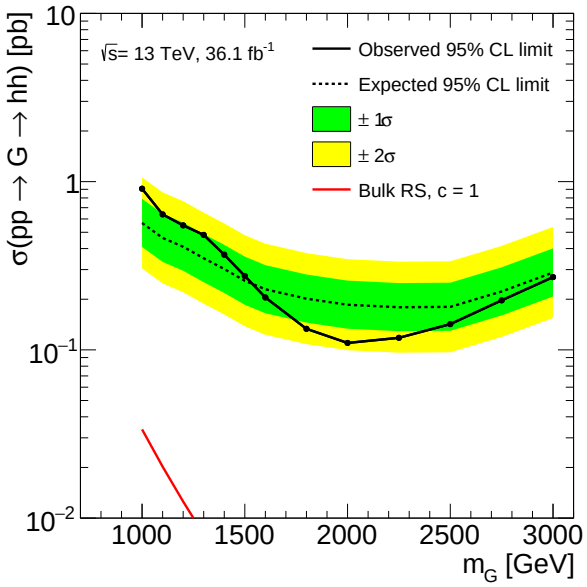

(c)

Figure 7.3: Observed (black solid line) and expected (black dashed line) upper limits at 95% confidence level on the production cross section times branching ratio as a function of resonance mass for the (a) heavy narrow-width scalar, (b) bulk RS model with $c = 2$ and (c) bulk RS model with $c = 1$. An additional (red) curve shows the predicted cross section as a function of resonance mass for each of the graviton models.

7.2.2 Impact of systematic uncertainties on upper limits

Figure 7.4 shows the individual impact of the systematic uncertainties on the expected upper limit on the production cross-section of heavy scalar resonance set at 95% confidence level as a function of resonance mass. The impact is assessed by calculating the ratio of the

expected limit with all nuisance parameters included in the likelihood fit to the expected limit calculated with all nuisance parameters included except the ones corresponding to a group of systematic uncertainties being investigated.

In Figures 7.4a and 7.4b, the impact of the background modelling systematic uncertainties for $t\bar{t}$, W+jets, multijet and single-top background is compared. For the lowest resonance masses, the uncertainty affecting the single-top normalization is the most dominant modelling uncertainty. For resonance masses from 1000 GeV to 1500 GeV, the normalization uncertainty for the W+jets background becomes dominant and from 1500 GeV upwards, the m_{hh} shape uncertainty for the $t\bar{t}$ background is the most dominant uncertainty.

The impact of the detector modelling systematic uncertainties is compared in Figures 7.4c, 7.4d and 7.4e. The most dominant ones are the b-tagging for track jets and large-R jet mass resolution uncertainties and their impact is similar across the whole resonance mass range. The impact of other detector modelling ucertainties is negligible. It was found that the total background statistics has the biggest impact on the expected upper limits as shown in Figure 7.4f.

7.2.3 Sensitivity comparison with the $b\bar{b}WW^*$ resolved analysis and $b\bar{b}b\bar{b}$ analysis

In ATLAS, another complementary analysis, in the same semi-leptonic $b\bar{b}WW^*$ channel, which focuses on the resolved topology was done in parallel to the (boosted) analysis presented in this thesis. The resolved analysis uses 2 small-R b-tagged jets to reconstruct the $h \to b\bar{b}$ decay which differs from the boosted analysis where large-R jets are used. Historically, the resolved analysis[1] was first established to search for resonance masses from 500 GeV to 3000 GeV. The author proposed the boosted analysis in order to increase sensitivity for resonance masses beyond 1000 GeV. Figure 7.5 compares the expected upper limits for the boosted analysis and the resolved analysis as a function heavy scalar resonance mass. The sensitivity reach of the boosted analysis surpasses the resolved analysis from resonance mass range of 1400 GeV to 3000 GeV, as can be seen from the more stringent expected upper limit by a factor of 3-5. The sentivity gain justifies the strategy of the boosted analysis to use large-R jets to reconstruct and identify the $h \to b\bar{b}$ decays for searches of TeV-scale resonances.

Recently, the ATLAS collaboration have published [82] a result on the search for di-Higgs production in the $b\bar{b}b\bar{b}$ decay mode with the 2015+2016 dataset. It is the only di-

[1]For the interested reader, the analysis strategy and results for the resolved analysis can be found in Reference [3].

Higgs analysis, thus far, by the ATLAS collaboration to have published results on both the resolved and boosted topology. Therefore, it is worth comparing the sensitivity of the boosted semi-leptonic $b\bar{b}WW^*$ analysis in this thesis with the $b\bar{b}b\bar{b}$ analysis. Figure 7.6 shows the observed and expected upper limits set at 95% confidence level for narrow-width scalar resonance production cross section times branching ratio by the $b\bar{b}b\bar{b}$ analysis. For a 2000 GeV scalar resonance, the expected upper limit by the $b\bar{b}b\bar{b}$ analysis on the $\sigma(\mathrm{S} \to hh)$ is approximately 0.006 pb. For the boosted analysis in this thesis, the expected upper limit on $\sigma(\mathrm{S} \to hh)$ for the same scalar resonance mass is 0.16 pb, which is a factor of 20 higher compared to the $b\bar{b}b\bar{b}$. This comparison shows that, even though the boosted semi-leptonic $b\bar{b}WW^*$ analysis improves the sensitivity of $b\bar{b}WW^*$ analysis over the resolved at high mass, it is not yet competitive to the sensitivity reach of the $b\bar{b}b\bar{b}$ channel. Looking towards the future, potential improvements can be made in boosted semi-leptonic $b\bar{b}WW^*$ channel by exploring new methods to identify jets from very high p_{T} $h \to b\bar{b}$ decays, which is presented in Chapter 8.

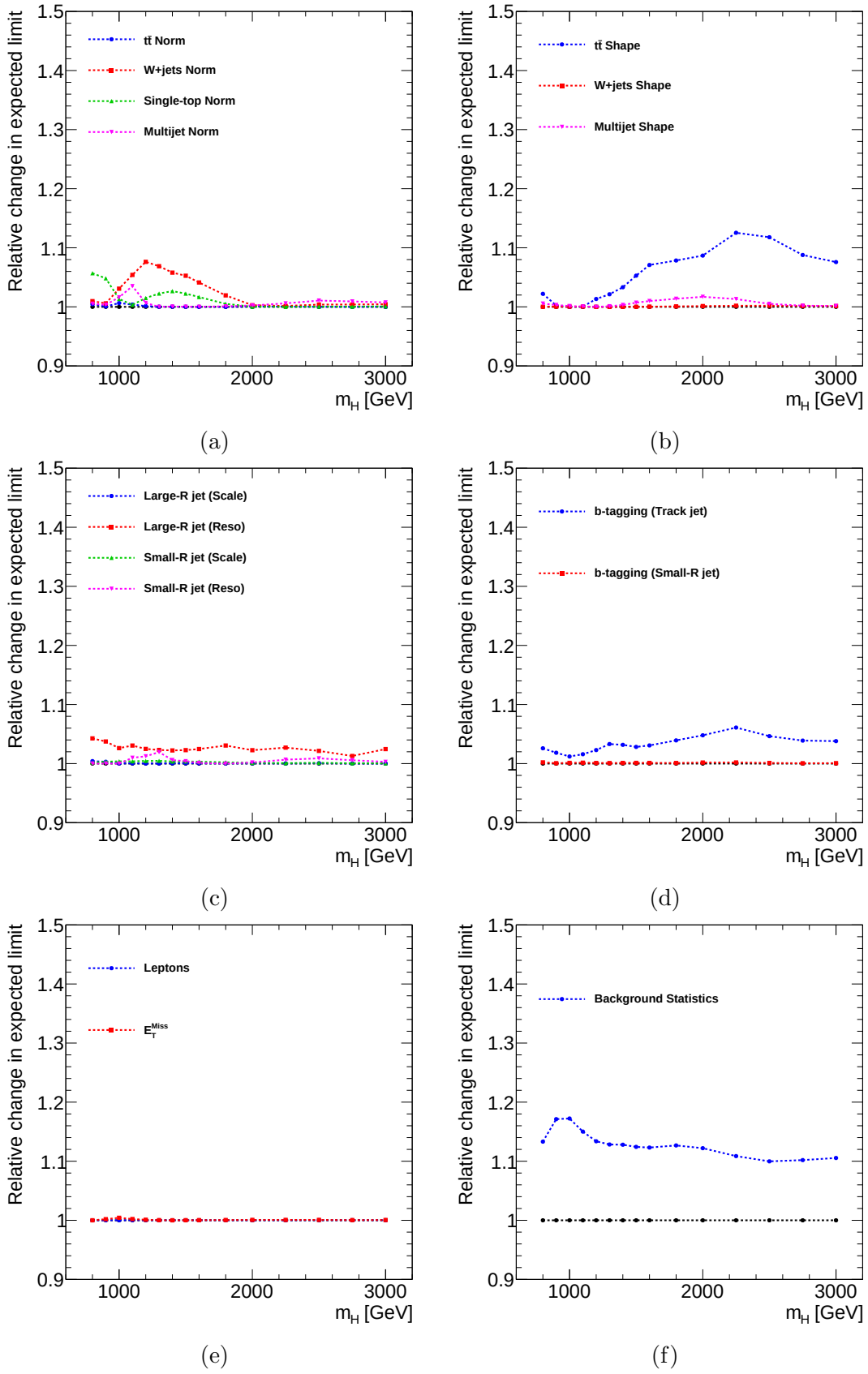

Figure 7.4: The impact of groups of systematic uncertainties on the expected confidence level exclusion limit, as a function of resonance mass. The impact is the ratio of the limit calculated using all systematic uncertainties sources to the limit calculated using all systematic uncertainty sources excluding those under investigation.

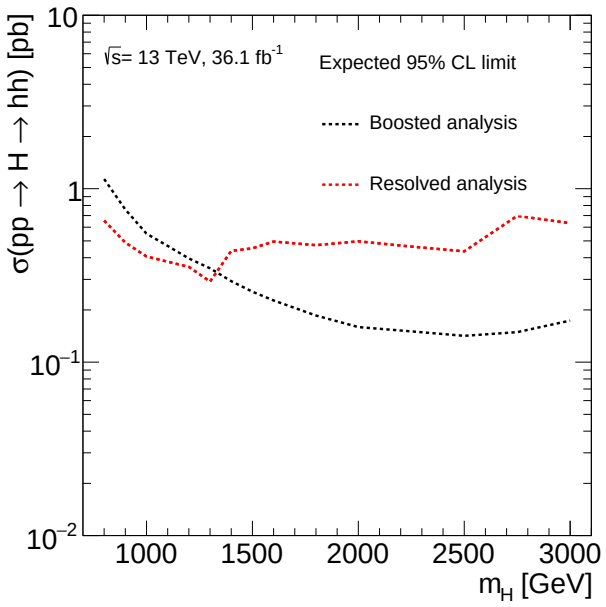

Figure 7.5: Expected upper limits at 95% C.L. as a function of heavy scalar resonance mass for the boosted (black) and resolved analysis (red) [3].

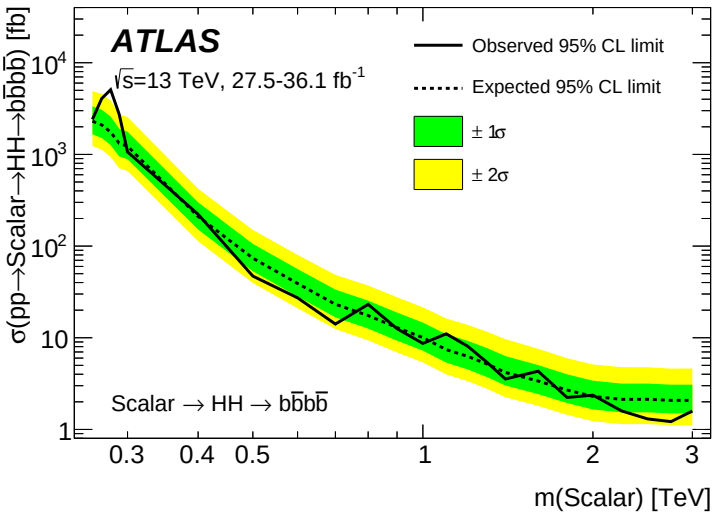

Figure 7.6: The observed and expected 95% confidence upper limits on the narrow-width scalar resonance production cross section times branching ratio ($hh \to b\bar{b}b\bar{b}$) as a function of resonance mass from the ATLAS $hh \to b\bar{b}b\bar{b}$ analysis with 2015+2016 dataset. The results are published in Reference [82].

Chapter 8

Advanced Subjet Reconstruction For Boosted $h \to b\bar{b}$ Identification

In ATLAS, the identification method to select candidate large-R jets from $h \to b\bar{b}$ decays uses the anti-k_t jet clustering algorithm with the radius parameter fixed to be $R = 0.2$ to build subjets. This subjet reconstruction algorithm is currently used as the baseline algorithm. Using ID tracks as inputs, the fixed radius track jet [202–204] approach works well to identify two b-jets within the large-R calorimeter jet until the hadronisation products from the two b-quarks from the Higgs boson decay begin to overlap due to the high p_{T} of the Higgs boson.

At this point, the jet clustering algorithm is not able to resolve the two subjets which leads to the loss of efficiency to identify the two b-jets within the large-R jet. This efficiency loss was seen in the search analysis presented in Chapter 6. As discussed in Section 6.1.5, the selection efficiency of the 2 track jets requirement within the large-R jet $h \to b\bar{b}$ candidate degrades as a function of the heavy scalar mass due to the inability of the jet algorithm to distinguish between two close-by b-jets coming from the boosted $h \to b\bar{b}$.

To mitigate this effect of the fixed angular scale of the anti-k_t jet algorithm, a study on three new subjet reconstruction algorithms in MC simulation is presented in this chapter. The techniques use variable radius track jets, exclusive-k_t subjets, or calorimeter subjets reconstructed in the rest frame of the Higgs jet. Section 8.1 lays out the definition of the signal and background jets used in this study with the metric used to asses the performance of the new algorithms. The three subjet reconstruction algorithms are presented in Section 8.2 and comparison of their performance to the fixed radius track jet algorithm is discussed in Section 8.3. The results in this chapter were published in Reference [4] and the author's main contributions are listed in the Preface at the beginning of this thesis.

8.1 Definitions

In this study, only large-R calorimeter jets with $p_{\mathrm{T}} > 250$ GeV, $|\eta| < 2.0$ and mass between 76 GeV and 146 GeV are considered. The signal jets of interest are jets originating from $h \to b\bar{b}$ decays (*Higgs jet*) while the background jets are jets from top quark decays (*top jet*) and jets from QCD-initiated multijet processes (*QCD jet*).

The signal and background jets are defined by identifying the presence of truth particles matched to the large-R jet and this procedure is called truth flavour-labelling. The procedure is done by geometrically matching generator-level truth particles to the jets. A truth particle is associated to a large-R jet if it is within $\Delta R < 1.0$ of the large-R jet axis. The same flavour-labelling procedure is also used for subjets with the exception that the ΔR requirement is < 0.3 of the subjet axis. If any truth particle is within $\Delta R < 0.3$ of more than one subjet, it is associated to the subjet closest in ΔR. The flavour-labelling definitions for the signal and background jets are as follow:

- Higgs jet: Large-R jets with one truth Higgs boson and two truth b-hadrons matched to the jet. The b-hadrons are required to have $p_{\mathrm{T}} > 5$ GeV. MC simulation samples of bulk-RS gravitons decaying to a pair of Higgs bosons with both Higgs bosons subsequently decaying to $b\bar{b}$ pair are used as a source for signal jets. Graviton masses between 300 GeV and 6000 GeV were generated to fully populate the Higgs boson p_{T} range of interests.
- Top jet: Large-R jets with one truth top quark. A POWHEG+PYTHIA6 MC simulated sample of all-hadronically decaying $t\bar{t}$ events is used as the source for top jets.
- QCD jet: All large-R jets in a PYTHIA8 QCD multijet MC simulated sample are considered as QCD jets. Unlike Higgs jets and top jets, there are no truth particle matching requirement for the large-R jets.

When selecting large-R jets as $h \to b\bar{b}$ candidates, the b-tagging information of the subjets are used. There are two categories for $h \to b\bar{b}$ candidates. The first category, referred to as *double b-tag*, is defined for large-R jets with at least two subjets where the two highest p_{T} subjets are both b-tagged by the MV2c10 algorithm. The second category is *single b-tag*, defined for large-R jets with at least one subjet, where at least one of the two highest p_{T} subjets is b-tagged using the MV2c10 algorithm.

The two metrics that are used to benchmark the performance of a given subjet reconstruction algorithm are the signal efficiency to identify candidate jets from a $h \to b\bar{b}$ decay,

and the background rejection, both for jets originating from a light quark or gluon (QCD jet) or a top quark (top jet). In the case of signal efficiency, two types of signal efficiency are defined. Given a sample of Higgs jet, $N(\text{Higgs jet})$, the double subjet b-labelling efficiency is defined as:

$$\epsilon_{\text{truth}}^{\text{Double subjet b-label}} = \frac{N(\text{Double subjet b-label} \,|\, \text{Higgs jet})}{N(\text{Higgs jet})}, \tag{8.1}$$

where $N(\text{Double subjet b-label} \,|\, \text{Higgs jet})$ is the number of Higgs jets with at least two subjets and each of the two highest p_{T} subjets has exactly one truth b-hadron. The double b-tagging efficiency for Higgs jets is defined as

$$\epsilon_{\text{reco}}^{\text{Double b-tag}} = \frac{N(\text{Double b-tag} \,|\, \text{Higgs jet})}{N(\text{Higgs jet})} \tag{8.2}$$

where $N(\text{Double b-tag} \,|\, \text{Higgs jet})$ represents the number of double b-tagged Higgs jets while the single b-tagging efficiency is defined as

$$\epsilon_{\text{reco}}^{\text{Single b-tag}} = \frac{N(\text{Single b-tag} \,|\, \text{Higgs jet})}{N(\text{Higgs jet})} \tag{8.3}$$

with $N(\text{Single b-tag} \,|\, \text{Higgs jet})$ is the number of single b-tagged Higgs jets. In the case of background rejection for QCD and top jets, the rejection is defined as the inverse of the efficiency to accept a background jet, where the initial ensemble of QCD or top jets is taken as the inclusive set of jets passing the kinematic requirements imposed on the large-R jet p_{T} and η.

8.2 New subjet reconstruction algorithms

8.2.1 Variable-R track jets

The first alternative to fixed radius track-based subjets is to use a "variable" radius (VR) jet clustering algorithm. Initially described in Reference [205], this jet algorithm modifies the conventional iterative recombination clustering algorithm (Equation 4.3) by making the radius parameter a function of the jet p_{T}:

$$R \longrightarrow R_{\text{eff}}(p_{\text{T}}) = \frac{\rho}{p_{\text{T}}} \tag{8.4}$$

The new parameter ρ determines how fast the effective jet size decreases with the transverse momentum of the jet. In addition to ρ, the VR jet algorithm requires two additional

parameters, R_{min} and R_{max}, to impose lower and upper cut-offs on the jet size, respectively. The additional parameters prevent the jets from becoming too large at low p_{T} and from shrinking below the detector resolution at high p_{T}. The effective jet size varies smoothly between R_{min} and R_{max}. In principle, VR formulations of C/A and k_t jet algorithms are also possible but this study is limited to the anti-k_t variant, as a simple extension to the fixed radius ($R = 0.2$) track jet reconstruction which uses the anti-k_t jet algorithm.

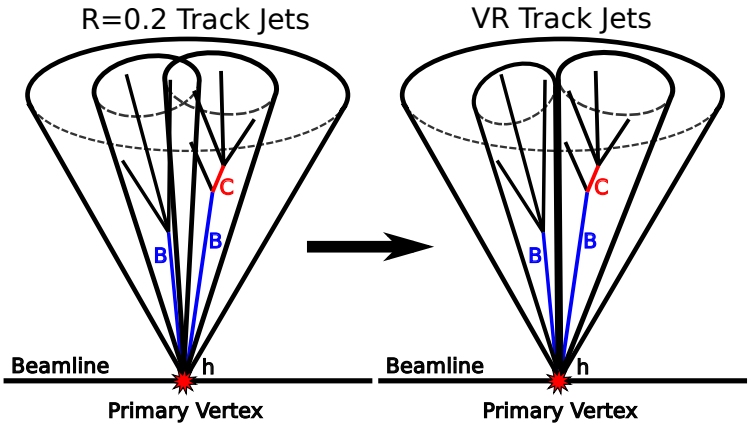

Figure 8.1: Illustration of $h \to b\bar{b}$ subjet reconstruction using variable radius track jet algorithm. Figure produced by a collaborator and published in Reference [4].

The ρ, R_{min} and R_{max} parameters are scanned to find physically motivated and sensible values for the parameters of the VR jet algorithm that are to be used in reconstructing track jets from boosted $h \to b\bar{b}$ decays. The scan for each parameter is performed by examining the truth subjets double b-labelling efficiency of Higgs jets for different values of a given parameter while using fixed values for the other parameters. The optimal value for each parameter is then chosen to be the value which gives the highest truth subjet double b-labelling efficiency.

In Figure 8.2, the truth subjet double b-labelling efficiency is shown for fixed radius track jets, as a function of the Higgs jet p_{T}, as a benchmark for comparing VR track jets with different ρ, R_{max} and R_{min} values. As seen in Figure 8.2a, VR track jets with $\rho =$ 30 GeV have the best truth subjet double b-labelling efficiency over the largest Higgs jet p_{T} range. In Figure 8.2b, the configuration for VR track jets with $\rho = 30$ GeV and $R_{\text{max}} = 0.4$, the $R_{\text{min}} = 0.06$ value is observed to be the optimal value because the truth subjet double b-labelling efficiency is the most stable as a function of Higgs jet p_{T} compared to other R_{min} values. The R_{max} value of 0.4 for VR track jets with $\rho = 30$ GeV and $R_{\text{min}} = 0.02$ gives the highest truth subjet double b-labelling efficiency across the whole Higgs jet p_{T} range as shown in Figure 8.2c.

Furthermore, it can be observed in Figure 8.2c that the truth subjet double b-labelling

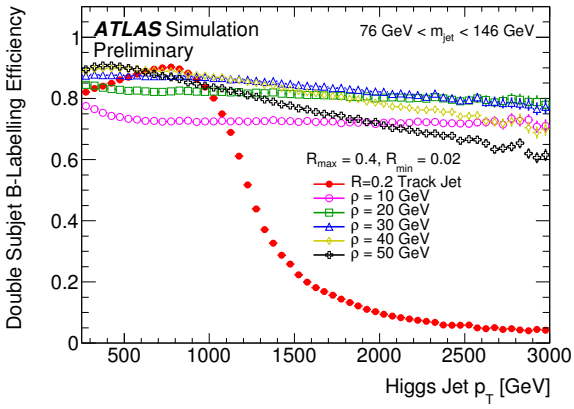

(a)

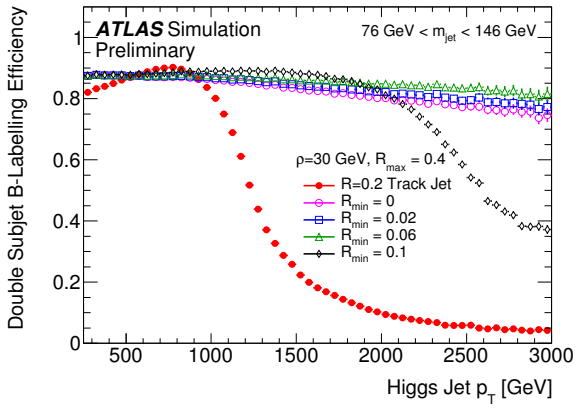

(b)

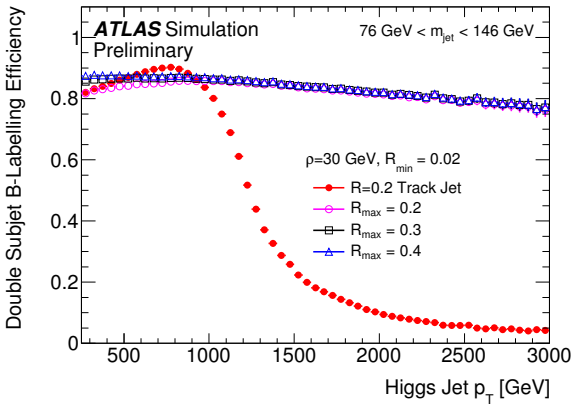

(c)

Figure 8.2: Efficiency of subjet double b-labelling at the truth level of a Higgs jet as a function of the Higgs jet p_T. (a) The efficiency for VR track jets with R_{min} = 0.02 and R_{max} = 0.4 for several ρ values. (b) The efficiency for VR track jets with ρ = 30 GeV and R_{max} = 0.4 for different values of R_{min}. (c) The efficiency for VR track jets with ρ = 30 GeV and R_{min} = 0.02 for varying values of R_{max}. The efficiency for R = 0.2 track jets is also included in all of the plots. The error bars include statistical uncertainties only. Figures produced by the author and published in Reference [4].

efficiency decreases at low Higgs jet p_{T} as the values of R_{max} is decreased, converging to that of the fixed radius track jets for R_{max}=0.2. This decrease in performance is expected for lower p_{T} Higgs jets because the jet is more spread out, lower p_{T} constituents which, when forced to cluster with a smaller radius jet algorithm, tend to spawn a greater number of associated VR track-jets within the large-R jet, leading to an increased probability that the b-hadrons will not be within the two highest p_{T} subjets. Allowing the subjets to grow beyond this bound, as is done with the VR jet algorithm, mitigates this effect. Lastly, for all VR parameter combinations, it can be seen that the truth subjet double b-labelling efficiency using VR track jets is substantially higher at high Higgs boson jet p_{T} compared to fixed radius track jets.

For Higgs jets with 600 GeV $< p_{\text{T}} <$ 1000 GeV, the $R = 0.2$ track jet approach performs

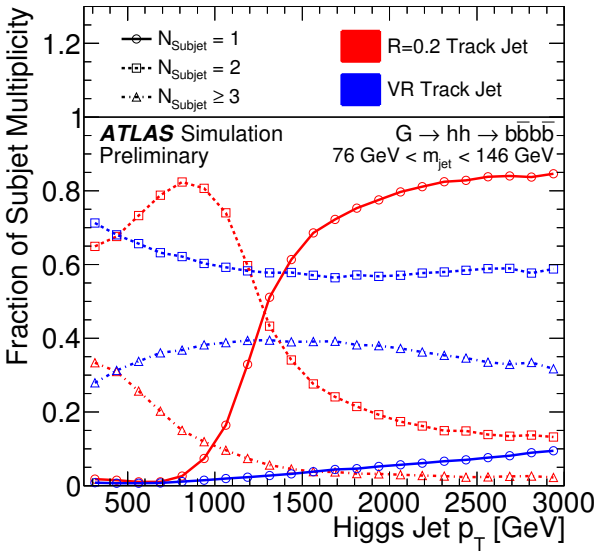

Figure 8.3: The subjet multiplicity fractions as a function of the Higgs jet p_{T} for Higgs jets with exactly 1 subjet (solid line), 2 subjets (dashed line) and at least 3 subjets (dotted line). The red line refers to fixed radius track jets (anti-k_t R = 0.2) while the blue line refers to variable radius track jets (ρ = 30 GeV and $R_{\mathrm{max}} = 0.4$, $R_{\mathrm{min}} = 0.02$). Figures produced by the author and published in Reference [4].

better than the VR track jet approach. To better understand why the truth double b-tagging performance of the $R = 0.2$ track jet algorithm is better than that of the VR track jet algorithm for Higgs jets with 600 GeV $< p_{\mathrm{T}} <$ 1000 GeV, a slight variation of truth double b-tagging is studied. In Figure 8.3, it is seen that for a large fraction of large-R jets (30% to 40%), there are three VR track jets, as opposed to the expected number of two. In these cases, only considering the two highest p_{T} subjets leads to an inefficiency in correctly labelling the jet as a Higgs jet when this additional track jet is the one that should have been queried for b-labelling. To mitigate this effect, the variation that is implemented considers the three highest p_{T} subjets, and requires that two out of the three be truth matched to a b-hadron. This truth double b-tagging variant efficiency is plotted vs Higgs jet p_{T} in Figure 8.4. The $R = 0.2$ and VR track jet efficiencies are higher when the third highest p_{T} subjet is considered, and the VR track jet efficiency is larger than the $R = 0.2$ track jet efficiency. This indicates that VR track jets reconstruct one of the b-hadrons as the third highest p_{T} subjet more frequently than $R = 0.2$ track jets.

8.2.2 Exclusive-k_t subjets

Another alternative to the fixed radius track jet algorithm is the exclusive-k_t (ExKt) algorithm, which uses a variation of the k_t jet clustering algorithm. The algorithm, which

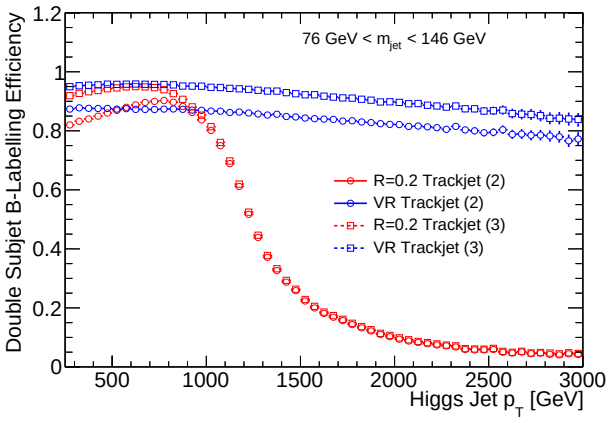

Figure 8.4: The efficiency, as function of Higgs jet p_{T}, for a Higgs jet to have two subjets matched to truth b-hadrons when considering the two highest p_{T} (circle marker) or the three highest p_{T} (square marker) associated subjets. Figure produced by the author.

uses exactly the same distance metric as the ordinary inclusive k_t jet clustering algorithm (Equations 4.3 and 4.4 with $p = 1$), begins by taking the topocluster constituents of large-R calorimeter jets and then reclusters them with the exclusive-k_t jet clustering algorithm until a certain fixed number of jets are obtained. For the purpose of $h \to b\bar{b}$ identification, the fixed number of jets is set to 2 and they are the subjets to be used for b-tagging.

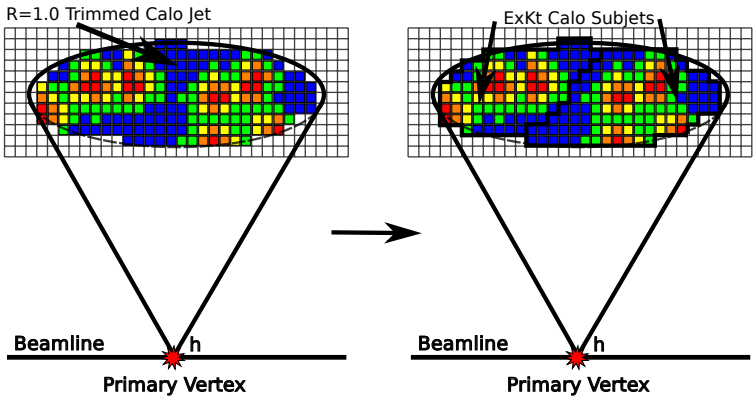

Figure 8.5: Illustration of $h \to b\bar{b}$ subjet reconstruction using exclusive-k_t algorithm. Figure produced by a collaborator and published in Reference [4].

A distinct feature of the exclusive-k_t jet algorithm is that it does not have a fixed distance parameter, unlike an inclusive jet algorithm, which suggests that there is no intrinsic angular lower bound on the distance between subjets. Furthermore, since exclusive-k_t jet algorithm with exactly two subjets is equivalent to reversing the jet clustering with the k_t jet algorithm for the last clustering step, exclusive-k_t effectively splits the large-R jet into two parts, each of which is used to define a region of interestthat is expected to contain one b-hadron from the $h \to b\bar{b}$ decay. This algorithm is particularly useful in the case of very high p_{T} Higgs

jets because the jet is divided into two components by construction, thereby more closely resembling the $h \to b\bar{b}$ topology.

8.2.3 Center-of-Mass subjets

Information of the inner structure (substructure) of jets in the center-of-mass (CoM) frame defined by the reconstructed jet four-momentum has been shown to offer discrimination between jets from hadronically-decaying high p_{T} W or Z bosons and QCD jets [206, 207] and that this algorithm can also be extended to identification of a high p_{T} Higgs boson decaying to a $b\bar{b}$ quark pair [208].

In this approach, the topocluster constituents belonging to the large-R calorimeter jet are boosted to the CoM frame of the large-R jet (*jet rest frame*). The CoM frame is defined as the reference frame in which the four-momentum of the large-R calorimeter jet is equal to $p_\mu = (m_{\mathrm{jet}}, 0, 0, 0)$ and m_{jet} is the invariant mass of the large-R calorimeter jet.

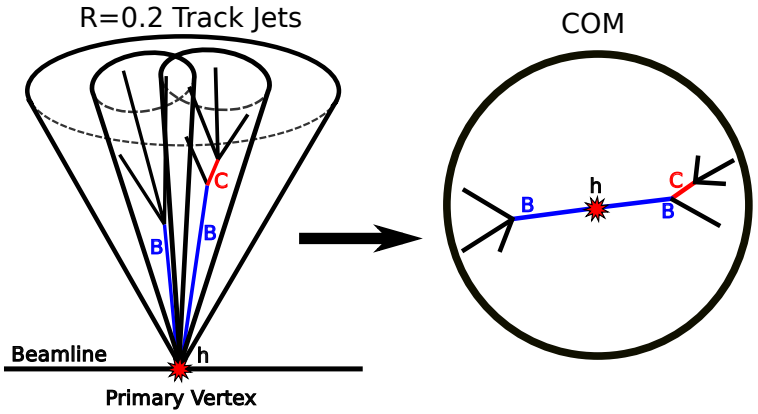

Figure 8.6: Illustration of $h \to b\bar{b}$ subjet reconstruction using CoM algorithm. Figure produced by a collaborator and published in Reference [4].

In the jet rest frame, the constituents of the large-R calorimeter jet are reclustered using the EECambridge jet algorithm [125] to form subjets. The EECambridge jet algorithm sequentially combines calorimeter cell clusters with the smallest angular separation $y_{ij} = 2 \times (1 - \cos\theta_{ij})$, where θ_{ij} is the angle between the momenta of the i^{th} and j^{th} energy cluster in the jet rest frame. The algorithm stops either when y_{ij} exceeds the cut-off value $y_{\mathrm{cut}}^{\mathrm{subjet}}$ or a certain fixed number of subjets is reached, and in this case, as with the exclusive-k_t algorithm described in Section 8.2.2, the CoM clustering algorithm stops when exactly 2 subjets are found, one for each of the b-quarks from the Higgs boson decay.

The track-to-subjet association, for the purpose of b-tagging, also adopts the idea of boosting the constituents, in this case tracks, to the CoM of the large-R calorimeter jet.

Tracks are initially associated to the large-R calorimeter jet if it is within $\Delta R < 1.0$ of the jet in the laboratory frame. They are then boosted to the large-R calorimeter jet rest frame. For each track, the angular distance y_{ij} between itself and the reconstructed subjets in the CoM is calculated and when $y_{ij} < y_{cut}^{track}$, the track is associated to the subjet. The chosen value of y_{cut}^{track} is 0.6. Finally, the subjets and tracks are boosted back to the laboratory frame after association.

8.3 Performance in simulation

To benchmark the performance of the VR, ExKt, and CoM subjet reconstruction algorithms, it is useful to compare performance metrics both with b-tagging and without b-tagging. Without directly applying the MV2c10 b-tagging discriminant it is still possible to study how well the alternative algorithms reconstruct the b-hadrons from Higgs boson decays using the b-hadron truth information. These comparisons are useful because the MV2c10 b-tagging performance itself drops at high p_{T} and additionally the MV2c10 BDT training, which is taken from the standard training for small-R calorimeter jets, is expected to be suboptimal when applied to both the standard $R = 0.2$ track jets and the subjets from the alternative algorithms. This is because the training includes kinematic observables which behave differently for different types of jet collections; these differences may propagate into the final performance obtained for the different subjet types. However, it is still important to apply MV2c10 to the alternative algorithms in order to benchmark their performance in as close a way as possible to what would be done in a physics analysis.

8.3.1 Comparisons without b-tagging

One metric to evaluate the subjet reconstruction algorithms performance is the ΔR separation between the subjet axis and the nearest matched truth b-hadron. For Higgs jets with low p_{T} (250 GeV $< p_{\mathrm{T}} <$ 400 GeV), $R = 0.2$ and VR track jets reconstruct axes closer to the truth b-hadrons than the ExKt and CoM subjets, as can be seen in Figures 8.7a and 8.7b. It is a well-known feature that track jets tend to have a better ΔR resolution than calorimeter-based jets [202].

For Higgs jets with high p_{T} (1500 GeV $< p_{\mathrm{T}} <$ 2000 GeV), the highest p_{T} $R = 0.2$ track jet's ΔR separation shows a pronounced shoulder (Figure 8.7e), which correspond to cases where the two b-hadrons become reconstructed as one track jet which is off-axis from both of the b-hadrons. However, the VR, ExKt, and CoM ΔR distributions exhibit the same qualitative features from low to high large-R jet p_{T}. For these same high p_{T} Higgs jets, the

second highest p_{T} $R = 0.2$ track jet retains a small ΔR separation to the truth b-hadron, however reconstructing two $R = 0.2$ track jets for Higgs jets in this p_{T} region is rare, as is indicated by the small area under the normalized distributions in Figure 8.7f.

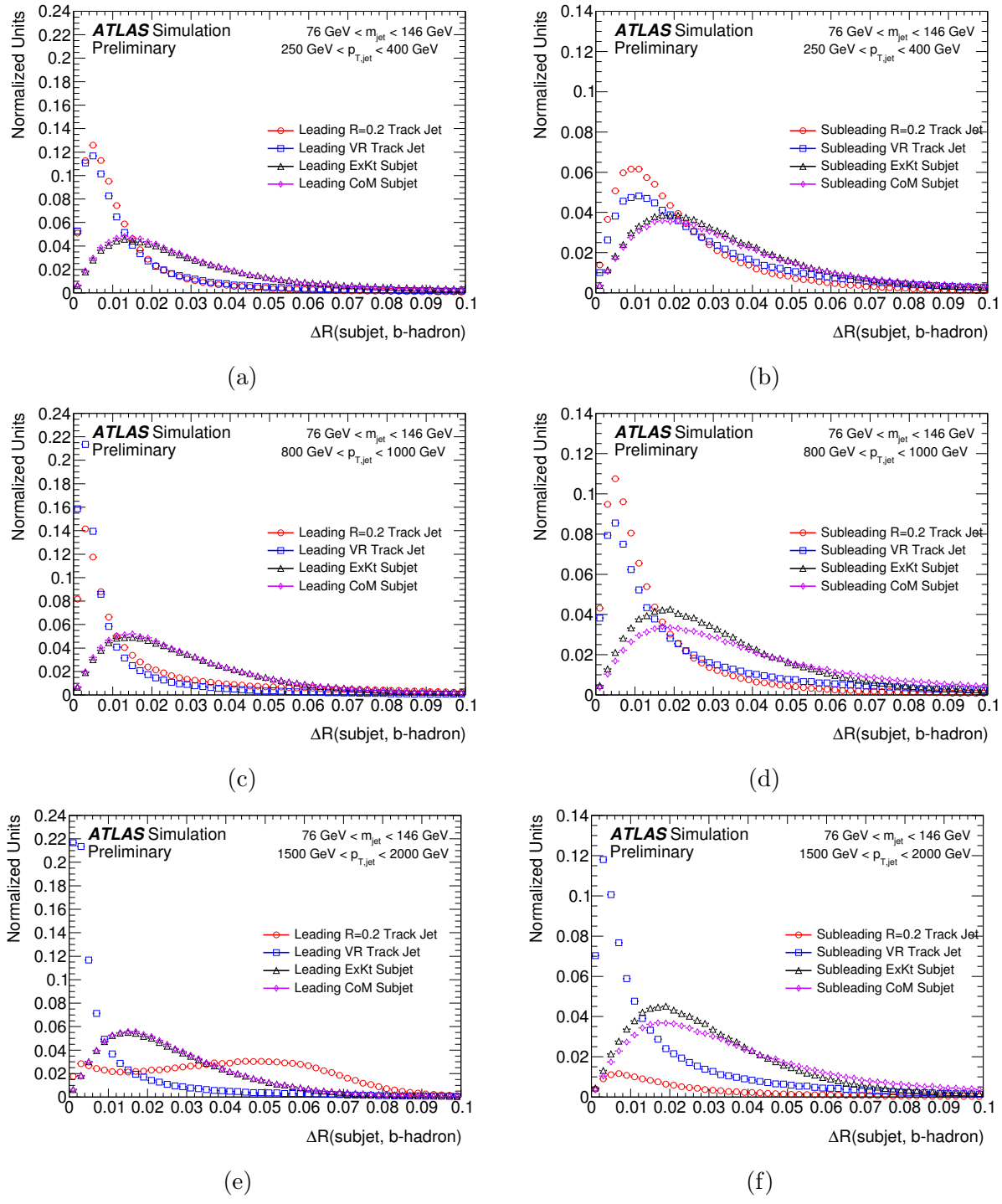

Figure 8.7: ΔR distributions between subjets and matched truth b-hadrons for three different Higgs jet p_{T} bins. The highest p_{T} subjets are on the left and the second highest p_{T} subjets are on the right. The error bars include statistical uncertainties only. Figures produced by the author and published in Reference [4].

The most direct performance comparison metric between the different subjet reconstruc-

tion algorithms which does not require b-tagging is the efficiency for a Higgs jet to have its two highest p_{T} associated subjets matched to truth b-hadrons. This assumes the ideal scenario where b-tagging algorithms are perfect and always be able to identify a reconstructed subjet with a b-hadron, which removes the reconstruction level performance of b-tagging algorithms out of the evaluation of the subjet reconstruction algorithms. This truth-level guided signal efficiency ($\epsilon_{\mathrm{truth}}^{\text{Double subjet } b\text{-label}}$) metric is plotted as a function of Higgs jet p_{T} in Figure 8.8. For Higgs jets with $p_{\mathrm{T}} < 1000$ GeV, all subjet reconstruction algorithm have high truth double b-labelled efficiencies. However, for Higgs jets with $p_{\mathrm{T}} > 1000$ GeV, the efficiency for $R = 0.2$ track jets decreases rapidly, while the other alternative algorithm retain a high efficiency up to 3000 GeV.

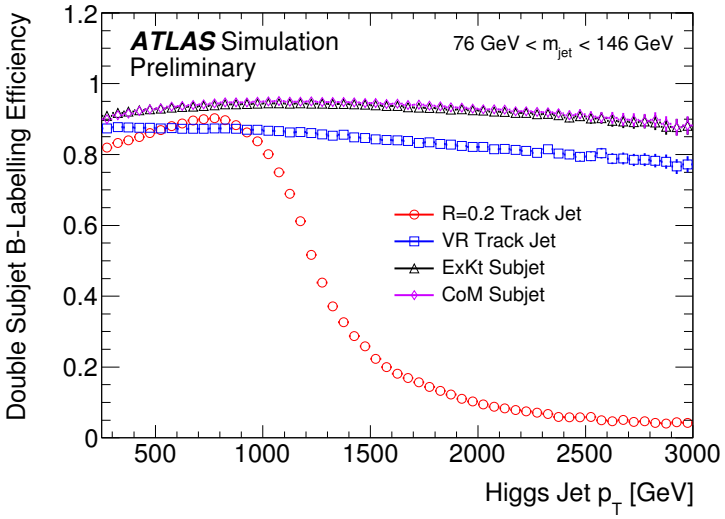

Figure 8.8: The efficiency for a Higgs jet to have its two highest p_{T} associated subjets matched to truth b-hadrons vs Higgs jet p_{T}. The error bars include statistical uncertainties only. Figure produced by the author and published in Reference [4].

8.3.2 Comparisons with b-tagging

Further insights into the performance of these algorithm can be gained by applying MV2c10-based b-tagging instead of truth b-tagging, however it must be stressed that the b-tagging BDT is trained on $R = 0.4$ calorimeter jets, so it will be suboptimal on all subjet algorithms considered here.

Based on the comparison results from Section 8.3.1, it is expected that all subjet reconstruction algorithm will result in similar b-tagging performance for low p_{T} Higgs jets, while the double b-tagging performance with fixed radius track jet algorithm should degrade significantly more than that of the alternative algorithms for high p_{T} Higgs jets. This can be seen in the receiver operating characteristic (ROC) curves shown in Figures 8.9 and 8.10, which

benchmark the double b-tagging performance of the algorithms by plotting the QCD jet and top jet rejection as a function of Higgs jet efficiency, respectively. The new subjet reconstruction algorithms outperform the standard fixed radius track jet algorithm; increasingly more at higher p_{T}.

The double b-tagging ROC curve for QCD jets in the p_{T} region 800 GeV $< p_{\mathrm{T}} <$ 1000 GeV confirms that in this region $R = 0.2$ track jets largely outperform VR track jets. However, in the 800 GeV $< p_{\mathrm{T}} <$ 1000 GeV region, $R = 0.2$ track jets outperform exclusive-k_t subjets. In this p_{T} region, the two b-hadrons from Higgs boson decays start to get closer. This makes it more difficult for a ΔR based track-to-jet matching in the laboratory frame, which happens to VR track jets and ExKt subjets. With the advantage of the track-to-jet association in the CoM frame of the Higgs boson, where the two b-hadrons are back to back, the performance of the CoM algorithm is better than that of the fixed radius track jet algorithm and also the other two new algorithms.

It is expected that the track-based subjets (fixed radius and VR) to reconstruct the b-hadron axes better than the ExKt and CoM subjets as they are shown to be more aligned with the truth b-hadrons axes, as shown in Figure 8.7. This should result in an improvement in the performance of the MV2c10 b-tagging algorithm on account of improved track-to-subjet association as well as determination of lower level b-tagging algorithms, such as JetFitter and IP3D, which depend on the subjet axis direction. However, because the tracks used by the b-tagging algorithms are collected within a radius around each jet axis which is greater than or equal to 0.239, this improvement in reconstruction will not lead to an improved association and an improved b-tagging discriminant reconstruction. In fact, when considering the performance of the various subjet reconstruction algorithms using reconstruction-level b-tagging as in Figures 8.9 or 8.10, CoM subjets are found to perform better than VR track jets indicating that this improvement in angular resolution is smaller than the level at which the angular resolution of the fixed radius track jets are sensitive to.

The single b-tagging performance of the algorithms is benchmarked for QCD and top jet backgrounds in Figures 8.11 and 8.12, respectively. Since all algorithms are typically able to reconstruct at least one subjet, the single b-tagging performance of the algorithms are quite similar, though the new subjet reconstruction algorithms do start to show an improvement over the fixed radius track jet algorithm for Higgs jets with high p_{T}.

Another useful way to represent the information in the ROC curves is to pick a fixed Higgs jet efficiency and plot the QCD and top jet rejection as a function of p_{T}. The signal efficiency is fixed by varying the selection on MV2c10 discriminant for the subjets dynamically as a function of the large-R jet p_{T}. Evaluating the QCD and top jet rejection for a fixed Higgs jet efficiency of 50% from the ROC curve data results in Figure 8.13. In comparing Figures 8.13a

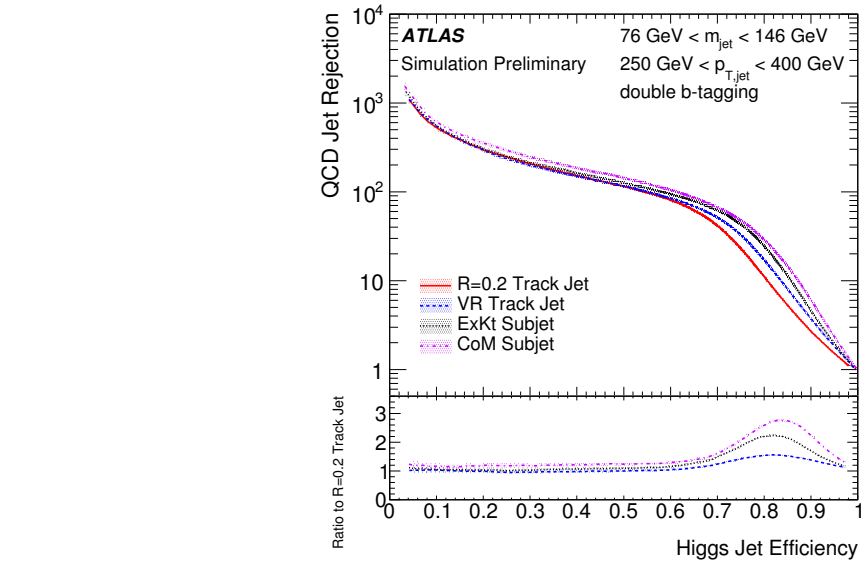

(a)

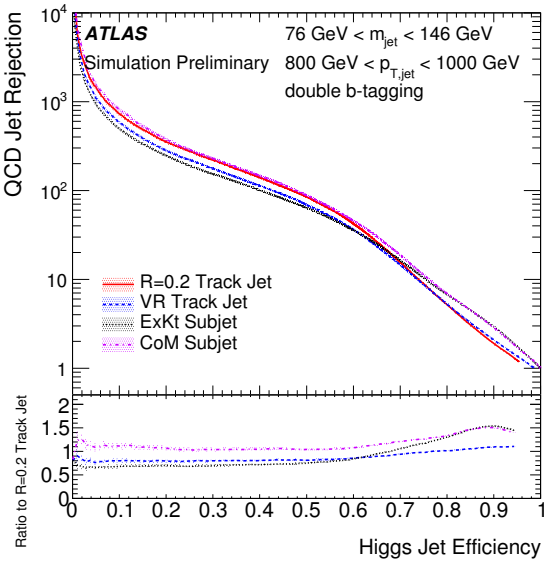

(b)

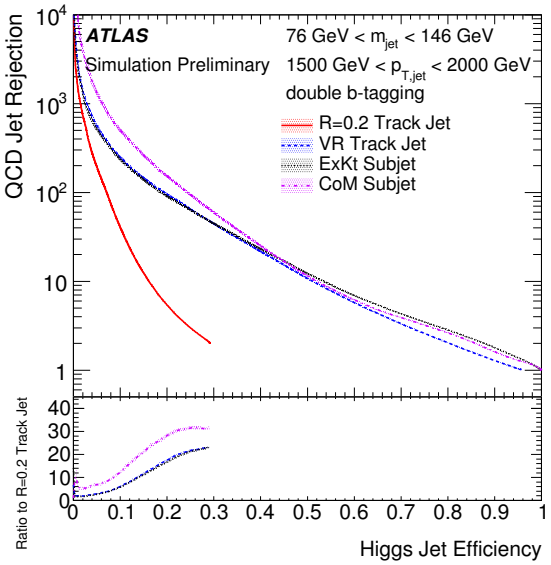

(c)

Figure 8.9: QCD jet rejection as function of $h \to b\bar{b}$ jet efficiency when applying double b-tagging on subjets found by the $R = 0.2$ track jet, VR track jet, ExKt subjet, and CoM subjet reconstruction in different p_T regions. The error bars include statistical uncertainties only. Figures produced by a collaborator and published in Reference [4].

and 8.13c in the case of QCD jets, the performance of double b-tagging is improved when using the alternative subjet reconstruction algorithms. However, at high p_{T} (> 1500 GeV) it is preferable to apply a single b-tagging selection as this allows for a tighter selection of MV2c10 on either of the two highest p_{T} subjets, the reconstruction of which has itself been improved by the alternative subjet finding algorithms as examined in Section 8.3.1. However, in the case of background top jets, applying a double b-tagging selection is better than single b-tagging.

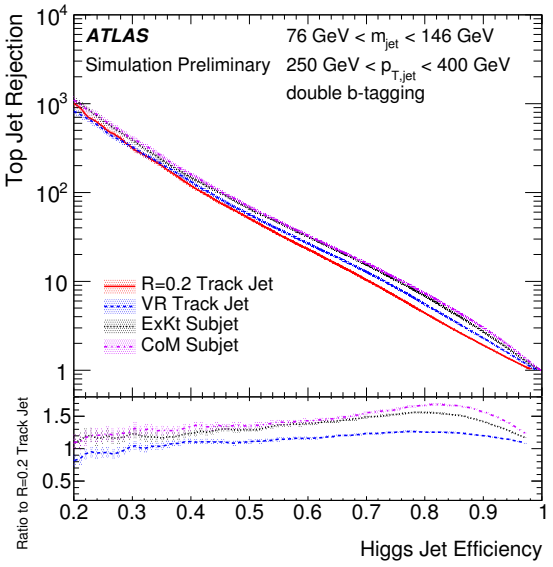

(a)

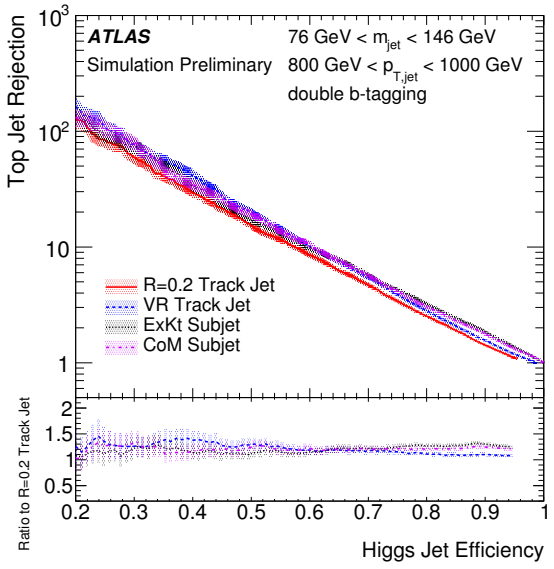

(b)

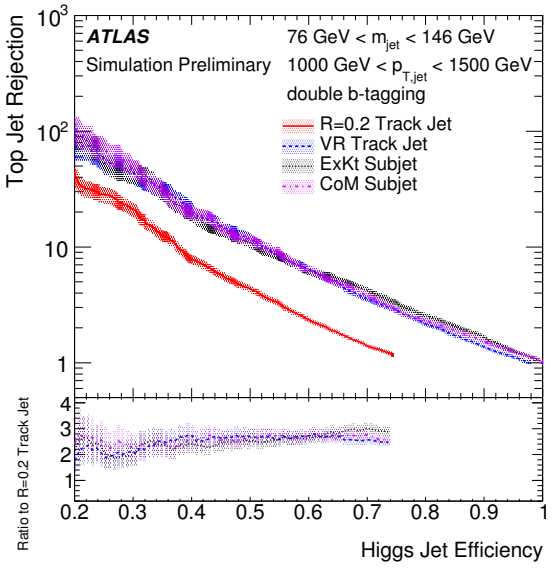

(c)

Figure 8.10: Top jet rejection as function of $h \to b\bar{b}$ jet efficiency when applying double b-tagging on subjets found by the $R = 0.2$ track jet, VR track jet, ExKt subjet, and CoM subjet reconstruction in different p_{T} regions. The error bars include statistical uncertainties only. Figures produced by a collaborator and published in Reference [4].

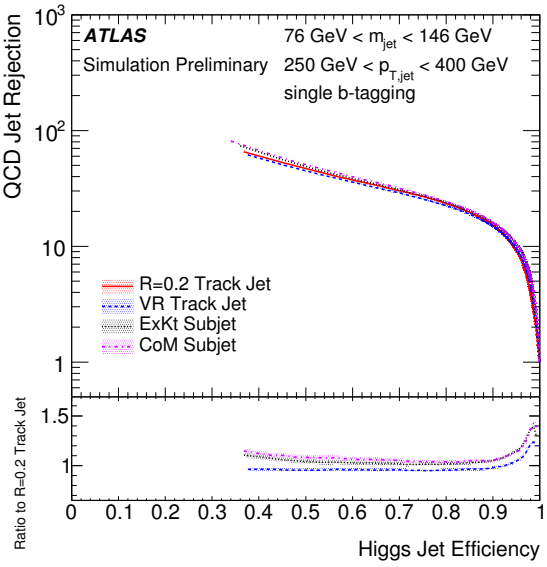

(a)

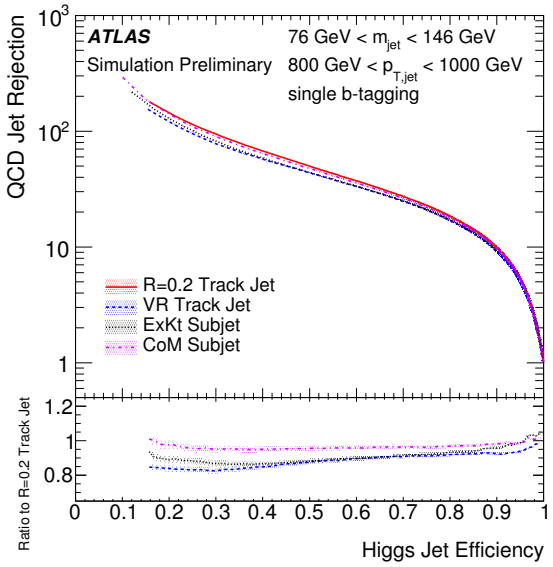

(b)

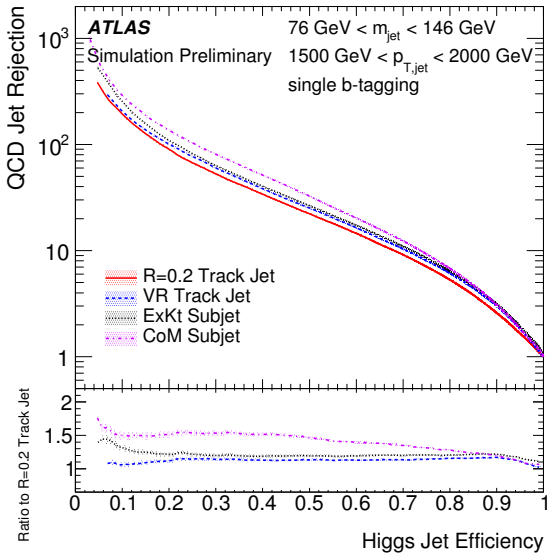

(c)

Figure 8.11: QCD jet rejection as function of $h \to b\bar{b}$ jet efficiency when applying single b-tagging on subjets found by the $R = 0.2$ track jet, VR track jet, ExKt subjet, and CoM subjet reconstruction in different large-R jet p_{T} regions. The error bars include statistical uncertainties only. Figures produced by a collaborator and published in Reference [4].

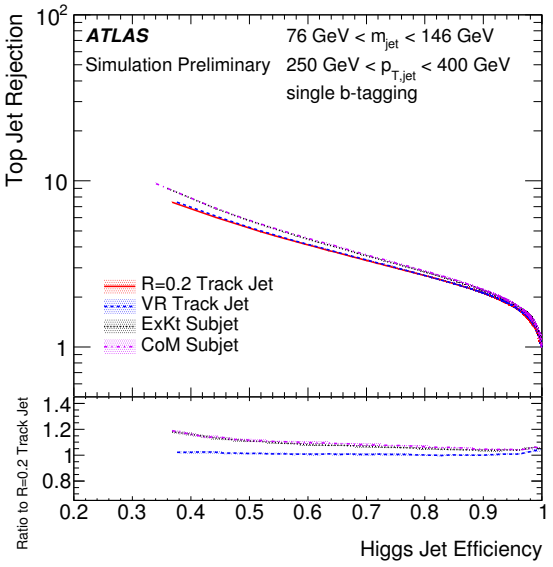

(a)

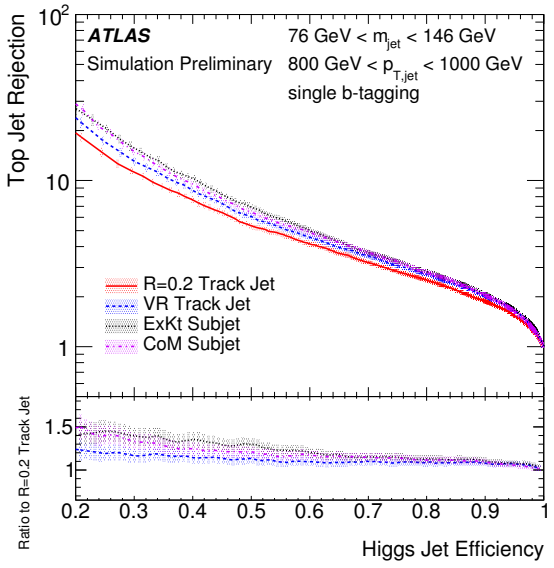

(b)

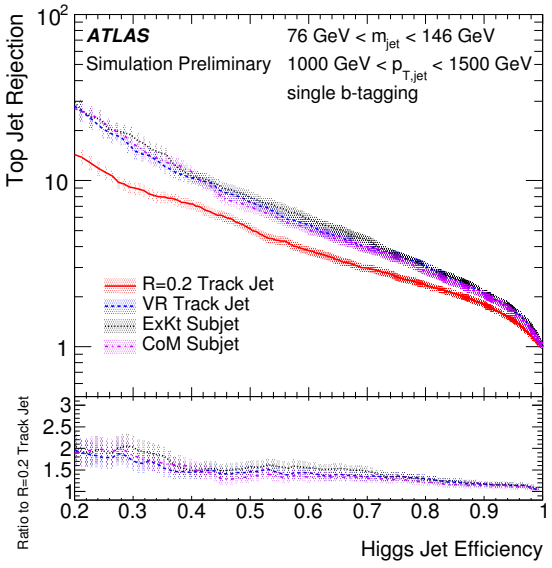

(c)

Figure 8.12: Top jet rejection as function of $h \to b\bar{b}$ jet efficiency when applying single b-tagging on subjets found by the $R = 0.2$ track jet, VR track jet, ExKt subjet, and CoM subjet reconstruction in different large-R jet p_{T} regions. The error bars include statistical uncertainties only. Figures produced by a collaborator and published in Reference [4].

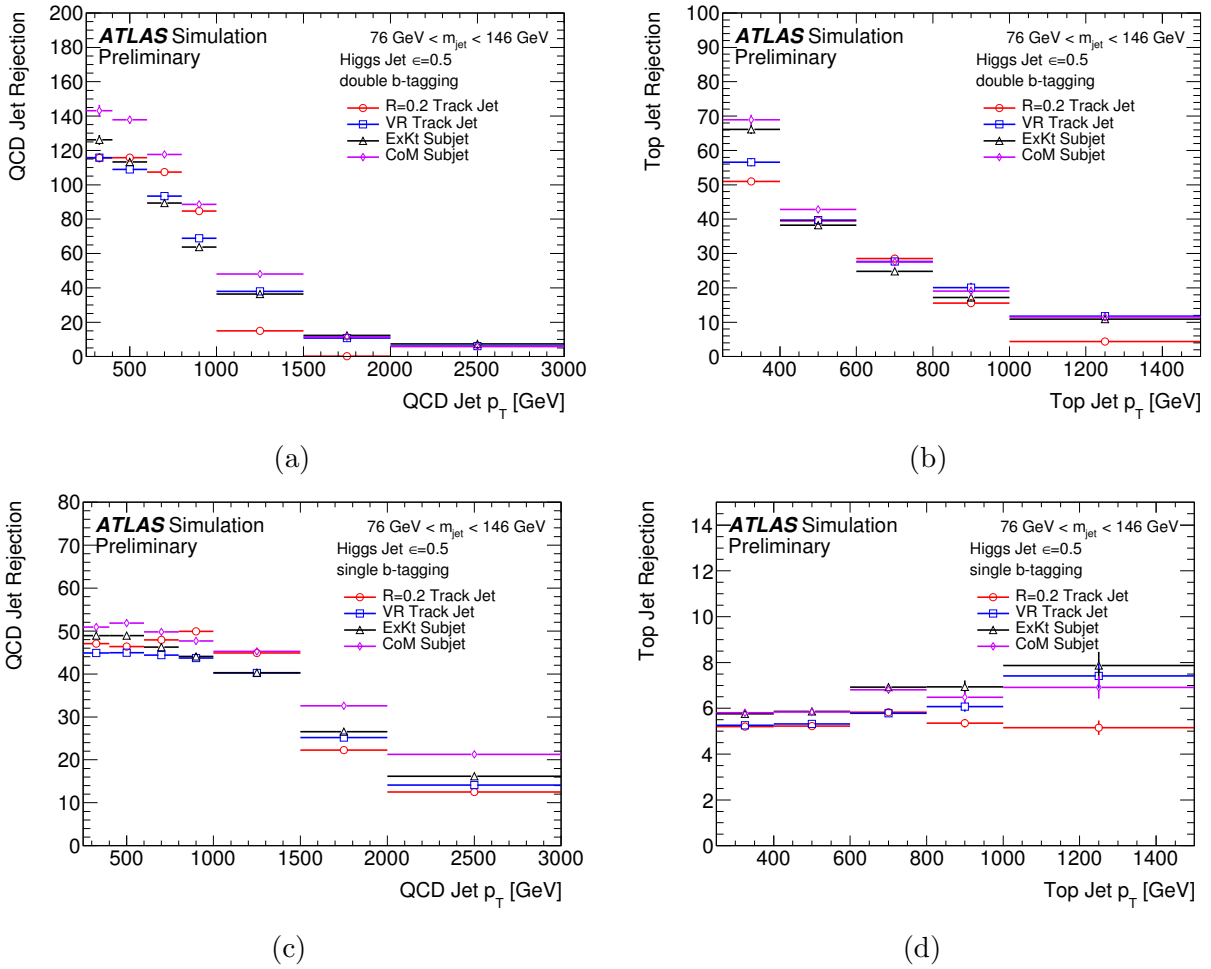

Figure 8.13: QCD (left) and top jet (right) double and single b-tagging rejection as a function of large-R jet p_{T} for a fixed Higgs jet efficiency of 50%. Upper plots show the double b-tagging rejection and the bottom plots show the single b-tagging rejection. The error bars include statistical uncertainties only. Figures produced by a collaborator and published in Reference [4].

Chapter 9

Conclusions

This thesis presented a search for resonant Higgs boson pair production using 36.1 fb^{-1} of $\sqrt{s} = 13$ TeV pp collision data recorded in 2015 and 2016 with the ATLAS detector at the LHC. The search analysis is conducted in the $b\bar{b}WW^*$ decay mode, which has the second highest branching ratio of all decay modes, and with the semi-leptonic final state consisting of a lepton, multiple jets and missing transverse momentum. The search focuses on "boosted" topology, for resonances with masses above 1000 GeV. In this kinematic region, the signal selection efficiency is improved through the use of large-R jets to reconstruct the boosted $h \to b\bar{b}$ decay. The large-R jets are identified to be consistent with $b\bar{b}$ decays by b-tagging fixed-radius track subjets within the large-R jets.

The observed data are compatible with the SM background expectation and no significant excesses of data events are observed. Upper limits on resonant Higgs boson pair production at 95% confidence level are calculated as a function of resonance mass for the selected benchmark signal models. This is the first result by the ATLAS collaboration on the search for TeV-scale resonant Higgs boson pair production in the $b\bar{b}WW^*$ decay mode. The work presented in this thesis is intended to assess the level of sensitivity of the $b\bar{b}WW^*$ decay mode by utilising a simple search analysis strategy and lay the groundwork for a more sophisticated strategy with the full ATLAS Run 2 dataset.

As it stands, the current sensitivity is not competitive compared to the ATLAS $b\bar{b}b\bar{b}$ analysis but there are wide ranging potential improvements that can be investigated to enhance the sensitivity. The strategy to reconstruct the hadronic W boson can be revised by considering large-R jets instead of small-R jets, which can improve the resolution of the reconstructed hadronic W boson and the reconstructed di-Higgs system invariant mass; although this strategy comes with the added complication of a reconstructed lepton within the large-R jet that can bias the measurement of the kinematics of the large-R jet. Together with the semi-leptonic final state, the larger branching ratio of the all-hadronic final state and

also the smaller SM background expectation in the fully-leptonic final state could potentially contribute to improvements in the sensitivity of the $b\bar{b}WW^*$ decay mode. In addition to improvements of the analysis strategy, new physics object reconstruction techniques can also lead to gains in sensitivitiy.

Three new subjet reconstruction algorithms, in the context of $h \to b\bar{b}$ identification, have been developed which have been shown to improve upon the baseline fixed-radius track jet algorithm for large-R jets with $p_{\mathrm{T}} > 1000$ GeV. The variable radius track jet, exclusive-k_t subjet, and center-of-mass subjet methods outperform the fixed radius track jet method in this p_{T} region for both double b-tagging and single b-tagging requirement. The CoM algorithm has the best performance among all the algorithms and across all large-R jet p_{T} ranges. The new algorithms improve the ability to identify large-R jets from $h \to b\bar{b}$ decay, which will increase the sensitivity of future searches for high mass resonant Higgs boson pair production; not just in $b\bar{b}WW^*$ decay mode but also the other decay modes such as $b\bar{b}b\bar{b}$.

Appendix A

Data vs total background prediction distributions

This appendix compiles the comparison of the observed data to the predicted total background for selected kinematic distributions in the control regions and the signal region. The kinematic distributions are shown for events in the top control region and in the in the 2-tag mBB control region are:

- The large-R jet $h \to b\bar{b}$ candidate p_{T}, η and ϕ.
- The reconstruted hadronic W boson p_{T}, η, ϕ and invariant mass.
- The reconstruted leptonic W boson p_{T}, η, ϕ and invariant mass.
- The reconstruted WW^* system p_{T}, η, ϕ and invariant mass.

They are shown in Figures A.1-A.4 for the top control region and Figures A.5-A.8 for the 2-tag mBB control region. For events in the 2-tag signal regions, the following kinematic distributions are presented:

- $E_{\mathrm{T}}^{\mathrm{miss}}$ and $m_{\mathrm{T}}^{\mathrm{W}}$
- The large-R jet $h \to b\bar{b}$ candidate p_{T}, η, ϕ and mass.
- The reconstruted hadronic W boson p_{T}, η, ϕ and invariant mass.
- The reconstruted leptonic W boson p_{T}, η, ϕ and invariant mass.
- The reconstruted WW^* system p_{T}, η, ϕ and invariant mass.

They are shown in Figures A.10-A.13.

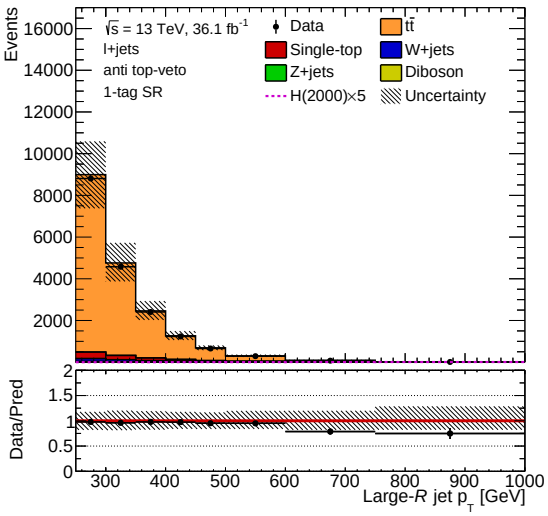

(a)

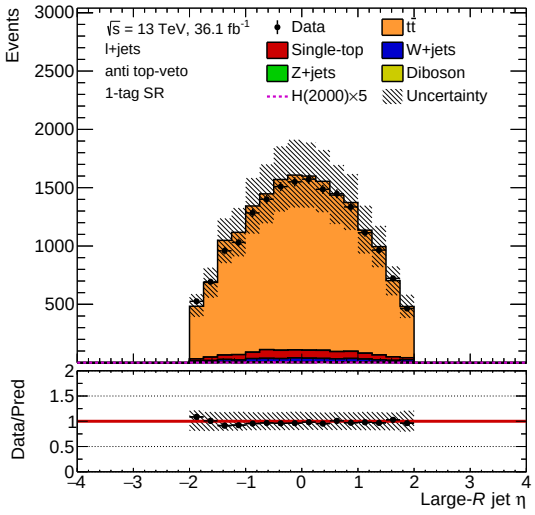

(b)

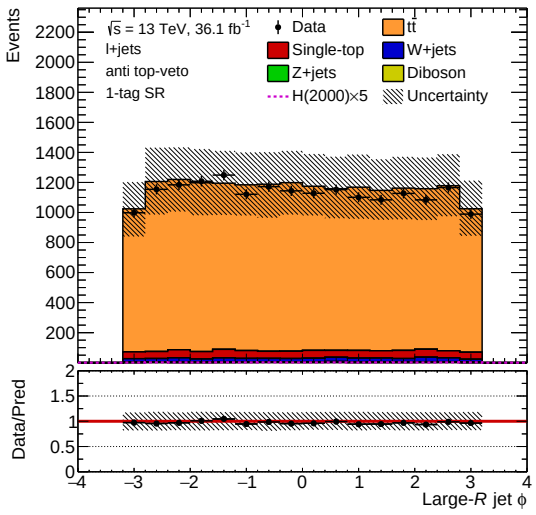

(c)

Figure A.1: Distributions of (a) p_{T}, (b) η and (c) ϕ of the large-R jet $h \to b\bar{b}$ candidate in the top control region of the observed data and the total background prediction. The hashed band represents the overall uncertainty on the total background prediction. The detector modelling and background modelling systematic uncertainties are taken into account in the overall uncertainty.

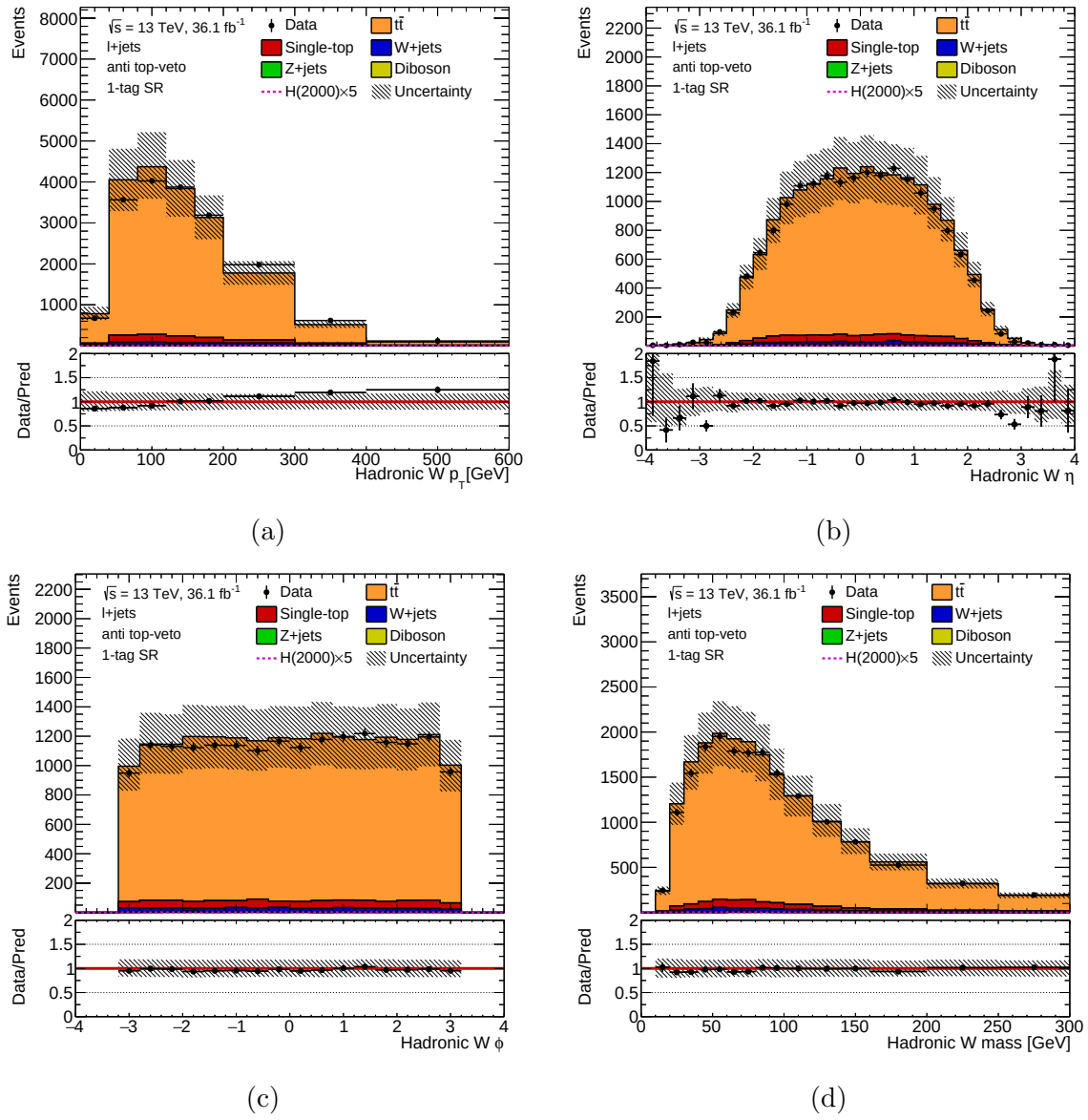

Figure A.2: Distributions of (a) p_{T}, (b) η, (c) ϕ and (d) mass of the reconstructed hadronic W boson in the top control region of the observed data and the total background prediction. The hashed band represents the overall uncertainty on the total background prediction. The detector modelling and background modelling systematic uncertainties are taken into account in the overall uncertainty.

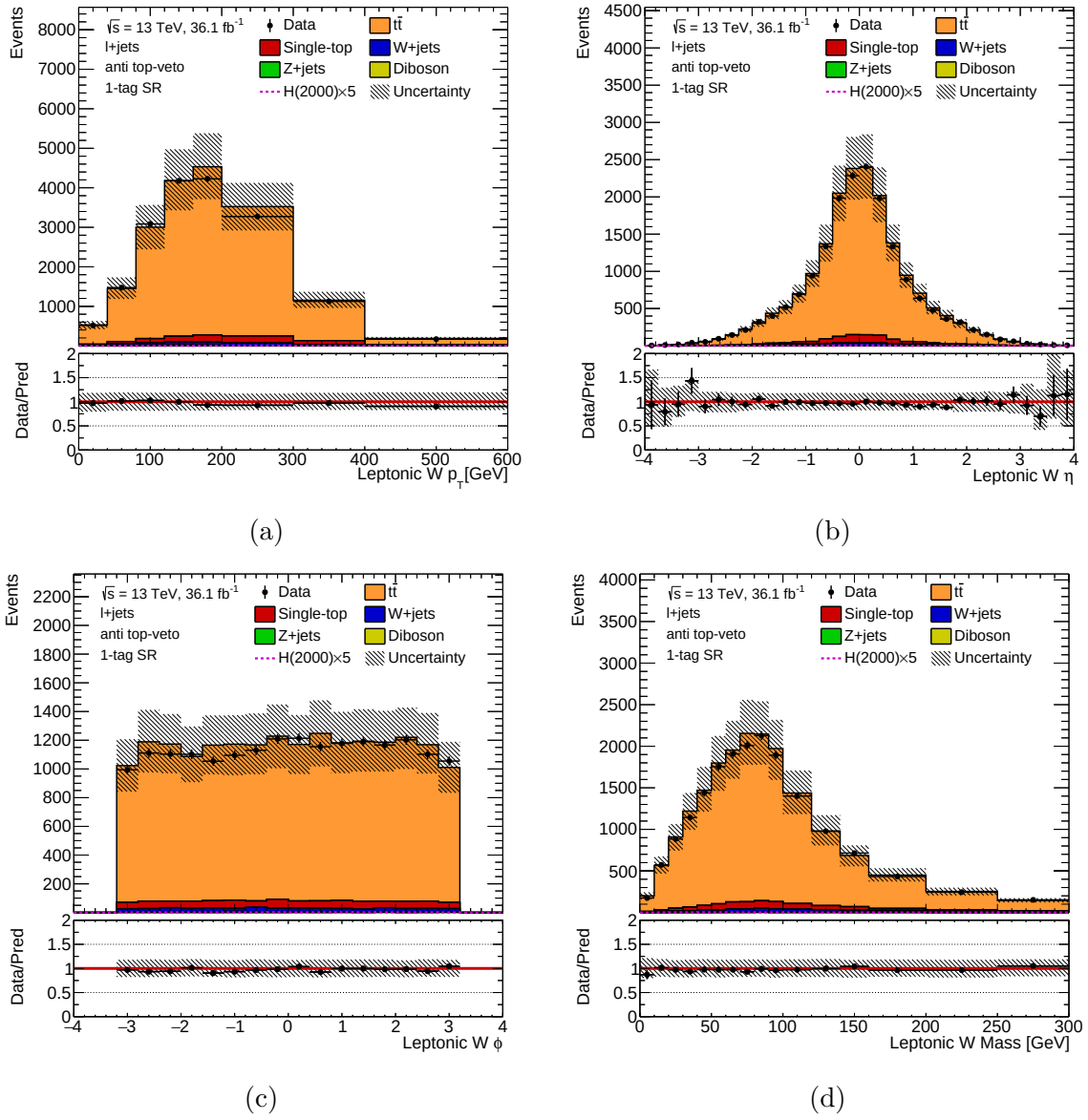

(a) (b)

(c) (d)

Figure A.3: Distributions of (a) p_{T}, (b) η, (c) ϕ and (d) mass of the reconstructed leptonic W boson in the top control region of the observed data and total the background prediction. The hashed band represents the overall uncertainty on the total background prediction. The detector modelling and background modelling systematic uncertainties are taken into account in the overall uncertainty.

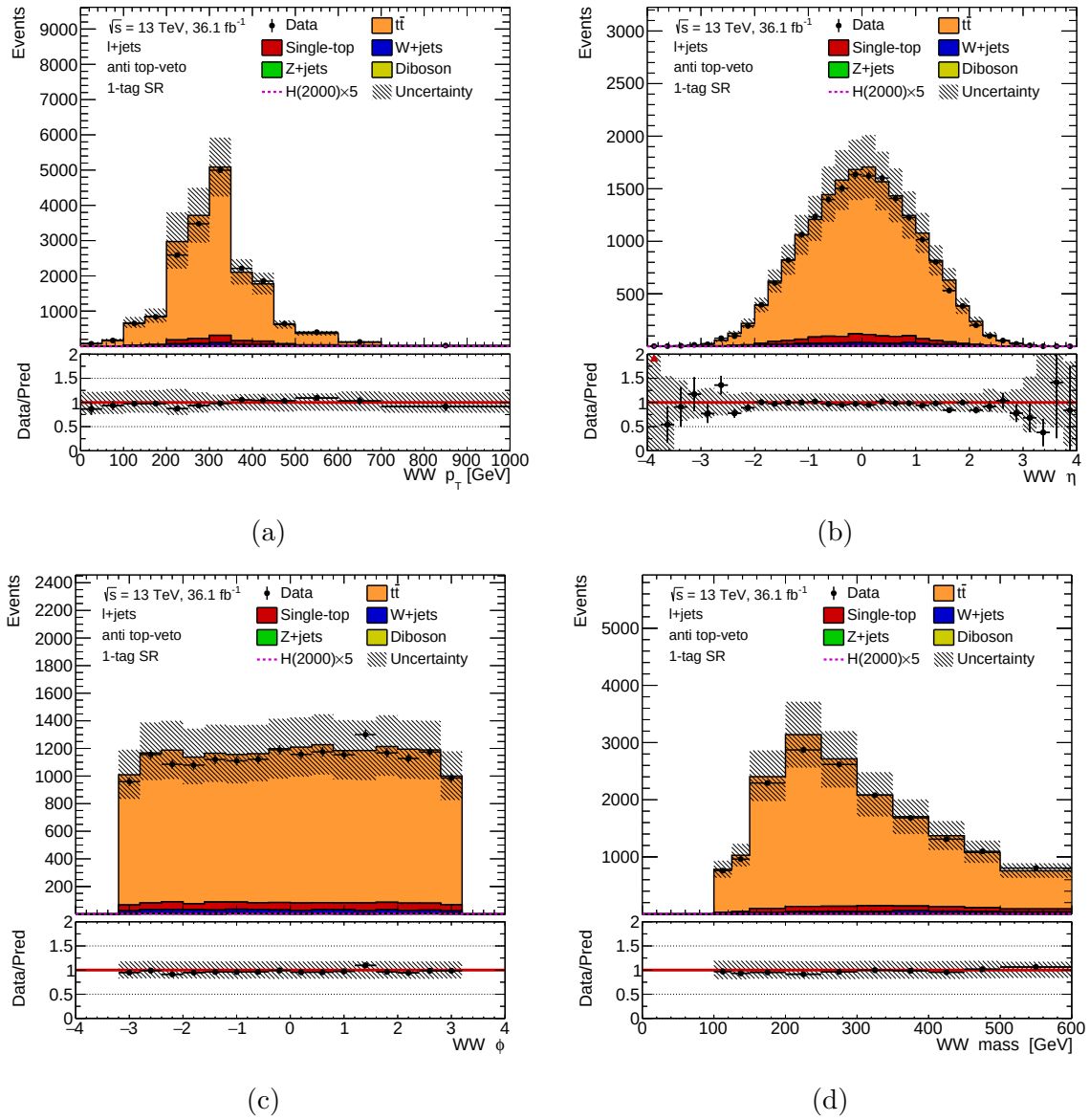

(a) (b)

(c) (d)

Figure A.4: Distributions of (a) p_{T}, (b) η, (c) ϕ and (d) mass of the reconstructed WW^* system in the top control region of the observed data and the total background prediction. The hashed band represents the overall uncertainty on the total background prediction. The detector modelling and background modelling systematic uncertainties are taken into account in the overall uncertainty.

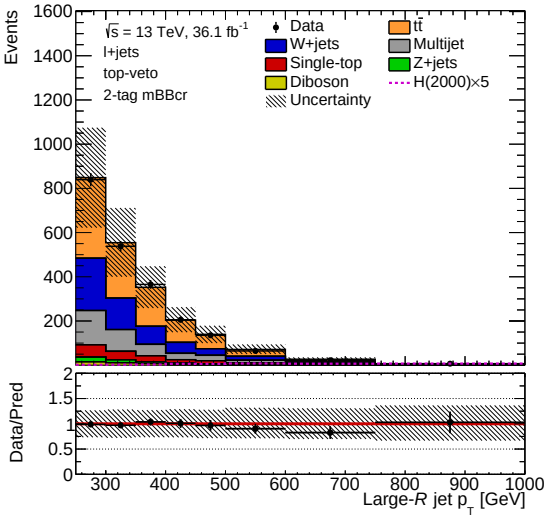

(a)

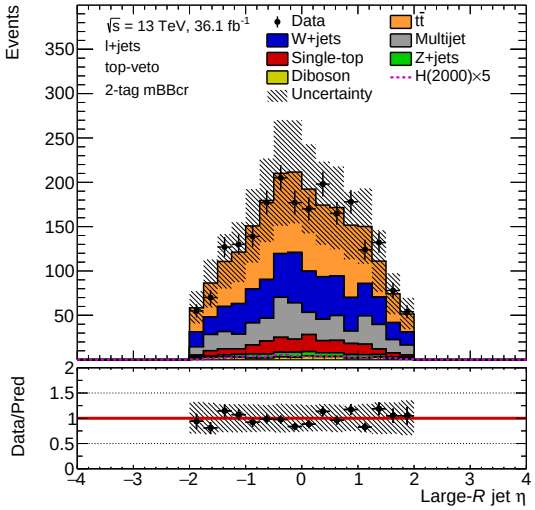

(b)

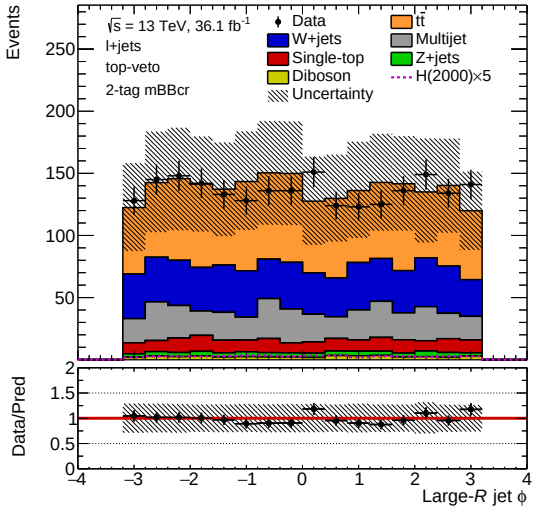

(c)

Figure A.5: Distributions of (a) p_{T}, (b) η and (c) ϕ of the large-R jet $h \to b\bar{b}$ candidate in the 2-tag mBB control region of the observed data and the total background prediction. The hashed band represents the overall uncertainty on the total background prediction. The detector modelling and background modelling systematic uncertainties are taken into account in the overall uncertainty.

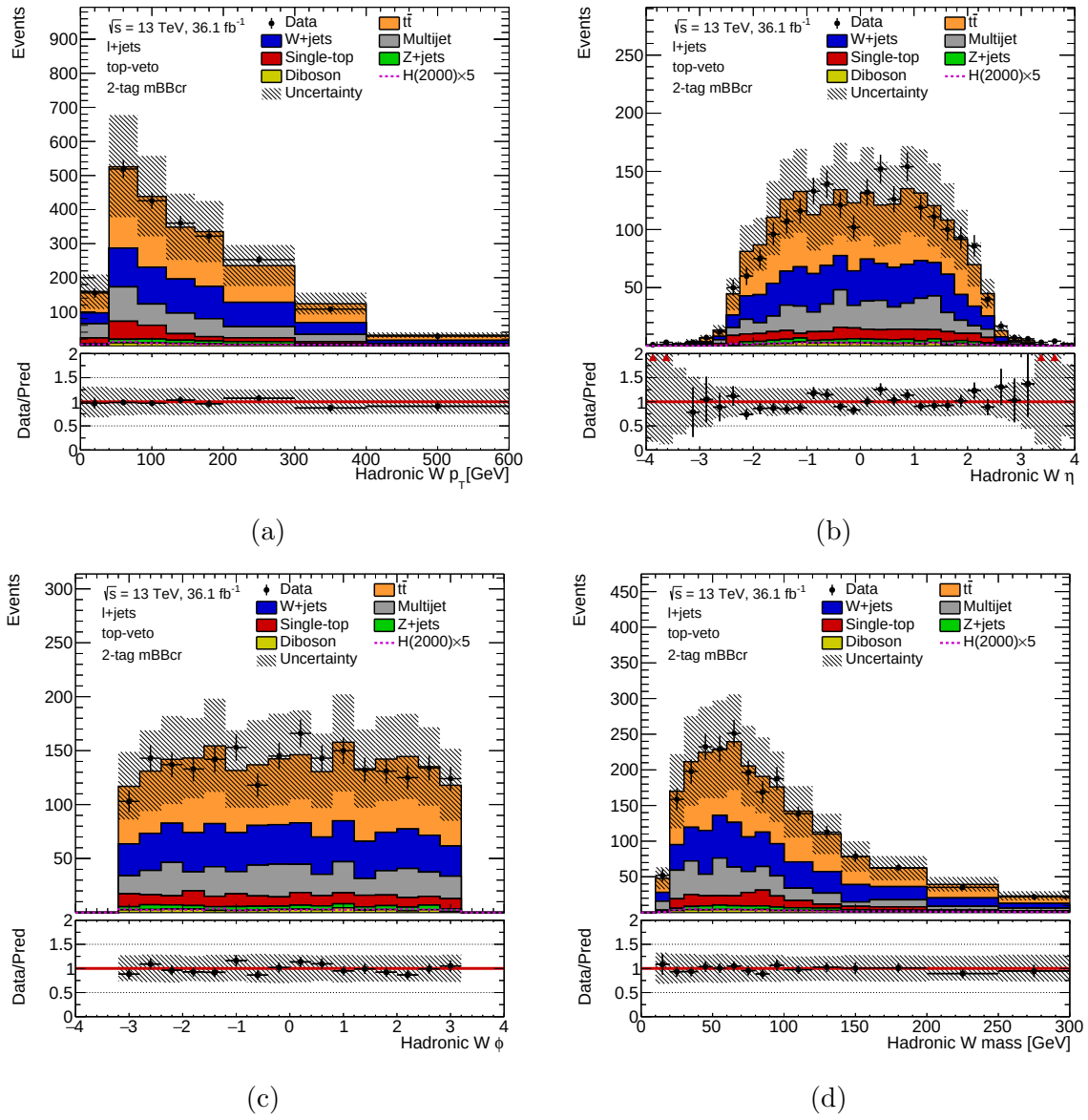

Figure A.6: Distributions of (a) p_{T}, (b) η, (c) ϕ and (d) mass of the reconstructed hadronic W boson in the 2-tag mBB control region of the observed data and the total background prediction. The hashed band represents the overall uncertainty on the total background prediction. The detector modelling and background modelling systematic uncertainties are taken into account in the overall uncertainty.

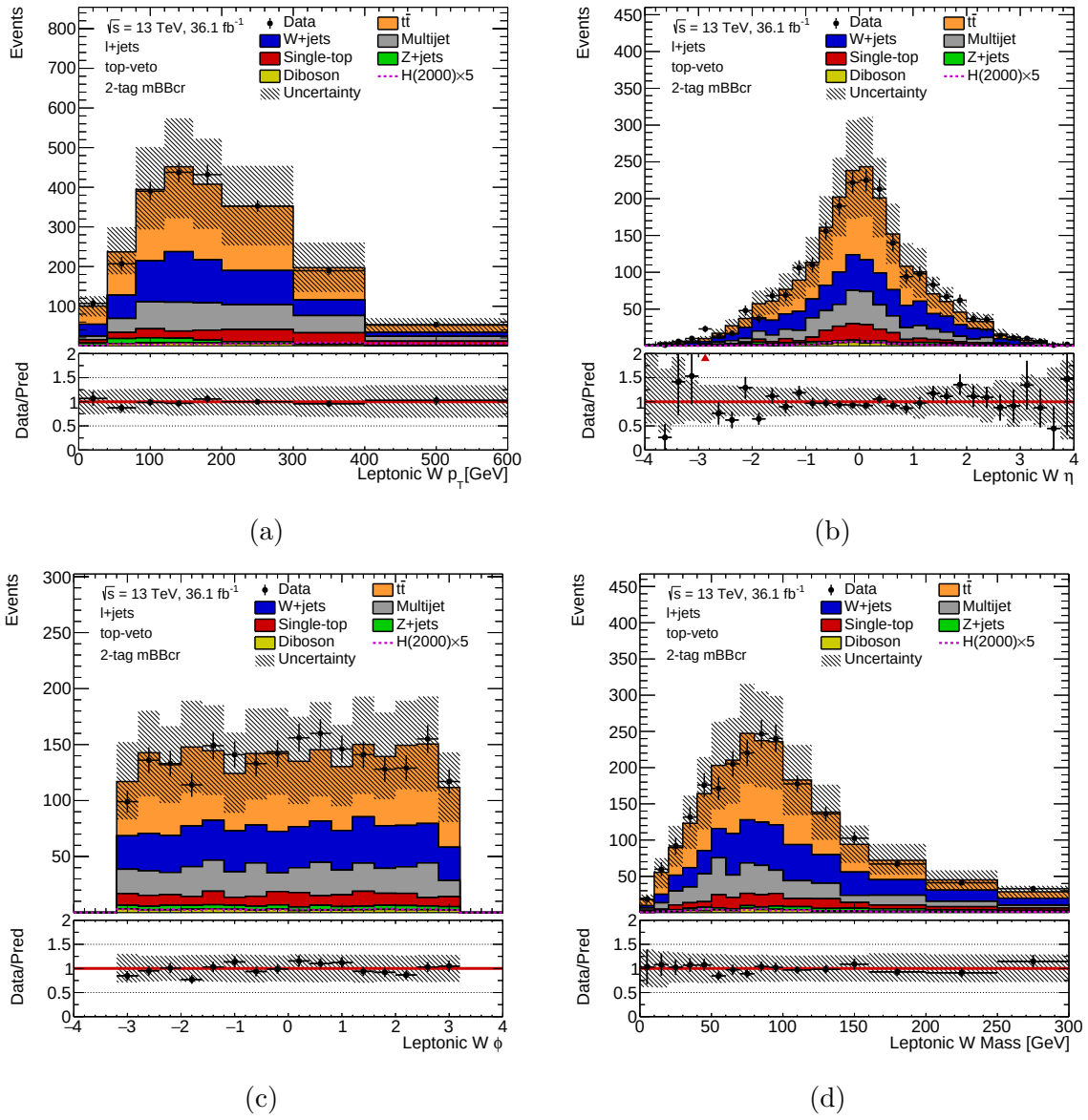

(a) (b)

(c) (d)

Figure A.7: Distributions of (a) p_{T}, (b) η, (c) ϕ and (d) mass of the reconstructed leptonic W boson in the 2-tag mBB control region of the observed data and the total background prediction. The hashed band represents the overall uncertainty on the total background prediction. The detector modelling and background modelling systematic uncertainties are taken into account in the overall uncertainty.

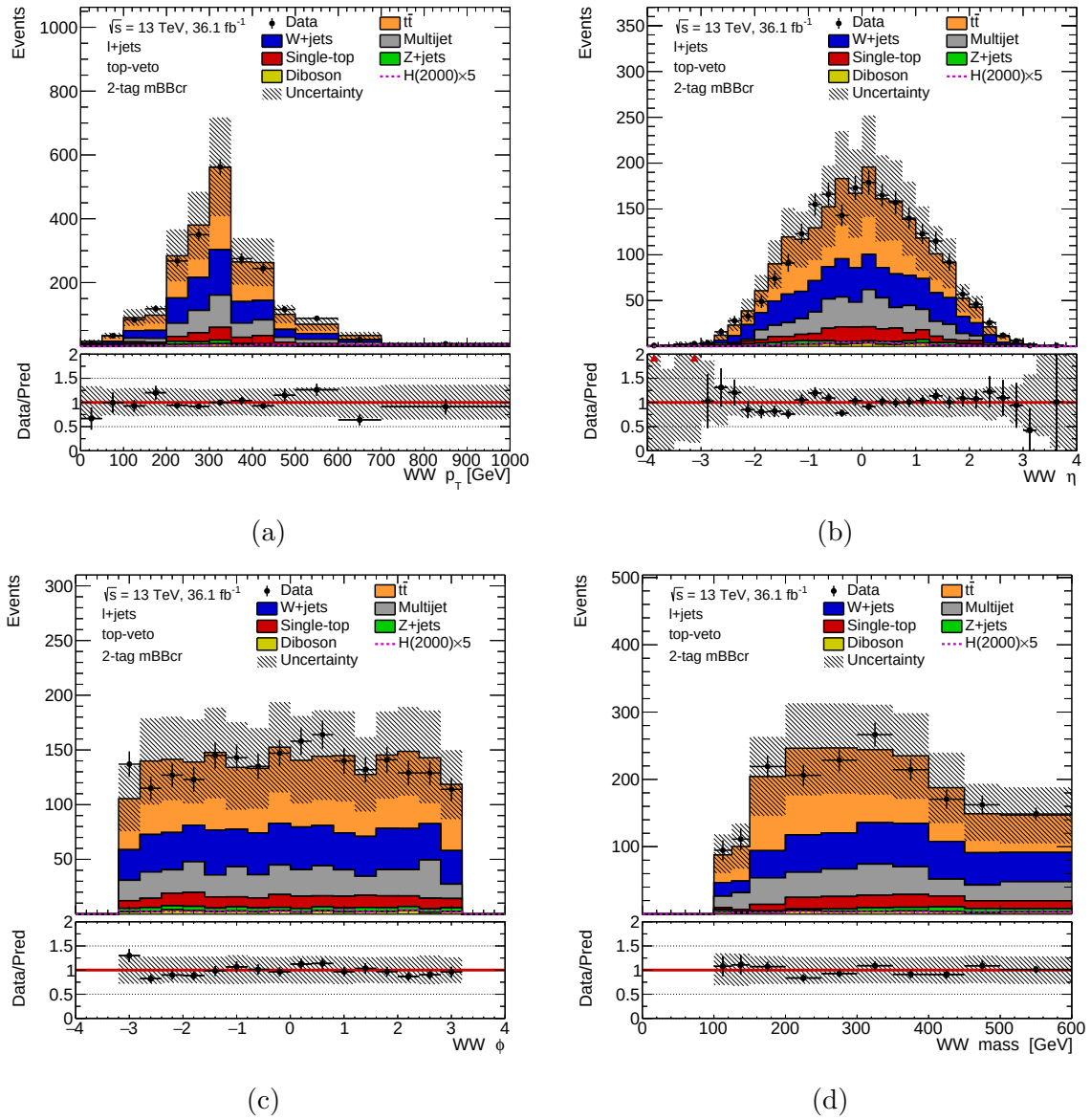

Figure A.8: Distributions of (a) p_{T}, (b) η, (c) ϕ and (d) mass of the reconstructed WW^* system in the 2-tag mBB control region of the observed data and the total background prediction. The hashed band represents the overall uncertainty on the total background prediction. The detector modelling and background modelling systematic uncertainties are taken into account in the overall uncertainty.

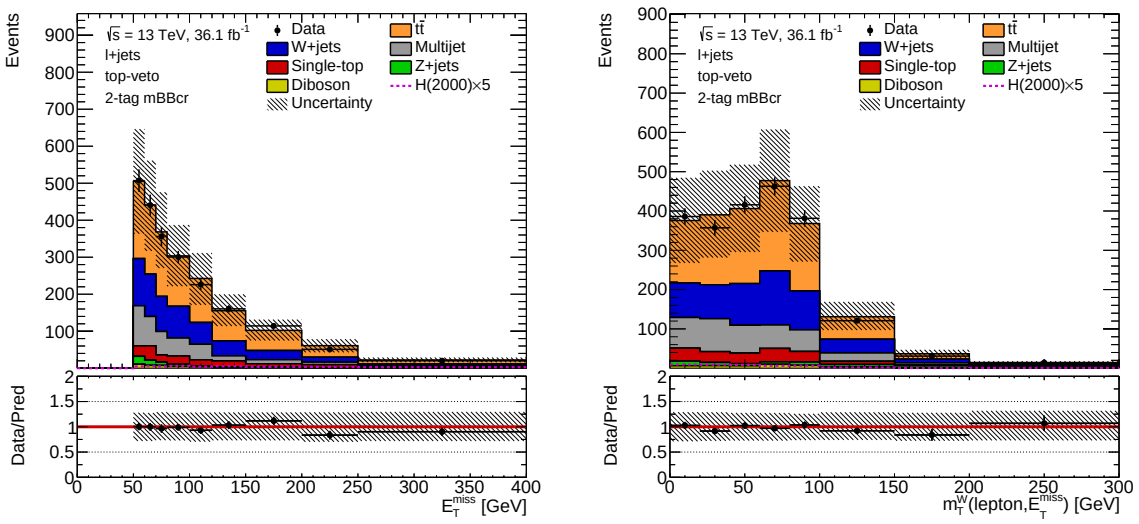

(a) (b)

Figure A.9: Distributions of (a) $E_{\mathrm{T}}^{\mathrm{miss}}$ and (b) $m_{\mathrm{T}}^{\mathrm{W}}$ and in the 2-tag signal region of the observed data and the total background prediction. The hashed band represents the overall uncertainty on the total background prediction. The detector modelling and background modelling systematic uncertainties are taken into account in the overall uncertainty.

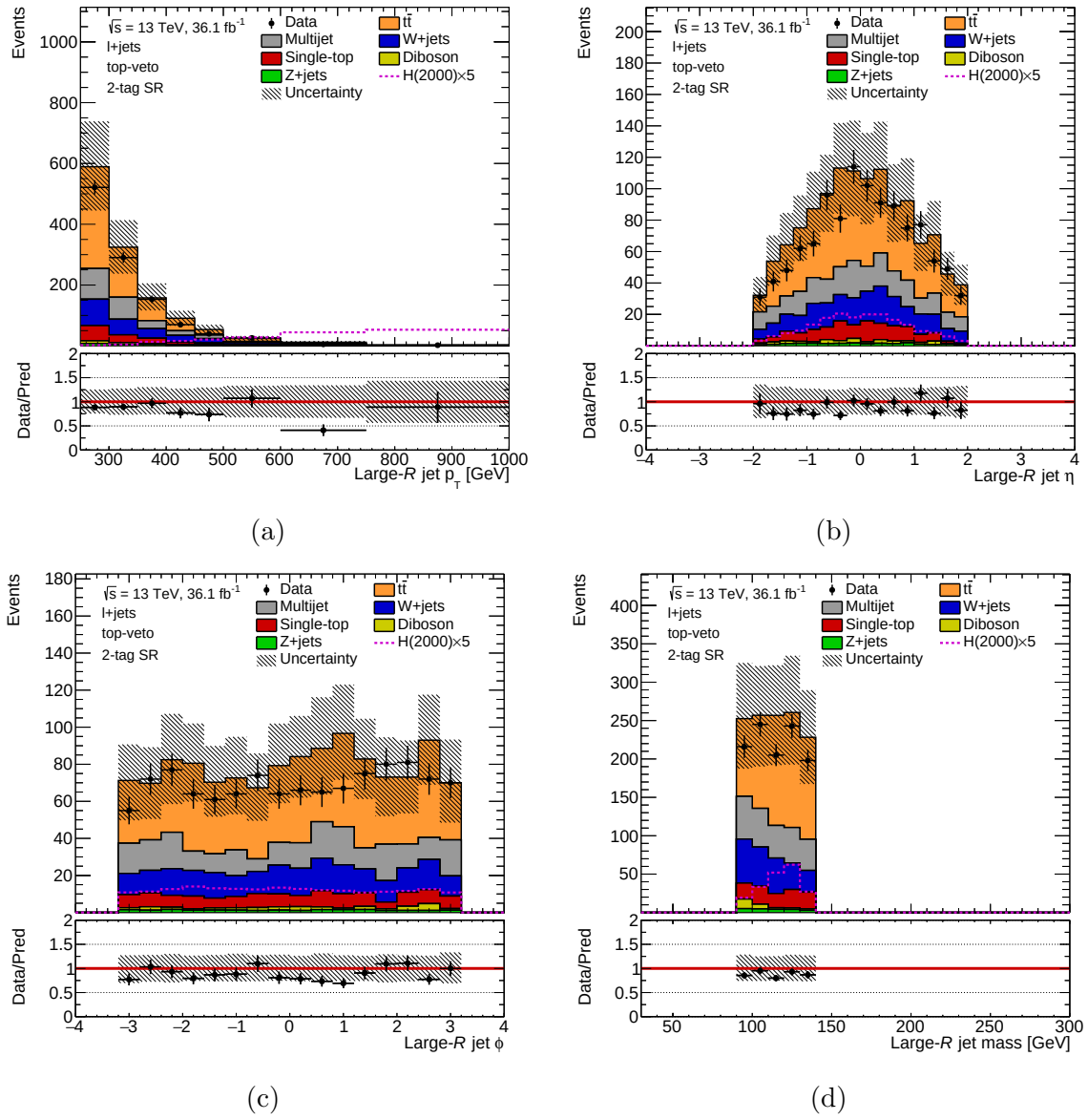

(a) (b)

(c) (d)

Figure A.10: Distributions of (a) p_{T}, (b) η, (c) ϕ, and mass of the large-R jet $h \to b\bar{b}$ candidate in the 2-tag signal region of the observed data and the total background prediction. The hashed band represents the overall uncertainty on the total background prediction. The detector modelling and background modelling systematic uncertainties are taken into account in the overall uncertainty.

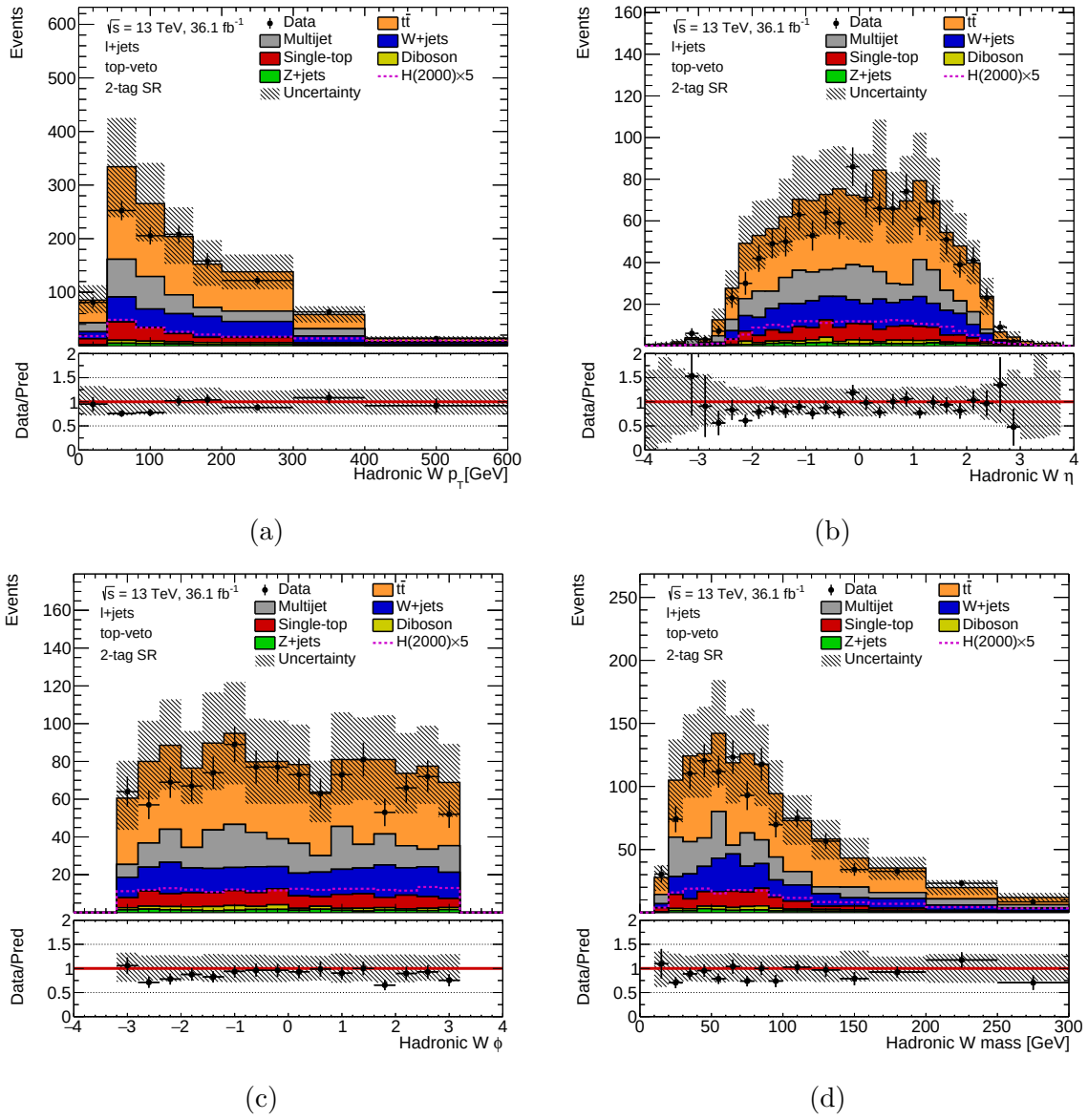

Figure A.11: Distributions of (a) p_{T}, (b) η, (c) ϕ and (d) mass of the reconstructed hadronic W boson in the 2-tag signal region of the observed data and the total background prediction. The hashed band represents the overall uncertainty on the total background prediction. The detector modelling and background modelling systematic uncertainties are taken into account in the overall uncertainty.

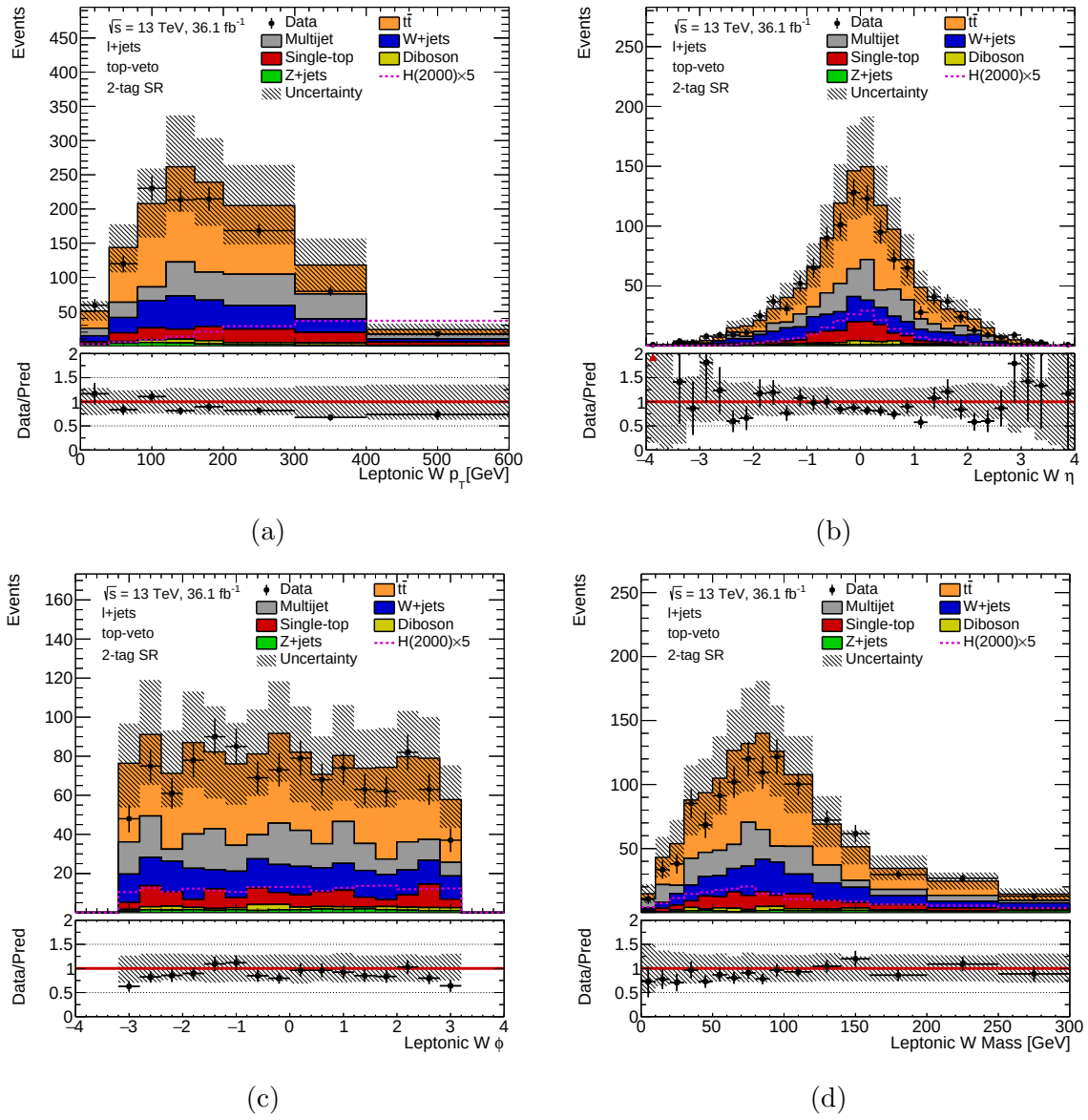

Figure A.12: Distributions of (a) p_{T}, (b) η, (c) ϕ and (d) mass of the reconstructed leptonic W boson in the 2-tag signal region of the observed data and the total background prediction. The hashed band represents the overall uncertainty on the total background prediction. The detector modelling and background modelling systematic uncertainties are taken into account in the overall uncertainty.

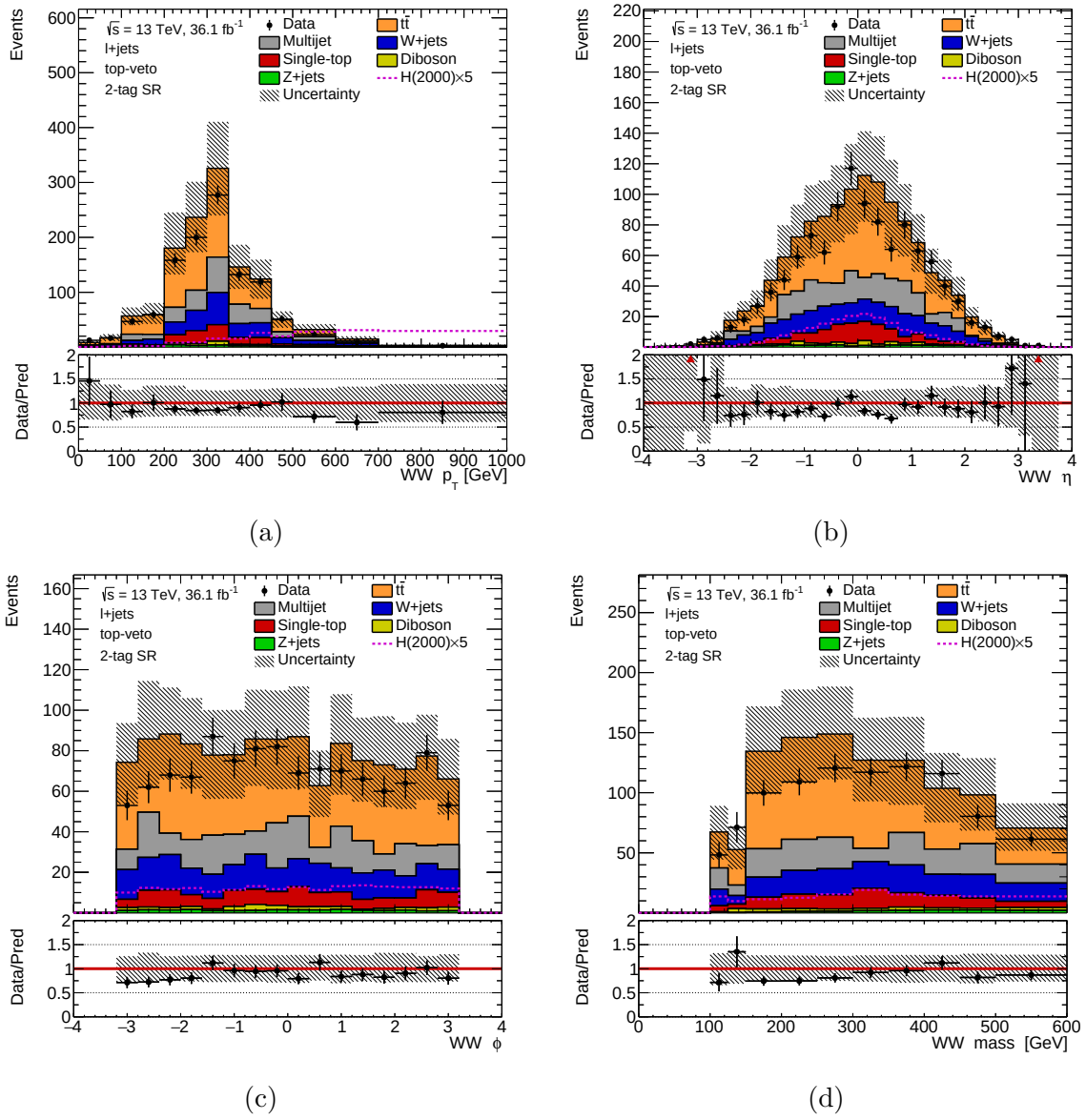

Figure A.13: Distributions of (a) p_{T}, (b) η, (c) ϕ and (d) mass of the reconstructed WW^* system in the 2-tag signal region of the observed data and the total background prediction. The hashed band represents the overall uncertainty on the total background prediction. The detector modelling and background modelling systematic uncertainties are taken into account in the overall uncertainty.

Appendix B

Graviton signal interpolation

For each of the RS graviton signal model, there are 4 mass points with generated MC samples. The mass spacing, which is significantly broader than the m_{hh} distribution of potential graviton signals could lead to an artificial loss of sensitivity for those resonances with masses between the generated mass points. For this reason, a procedure to generate m_{hh} templates to be used in the limit-setting for these intermediate mass points, by the method of signal interpolation, has been developed and is presented in this Appendix. For the m_{hh} templates, the normalisation (Appendix B.1) and shape predictions (Appendix B.2) is needed for each mass point.

B.1 Normalisation interpolation

The normalisation prediction for the intermediate graviton signal mass points is obtained by interpolating the ratio of acceptance between the graviton and the heavy scalar signal samples. The ratio of acceptance as function of resonance mass is fitted with a 3^{rd} order polynominal function ($f(m_{\mathrm{X}})$). Figure B.1 shows the acceptance ratio between the graviton and the heavy scalar signal samples as a function of resonance mass overlaid with the fitted function. The predicted number of events for a graviton signal mass point ($N_{G(X)}$), is calculated as

$$N_{G(X)} = f(m_{\mathrm{X}}) \times A_H \times \sigma_{G(X)} \times \mathcal{L} \tag{B.1}$$

where A_H is the acceptance of the heavy scalar signal MC samples, $\sigma_{G(X)}$ is the cross section of the graviton signal with mass X GeV and $\mathcal{L}$ is the luminosity used in the analysis.

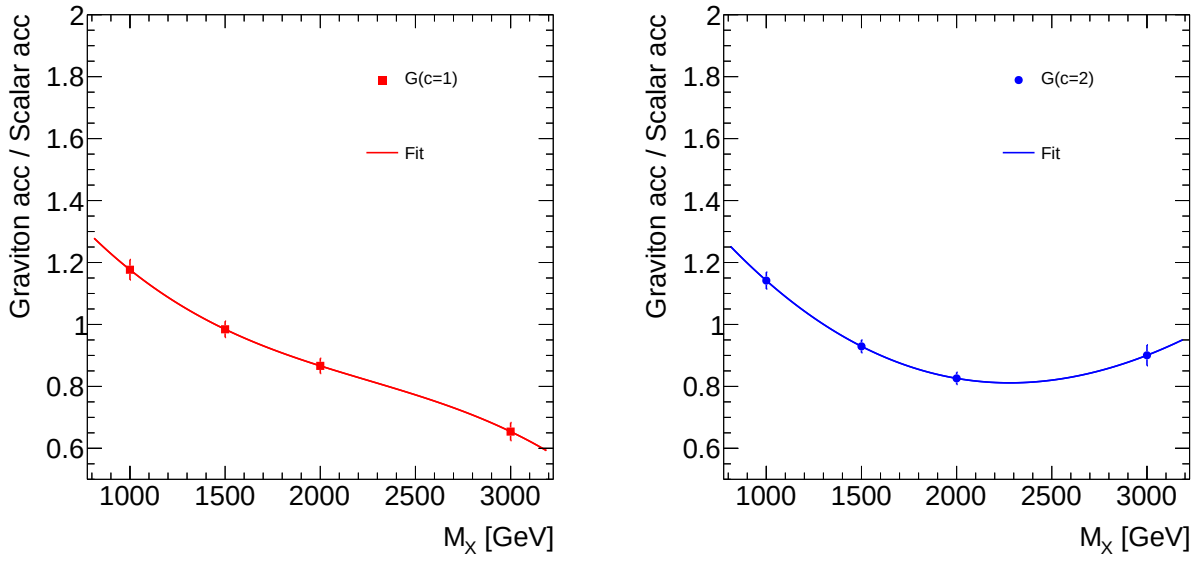

(a) (b)

Figure B.1: Ratio of acceptance between the generated graviton and heavy scalar signal samples as a function of resonance mass, for RS graviton models with parameter (a) c = 1 and (b) c = 2. The error bar represents the statistical uncertainty on the ratio of acceptance from the MC signal samples statistical uncertainty.

B.2 m_{hh} shape interpolation

RS graviton signal m_{hh} distributions for the intermediate masses between those of the MC samples are generated from a functional form by interpolating the parameters of the function between the existing samples. The chosen functional form is a Bukin function [209] because the function reasonably describes the shape of the m_{hh} distribution for all generated graviton signal MC samples, as shown in Figures B.2 and B.3.

The six bukin function parameter values necessary to interpolate the signal m_{hh} distributions are extracted for every mass point and for each RS graviton signal model. The dependence of each parameter on the RS graviton mass is itself parameterised, as shown in Figures B.4 and B.5.

For each intermediate mass point, the six Bukin fit parameters are found by interpolating using the functional forms found in the previous step. Pseudo-data based on these parameter values is then generated with the distribution subsequently scaled to match the expected number of events (Equation B.1). Comparisons of the pseudo-data distributions to those from MC are shown in Figures B.6 and B.7. Good agreement is observed across all mass points for all RS graviton signal models.

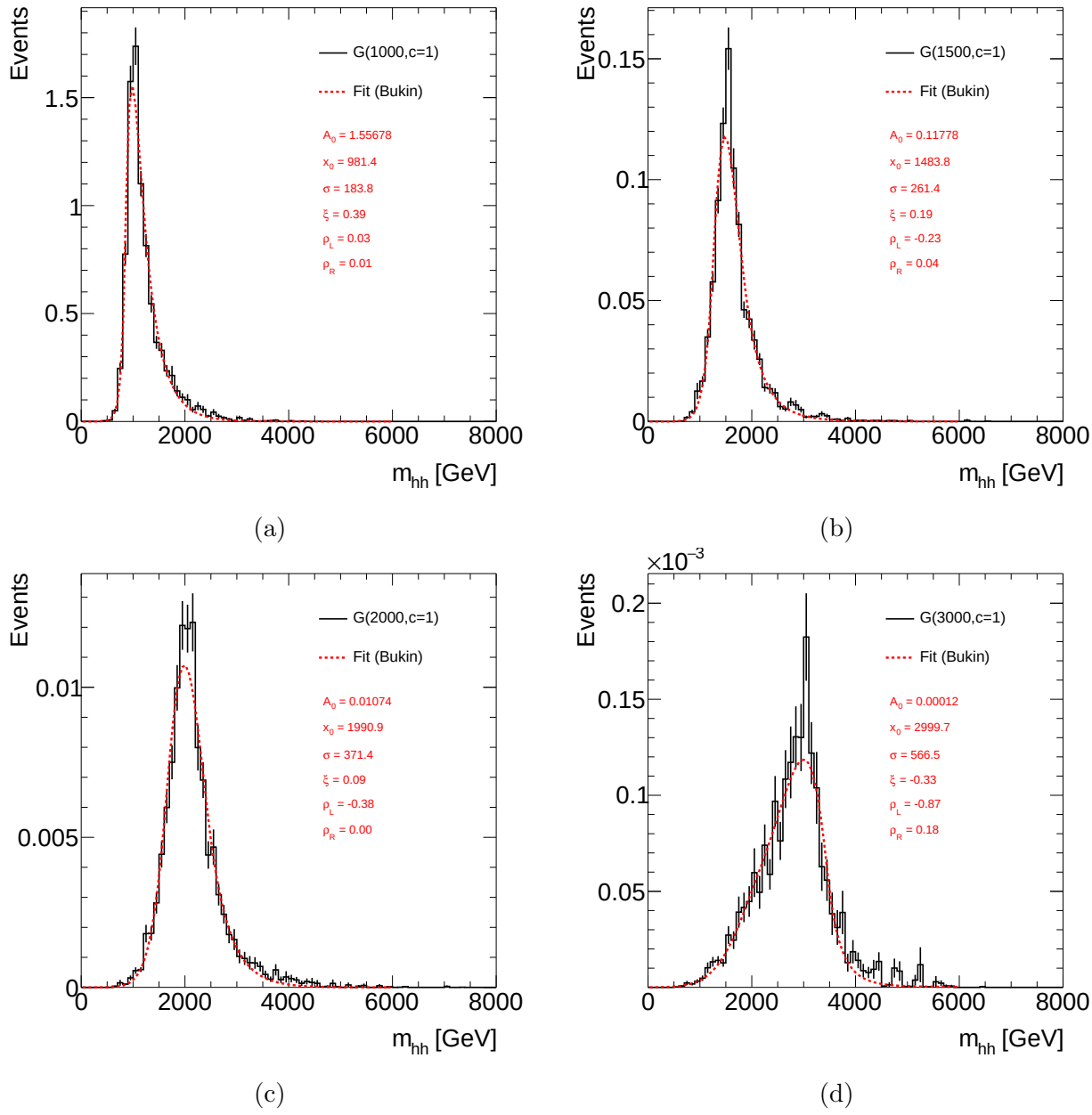

Figure B.2: Reconstructed m_{hh} distributions for RS c = 1 graviton MC generated samples with masses of (a) 1000 GeV, (b) 1500 GeV, (c) 2000 GeV and (d) 3000 GeV. The dashed red line is the fit to the m_{hh} distribution using a Bukin function. The parameters of the Bukin functional fit are also shown. The error bars only include statistical uncertainties.

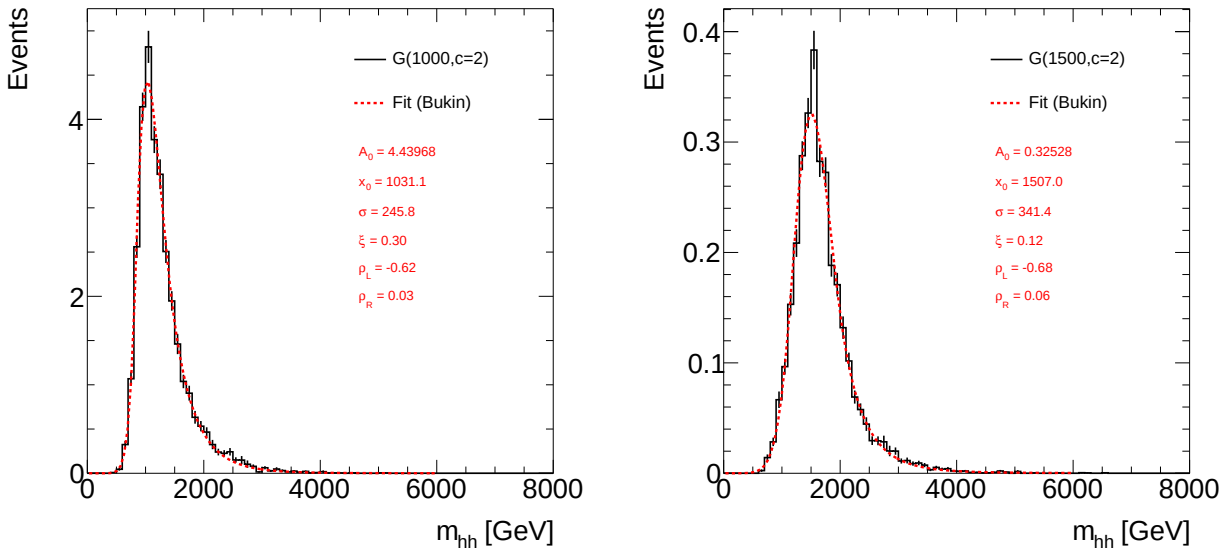

(a)

(b)

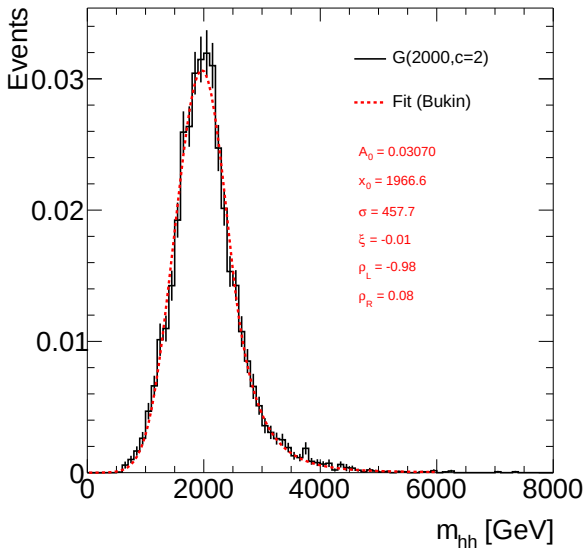

(c)

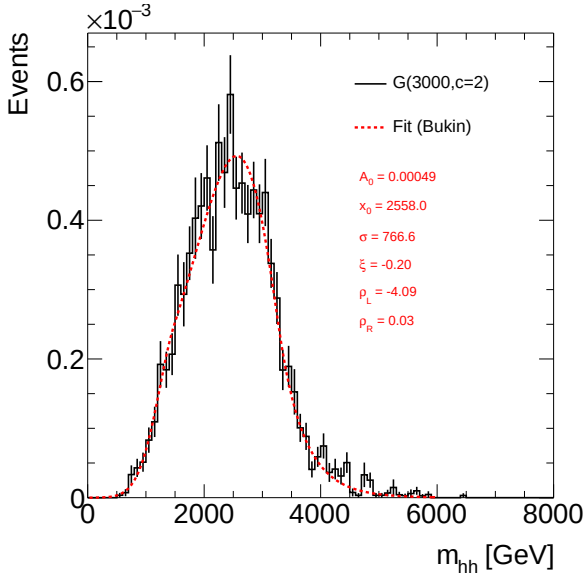

(d)

Figure B.3: Reconstructed m_{hh} distributions for RS c = 2 graviton MC generated samples with masses of (a) 1000 GeV, (b) 1500 GeV, (c) 2000 GeV and (d) 3000 GeV. The dashed red line is the fit to the m_{hh} distribution using a Bukin function. The parameters of the Bukin functional fit are also shown. The error bars only include statistical uncertainties.

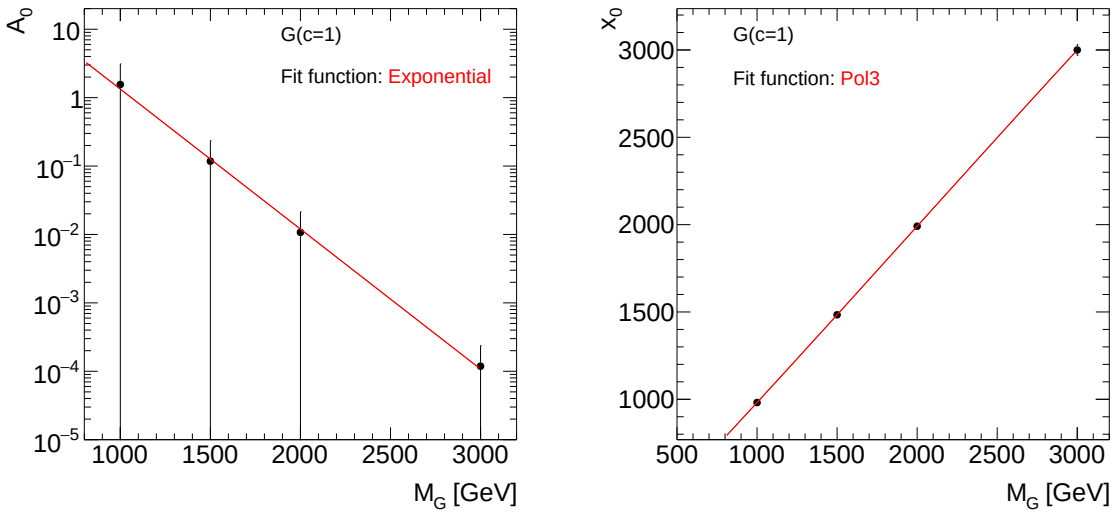

(a)

(b)

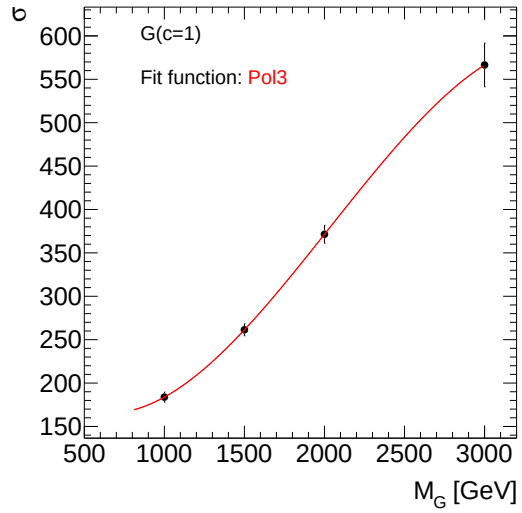

(c)

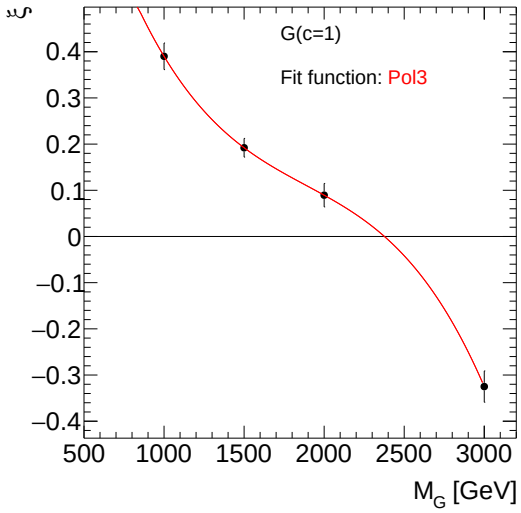

(d)

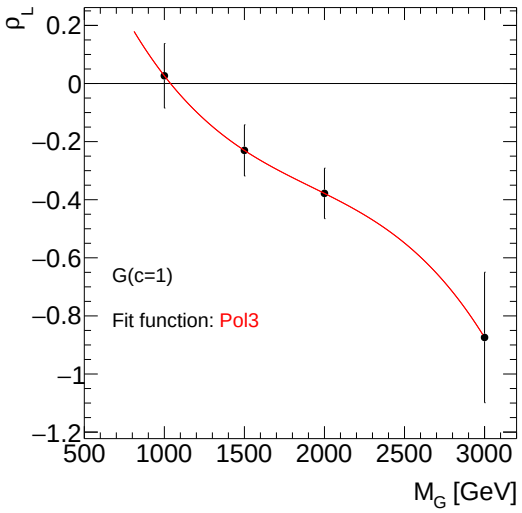

(e)

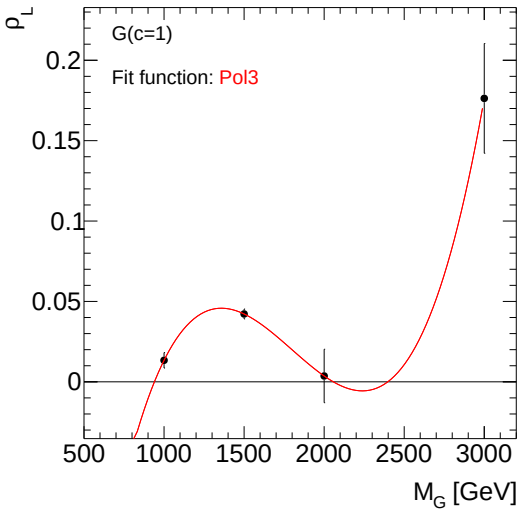

(f)

Figure B.4: The Bukin fit parameters, (a) A_0, (b) x_0, (c) σ, (d) ξ, (e) ρ_L and (f) ρ_R, as a function of generated RS c = 1 graviton signal sample mass. The red line is a fit to parameterize the bukin function parameters as a function of graviton signal mass.

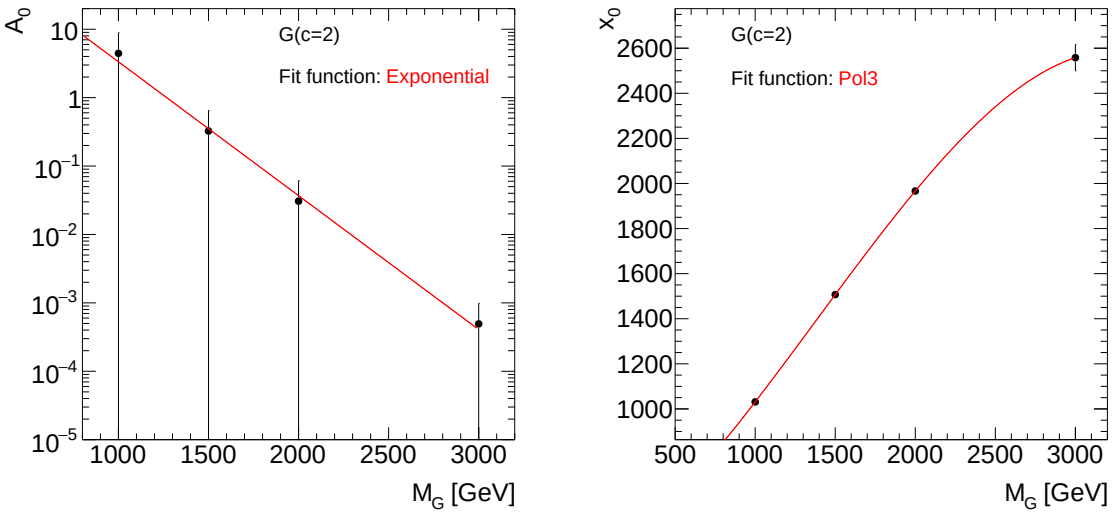

(a)

(b)

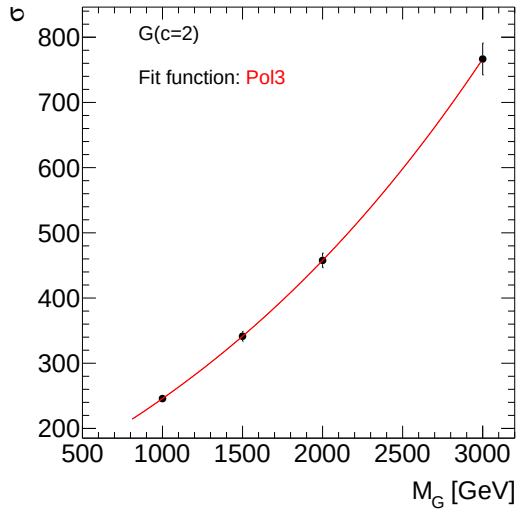

(c)

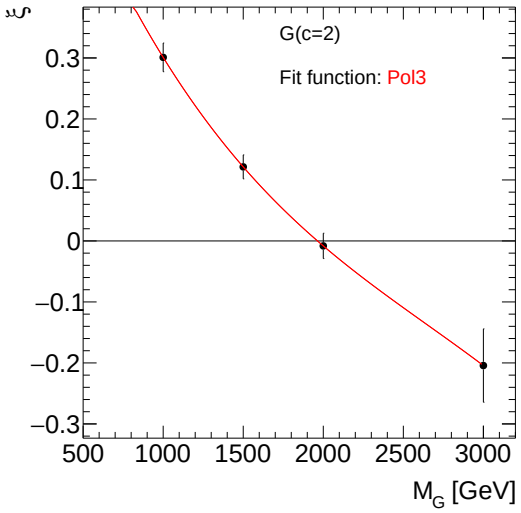

(d)

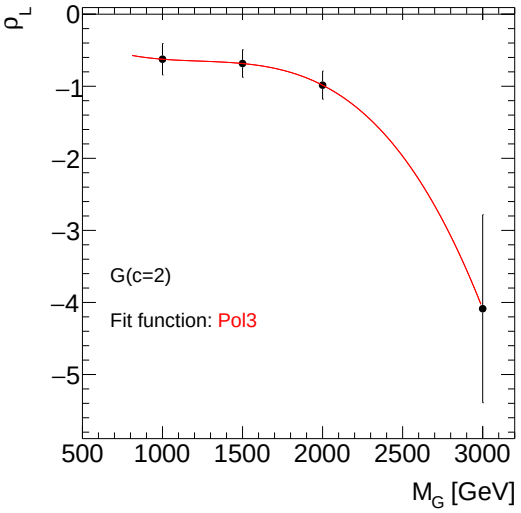

(e)

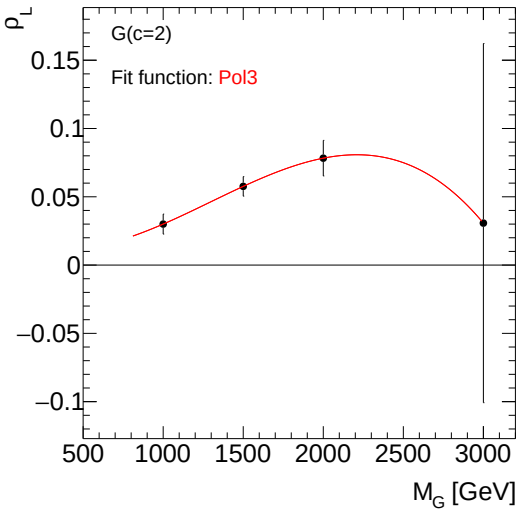

(f)

Figure B.5: The Bukin fit parameters, (a) A_0, (b) x_0, (c) σ, (d) ξ, (e) ρ_L and (f) ρ_R, as a function of generated RS c = 2 graviton signal sample mass. The red line is a fit to parameterize the bukin function parameters as a function of graviton signal mass.

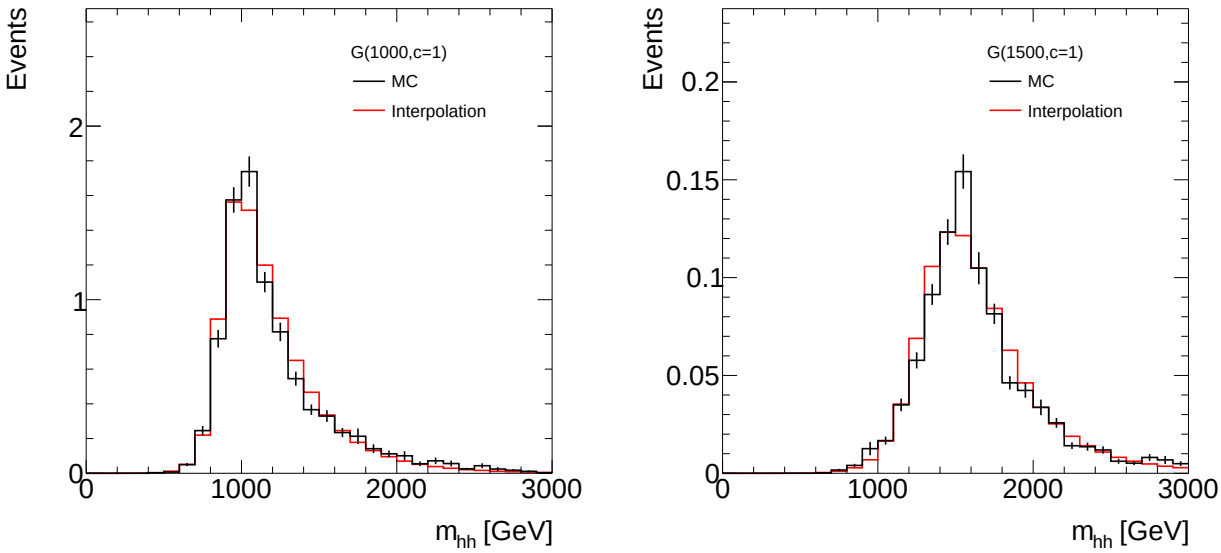

Figure B.6: The m_{hh} distributions of RS gravitons c = 1 MC generated samples with masses of (a) 1000 GeV, (b) 1500 GeV, (c) 2000 GeV and (d) 3000 GeV, shown as black histograms. The m_{hh} distributions generated from the signal interpolation procedure are shown as red histograms.

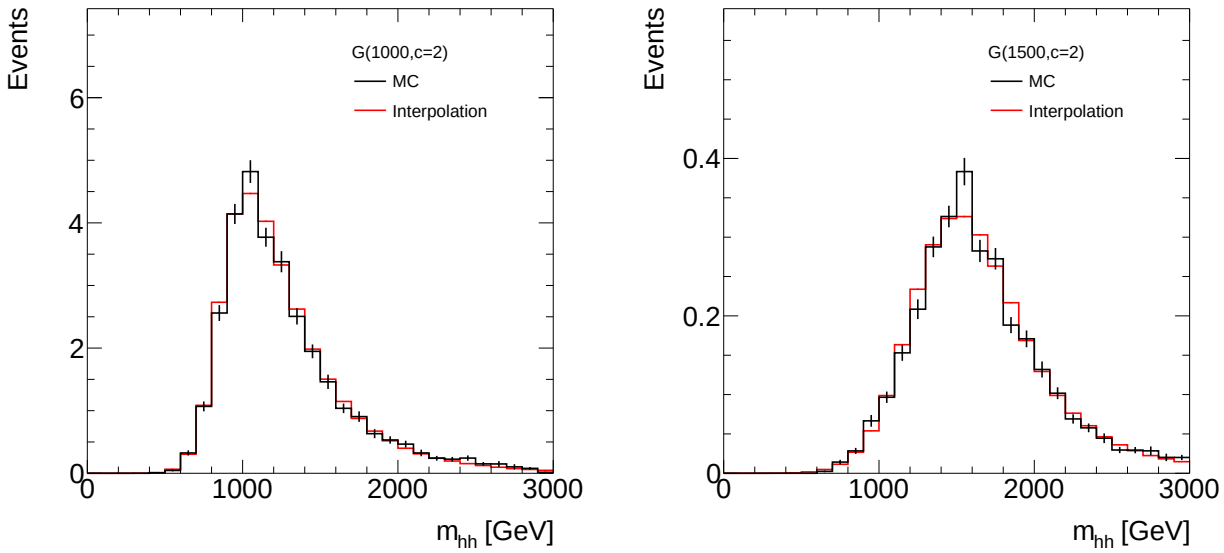

Figure B.7: The m_{hh} distributions of RS gravitons c = 2 MC generated samples with masses of (a) 1000 GeV, (b) 1500 GeV, (c) 2000 GeV and (d) 3000 GeV, shown as black histograms. The m_{hh} distributions generated from the signal interpolation procedure are shown as red histograms.

Appendix C

Truth level based subjet b-tagging efficiency

The goal of tagging a Higgs boson decaying to $b\bar{b}$ is to identify the presence of the two b-hadrons via the use of regions of interest defined by subjets within the large-R jet. However, if these regions of interest do not accurately reconstruct the directions of the b-hadrons, then the ability to make a positive identification of a Higgs jet when it is seeded by a Higgs boson, is hindered. In some cases, this may be due to the presence of additional radiation in a subjet which biases its direction away from the b-hadron (e.g. in ExKt or CoM) or due to the algorithm reconstructing more than two subjets (in the case of the fixed and variable radius track jets), which causes combinatorial difficulties when determining which of the subjets to use to identify the jet as a Higgs jet or not. Knowing the precise composition of these cases can provide added insight into the failures and merits of each technique.

Figures C.1 and C.2 show (for the p_{T} bins used in the main body of the note and for a set of more finely balanced p_{T} bins, respectively) the decomposition of the labelling of subjets within the sample of signal Higgs jets for different Higgs jet p_{T} intervals. On the x-axis of each plot is the subjet reconstruction algorithm, with variable radius track jets on the left, exclusive-k$_t$ and CoM subjets in the center, and fixed radius track jets on the right. On the y-axis are the various categories of how a large-R jet can be decomposed into subjets, showing separately the categories for one, two, three, four, and five or greater subjets as determined by the respective algorithm. Each category is further subdivided into the manner in which the set of subjetshas the pair of b-hadrons distributed among them. For example, in the case of two subjets, the "(20/02)" label means that either both b-hadrons were matched to the leading subjet ("20") or both were matched to the subleading subjet ("02"). A more precise description of all the categories is as follows :

- **1 subjet:** Higgs jet has exactly 1 subjet.

  - **(0):** The only subjet has no associated b-hadron.
  - **(1):** The only subjet has exactly 1 associated b-hadron.
  - **(2):** The only subjet has exactly 2 associated b-hadrons.

- **2 subjets:** Higgs jet has exactly 2 subjets.
  - **(00):** Neither subjet has any associated b-hadrons.
  - **(10/01):** Either the leading subjet or the sub-leading subjet has exactly 1 associated b-hadron.
  - **(11):** Both subjets have exactly one associated b-hadron
  - **(20/02):** Either the leading subjet or the sub-leading subjet has exactly 2 associated b-hadrons.

- **3 subjets:** Higgs jet has exactly 3 subjets.
  - **(000):** None of the subjets have any associated b-hadrons.
  - **(100/010):** Either the leading subjet or the sub-leading subjet has exactly 1 associated b-hadron.
  - **(110):** The leading and sub-leading subjets each have exactly 1 associated b-hadron.
  - **(101/011):** The third leading subjet and one of either the leading or subleading subjets have exactly 1 associated b-hadron.
  - **(200/020/002):** Either the leading subjet or the sub-leading subjet or the sub-sub-leading subjet has exactly 2 associated b-hadron.
  - **(001):** Only the third leading subjet has exactly one associated b-hadron.

- **4 subjets:** Higgs jet has exactly 4 subjets.
  - **(1100):** The leading and sub-leading subjets have exactly 1 associated b-hadron.
  - **(Others):** Does not fall into the subjet category above.

- **More than 4 subjets:** Higgs jet has more than 4 subjets.

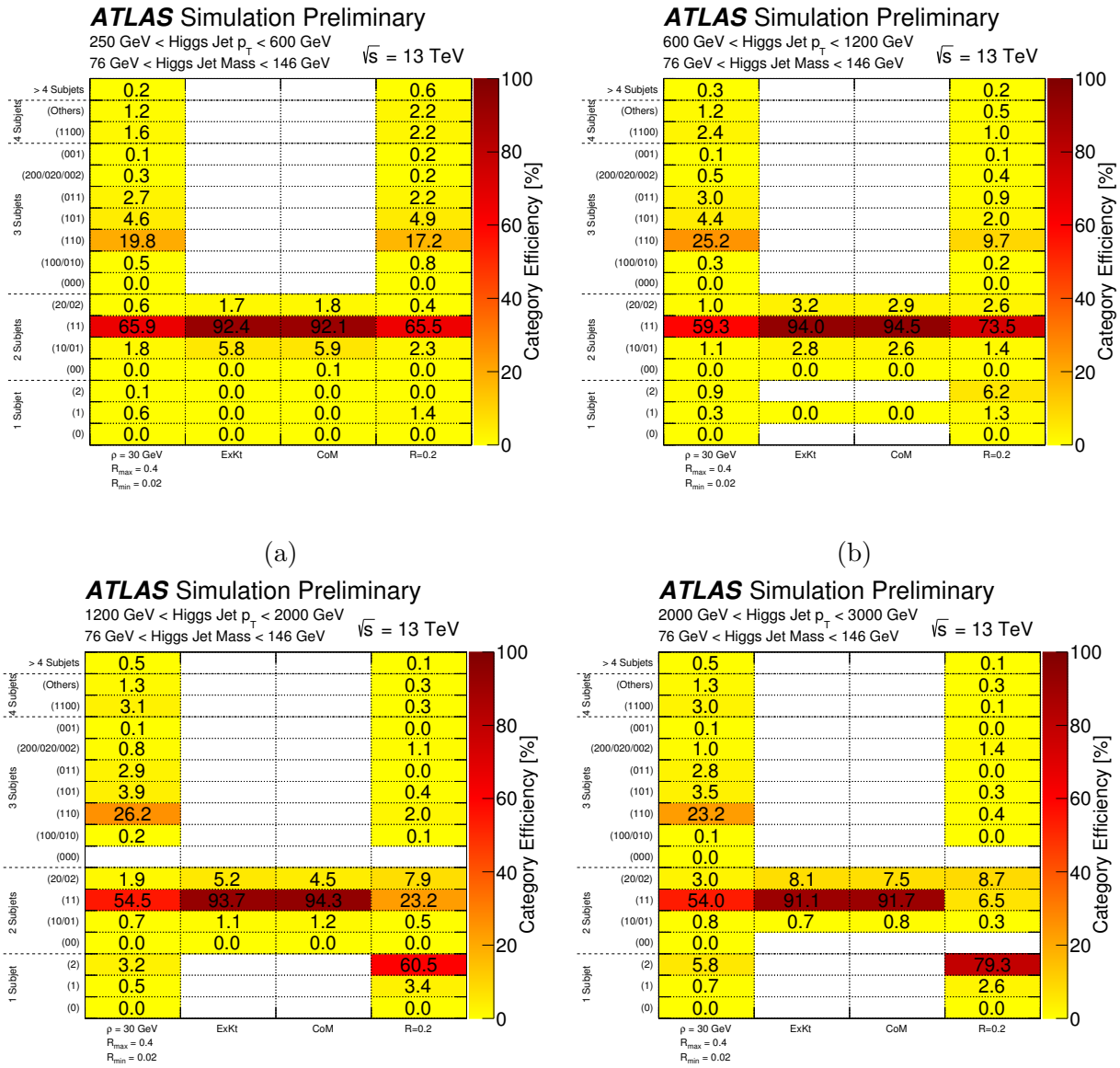

(a)

(b)

(c)

(d)

Figure C.1: Category efficiency matrix for different subjet collections in various Higgs jet p_{T} regimes. Figures produced by the author and published in Reference [4]

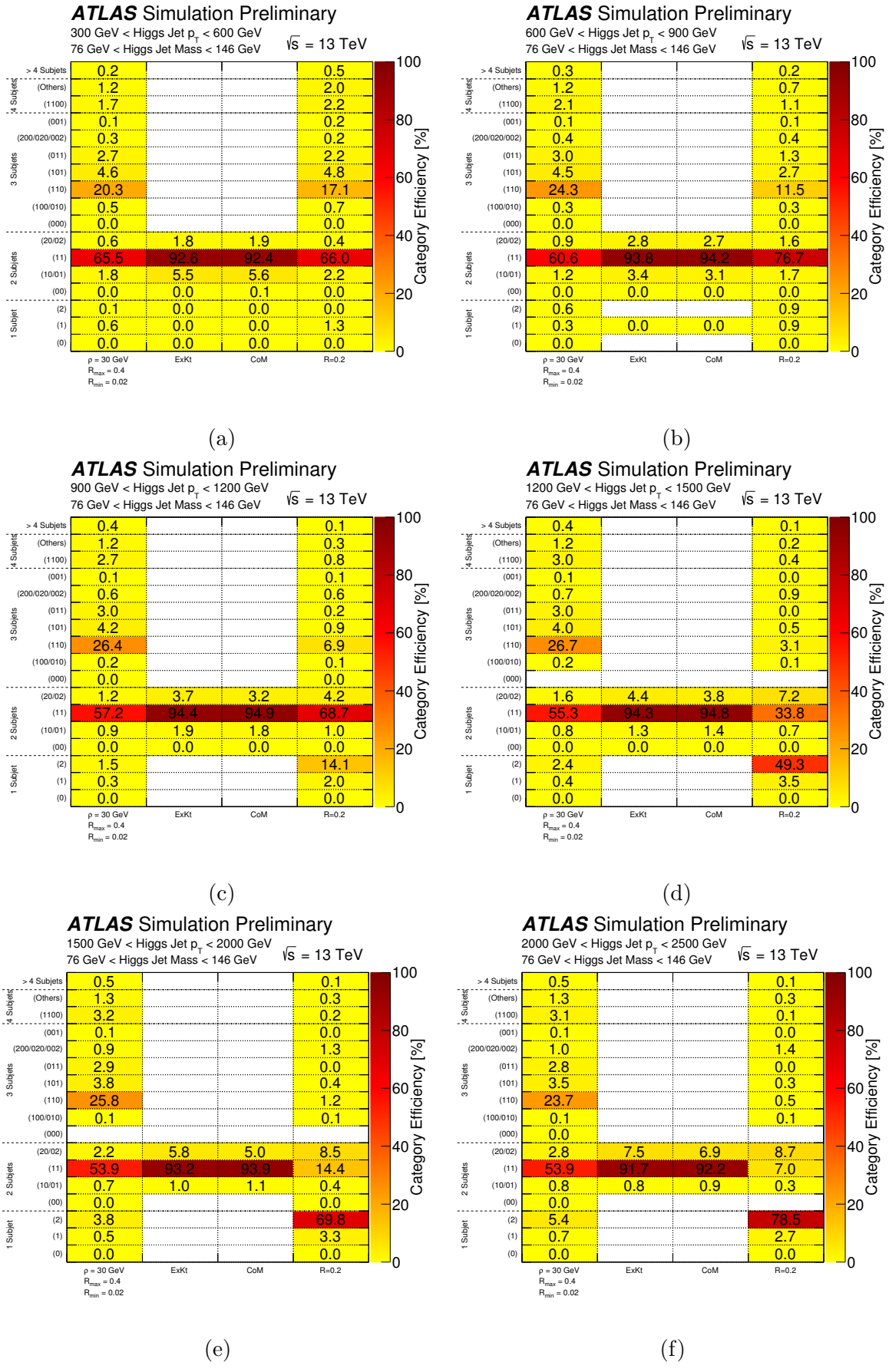

Figure C.2: Category efficiency matrix for different subjet collections in various fine Higgs jet p_{T} bins. Figures produced by the author and published in Reference [4].

Bibliography

[1] ATLAS Collaboration, *Jet mass reconstruction with the ATLAS Detector in early Run 2 data*, ATLAS-CONF-2016-035, 2016. `http://cds.cern.ch/record/2200211`.

[2] *WSMaker Twiki (ATLAS Collaboration Internal)*, `https://twiki.cern.ch/twiki/bin/view/AtlasProtected/WorkspaceMaker`.

[3] B. Tannenwald and H. Kagan, *Measurement of W-Helicity Fractions in $t\bar{t}$ decays and Search for Exotic Dihiggs Production in the $b\bar{b}WW^*$ Decay Channel Using the ATLAS Detector*, CERN-THESIS-2017-135, 2017. `https://cds.cern.ch/record/2282442`.

[4] ATLAS Collaboration, *Variable Radius, Exclusive-k_T, and Center-of-Mass Subjet Reconstruction for Higgs($\to b\bar{b}$) Tagging in ATLAS*, ATL-PHYS-PUB-2017-010, 2017. `https://cds.cern.ch/record/2268678`.

[5] N. Norjoharuddeen, *W/Top/H tagging in ATLAS at BOOST 2017*, `https://indico.cern.ch/event/579660/contributions/2496137`.

[6] M. E. Peskin and D. V. Schroeder, *An Introduction to Quantum Field Theory*. Addison-Wesley, 1995.

[7] M. D. Schwartz, *Quantum Field Theory and the Standard Model*. Cambridge University Press, 2014.

[8] D. J. Gross and F. Wilczek, *Ultraviolet Behavior of Nonabelian Gauge Theories*, Phys. Rev. Lett. **30** (1973) 1343–1346.

[9] H. D. Politzer, *Reliable Perturbative Results for Strong Interactions?*, Phys. Rev. Lett. **30** (1973) 1346–1349.

[10] B. Andersson, G. Gustafson, G. Ingelman, and T. Sjostrand, *Parton Fragmentation and String Dynamics*, Phys. Rept. **97** (1983) 31–145.

[11] B. R. Webber, *A QCD Model for Jet Fragmentation Including Soft Gluon Interference*, Nucl. Phys. **B238** (1984) 492–528.

[12] S. L. Glashow, *Partial Symmetries of Weak Interactions*, Nucl. Phys. **22** (1961) 579–588.

[13] S. Weinberg, *A Model of Leptons*, Phys. Rev. Lett. **19** (1967) 1264–1266.

[14] A. Salam, *Weak and Electromagnetic Interactions*, Conf. Proc. **C680519** (1968) 367–377.

[15] S. L. Glashow, J. Iliopoulos, and L. Maiani, *Weak Interactions with Lepton-Hadron Symmetry*, Phys. Rev. **D2** (1970) 1285–1292.

[16] G. 't Hooft, *Renormalization of Massless Yang-Mills Fields*, Nucl. Phys. **B33** (1971) 173–199.

[17] UA1 Collaboration, *Experimental Observation of Isolated Large Transverse Energy Electrons with Associated Missing Energy at* $\sqrt{s} = 540 - GeV$, Phys. Lett. **B122** (1983) 103–116.

[18] UA2 Collaboration, *Observation of Single Isolated Electrons of High Transverse Momentum in Events with Missing Transverse Energy at the CERN anti-p p Collider*, Phys. Lett. **B122** (1983) 476–485.

[19] UA1 Collaboration, *Experimental Observation of Lepton Pairs of Invariant Mass Around 95-GeV/*c^2 *at the CERN SPS Collider*, Phys. Lett. **B126** (1983) 398–410.

[20] UA2 Collaboration, *Evidence for* $Z0 - -- > e + e-$ *at the CERN anti-p p Collider*, Phys. Lett. **B129** (1983) 130–140.

[21] F. Englert and R. Brout, *Broken Symmetry and the Mass of Gauge Vector Mesons*, Phys. Rev. Lett. **13** (1964) 321–323.

[22] P. W. Higgs, *Broken symmetries, massless particles and gauge fields*, Phys. Lett. **12** (1964) 132–133.

[23] P. W. Higgs, *Broken Symmetries and the Masses of Gauge Bosons*, Phys. Rev. Lett. **13** (1964) 508–509.

[24] A. Djouadi, *The Anatomy of electro-weak symmetry breaking. I: The Higgs boson in the standard model*, Phys. Rept. **457** (2008) 1–216, `arXiv:hep-ph/0503172`.

[25] G. Bachy, A. Hofmann, S. Myers, E. Picasso, and G. Plass, *The LEP collider*, Part. Accel. **26** (1990) 19–32.

[26] ALEPH Collaboration, DELPHI Collaboration, L3 Collaboration, OPAL Collaboration, The LEP Working Group for Higgs boson searches, *Search for the standard model Higgs boson at LEP*, Phys. Lett. **B565** (2003) 61–75, `arXiv:hep-ex/0306033`.

[27] S. Holmes, R. S. Moore, and V. Shiltsev, *Overview of the Tevatron Collider Complex: Goals, Operations and Performance*, JINST **6** (2011) T08001, `1106.0909`.

[28] CDF and D0 Collaborations, *Evidence for a particle produced in association with weak bosons and decaying to a bottom-antibottom quark pair in Higgs boson searches at the Tevatron*, Phys. Rev. Lett. **109** (2012) 071804, `arXiv:1207.6436`.

[29] ATLAS Collaboration, *Observation of a new particle in the search for the Standard Model Higgs boson with the ATLAS detector at the LHC*, Phys. Lett. **B716** (2012) 1–29, arXiv:1207.7214.

[30] CMS Collaboration, *Observation of a new boson at a mass of 125 GeV with the CMS experiment at the LHC*, Phys. Lett. **B716** (2012) 30–61, arXiv:1207.7235.

[31] CMS Collaboration, *Constraints on the spin-parity and anomalous HVV couplings of the Higgs boson in proton collisions at 7 and 8 TeV*, Phys. Rev. **D92** (2015) no. 1, 012004, arXiv:1411.3441.

[32] ATLAS Collaboration, *Study of the spin and parity of the Higgs boson in diboson decays with the ATLAS detector*, Eur. Phys. J. **C75** (2015) no. 10, 476, arXiv:1506.05669.

[33] ATLAS and CMS Collaborations, *Combined Measurement of the Higgs Boson Mass in pp Collisions at $\sqrt{s} = 7$ and 8 TeV with the ATLAS and CMS Experiments*, Phys. Rev. Lett. **114** (2015) 191803, arXiv:1503.07589.

[34] LHC Higgs Cross Section Working Group Collaboration, D. de Florian et al., *Handbook of LHC Higgs Cross Sections: 4. Deciphering the Nature of the Higgs Sector*, arXiv:1610.07922.

[35] ATLAS Collaboration, *Higgs Pair Production in the $H(\to \tau\tau)H(\to b\bar{b})$ channel at the High-Luminosity LHC*, ATL-PHYS-PUB-2015-046, 2015. https://cds.cern.ch/record/2065974.

[36] ATLAS Collaboration, *Projected sensitivity to non-resonant Higgs boson pair production in the $b\bar{b}b\bar{b}$ final state using protonproton collisions at HL-LHC with the ATLAS detector*, ATL-PHYS-PUB-2016-024, 2016. http://cds.cern.ch/record/2221658.

[37] ATLAS Collaboration, *Study of the double Higgs production channel $H(\to b\bar{b})H(\to \gamma\gamma)$ with the ATLAS experiment at the HL-LHC*, ATL-PHYS-PUB-2017-001, 2017. http://cds.cern.ch/record/2243387.

[38] CMS Collaboration, *Projected performance of Higgs analyses at the HL-LHC for ECFA 2016*, CMS-PAS-FTR-16-002, 2017. https://cds.cern.ch/record/2266165.

[39] M. J. Dolan, C. Englert, and M. Spannowsky, *Higgs self-coupling measurements at the LHC*, JHEP **10** (2012) 112, arXiv:1206.5001.

[40] D. Wardrope, E. Jansen, N. Konstantinidis, B. Cooper, R. Falla, and N. Norjoharuddeen, *Non-resonant Higgs-pair production in the $b\bar{b}$ $b\bar{b}$ final state at the LHC*, Eur. Phys. J. **C75** (2015) no. 5, 219, arXiv:1410.2794.

[41] D. E. Ferreira de Lima, A. Papaefstathiou, and M. Spannowsky, *Standard model Higgs boson pair production in the ($b\bar{b}$)($b\bar{b}$) final state*, JHEP **08** (2014) 030, arXiv:1404.7139.

[42] J. K. Behr, D. Bortoletto, J. A. Frost, N. P. Hartland, C. Issever, and J. Rojo, *Boosting Higgs pair production in the $b\bar{b}b\bar{b}$ final state with multivariate techniques*, Eur. Phys. J. **C76** (2016) no. 7, 386, arXiv:1512.08928.

[43] K. Agashe, H. Davoudiasl, G. Perez, and A. Soni, *Warped Gravitons at the LHC and Beyond*, Phys. Rev. **D76** (2007) 036006, arXiv:hep-ph/0701186.

[44] B. Grinstein and M. Trott, *A Higgs-Higgs bound state due to new physics at a TeV*, Phys. Rev. **D76** (2007) 073002, arXiv:0704.1505.

[45] R. Grober and M. Muhlleitner, *Composite Higgs Boson Pair Production at the LHC*, JHEP **06** (2011) 020, arXiv:1012.1562.

[46] R. Contino, M. Ghezzi, M. Moretti, G. Panico, F. Piccinini, and A. Wulzer, *Anomalous Couplings in Double Higgs Production*, JHEP **08** (2012) 154, arXiv:1205.5444.

[47] M. J. Dolan, C. Englert, and M. Spannowsky, *New Physics in LHC Higgs boson pair production*, Phys. Rev. **D87** (2013) no. 5, 055002, arXiv:1210.8166.

[48] J. Cao, Z. Heng, L. Shang, P. Wan, and J. M. Yang, *Pair Production of a 125 GeV Higgs Boson in MSSM and NMSSM at the LHC*, JHEP **04** (2013) 134, arXiv:1301.6437.

[49] R. Costa, M. Mhlleitner, M. O. P. Sampaio, and R. Santos, *Singlet Extensions of the Standard Model at LHC Run 2: Benchmarks and Comparison with the NMSSM*, JHEP **06** (2016) 034, arXiv:1512.05355.

[50] M. Gouzevitch, A. Oliveira, J. Rojo, R. Rosenfeld, G. P. Salam, and V. Sanz, *Scale-invariant resonance tagging in multijet events and new physics in Higgs pair production*, JHEP **07** (2013) 148, arXiv:1303.6636.

[51] U. Ellwanger, *Higgs pair production in the NMSSM at the LHC*, JHEP **08** (2013) 077, arXiv:1306.5541.

[52] J. M. No and M. Ramsey-Musolf, *Probing the Higgs Portal at the LHC Through Resonant di-Higgs Production*, Phys. Rev. **D89** (2014) no. 9, 095031, arXiv:1310.6035.

[53] C.-R. Chen and I. Low, *Double take on new physics in double Higgs boson production*, Phys. Rev. **D90** (2014) no. 1, 013018, arXiv:1405.7040.

[54] J. Cao, D. Li, L. Shang, P. Wu, and Y. Zhang, *Exploring the Higgs Sector of a Most Natural NMSSM and its Prediction on Higgs Pair Production at the LHC*, JHEP **12** (2014) 026, arXiv:1409.8431.

[55] F. Goertz, A. Papaefstathiou, L. L. Yang, and J. Zurita, *Higgs boson pair production in the D=6 extension of the SM*, JHEP **04** (2015) 167, arXiv:1410.3471.

[56] S. Dawson, A. Ismail, and I. Low, *Whats in the loop? The anatomy of double Higgs production*, Phys. Rev. **D91** (2015) no. 11, 115008, arXiv:1504.05596.

[57] A. Azatov, R. Contino, G. Panico, and M. Son, *Effective field theory analysis of double Higgs boson production via gluon fusion*, Phys. Rev. **D92** (2015) no. 3, 035001, arXiv:1502.00539.

[58] B. Batell, M. McCullough, D. Stolarski, and C. B. Verhaaren, *Putting a Stop to di-Higgs Modifications*, JHEP **09** (2015) 216, arXiv:1508.01208.

[59] D. Buttazzo, F. Sala, and A. Tesi, *Singlet-like Higgs bosons at present and future colliders*, JHEP **11** (2015) 158, arXiv:1505.05488.

[60] W.-J. Zhang, W.-G. Ma, R.-Y. Zhang, X.-Z. Li, L. Guo, and C. Chen, *Double Higgs boson production and decay in Randall-Sundrum model at hadron colliders*, Phys. Rev. **D92** (2015) 116005, arXiv:1512.01766.

[61] L. Wu, J. M. Yang, C.-P. Yuan, and M. Zhang, *Higgs self-coupling in the MSSM and NMSSM after the LHC Run 1*, Phys. Lett. **B747** (2015) 378–389, arXiv:1504.06932.

[62] P. Huang, A. Joglekar, M. Li, and C. E. M. Wagner, *Corrections to di-Higgs boson production with light stops and modified Higgs couplings*, Phys. Rev. **D97** (2018) no. 7, 075001, 1711.05743.

[63] Particle Data Group Collaboration, C. Patrignani et al., *Review of Particle Physics*, Chin. Phys. **C40** (2016) no. 10, 100001.

[64] G. C. Branco, P. M. Ferreira, L. Lavoura, M. N. Rebelo, M. Sher, and J. P. Silva, *Theory and phenomenology of two-Higgs-doublet models*, Phys. Rept. **516** (2012) 1–102, arXiv:1106.0034.

[65] A. L. Fitzpatrick, J. Kaplan, L. Randall, and L.-T. Wang, *Searching for the Kaluza-Klein Graviton in Bulk RS Models*, JHEP **09** (2007) 013, arXiv:hep-ph/0701150.

[66] H. E. Haber, *Low-energy supersymmetry and its phenomenology*, Nucl. Phys. Proc. Suppl. **101** (2001) 217–236, arXiv:hep-ph/0103095.

[67] N. Arkani-Hamed, S. Dimopoulos, and G. Dvali, *The Hierarchy problem and new dimensions at a millimeter*, Phys. Lett. **B429** (1998) 263–272, arXiv:hep-ph/9803315.

[68] L. Randall and R. Sundrum, *A Large mass hierarchy from a small extra dimension*, Phys. Rev. Lett. **83** (1999) 3370–3373, arXiv:hep-ph/9905221.

[69] M. Gabella. The Randall-Sundrum Model, 2006. http://www-thphys.physics.ox.ac.uk/people/MaximeGabella/rs.pdf.

[70] ATLAS Collaboration, *Search for Higgs boson pair production in the $b\bar{b}b\bar{b}$ final state from pp collisions at $\sqrt{s} = 8$ TeV with the ATLAS detector*, Eur. Phys. J. **C75** (2015) no. 9, 412, arXiv:1506.00285.

[71] ATLAS Collaboration, *Search For Higgs Boson Pair Production in the $\gamma\gamma b\bar{b}$ Final State using pp Collision Data at $\sqrt{s} = 8$ TeV from the ATLAS Detector*, Phys. Rev. Lett. **114** (2015) no. 8, 081802, arXiv:1406.5053.

[72] ATLAS Collaboration, *Searches for Higgs boson pair production in the $hh \to bb\tau\tau, \gamma\gamma WW^*, \gamma\gamma bb, bbbb$ channels with the ATLAS detector*, Phys. Rev. **D92** (2015) 092004, arXiv:1509.04670.

[73] CMS Collaboration, *Search for resonant pair production of Higgs bosons decaying to two bottom quarkantiquark pairs in protonproton collisions at 8 TeV*, Phys. Lett. **B749** (2015) 560–582, arXiv:1503.04114.

[74] CMS Collaboration, *Search for heavy resonances decaying to two Higgs bosons in final states containing four b quarks*, Eur. Phys. J. **C76** (2016) no. 7, 371, arXiv:1602.08762.

[75] CMS Collaboration, *Search for two Higgs bosons in final states containing two photons and two bottom quarks in proton-proton collisions at 8 TeV*, Phys. Rev. **D94** (2016) no. 5, 052012, arXiv:1603.06896.

[76] CMS Collaboration, *Search for Higgs boson pair production in the $bb\tau\tau$ final state in proton-proton collisions at $\sqrt{(}s) = 8$* TeV, Phys. Rev. **D96** (2017) no. 7, 072004, arXiv:1707.00350.

[77] *Search for resonant pair production of Higgs bosons decaying to $b\bar{b}$ and $\tau^+\tau^-$ in proton-proton collisions at $\sqrt{s} = 8$ TeV*, CMS-PAS-EXO-15-008, 2015. https://cds.cern.ch/record/2125293.

[78] CMS Collaboration, *Searches for a heavy scalar boson H decaying to a pair of 125 GeV Higgs bosons hh or for a heavy pseudoscalar boson A decaying to Zh, in the final states with $h \to \tau\tau$*, Phys. Lett. **B755** (2016) 217–244, arXiv:1510.01181.

[79] Auxiliary Figure 8: Searches for Higgs boson pair production in the $hh \to bb\tau\tau, \gamma\gamma WW^*, \gamma\gamma bb, bbbb$ channels with the ATLAS detector. https://atlas.web.cern.ch/Atlas/GROUPS/PHYSICS/PAPERS/HIGG-2013-33/.

[80] Summary of run-I $\sigma(gg \to X) \times B(X \to HH)$ 95% CL upper limits assuming spin-0 hypothesis. https://twiki.cern.ch/twiki/bin/view/CMSPublic/SummaryResultsHIG#Summary_of_run_I_sigma_gg_to_X_t.

[81] ATLAS Collaboration, *Search for Higgs boson pair production in the $b\bar{b}\gamma\gamma$ final state using pp collision data at $\sqrt{s} = 13$ TeV with the ATLAS detector*, ATLAS-CONF-2016-004, 2016. http://cds.cern.ch/record/2138949.

[82] ATLAS Collaboration, *Search for pair production of Higgs bosons in the $b\bar{b}b\bar{b}$ final state using proton-proton collisions at $\sqrt{s} = 13$ TeV with the ATLAS detector*, arXiv:1804.06174.

[83] CMS Collaboration, *Search for resonant pair production of Higgs bosons decaying to bottom quark-antiquark pairs in proton-proton collisions at 13 TeV*, CMS-PAS-HIG-17-009, 2017. https://cds.cern.ch/record/2292044.

[84] CMS Collaboration, *Search for a massive resonance decaying to a pair of Higgs bosons in the four b quark final state in proton-proton collisions at $\sqrt{s} = 13$ TeV*, Phys. Lett. **B781** (2018) 244–269, arXiv:1710.04960.

[85] CMS Collaboration, *Search for Higgs boson pair production in the final state containing two photons and two bottom quarks in proton-proton collisions at $\sqrt{s} = 13$ TeV*, CMS-PAS-HIG-17-008, 2017. https://cds.cern.ch/record/2273383.

[86] CMS Collaboration, *Search for Higgs boson pair production in events with two bottom quarks and two tau leptons in protonproton collisions at $\sqrt{s}$ =13TeV*, Phys. Lett. **B778** (2018) 101–127, arXiv:1707.02909.

[87] CMS Collaboration, *Search for heavy resonances decaying into two Higgs bosons or into a Higgs and a vector boson in proton-proton collisions at 13 TeV*, CMS-PAS-B2G-17-006. https://cds.cern.ch/record/2296716.

[88] CMS Collaboration, *Search for resonant and nonresonant Higgs boson pair production in the $\mathrm{b\bar{b}}\ell\nu\ell\nu$ final state in proton-proton collisions at $\sqrt{s} = 13$ TeV*, JHEP **01** (2018) 054, arXiv:1708.04188.

[89] L. Evans and P. Bryant, *LHC Machine*, JINST **3** (2008) S08001.

[90] J. Haffner, *The CERN accelerator complex. Complexe des acclrateurs du CERN*, OPEN-PHO-ACCEL-2013-056, Oct, 2013. https://cds.cern.ch/record/1621894.

[91] ATLAS Collaboration, *The ATLAS Experiment at the CERN Large Hadron Collider*, JINST **3** (2008) S08003.

[92] CMS Collaboration, *The CMS Experiment at the CERN LHC*, JINST **3** (2008) S08004.

[93] LHCb Collaboration, *The LHCb Detector at the LHC*, JINST **3** (2008) S08005.

[94] ALICE Collaboration, *The ALICE experiment at the CERN LHC*, JINST **3** (2008) S08002.

[95] J. Pequenao, *Computer generated image of the whole ATLAS detector*, CERN-GE-0803012, Mar, 2008. https://cds.cern.ch/record/1095924.

[96] ATLAS Collaboration, *ATLAS magnet system: Technical Design Report, 1.* Technical Design Report ATLAS. CERN, Geneva, 1997.

[97] ATLAS Collaboration, *ATLAS inner detector: Technical Design Report, 1.* Technical Design Report ATLAS. CERN, Geneva, 1997. https://cds.cern.ch/record/331063.

[98] S. Haywood, L. Rossi, R. Nickerson, and A. Romaniouk, *ATLAS inner detector: Technical Design Report, 2.* Technical Design Report ATLAS. CERN, Geneva, 1997. https://cds.cern.ch/record/331064.

[99] ATLAS Collaboration, *Studies of radial distortions of the ATLAS Inner Detector*, ATL-PHYS-PUB-2018-003, 2018. https://cds.cern.ch/record/2309785.

[100] M. Capeans, G. Darbo, K. Einsweiller, M. Elsing, T. Flick, M. Garcia-Sciveres, C. Gemme, H. Pernegger, O. Rohne, and R. Vuillermet, *ATLAS Insertable B-Layer Technical Design Report.* No. CERN-LHCC-2010-013. ATLAS-TDR-19. Geneva, Sep, 2010. https://cds.cern.ch/record/1291633.

[101] ATLAS Collaboration, *Performance of the ATLAS Transition Radiation Tracker in Run 1 of the LHC: tracker properties*, JINST **12** (2017) no. 05, P05002, arXiv:1702.06473.

[102] J. Pequenao, *Computer Generated image of the ATLAS calorimeter*, CERN-GE-0803015, Mar, 2008. https://cds.cern.ch/record/1095927.

[103] ATLAS Collaboration, *ATLAS calorimeter performance: Technical Design Report.* Technical Design Report ATLAS. CERN, Geneva, 1996. https://cds.cern.ch/record/331059.

[104] ATLAS Collaboration, *ATLAS muon spectrometer: Technical Design Report.* Technical Design Report ATLAS. CERN, Geneva, 1997. https://cds.cern.ch/record/331068.

[105] J. Pequenao, *Computer generated image of the ATLAS Muons subsystem*, Cern-ge-0803017, Mar, 2008. https://cds.cern.ch/record/1095929.

[106] ATLAS Collaboration, *Performance of the ATLAS Trigger System in 2015*, Eur. Phys. J. **C77** (2017) no. 5, 317, arXiv:1611.09661.

[107] ATLAS Collaboration, *Performance of the ATLAS Trigger System in 2010*, Eur. Phys. J. **C72** (2012) 1849, arXiv:1110.1530.

[108] ATLAS TDAQ Collaboration, *The ATLAS Data Acquisition and High Level Trigger system*, JINST **11** (2016) no. 06, P06008.

[109] ATLAS Experiment Public Results: LuminosityPublicResultsRun2. https://twiki.cern.ch/twiki/bin/view/AtlasPublic/LuminosityPublicResultsRun2.

[110] ATLAS Collaboration, *The ATLAS Simulation Infrastructure*, Eur. Phys. J. **C70** (2010) 823–874, arXiv:1005.4568.

[111] S. Agostinelli et al., *GEANT4: A Simulation toolkit*, Nucl. Instrum. Meth. **A506** (2003) 250–303.

[112] T. Cornelissen, M. Elsing, I. Gavrilenko, W. Liebig, E. Moyse, and A. Salzburger, *The new ATLAS track reconstruction (NEWT)*, Journal of Physics: Conference Series **119** (2008) no. 3, 032014. http://stacks.iop.org/1742-6596/119/i=3/a=032014.

[113] ATLAS Collaboration, *Reconstruction of primary vertices at the ATLAS experiment in Run 1 protonproton collisions at the LHC*, Eur. Phys. J. **C77** (2017) no. 5, 332, arXiv:1611.10235.

[114] ATLAS Collaboration, *Electron efficiency measurements with the ATLAS detector using 2012 LHC protonproton collision data*, Eur. Phys. J. **C77** (2017) no. 3, 195, arXiv:1612.01456.

[115] ATLAS Collaboration, *Electron efficiency measurements with the ATLAS detector using the 2015 LHC proton-proton collision data*, ATLAS-CONF-2016-024, 2016. http://cds.cern.ch/record/2157687.

[116] Electron identification efficiency measured with Z→ee events using 2016 data. https://atlas.web.cern.ch/Atlas/GROUPS/PHYSICS/PLOTS/EGAM-2016-002.

[117] ATLAS Collaboration, *Electron and photon energy calibration with the ATLAS detector using LHC Run 1 data*, Eur. Phys. J. **C74** (2014) no. 10, 3071, arXiv:1407.5063.

[118] ATLAS Collaboration, *Electron and photon energy calibration with the ATLAS detector using data collected in 2015 at* $\sqrt{s}$ *= 13 TeV*, ATL-PHYS-PUB-2016-015, 2016. https://cds.cern.ch/record/2203514.

[119] ATLAS Collaboration, *Muon reconstruction performance of the ATLAS detector in protonproton collision data at* $\sqrt{s}$ *=13 TeV*, Eur. Phys. J. **C76** (2016) no. 5, 292, arXiv:1603.05598.

[120] ATLAS Muon Combined Performance with the full 2016 dataset. https://atlas.web.cern.ch/Atlas/GROUPS/PHYSICS/PLOTS/MUON-2017-001.

[121] Isolation selection efficiency with improved background subtraction on 2016 Data. https://atlas.web.cern.ch/Atlas/GROUPS/PHYSICS/PLOTS/MUON-2017-004.

[122] G. P. Salam, *Towards Jetography*, Eur. Phys. J. **C67** (2010) 637–686, arXiv:0906.1833.

[123] S. Catani, Y. L. Dokshitzer, M. H. Seymour, and B. R. Webber, *Longitudinally invariant* K_t *clustering algorithms for hadron hadron collisions*, Nucl. Phys. **B406** (1993) 187–224.

[124] S. D. Ellis and D. E. Soper, *Successive combination jet algorithm for hadron collisions*, Phys. Rev. **D48** (1993) 3160–3166, arXiv:hep-ph/9305266.

[125] Y. L. Dokshitzer, G. D. Leder, S. Moretti, and B. R. Webber, *Better jet clustering algorithms*, JHEP **08** (1997) 001, arXiv:hep-ph/9707323.

[126] M. Wobisch and T. Wengler, *Hadronization corrections to jet cross-sections in deep inelastic scattering*, in *Monte Carlo generators for HERA physics. Proceedings, Workshop, Hamburg, Germany, 1998-1999*, pp. 270–279. 1998. arXiv:hep-ph/9907280. https://inspirehep.net/record/484872/files/arXiv:hep-ph_9907280.pdf.

[127] M. Cacciari, G. P. Salam, and G. Soyez, *The Anti-k(t) jet clustering algorithm*, JHEP **04** (2008) 063, arXiv:0802.1189.

[128] M. Cacciari, G. P. Salam, and G. Soyez, *FastJet User Manual*, Eur. Phys. J. **C72** (2012) 1896, arXiv:1111.6097.

[129] M. Cacciari, G. P. Salam, and G. Soyez, *The Catchment Area of Jets*, JHEP **04** (2008) 005, arXiv:0802.1188.

[130] ATLAS Collaboration, *Topological cell clustering in the ATLAS calorimeters and its performance in LHC Run 1*, Eur. Phys. J. **C77** (2017) 490, arXiv:1603.02934.

[131] ATLAS Collaboration, *Jet energy scale measurements and their systematic uncertainties in proton-proton collisions at $\sqrt{s} = 13$ TeV with the ATLAS detector*, Phys. Rev. **D96** (2017) no. 7, 072002, arXiv:1703.09665.

[132] ATLAS Collaboration, *Performance of pile-up mitigation techniques for jets in pp collisions at $\sqrt{s} = 8$ TeV using the ATLAS detector*, Eur. Phys. J. **C76** (2016) no. 11, 581, arXiv:1510.03823.

[133] JVT Public Plots for ICHEP 2016. https://atlas.web.cern.ch/Atlas/GROUPS/PHYSICS/PLOTS/JETM-2016-011.

[134] ATLAS Collaboration, *Selection of jets produced in 13TeV proton-proton collisions with the ATLAS detector*, ATLAS-CONF-2015-029, 2015. http://cds.cern.ch/record/2037702.

[135] D. Krohn, J. Thaler, and L.-T. Wang, *Jet Trimming*, JHEP **02** (2010) 084, arXiv:0912.1342.

[136] ATLAS Collaboration, *Performance of jet substructure techniques for large-R jets in proton-proton collisions at $\sqrt{s} = 7$ TeV using the ATLAS detector*, JHEP **09** (2013) 076, arXiv:1306.4945.

[137] M. Cacciari and G. P. Salam, *Pileup subtraction using jet areas*, Phys. Lett. **B659** (2008) 119–126, arXiv:0707.1378.

[138] ATLAS Collaboration, *Performance of Impact Parameter-Based b-tagging Algorithms with the ATLAS Detector using Proton-Proton Collisions at sqrts = 7 TeV*, ATLAS-CONF-2010-091, 2010. http://cds.cern.ch/record/1299106.

[139] ATLAS Collaboration, *Performance of b-Jet Identification in the ATLAS Experiment*, JINST **11** (2016) no. 04, P04008, arXiv:1512.01094.

[140] G. Piacquadio and C. Weiser, *A new inclusive secondary vertex algorithm for b-jet tagging in ATLAS*, Journal of Physics: Conference Series **119** (2008) no. 3, 032032. http://stacks.iop.org/1742-6596/119/i=3/a=032032.

[141] ATLAS Collaboration, *Expected performance of the ATLAS b-tagging algorithms in Run-2*, ATL-PHYS-PUB-2015-022, 2015. https://cds.cern.ch/record/2037697.

[142] ATLAS Collaboration, *Optimisation of the ATLAS b-tagging performance for the 2016 LHC Run*, ATL-PHYS-PUB-2016-012, 2016. http://cds.cern.ch/record/2160731.

[143] ATLAS Collaboration, *Measurements of b-jet tagging efficiency with the ATLAS detector using $t\bar{t}$ events at $\sqrt{s} = 13$ TeV*, arXiv:1805.01845.

[144] ATLAS Collaboration, *Measurement of b-tagging Efficiency of c-jets in $t\bar{t}$ Events Using a Likelihood Approach with the ATLAS Detector*, ATLAS-CONF-2018-001, 2018. https://cds.cern.ch/record/2306649.

[145] ATLAS Collaboration, *Calibration of light-flavour jet b-tagging rates on ATLAS proton-proton collision data at $\sqrt{s} = 13$ TeV*, ATLAS-CONF-2018-006, 2018. https://cds.cern.ch/record/2314418.

[146] ATLAS Collaboration, *Performance of missing transverse momentum reconstruction with the ATLAS detector using proton-proton collisions at $\sqrt{s} = 13$ TeV*, arXiv:1802.08168.

[147] ATLAS Collaboration, *Jet reconstruction and performance using particle flow with the ATLAS Detector*, Eur. Phys. J. **C77** (2017) no. 7, 466, arXiv:1703.10485.

[148] CMS Collaboration, *Particle-flow reconstruction and global event description with the CMS detector*, JINST **12** (2017) no. 10, P10003, arXiv:1706.04965.

[149] M. Son, C. Spethmann, and B. Tweedie, *Diboson-Jets and the Search for Resonant Zh Production*, JHEP **08** (2012) 160, arXiv:1204.0525.

[150] A. Katz, M. Son, and B. Tweedie, *Jet Substructure and the Search for Neutral Spin-One Resonances in Electroweak Boson Channels*, JHEP **03** (2011) 011, arXiv:1010.5253.

[151] S. Schaetzel and M. Spannowsky, *Tagging highly boosted top quarks*, Phys. Rev. **D89** (2014) no. 1, 014007, arXiv:1308.0540.

[152] A. J. Larkoski, F. Maltoni, and M. Selvaggi, *Tracking down hyper-boosted top quarks*, JHEP **06** (2015) 032, arXiv:1503.03347.

[153] S. Bressler, T. Flacke, Y. Kats, S. J. Lee, and G. Perez, *Hadronic Calorimeter Shower Size: Challenges and Opportunities for Jet Substructure in the Superboosted Regime*, Phys. Lett. **B756** (2016) 137–141, arXiv:1506.02656.

[154] A. Cukierman and B. Nachman, *Mathematical Properties of Numerical Inversion for Jet Calibrations*, Nucl. Instrum. Meth. **A858** (2017) 1–11, arXiv:1609.05195.

[155] ATLAS Collaboration, *In-situ measurements of the ATLAS large-radius jet response in 13 TeV pp collisions*, ATLAS-CONF-2017-063, 2017. https://cds.cern.ch/record/2275655.

[156] Public plots: Large-R jet pT and mass scale uncertainties using in-situ track-based measurements. http://atlas.web.cern.ch/Atlas/GROUPS/PHYSICS/PLOTS/JETM-2016-001/.

[157] ATLAS Collaboration, *Study of the material of the ATLAS inner detector for Run 2 of the LHC*, JINST **12** (2017) no. 12, P12009, arXiv:1707.02826.

[158] ATLAS Collaboration, *Performance of the ATLAS Track Reconstruction Algorithms in Dense Environments in LHC Run 2*, Eur. Phys. J. **C77** (2017) no. 10, 673, arXiv:1704.07983.

[159] ATLAS Collaboration, *Early Inner Detector Tracking Performance in the 2015 data at $\sqrt{s}$ = 13 TeV*, ATL-PHYS-PUB-2015-051, 2015. http://cds.cern.ch/record/2110140.

[160] B. Hespel, D. Lopez-Val, and E. Vryonidou, *Higgs pair production via gluon fusion in the Two-Higgs-Doublet Model*, JHEP **09** (2014) 124, arXiv:1407.0281.

[161] J. Alwall, R. Frederix, S. Frixione, V. Hirschi, F. Maltoni, O. Mattelaer, H. S. Shao, T. Stelzer, P. Torrielli, and M. Zaro, *The automated computation of tree-level and next-to-leading order differential cross sections, and their matching to parton shower simulations*, JHEP **07** (2014) 079, arXiv:1405.0301.

[162] H.-L. Lai, M. Guzzi, J. Huston, Z. Li, P. M. Nadolsky, J. Pumplin, and C. P. Yuan, *New parton distributions for collider physics*, Phys. Rev. **D82** (2010) 074024, arXiv:1007.2241.

[163] M. Bahr et al., *Herwig++ Physics and Manual*, Eur. Phys. J. **C58** (2008) 639–707, arXiv:0803.0883.

[164] M. H. Seymour and A. Siodmok, *Constraining MPI models using σ_{eff} and recent Tevatron and LHC Underlying Event data*, JHEP **10** (2013) 113, arXiv:1307.5015.

[165] T. Sjöstrand, S. Mrenna, and P. Z. Skands, *A brief introduction to PYTHIA 8.1*, Comput.Phys.Commun. **178** (2008) 852–867, arXiv:0710.3820.

[166] ATLAS Collaboration, *ATLAS Pythia 8 tunes to 7 TeV data*, ATL-PHYS-PUB-2014-021, 2014. https://cds.cern.ch/record/1966419.

[167] R. D. Ball, V. Bertone, F. Cerutti, L. Del Debbio, S. Forte, A. Guffanti, J. I. Latorre, J. Rojo, and M. Ubiali, *Impact of Heavy Quark Masses on Parton Distributions and LHC Phenomenology*, Nucl. Phys. **B849** (2011) 296–363, arXiv:1101.1300.

[168] P. Nason, *A New method for combining NLO QCD with shower Monte Carlo algorithms*, JHEP **11** (2004) 040, arXiv:hep-ph/0409146.

[169] S. Frixione, P. Nason, and C. Oleari, *Matching NLO QCD computations with Parton Shower simulations: the POWHEG method*, JHEP **11** (2007) 070, arXiv:0709.2092.

[170] S. Alioli, P. Nason, C. Oleari, and E. Re, *A general framework for implementing NLO calculations in shower Monte Carlo programs: the POWHEG BOX*, JHEP **06** (2010) 043, arXiv:1002.2581.

[171] T. Sjöstrand, S. Mrenna, and P. Z. Skands, *PYTHIA 6.4 Physics and Manual*, JHEP **0605** (2006) 026, arXiv:hep-ph/0603175.

[172] P. M. Nadolsky, H.-L. Lai, Q.-H. Cao, J. Huston, J. Pumplin, D. Stump, W.-K. Tung, and C. P. Yuan, *Implications of CTEQ global analysis for collider observables*, Phys. Rev. **D78** (2008) 013004, arXiv:0802.0007.

[173] P. Z. Skands, *Tuning Monte Carlo Generators: The Perugia Tunes*, Phys. Rev. **D82** (2010) 074018, arXiv:1005.3457.

[174] M. Czakon and A. Mitov, *Top++: A Program for the Calculation of the Top-Pair Cross-Section at Hadron Colliders*, Comput. Phys. Commun. **185** (2014) 2930, arXiv:1112.5675.

[175] M. Aliev, H. Lacker, U. Langenfeld, S. Moch, P. Uwer, and M. Wiedermann, *HATHOR: HAdronic Top and Heavy quarks crOss section calculatoR*, Comput. Phys. Commun. **182** (2011) 1034–1046, arXiv:1007.1327.

[176] P. Kant, O. M. Kind, T. Kintscher, T. Lohse, T. Martini, S. Mlbitz, P. Rieck, and P. Uwer, *HatHor for single top-quark production: Updated predictions and uncertainty estimates for single top-quark production in hadronic collisions*, Comput. Phys. Commun. **191** (2015) 74–89, arXiv:1406.4403.

[177] N. Kidonakis, *Two-loop soft anomalous dimensions for single top quark associated production with a W- or H-*, Phys. Rev. **D82** (2010) 054018, arXiv:1005.4451.

[178] T. Gleisberg, S. Hoeche, F. Krauss, M. Schonherr, S. Schumann, F. Siegert, and J. Winter, *Event generation with SHERPA 1.1*, JHEP **02** (2009) 007, arXiv:0811.4622.

[179] T. Gleisberg and S. Hoeche, *Comix, a new matrix element generator*, JHEP **12** (2008) 039, arXiv:0808.3674.

[180] F. Cascioli, P. Maierhofer, and S. Pozzorini, *Scattering Amplitudes with Open Loops*, Phys. Rev. Lett. **108** (2012) 111601, arXiv:1111.5206.

[181] S. Hoeche, F. Krauss, M. Schonherr, and F. Siegert, *QCD matrix elements + parton showers: The NLO case*, JHEP **04** (2013) 027, arXiv:1207.5030.

[182] R. D. Ball et al., *Parton distributions for the LHC Run II*, JHEP **04** (2015) 040, arXiv:1410.8849.

[183] K. Melnikov and F. Petriello, *Electroweak gauge boson production at hadron colliders through O(alpha(s)**2)*, Phys. Rev. **D74** (2006) 114017, arXiv:hep-ph/0609070.

[184] ATLAS Collaboration, *Summary of ATLAS Pythia 8 tunes*, ATL-PHYS-PUB-2012-003, 2012. https://cds.cern.ch/record/1474107.

[185] A. D. Martin, W. J. Stirling, R. S. Thorne, and G. Watt, *Parton distributions for the LHC*, Eur. Phys. J. **C63** (2009) 189–285, arXiv:0901.0002.

[186] D. J. Lange, *The EvtGen particle decay simulation package*, Nucl. Instrum. Meth. **A462** (2001) 152–155.

[187] ATLAS Collaboration, *Comparison of Monte Carlo generator predictions to ATLAS measurements of top pair production at 7 TeV*, ATL-PHYS-PUB-2015-002, 2015. https://cds.cern.ch/record/1981319.

[188] ATLAS Collaboration, *ATLAS simulation of boson plus jets processes in Run 2*, ATL-PHYS-PUB-2017-006, 2017. https://cds.cern.ch/record/2261937.

[189] ATLAS Collaboration, *Multi-Boson Simulation for 13 TeV ATLAS Analyses*, ATL-PHYS-PUB-2017-005, 2017. https://cds.cern.ch/record/2261933.

[190] ATLAS Collaboration, *Jet Calibration and Systematic Uncertainties for Jets Reconstructed in the ATLAS Detector at* $\sqrt{s} = 13$ *TeV*, ATL-PHYS-PUB-2015-015, 2015. http://cds.cern.ch/record/2037613.

[191] ATLAS Collaboration, *Luminosity determination in pp collisions at* $\sqrt{s} = 8$ *TeV using the ATLAS detector at the LHC*, Eur. Phys. J. **C76** (2016) no. 12, 653, arXiv:1608.03953.

[192] S. Frixione, E. Laenen, P. Motylinski, B. R. Webber, and C. D. White, *Single-top hadroproduction in association with a W boson*, JHEP **07** (2008) 029, arXiv:0805.3067.

[193] S. Dulat, T.-J. Hou, J. Gao, M. Guzzi, J. Huston, P. Nadolsky, J. Pumplin, C. Schmidt, D. Stump, and C. P. Yuan, *New parton distribution functions from a global analysis of quantum chromodynamics*, Phys. Rev. **D93** (2016) no. 3, 033006, arXiv:1506.07443.

[194] L. A. Harland-Lang, A. D. Martin, P. Motylinski, and R. S. Thorne, *Parton distributions in the LHC era: MMHT 2014 PDFs*, Eur. Phys. J. **C75** (2015) no. 5, 204, arXiv:1412.3989.

[195] J. S. Conway, *Incorporating Nuisance Parameters in Likelihoods for Multisource Spectra*, in *Proceedings, PHYSTAT 2011 Workshop on Statistical Issues Related to Discovery Claims in Search Experiments and Unfolding, CERN,Geneva, Switzerland 17-20 January 2011*, pp. 115–120. 2011. arXiv:1103.0354.

[196] G. Cowan, K. Cranmer, E. Gross, and O. Vitells, *Asymptotic formulae for likelihood-based tests of new physics*, Eur. Phys. J. **C71** (2011) 1554, arXiv:1007.1727.

[197] A. L. Read, *Presentation of search results: The CL(s) technique*, J. Phys. **G28** (2002) 2693–2704.

[198] K. Cranmer, G. Lewis, L. Moneta, A. Shibata, and W. Verkerke, *HistFactory: A tool for creating statistical models for use with RooFit and RooStats*, CERN-OPEN-2012-016, 2012. https://cds.cern.ch/record/1456844.

[199] L. Moneta, K. Belasco, K. S. Cranmer, S. Kreiss, A. Lazzaro, D. Piparo, G. Schott, W. Verkerke, and M. Wolf, *The RooStats Project*, PoS **ACAT2010** (2010) 057, arXiv:1009.1003.

[200] W. Verkerke, *Statistical Software for the LHC*, 2008. https://cds.cern.ch/record/1099988.

[201] R. Brun and F. Rademakers, *ROOT: An object oriented data analysis framework*, Nucl. Instrum. Meth. **A389** (1997) 81–86.

[202] ATLAS Collaboration, *Flavor Tagging with Track Jets in Boosted Topologies with the ATLAS Detector*, ATL-PHYS-PUB-2014-013, 2014. http://cds.cern.ch/record/1750681.

[203] ATLAS Collaboration, *Expected Performance of Boosted Higgs ($\rightarrow b\bar{b}$) Boson Identification with the ATLAS Detector at $\sqrt{s} = 13$ TeV*, ATL-PHYS-PUB-2015-035, 2015. http://cds.cern.ch/record/2042155.

[204] ATLAS Collaboration, *Boosted Higgs ($\rightarrow b\bar{b}$) Boson Identification with the ATLAS Detector at $\sqrt{s} = 13$ TeV*, ATLAS-CONF-2016-039, 2016. https://cds.cern.ch/record/2206038.

[205] D. Krohn, J. Thaler, and L.-T. Wang, *Jets with Variable R*, JHEP **06** (2009) 059, arXiv:0903.0392.

[206] C. Chen, *New approach to identifying boosted hadronically-decaying particle using jet substructure in its center-of-mass frame*, Phys. Rev. **D85** (2012) 034007, arXiv:1112.2567.

[207] ATLAS Collaboration, *Measurement of the cross-section of high transverse momentum vector bosons reconstructed as single jets and studies of jet substructure in pp collisions at $\sqrt{s} = 7$ TeV with the ATLAS detector*, New J. Phys. **16** (2014) no. 11, 113013, arXiv:1407.0800.

[208] C. Chen, *Identification of a bottom quark-antiquark pair in a single jet with high transverse momentum and its application*, Phys. Rev. **D92** (2015) no. 9, 093010, arXiv:1507.06913.

[209] A. D. Bukin, *Fitting function for asymmetric peaks*, arXiv:0711.4449.